
Electronic Thesis and Dissertation Repository

12-17-2021 11:00 AM

Brown Dwarf Atmospheres at High Cadence and Spectral Resolution: A Speed Limit on Brown Dwarf Rotation and a Spectroscopic Atlas of a 1050 K Atmosphere

Megan E. Tannock, *The University of Western Ontario*

Supervisor: Metchev, Stanimir A., *The University of Western Ontario*

A thesis submitted in partial fulfillment of the requirements for the Doctor of Philosophy degree in Astronomy

© Megan E. Tannock 2021

Follow this and additional works at: <https://ir.lib.uwo.ca/etd>



Part of the [Stars, Interstellar Medium and the Galaxy Commons](#)

Recommended Citation

Tannock, Megan E., "Brown Dwarf Atmospheres at High Cadence and Spectral Resolution: A Speed Limit on Brown Dwarf Rotation and a Spectroscopic Atlas of a 1050 K Atmosphere" (2021). *Electronic Thesis and Dissertation Repository*. 8354.

<https://ir.lib.uwo.ca/etd/8354>

This Dissertation/Thesis is brought to you for free and open access by Scholarship@Western. It has been accepted for inclusion in Electronic Thesis and Dissertation Repository by an authorized administrator of Scholarship@Western. For more information, please contact wlsadmin@uwo.ca.

Abstract

Brown dwarfs are sub-stellar objects that form like stars but are not sufficiently massive to sustain hydrogen fusion in their cores. Characterized by cool, molecule-rich atmospheres, brown dwarfs demonstrate great diversity in spectroscopic appearance and share many properties with giant exoplanets. In this thesis I present two investigations: the first is a detailed photometric and spectroscopic study of the three most rapidly rotating brown dwarfs. The second examines a spectrum of a cool brown dwarf at unprecedented spectral resolution and signal-to-noise ratio to study the accuracy of theoretical model photospheres.

Photometric monitoring of brown dwarfs has revealed that periodic variability is common and that brown dwarf atmospheres are composed of patchy, multi-layer clouds of varying thicknesses and compositions. In my first paper, I present the discovery of rapid photometric variability in three brown dwarfs from long-duration photometric monitoring with the Spitzer Space Telescope. Using moderate-resolution infrared spectroscopy I find a large degree of rotational broadening in each of these brown dwarfs, confirming that the rapid variability is due to fast rotation. These three brown dwarfs have the shortest rotation periods ever measured, between 1.08 and 1.23 hours. When put in context with the entire sample of brown dwarfs with known rotation periods, the clustering near the short-period end suggests that brown dwarfs are unlikely to spin much faster than once an hour.

In my second paper, I study the atmospheric composition of a cold 1050 ± 50 K (T6-type) brown dwarf. Even the most up-to-date theoretical model photospheres do not completely reproduce observed spectroscopic features in cold brown dwarfs, limiting our ability to constrain their fundamental properties. I compare the observed data to these models to assess their accuracy and completeness. I draw conclusions about which models are the most reliable and which spectroscopic regions should be used to estimate physical parameters of cold brown dwarfs and, by extension, exoplanets. Additionally, I present the first unambiguous detections of hydrogen sulfide in an extra-solar atmosphere. These data comprise the most detailed atlas of spectroscopic lines in a cold brown dwarf available to date.

Summary for Lay Audience

In between stars and planets there is a class of astronomical object called brown dwarfs. Brown dwarfs share properties with both stars and planets; they are formed in the same way as stars, but have much lower masses, and they have thick, cloudy atmospheres similar to giant planets like Jupiter. The clouds in the atmospheres of brown dwarfs are made up of a variety of materials, and they tend to be patchy and varied in thickness. Storms, similar to Jupiter's great red spot, can develop and evolve in the atmospheres of brown dwarfs.

The varying thickness and composition of the clouds means that different parts of a brown dwarf's surface emit different amounts of light. As brown dwarfs rotate, different clouds and atmospheric structures will face the Earth at a given time, so the amount of light we measure will change over time. When we see a repeated pattern in the amount of light we measure, we know we are seeing the same surface features going in and out of view, and so we can measure how fast brown dwarfs are rotating. In the first half of this thesis, I present the discovery of the fastest-ever rotating brown dwarfs. They have rotation periods of approximately one hour, which is nearly ten times faster than Jupiter, and 24 times faster than the Earth. I explore the consequences of this fast rotation and put these speedy spinners in context with the rest of the known rotation periods for brown dwarfs.

The clouds on brown dwarfs are composed of many materials we are familiar with, like water, carbon monoxide, and methane. A key tool in understanding these materials, how they interact, and the physics governing all of this, are atmospheric models. In the second half of this thesis, I study these molecules and rigorously test the available models with one of the highest-resolution brown dwarf data sets ever observed. I draw conclusions about which of the currently-available models are the most reliable and describe how to measure fundamental properties of brown dwarfs, like their temperatures, with these models.

Co-Authorship Statement

The following authors contributed to Chapter 2: Megan Tannock, Stanimir Metchev, Aren Heinze, Paulo Miles-Páez, Jonathan Gagné, Adam Burgasser, Mark Marley, Dániel Apai, Genaro Suárez, and Peter Plavchan.

MT reduced the photometric data, observed and reduced the spectroscopic data for the L3.5 dwarf, wrote the spectroscopic model fitting code, performed the comparison between data and models, performed the photometric and spectroscopic analysis and calculations, generated all figures, and wrote the text. SM, AH, AB, MM, DA, and PP were co-investigators on the original telescope proposal to obtain the photometric data used in this work. SM oversaw the project and provided guidance. AH wrote the aperture photometry code, light-curve fitting code, and MCMC used in this analysis, and provided helpful guidance. PMP provided comments on the final manuscript. JG observed and provided the reduced spectrum of the L8 dwarf, and comments on the final manuscript. AB observed and provided the reduced spectrum of the T7 dwarf, and comments on the final manuscript. MM computed the oblatenesses, and provided comments on the final manuscript. DA provided comments on the final manuscript. GS provided guidance on how to compute the vertical offsets and provided comments on the final manuscript. PP provided comments on the final manuscript.

The following authors contributed to Chapter 3: Megan Tannock, Stanimir Metchev, Callie Hood, Gregory Mace, Jonathan Fortney, Caroline Morley, and Daniel Jaffe.

MT observed and reduced the spectroscopic data, wrote the spectroscopic model fitting code, performed the comparison between data and models, performed the analysis and calculations, generated all figures, and wrote the text. SM oversaw the project and provided guidance. CH generated the updated spectroscopic models and provided comments on the final manuscript. GM suggested the original idea for this work, provided guidance on the data reductions and analysis, and provided comments on the final manuscript. JF provided helpful discussions on the analysis and provided comments on the final manuscript. CM provided comments on the final manuscript. DJ provided comments on the final manuscript.

Permissions

All figures in Chapter 1 of this thesis which are reproductions from published works are accompanied by their original citations. Additional permissions and licensing are listed here:

Figures 1.1, 1.2, 1.3, and 1.4 have been reproduced with permission from the American Physical Society under license RNP/21/NO V/046839.

Figures 1.5, 1.8, and 1.12 have been reproduced with the consent of the original authors and with permission from the AAS Journals.

Figure 1.6 has been reproduced with permission from Springer Nature under license 5191481281975.

Figure 1.9 has been reproduced with permission from The American Association for the Advancement of Science under license 5191491233482.

Figure 1.10 has been reproduced with permission from the original creator Dániel Apai.

Figure 1.11 has been reproduced with permission from The American Association for the Advancement of Science under license 5191491460056.

Figures 1.14 and 1.15 have been reproduced with permission from the CCC under licence ID 1162413-1.

Figure 1.16 has been reproduced with permission from the CCC under licence ID 1162414-1.

Chapter 2 of this thesis is a version of Megan E. Tannock et al. 2021 AJ 161 224, DOI: [10.3847/1538-3881/abeb67](https://doi.org/10.3847/1538-3881/abeb67), and has been reproduced with permission from the the AAS Journals.

Epigraph

“Nothing is impossible. Not if you can imagine it. That’s what being a scientist is all about.”

- Professor Hubert J. Farnsworth, Futurama (2000)

Acknowledgements

I have been very fortunate to have a huge crowd cheering me on from all across Canada and around the world. I am very grateful for the amazing research and travel opportunities I have had during grad school, and for every single person who helped make this thesis possible. Thank you to everyone who ever helped me with an assignment, proof-read a document for me, listened to me give a practice talk, hung out with me at a conference, grabbed a mid-afternoon iced coffee with me, or just sat with me when I needed a friend.

First and foremost I want to thank my PhD supervisor, Dr. Stanimir Metchev. At all times since I have met you, you have been kind and patient. I have learned so much from you, and I am so proud of the scientist I have become under your guidance. Thank you for all of your help and encouragement. It has been a pleasure to work with you these last 6 years.

I want to thank all of my collaborators, co-authors, and anonymous journal referees for your help and the hard work you put into these papers. None of this work would have been possible without you. Thank you to Sarah, Tristan, James, Pegah, Ruth, and Kristi for being the beta readers of Chapters 1 and 4 of this thesis. Thanks to Dad for catching all my typos.

Thank you to all of my mentors at Western, both official and unofficial. In particular, Tamie, Sarah, Pauline, and Peter. Thank you to Paulo and Genaro for your help and encouragement. Thank you to my Academic Committee members, Paul and Alex. Thank you to all of the P&A department staff and custodians, especially Brian.

A special thank you to Amanda, for being the best friend, roommate, colleague, and belay partner a girl could have asked for. I wouldn't have made it through without you

I have made a number of incredible friends in London: Pegah, Robin, Cam, Ellie, Keegan, Moh, Dan, Isabelle, Dave, Amy, Kendra, Sebastian, Ghazal, Emily, Tristan, Chris, Amgad, John, Sarah, James, and Rachel. Thank you for the good times and all of the support and laughs. I will always treasure our adventures around London, from Junction to the Morrissey House and everywhere in between.

Thank you to my original physics crew from back at UVic: Kristi, Matthew, Ruth, and Jacqui. You all inspire me. A big thank you to Dr. Kim Venn, who was the very first person who told me I would be good at research. Thank you to Dr. Karun Thanjavur for your continued support over the last decade.

To my three best friends of the last 15 years, Megan, Chelsea, and Emma: our daily chats and your unconditional love and support have kept me going through all of this. Thank you for always being there for me. I can't wait to take that "when we all turn 30" vacation (last year...) that we will realistically take in our 40s.

Thank you to my ever-supportive boyfriend Ben. You have seen me at my best and worst during this degree, and you stuck by me. Thanks for laughing with me and always keeping me grounded. Thank you to Kurt and Carla for welcoming me into your family while I was so far away from my own.

Thank you to my parents, Mary and Shane, my brother, Kevin, and the rest of my family back on the Island. It has been hard to be so far from home, sometimes unbearable, but I felt your support every minute of every day. I love you all so much. Shout out to all the dogs: Copper, Sawyer, Annie, and our newest family member, Dino.

And thanks to me, for being honest with myself, doing my best, and working hard. I am not the same person I was when I started grad school, and I am better off for it.

No thanks at all to COVID-19. This all could have been over a lot sooner without you.



Myself and my trusty thesis assistant/sidekick, Dino. Photo courtesy of Ben Nehring.

The majority of the work presented in this thesis was conducted at the University of Western Ontario, which is located on the traditional territories of the Anishinaabek, Haudenosaunee, Lūnaapéewak, and Chonnonton Nations. Modern astronomy research, including the work presented here, builds upon the extensive history of Indigenous astronomy, and I am very honoured to contribute to such an ancient field of study. I wish to recognize and acknowledge the very significant cultural role and reverence that the summit of Maunakea has always held within the Indigenous Hawaiian community. I am very fortunate and grateful to have had the opportunity to visit and conduct observations from this mountain.

This work was supported by an Ontario Graduate Scholarship.

Keywords: astrophysics, brown dwarfs, variability, stellar rotation, atmospheres, chemistry, photometry, spectroscopy

Contents

Abstract	ii
Summary for Lay Audience	iii
Co-Authorship Statement	iv
Permissions	v
Epigraph	vi
Acknowledgements	vii
List of Figures	xiv
List of Tables	xvi
1 Introduction	1
1.1 Basic Brown Dwarf Properties	2
1.1.1 Brown Dwarf Formation and Interiors	2
1.1.2 Effective Temperature and the Classification System	5
1.1.3 Atmospheric Structure and Clouds	13
1.2 Rotation and Variability	16
1.2.1 Photometric Variability Due to Clouds	17
1.2.2 Other Sources of Variability	19
1.2.3 Overview of Previous Variability Studies	23
1.2.4 Viewing Geometry	25
1.3 Brown Dwarf Atmospheric Chemistry	28
1.3.1 Detailed Chemistry by Spectral Type	28
1.3.2 Challenges in Understanding Brown Dwarf Chemistry	31
1.3.3 Atmospheric Models	33
1.4 What This Thesis Addresses and Project Motivation	36

2	Weather on Other Worlds. V. The Three Most Rapidly Rotating Ultra-Cool Dwarfs	48
2.1	Introduction	48
2.2	Spitzer Photometry, Variability, and Periods	49
2.2.1	Warm Spitzer Observations	49
2.2.2	Photometry and Initial Variability Assessment	50
2.2.3	Simultaneous Fitting for Pixel Phase and Astrophysical Variability	53
2.2.4	Discussion of Photometric Variability: Periods and Mechanisms	58
2.3	Spectroscopic Observations	59
2.3.1	Magellan/FIRE Spectroscopy: 2MASS J0348-6022 (T7) and 2MASS J1219+3128 (L8)	60
2.3.2	Gemini/GNIRS Spectroscopy: 2MASS J0407+1546 (L3)	64
2.4	Confirmation of Rapid Rotations and Determination of Physical Parameters	65
2.4.1	2MASS J0348-6022 (T7)	68
2.4.2	2MASS J1219+3128 (L8)	73
2.4.3	2MASS J0407+1546 (L3.5)	73
2.5	Discussion	77
2.5.1	The Three Most Rapidly Rotating Ultra-cool Dwarfs: Possibility for Auroral Emissions	77
2.5.2	Proximity to Rotational Break-up and Oblateness	81
2.6	Conclusions	83
2.7	Appendix: All Known Brown Dwarf Rotation Periods	83
3	IGRINS Spectroscopy of the T6 Dwarf 2MASS J08173001-6155158: Verification of Water, Methane, and Ammonia Line Lists and a Near-Infrared Spectroscopic Atlas of a Cold Brown Dwarf	95
3.1	Introduction	95
3.2	Spectroscopy with IGRINS on Gemini South	97
3.2.1	Data Reduction	97
3.2.2	Confirmation of Wavelength Calibration and Masking of Telluric Lines	100
3.3	Model Fitting and Parameter Determination	101
3.3.1	Fitting of Photospheric Models	102
3.3.2	Determination of Physical Parameters	103
3.4	Molecule-by-Molecule Analysis of the Model Spectra	107
3.4.1	Water	110
3.4.2	Methane	111

3.4.3	Carbon Monoxide	112
3.4.4	Ammonia	116
3.4.5	Hydrogen Sulfide	117
3.4.6	Shortcomings of the Models and Unidentified Lines	118
3.5	Lessons Learned	120
3.5.1	Fitted Spectroscopic Parameters	122
3.5.2	Specific Molecules	123
3.6	Conclusions	124
3.7	Appendix: The Full Suite of Model Fits for Every IGRINS Order	124
4	Summary and Conclusions	158
4.1	Future Work	160
	Curriculum Vitae	164

List of Figures

1.1	Luminosity of brown dwarfs as a function of age	4
1.2	Core temperature of brown dwarfs as a function of age	5
1.3	Radius of brown dwarfs as a function of age.	6
1.4	Effective temperature of brown dwarfs as a function of age	7
1.5	Effective temperature of brown dwarfs as a function of spectral type	9
1.6	Infrared spectra of ultra-cool dwarfs and Jupiter	11
1.7	Colour-magnitude diagram of ultra-cool dwarfs	12
1.8	Model spectra of two brown dwarfs with different cloud coverage	14
1.9	Illustration of the cloud and gas layers in Jupiter, and T, L, and M dwarfs	15
1.10	Illustration of patchy cloud layers in brown dwarf atmospheres	17
1.11	Models of two main atmospheric structures and their impacts on light curves	20
1.12	Mid-infrared light curves of L and T dwarfs	21
1.13	Schematic of the viewing geometry of rotating objects	26
1.14	Detailed near-infrared spectral sequence of ultra-cool dwarfs (0.95–2.3 μm)	29
1.15	Detailed near-infrared spectral sequence of ultra-cool dwarfs (0.95–1.35 μm)	30
1.16	Pressure-temperature profiles and condensation curves for brown dwarfs	31
2.1	Periodogram-based variability assessment	51
2.2	Lomb-Scargle periodogram power distributions	52
2.3	Spitzer mid-infrared light curves	54
2.4	Flux as a function of detector position	56
2.5	FIRE spectra of 2MASS J0348–6022 (T7)	62
2.6	FIRE spectra of 2MASS J1219+3128 (L8)	63
2.7	GNIRS spectra of 2MASS J0407+1546 (L3.5)	65
2.8	Photospheric model fits to the narrow wavelength regions of 2MASS J0348–6022	71
2.9	Photospheric model fits to the full-band spectra of 2MASS J0348–6022	72
2.10	Photospheric model fits to the narrow wavelength regions of 2MASS J1219+3128	74
2.11	Photospheric model fits to the full-band spectra of 2MASS J1219+3128	75
2.12	Photospheric model fits to the full spectral coverage of 2MASS J0407+1546	76

2.13	Rotation period as a function of spectral type for brown dwarfs	78
3.1	A sample IGRINS order showing spectra and SNR for all observing epochs . . .	99
3.2	The full <i>H</i> - and <i>K</i> -band IGRINS spectra of 2MASS J08173001–6155158 . . .	100
3.3	Results of the model fitting to 2MASS J08173001–6155158 for the <i>H</i> band . .	105
3.4	Results of the model fitting of 2MASS J08173001–6155158 for the <i>K</i> band . .	106
3.5	A sample order where models are well matched to the data	108
3.6	A sample order where models are poorly matched to the data	110
3.7	A sample order with prominent CH ₄ lines, and the improvement made with updated line lists	113
3.8	A sample order with CO lines, and a model with increased CO abundance . . .	115
3.9	A sample order showing a clear detection of NH ₃ lines	117
3.10	A sample order showing a clear detection of H ₂ S lines	118
3.11	An example of the analysis to identify discrepancies between models and data .	120
3.12	A sample order showing an unidentified absorption feature	122
3.13	The IGRINS <i>H</i> -band spectrum shown for each of the 26 orders with models, residuals, and Earth’s transmittance spectrum	125
3.14	The IGRINS <i>K</i> -band spectrum shown for each of the 23 orders with models, residuals, and Earth’s transmittance spectrum	139

List of Tables

2.1	Spitzer photometry and results from Markov Chain Monte Carlo analysis of periods and peak-to-trough amplitudes	57
2.2	Magellan/FIRE and Gemini North/GNIRS spectroscopic observations	61
2.3	Best-fit photospheric model parameters for the narrow-wavelength regions	69
2.4	Best-fit photospheric model parameters for the full bands	70
2.5	Physical parameters for the three L and T dwarfs	80
2.6	Known L-, T-, and Y-dwarf rotation periods	84
2.6	Known L-, T-, and Y-dwarf rotation periods	85
3.1	Gemini/IGRINS spectroscopic observations of 2MASS J08173001–6155158	98
3.2	Wavelengths of the IGRINS orders and the major molecular absorbers	104
3.3	Physical parameters of 2MASS J08173001–6155158	107
3.4	Literature references for the line lists of each model photosphere family	109
3.5	Wavelengths of discrepancies in the models and unidentified lines	121

Chapter 1

Introduction

Brown dwarfs are intermediate objects between stars and planets — they are not massive enough to sustain hydrogen fusion, and are therefore not stars, but are also too massive to be classified as planets under some classification schemes. Brown dwarfs form in the same way as stars, but are similar to gas giant planets in their temperature and chemical makeup. They have atmospheric temperatures that range from hundreds of Kelvin, even cooler than the surface temperature of the Earth, up to thousands of Kelvin, as hot as the coolest stars. In this temperature range, brown dwarf atmospheres are rife with interesting molecules like carbon monoxide, methane, ammonia, and even water.

Brown dwarfs play a key role in the study of sub-stellar atmospheres and understanding the formation and evolution of our exoplanetary neighbours. In almost every case, the overwhelming light from the host star prevents us from directly observing exoplanets, forcing us to rely on indirect measurements and theory. Luckily, brown dwarfs make excellent analogues for studying high-mass planets; they have similar atmospheric temperatures, radii, and atmospheric content, and most brown dwarfs are far away from the overwhelming light of a host star and are therefore more observationally accessible.

Since the first confirmed identification of the brown dwarfs Teide 1 ([Rebolo et al., 1995](#)) and Gliese 229B ([Oppenheimer et al., 1995](#)), the study of brown dwarfs has grown immensely. [Mužić et al. \(2017\)](#) estimate that the Milky Way contains 25 – 100 billion brown dwarfs, and we are now starting to see how dynamic and varied these objects are.

1.1 Basic Brown Dwarf Properties

1.1.1 Brown Dwarf Formation and Interiors

In the past, brown dwarfs were commonly distinguished from stars and planets by their masses, regardless of where they are located or how they formed. At the high-mass end, stars support sustained hydrogen burning, while brown dwarfs do not. A mass of $\sim 0.070 M_{\odot}$ (or $73 M_{\text{Jup}}$; where M_{\odot} and M_{Jup} are the masses of the Sun and Jupiter, respectively) is required for sustained hydrogen fusion (Hayashi & Nakano, 1963). On the other end of the mass scale, we sometimes discern between brown dwarfs and planets at the minimum mass limit of deuterium (heavy hydrogen; ^2H) fusion, $M \gtrsim 0.012 M_{\odot}$ ($13 M_{\text{Jup}}$; Dantona & Mazzitelli 1985; Chabrier et al. 2000; Boss et al. 2007).

It is possible for high mass brown dwarfs ($M \gtrsim 0.07 M_{\odot}$) to burn hydrogen through a truncated proton-proton (p-p) chain in their early lives, sometimes for billions of years (Burrows & Liebert, 1993). The thermonuclear reactions relevant for brown dwarfs are the first two steps of the p-p I chain:



and



where p represents a proton, or hydrogen atom (^1H), d is deuterium (^2H), e^+ is a positron, ν is a neutrino, and γ is a photon (e.g., Burrows & Liebert 1993). These reactions occur for core temperatures (T_c) of 3×10^6 K and 6×10^5 K, respectively.

The first reaction occurs for the most massive brown dwarfs, forming deuterium, and the second occurs for brown dwarfs with $M \gtrsim 0.012 M_{\odot}$, depleting both primordial deuterium, as well as any deuterium formed from earlier reactions. The core temperatures of brown dwarfs are not high enough to complete the p-p I chain by overcoming the Coulomb barrier of the ${}^3\text{He}$ - ${}^3\text{He}$ reaction to form ${}^4\text{He}$ ($T_c = 6 \times 10^6$ K).

It has been argued (e.g., Chabrier et al. 2005) that the deuterium burning limit as a distinction between brown dwarfs and planets is a poor criterion, as the deuterium burning limit depends not only on mass, but also on the chemical makeup of the object. Spiegel et al. (2011) found that deuterium burning generally occurs for masses above $13 M_{\text{Jup}}$, but this limit is dependent on helium abundance, deuterium abundance, and overall metallicity (the fraction of mass that is not hydrogen or helium). They found that the minimum deuterium burning mass ranges from $11.0 M_{\text{Jup}}$ to $16.3 M_{\text{Jup}}$, depending on the composition of the object.

Chabrier et al. (2005) suggested planets should be distinguished from brown dwarfs and stars, based on formation mechanisms, thus removing the ambiguity associated with mass

limits. They proposed that objects of any mass formed from the gravitational collapse of a giant molecular cloud (in multi-object systems or in isolation) are either stars or brown dwarfs, and any objects formed in a protoplanetary disk around a parent star (or brown dwarf) are planets. Objects of the latter type should also have enhanced abundances of heavy elements. In this scenario, the highest mass brown dwarfs are still distinguished from stars by sustained hydrogen burning. We will assume this definition for a brown dwarf in this thesis, where anything formed from a giant molecular cloud with a mass below the limit for sustained hydrogen burning is a brown dwarf.

Main sequence stars exist in thermal equilibrium, supported by the stable hydrogen fusion in their cores. Because brown dwarfs form from cores with too little mass to support stable hydrogen burning, they cannot reach thermal equilibrium, and they never leave the Hayashi track (the luminosity–temperature relationship followed by newly formed stars with masses less than $3 M_{\odot}$) like main sequence stars (Burrows & Liebert, 1993). As such, all brown dwarf interiors are convective for their entire lives, and the initial formation conditions play a large role in determining the physical properties of brown dwarfs (temperature, rotation rates, etc.).

The main energy source powering the luminosity for brown dwarfs is heat retained from their formation and gravitational collapse of their parent molecular cloud. Those which are massive enough to sustain deuterium burning or, at very high brown dwarf masses, lithium ($M \gtrsim 0.065 M_{\odot}$; Chabrier et al. 2000) or hydrogen burning, have an additional interior source of energy for a short time, maintaining their luminosity for the early stages of their lives (Basri & Brown, 2006). Without hydrogen burning to provide an on-going energy source to support the outer layers, brown dwarfs contract under gravity in their early lives, and spend the remainder of their lives cooling, as shown in Figure 1.1.

Although their atmospheres are relatively cool, the core temperatures of brown dwarfs are quite hot, approximately millions of Kelvin, as shown in Figure 1.2. This is not hot enough to overcome the Coulomb barrier, thus preventing most nuclear reactions (like hydrogen and helium fusion) from taking place, and effectively fixing the distance between particles (primarily hydrogen) in the interior of brown dwarfs. As a result, the radius (R) is related to the mass (M) as $R \propto M^{1/3}$ when considering Coulomb effects (Burrows & Liebert, 1993; Burrows et al., 2001). It is, however, hot enough to ionize hydrogen, and so the outer layers of a brown dwarf are supported from gravitational collapse by electron degeneracy pressure (Chabrier & Baraffe, 2000). Under the condition of electron degeneracy, the radius is related to the mass by $R \propto M^{-1/3}$. These two competing effects cancel each other out and result in a roughly constant radius ($R \sim 0.8 - 1.0 R_{\text{Jup}}$; Chabrier et al. 2000) over the mass range of brown dwarfs. Figure 1.3 shows how the radii of brown dwarfs change over time, settling to near constant radii after about 500 Myr. The youngest brown dwarfs that have not yet finished contracting under

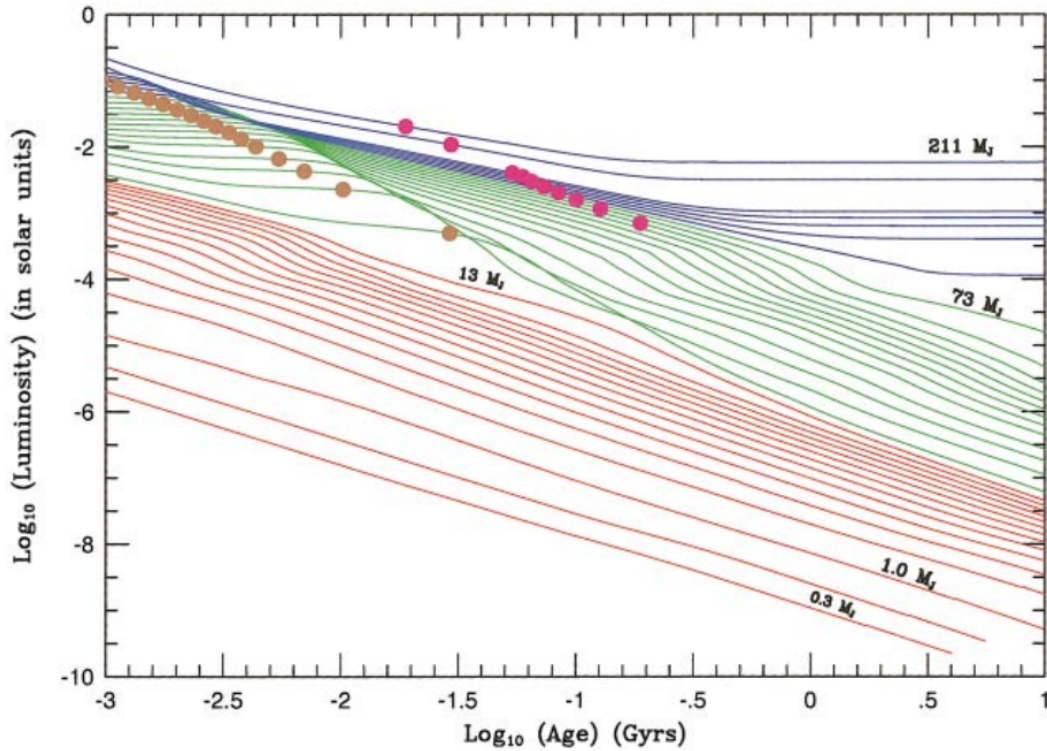


Figure 1.1: The log of luminosity as a function of the log of age for low mass stars and brown dwarfs. Each line represents the evolution of an object with a different mass, decreasing from top to bottom. The brown and pink dots indicate the ages at which 50% of the deuterium and lithium are burned, respectively, for each mass track. For the highest-mass objects (stars, blue lines), the luminosity becomes constant at late ages as sustained hydrogen burning provides a source of energy. Brown dwarfs with masses above the deuterium burning limit ($13 M_{\text{Jup}}$; green) have constant luminosities initially, and then fade for the remainder of their lives after deuterium and lithium are depleted. Brown dwarfs with masses below the deuterium burning limit (red), fade in brightness for their entire lives. This figure is from [Burrows et al. \(2001\)](#).

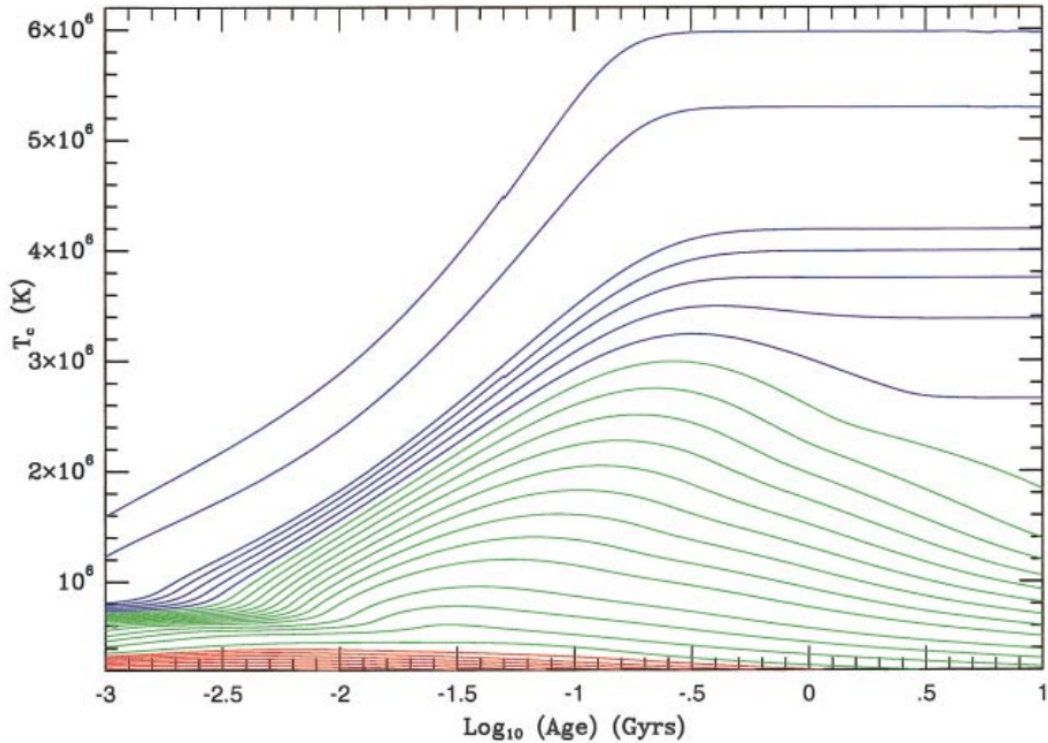


Figure 1.2: The core temperature as a function of the log of age for low-mass stars and brown dwarfs. The colour scheme of this figure is the same as Figure 1.1. For the highest-mass objects (stars, blue lines), the core temperature becomes constant at late ages as sustained hydrogen burning provides a constant source of energy. The massive brown dwarfs (green) have constant core temperatures initially as they burn deuterium (the dense region at the lower left of this figure), but the deuterium depletes quickly (<100 Myr, or $\log_{10}(\text{Age}) = -1$), and brown dwarfs then contract, so their cores heat up (the bump around 300 Myr, or $\log_{10}(\text{Age}) \approx -0.5$) before cooling for the remainder of their lives. The core temperature of brown dwarfs with masses less than deuterium burning limit (red) slowly cool after their initial contraction. This figure is from [Burrows et al. \(2001\)](#).

gravity will be relatively large and “puffy” compared to the oldest brown dwarfs ([Kirkpatrick, 2005](#)).

1.1.2 Effective Temperature and the Classification System

An important property of brown dwarfs is the temperature of their atmospheres. The “effective temperature” (T_{eff} ; the temperature of a blackbody that would emit the same amount of radiation) is typically used as an approximation of the surface (outer atmosphere) temperature, determines the overall luminosity of a brown dwarf (because of their near constant radii), and influences which molecules may form in its atmosphere.

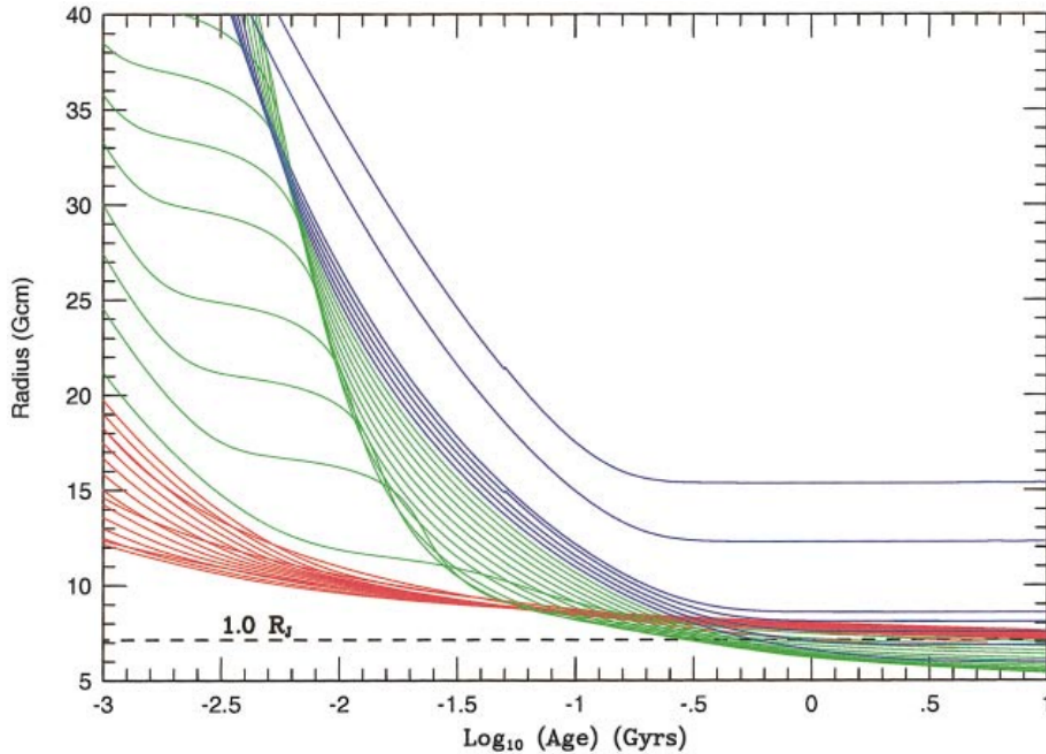


Figure 1.3: The radius as a function of the log of age for low-mass stars and brown dwarfs. The colour scheme of this figure is the same as Figure 1.1. The deuterium-burning brown dwarfs (green lines) contract until deuterium burning ignites, then stabilize for a short time until the deuterium depletes, and then continue to contract down to approximately the radius of Jupiter ($1.0 R_J$ in this figure, dashed line). All brown dwarfs (green and red lines), and even the lowest mass stars (blue) contract to approximately the radius of Jupiter after 500 Myr ($\log_{10}(\text{Age}) = -0.3$). This figure is from [Burrows et al. \(2001\)](#).

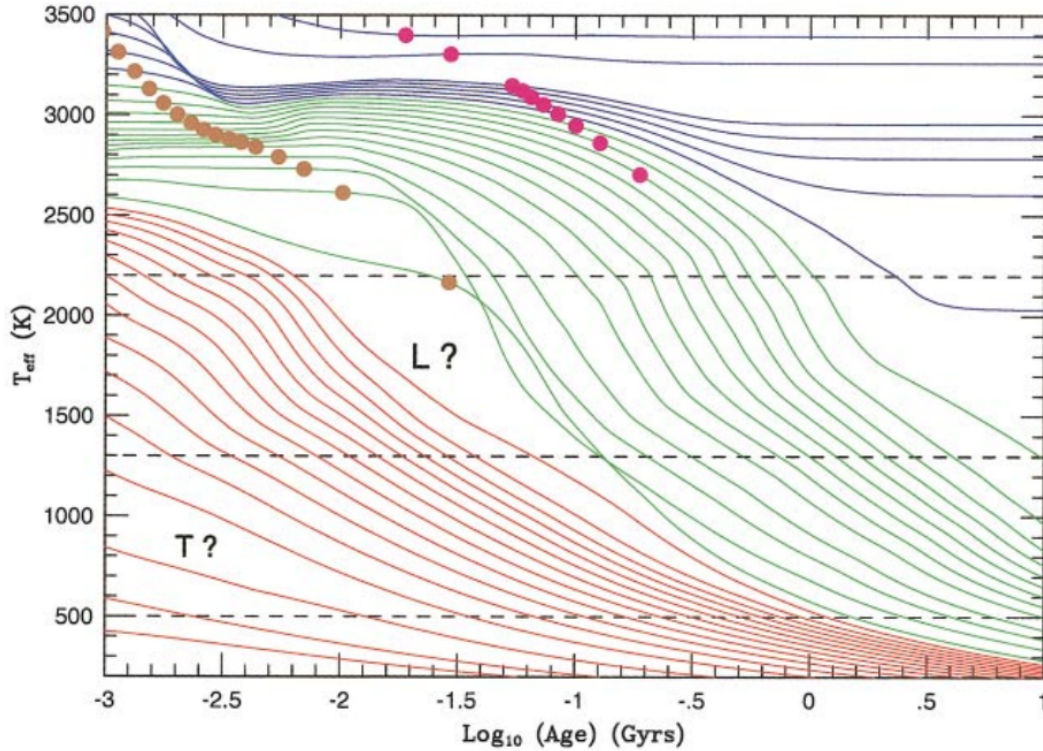


Figure 1.4: Effective temperature as a function of the log of age for low-mass stars and brown dwarfs. The colour-scheme is the same as in Figure 1.1. The top unlabelled region is where low-mass stars would lie, and the dashed lines show approximate regions where objects of spectral types L and T would lie (see Section 1.1.2). This bottom region is also shared with the Y spectral type (Cushing et al., 2011). The lines of constant mass cross these regions, indicating that brown dwarfs evolve through the spectral sequence from L- to T- to Y-type over their lives. This figure is from Burrows et al. (2001).

The effective temperatures and luminosities of brown dwarfs are dependent almost entirely on their mass and age (Burrows et al., 1997). Figure 1.4 shows the evolution of effective temperature for low-mass stars and brown dwarfs. As hydrogen burning stabilizes in stars, their effective temperatures become constant over time. Brown dwarfs with sufficient mass for deuterium burning have constant effective temperatures in their early lives, but the deuterium burning is efficient and quickly depletes the available fuel in less than ~ 100 Myr (Burrows et al., 2001), leaving them to cool for the remainder of their lives (for comparison, hydrogen burning in dwarf stars can last several billion years). After ~ 10 Gyr the highest-mass brown dwarfs ($\sim 73 M_{\text{Jup}}$) cool to effective temperatures of approximately 1300 K, and the lowest-mass brown dwarfs ($< 13 M_{\text{Jup}}$) cool to less than 500 K.

As discussed in Section 1.1.1, brown dwarfs have approximately constant radii, regardless of their mass or effective temperature. With a measure of a brown dwarf's luminosity (L), it is

possible to approximate the effective temperature using the Stefan-Boltzmann Law:

$$L = 4\pi R^2 \sigma T_{\text{eff}}^4 \quad (1.3)$$

where R is the radius of the object, and σ is the Stefan-Boltzmann constant.

Stars and brown dwarfs alike are classified by the characteristics of their electromagnetic spectra. Spectral types under the Morgan-Keenan classification system correspond to specific atmospheric characteristics and effective temperature ranges, as determined by the spectroscopic signatures of the dominant opacity sources present. The coolest stars, in the temperature range just above brown dwarfs, are known as M dwarfs ($T_{\text{eff}} \gtrsim 2300$ K). Brown dwarfs ($T_{\text{eff}} \lesssim 2300$ K) are divided into three spectral types: L, T, and, Y (Kirkpatrick et al., 1999; McLean et al., 2003; Cushing et al., 2011; Liu et al., 2011), where L-types are the warmest and Y-types are the coolest. These spectral types are each further divided into ten sub-types in a “near-infrared spectral sequence” based on effective temperature and the strengths of absorption features in their spectra (i.e., L0, L1, up to L9, where 0 corresponds to hotter, “earlier” types, and 9 corresponds to cooler, “later” types). These spectral types are sometimes accompanied by a suffix representing the surface gravity (β for intermediate surface gravity and γ for low surface gravity). The highest mass brown dwarfs and lowest mass stars (M7 or later/cooler, $T_{\text{eff}} \lesssim 2700$ K) are sometimes classified together as “ultra-cool dwarfs” (Kirkpatrick et al., 1997; Kirkpatrick, 1998). In the remainder of this section I will briefly describe the defining features of the L, T, and Y spectral types. Their chemistry will be explored in greater detail in Section 1.3.

The diversity of molecules present in the atmospheres of brown dwarfs can result in considerable differences in spectroscopic appearance, even at the same effective temperatures and within spectral sub-types. This means that the brown dwarf spectroscopic sequence is not a linear sequence in effective temperature, as shown in Figure 1.5. As seen in Figure 1.4, the lines of constant mass (e.g., the evolution in effective temperature for an object of a given mass) cross the rough boundaries between spectral types, indicating that brown dwarfs change spectral type and evolve through the spectral sequence over their lifetimes (Chabrier & Baraffe, 2000; Burrows et al., 2001). Because brown dwarfs cool over time, the dominant opacity sources, which are almost entirely dependent on temperature, are also changing over their lifetimes. Two brown dwarfs of the same effective temperature can therefore have different spectroscopic properties depending on their chemical composition and other properties such as surface gravity, g ($g = GM/R^2$, where G is the gravitational constant, M is the mass, and R is the radius; usually given as $\log g$).

A sample of infrared spectra are shown in Figure 1.6 for late-M, mid-L, and late-T type

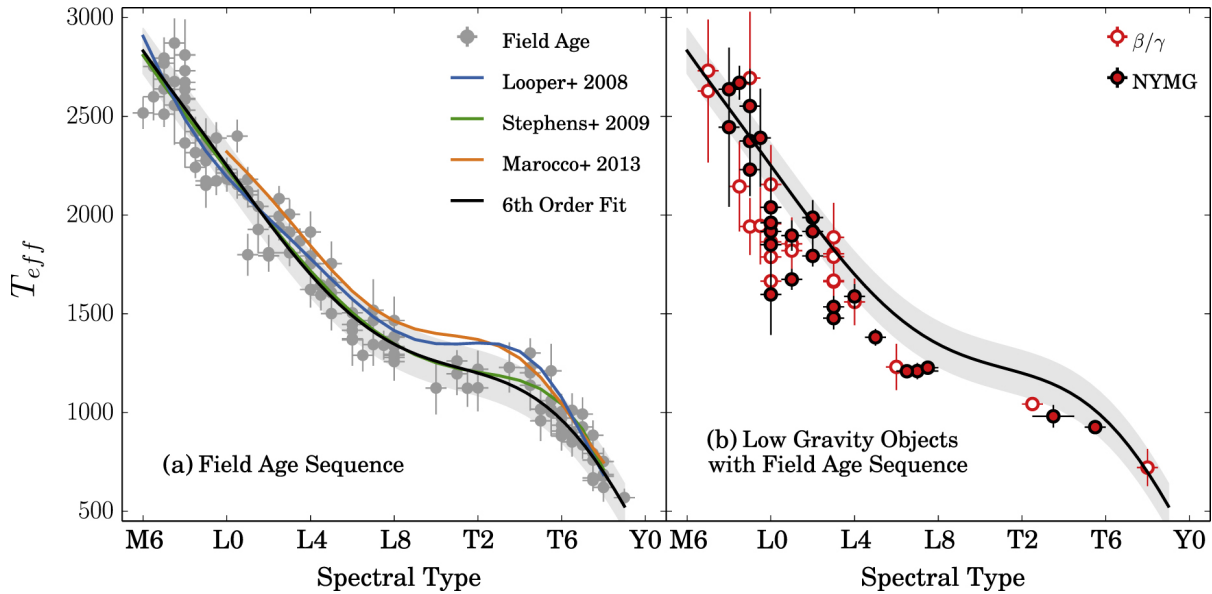


Figure 1.5: The effective temperature for brown dwarfs does not change linearly with spectral type, as spectral types are dependent on the absorption features due to the molecular species present in the atmospheres, and a variety of molecules can exist at effective temperatures less than 2600 K. In this figure, solid lines indicate polynomial fits in various publications, and grey shaded areas indicate the uncertainties on the black fit lines. In the left panel, grey points indicate field age objects (≥ 500 Myr). In the right panel, unfilled red points indicate objects with spectroscopic signatures of intermediate (β) or low (γ) surface gravity, and black points with red fill indicate objects with an association with a nearby young moving group, implying youth, and therefore low gravity due to their larger radii. By comparing the two panels, we see that in addition to effective temperature, surface gravity plays a large role in the categorization of spectral type. This figure is from [Filippazzo et al. \(2015\)](#). © AAS. Reproduced with permission.

ultra-cool dwarfs. Jupiter is also shown for comparison. The transition from M- to L-type in the spectral sequence occurs over a fairly linear decrease in effective temperature (Figure 1.5) and is generally denoted by the presence of condensates (liquids and solids) in the atmosphere (Tsuji et al., 1996). The mid-M and mid-L dwarfs in Figure 1.6 are the most similar of the set, and water and carbon monoxide are prominent opacity sources in these spectral types (Cushing et al., 2006). The transition from L- to T-type, however, occurs over fairly constant temperature (~ 1200 K– 1400 K), and is a region of particularly interesting atmospheric changes. The dominant carbon-bearing molecule switches from carbon monoxide to methane (see details in Section 1.3.1), and the difference between the mid-L and late-T dwarfs in Figure 1.6 are dramatic, as methane molecular bands alter the spectra so they look nothing like blackbodies (approximately what we observe for stars).

The spectral types L9 and T0 mark the official transition from L- to T-types, but frequently spectral types between L8 and T3 are included in the discussion of the “L/T transition” due to their similar properties (e.g., T_{eff} , luminosity). The L/T transition, and the brown dwarfs that fall under these spectral types, are of particular interest in the brown dwarf community because we observe a large diversity in their observed properties, despite the relatively narrow effective temperature range over which the L/T transition takes place.

As we follow the spectral sequence from L- to T-type, it would be expected that the colours¹ of brown dwarfs would become redder; if brown dwarfs behaved as blackbodies, the peaks of their spectral energy distributions would shift to longer wavelengths. What we observe, however, is that the reddening trend persists for the early L dwarfs, but at the L/T transition, we find a rapid reversal in colours. As effective temperatures drop below ~ 1300 K, there is a shift from red colours to blue (changing by ~ 2 magnitudes in brightness), yet only an effective temperature drop of 100 K– 200 K (Burrows & Sharp, 1999; Lodders, 1999; Kirkpatrick, 2005). This behaviour is shown in the colour-magnitude diagram in Figure 1.7. This trend is partially explained by the methane opacity lowering the flux at longer wavelengths, but has been difficult to reproduce with models (e.g., Tsuji 2002; see Section 1.3.3).

The transition from T- to Y-type in the spectral sequence occurs over a linear decrease in effective temperature. Y dwarfs have effective temperatures less than 500 K, and are the lowest-mass products of star-formation (Cushing et al., 2011). Y dwarfs also display deep absorption features from water and methane, but with the addition of ammonia. Y dwarfs closely resemble

¹A note on nomenclature: the “colour” of an object is its difference in brightness (in magnitudes) at two wavelengths. By convention, a colour is the magnitude of an object in the longer wavelength (more “red”) subtracted from its magnitude in the shorter wavelength (more “blue”). In terms of magnitudes, a smaller number is brighter, and a larger number is fainter, so if a colour is positive, that means it is “redder” and if it is negative, it is “bluer.”

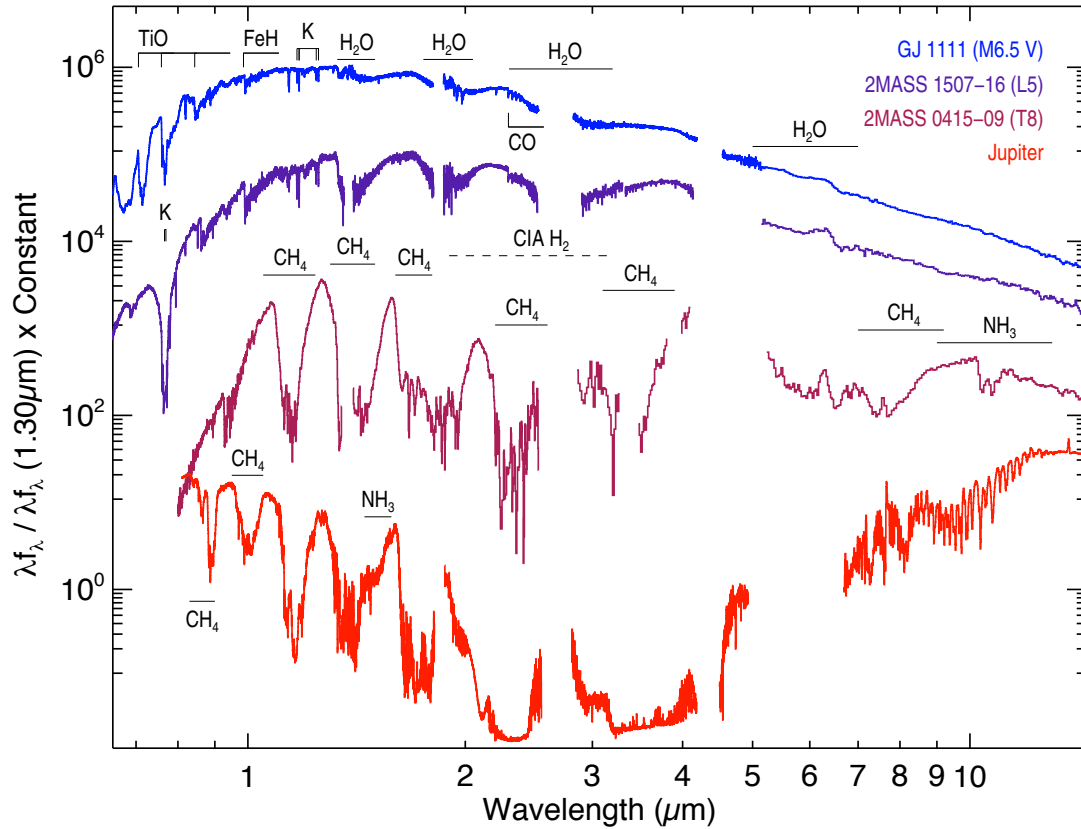


Figure 1.6: The changes in near- to mid-infrared spectral features for M, L, and T dwarfs, and Jupiter. The fluxes are normalized to unity at $1.3 \mu\text{m}$ and multiplied by constants for clarity. The M dwarf ($T_{\text{eff}} \sim 2700 \text{ K}$) displays few molecular features, primarily H_2O , CO , and FeH . The L dwarf ($T_{\text{eff}} \sim 1600 \text{ K}$) displays similar features, but more pronounced than the M dwarf. The T dwarf ($T_{\text{eff}} \sim 700 \text{ K}$) and Jupiter ($T_{\text{eff}} \sim 150 \text{ K}$) display primarily CH_4 features, as well as NH_3 . The peak flux shifts from shorter wavelengths in the M dwarf to longer wavelengths in the L dwarf, displaying a “reddening” effect (meaning it is brighter at longer wavelengths). Collision-induced absorption due to molecular hydrogen is indicated by “CIA H_2 .” This figure is from [Marley & Leggett \(2009\)](#), adapted from [Cushing et al. \(2006\)](#).

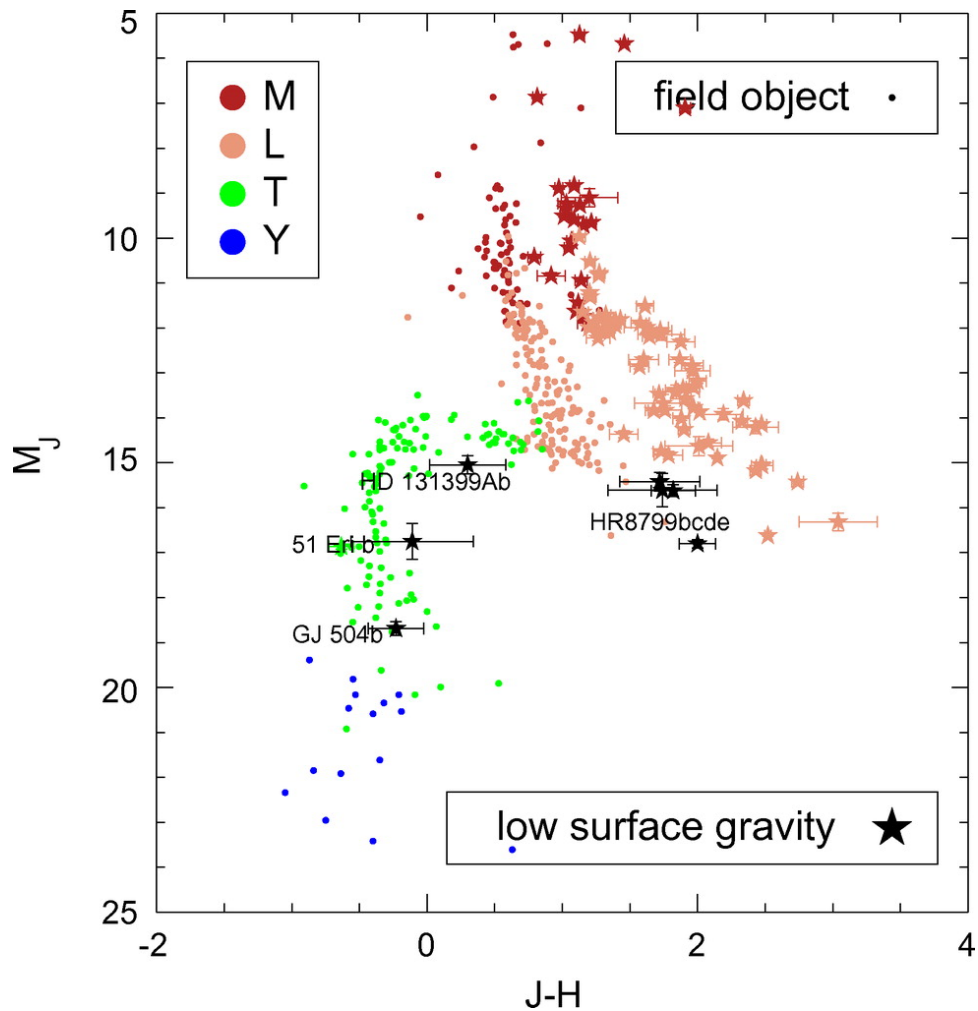


Figure 1.7: A near-infrared colour-magnitude diagram of ultra-cool dwarfs and directly imaged giant planets (black stars). M_J is the magnitude in the J band (central wavelength $1.22 \mu\text{m}$), and $J-H$ is the difference of the magnitudes in the J and H bands (i.e., the colour; the H band central wavelength is $1.63 \mu\text{m}$). “Red” colours are to the right of this figure, and “blue” colours are to the left. From M to L dwarfs, colours become slightly redder, and from L to T dwarfs, the colours abruptly become bluer until becoming approximately constant at later T-types and into the Y dwarfs. Low gravity objects (star symbols) show the same behaviour as the M and L dwarfs, but shifted to redder colours. The shift to bluer colours in the T and Y dwarfs occurs due to methane absorption at $2.2\mu\text{m}$ and the dispersion of silicate clouds. This figure is from [Biller \(2017\)](#).

giant planets, and may even host water-ice in their atmospheres (Morley et al., 2014b).

Brown dwarf spectra are also heavily influenced by pressure and surface gravity. The pressure influences which molecules will form, and contributes to line broadening. Spectroscopic signatures related to surface gravity can be also used as markers for age, as young brown dwarfs will typically have lower surface gravity than their older counterparts because they haven't finished their initial contraction (Knapp et al., 2004). The local pressure at a given altitude within the atmosphere also influences at what altitudes different molecules/grains will settle, resulting in layered, cloudy atmospheres.

1.1.3 Atmospheric Structure and Clouds

As brown dwarfs cool, gases in their atmospheres condense into larger grains and vapours in the form of clouds. Clouds affect the atmospheres (and therefore spectral energy distributions) of brown dwarfs in many ways. The main effect is increased opacity: thicker clouds result in higher opacities. The relative strengths of spectral lines are heavily influenced by the presence of clouds. To understand how cloud opacity affects spectra, we must also consider the gas opacity producing the spectrum — we have two cases: wavelengths where gas opacity is low, so the flux we measure originates in the deep, hot layers of the atmosphere; and wavelengths where gas opacity is high, so the flux we measure originates in the higher, cooler layers of the atmosphere. If gas opacity is low, clouds increase opacity and decrease flux, resulting in fainter objects. If gas opacity is high, we have the opposite effect as clouds retain heat, warming the upper layers of the atmosphere with the increased temperature gradient, and increasing the flux. The combination of these two cases means that generally, cloud-free objects have stronger absorption features and cloudy objects have weaker absorption features (Ackerman & Marley, 2001; Kirkpatrick, 2005). Two model spectra, one with iron and silicate clouds and one without clouds, and otherwise identical physical parameters from Morley et al. (2012) are shown in Figure 1.8, illustrating this effect.

Brown dwarf atmospheres become hotter, denser, and have higher pressures from higher altitudes to lower altitudes. Since the molecules which may form depend on both the local temperature and the local pressure, the clouds of brown dwarfs are made up of various layers of gases, vapours, hazes, and dusts. Even at the temperatures of the earliest L dwarfs (1700–2300 K), opaque dust clouds composed of iron, silicates, and other metal oxides are able to form (Fegley & Lodders, 1996; Tsuji et al., 1996). Near the L/T transition, the silicate and oxide clouds drop deeper into the atmosphere under a layer of opaque methane gas, where they can no longer be seen, and so the early T dwarfs appear relatively cloud-free (Ackerman & Marley, 2001; Burgasser et al., 2002b; Lodders & Fegley, 2006). For later T-types, the atmospheres

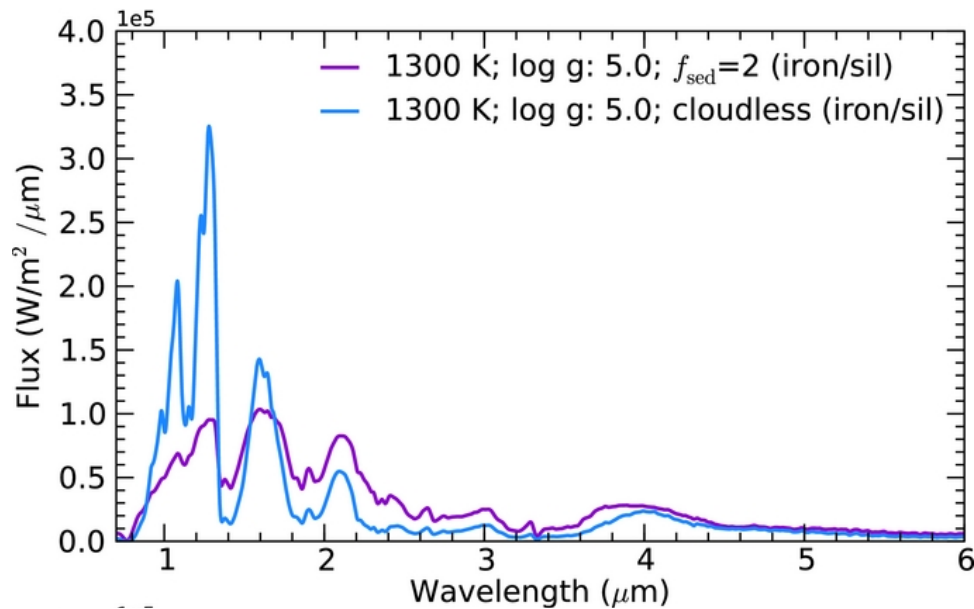


Figure 1.8: Model spectra for two simulated brown dwarfs at the L/T transition. Although the models have identical effective temperatures and surface gravities, their spectra are very different due to the presence of clouds (the purple model contains clouds and the blue model does not). In these models, opaque iron and silicate clouds suppress flux in the *Y* band (central wavelength $1.02 \mu\text{m}$), *J* band (central wavelength $1.22 \mu\text{m}$), and *H* band (central wavelength $1.63 \mu\text{m}$). Without clouds, the flux comes from deep, hot layers of the atmosphere. At longer wavelengths, including the *K* band (central wavelength $2.19 \mu\text{m}$) and mid-infrared, the flux comes from higher layers of the atmosphere than where the clouds lie, so the addition of clouds increases the flux. This figure is from [Morley et al. \(2012\)](#). © AAS. Reproduced with permission.

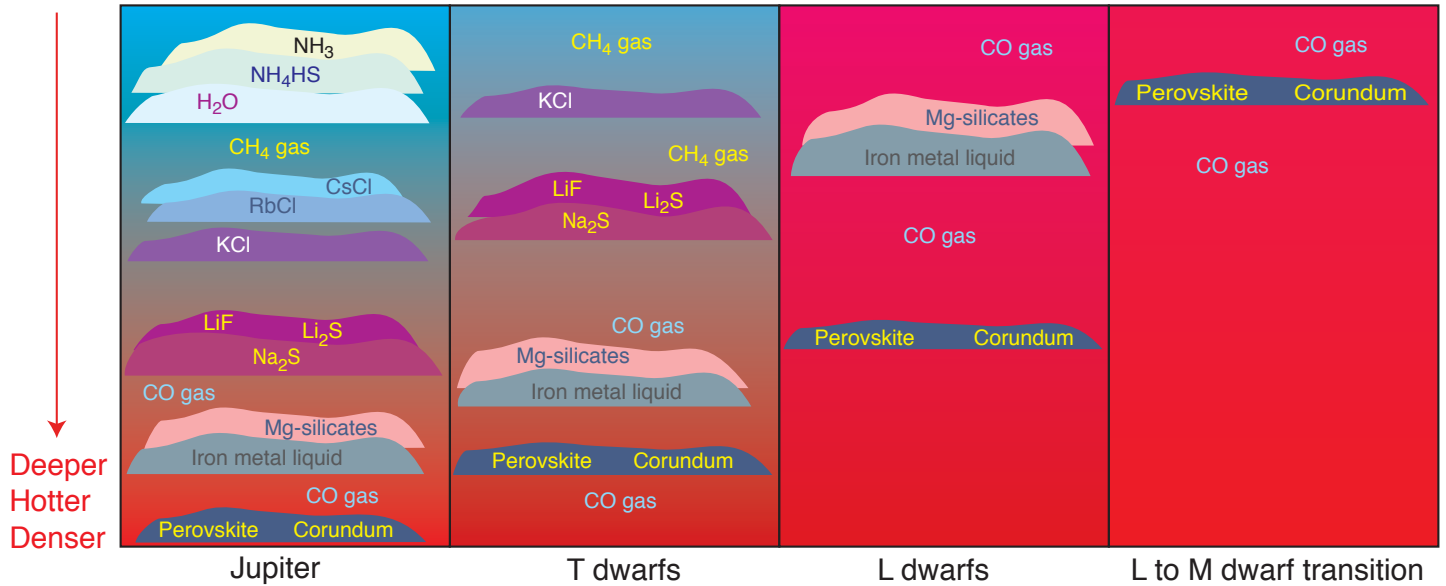


Figure 1.9: A cartoon representation of the cloud and gas layers in Jupiter, T and L dwarfs, and the coolest M dwarfs. The coldest objects (Jupiter and the T dwarfs) have the most cloud layers and diversity in molecular species, while in the hotter objects, less variety in condensates form, resulting in fewer cloud layers. The vertical direction loosely indicates depth and temperature within the atmosphere with the top of the figure being the cool outer most layers, and the bottom being deeper and hotter in the atmosphere. This figure is from [Lodders \(2004\)](#).

are cooler and there is even more variety in molecules. Clouds re-appear in mid- to late-T and Y dwarfs above the methane gas and are composed of alkali salts and sulfides ([Lodders, 1999](#); [Morley et al., 2012](#)). Figure 1.9 shows a simple cartoon of possible cloud layer compositions for ultra-cool dwarfs compared to Jupiter. For cooler objects, clouds of a particular molecule will sink deeper, and the atmosphere above a cloud of a particular composition will lack the molecules and elements contained in the cloud.

The thickness of the atmosphere and cloud layers depends on the surface gravity of the object. At low gravities, condensates can settle higher in the atmosphere, resulting in thicker, more opaque clouds and obscuring the hotter, deeper layers. This reduces the total flux at shorter wavelengths, and causes redder colours, as seen in Figures 1.6 and 1.7.

Clouds also present a partial explanation for the colour-reversal at the L/T transition: radiation from the hot interiors of brown dwarfs is absorbed by clouds and re-emitted at longer wavelengths, resulting in reddening through the L-types (where clouds are present). At the L/T transition, clouds dissipate and this effect is lessened, resulting in bluer colours for T-type brown dwarfs.

The dusty, cloudy nature of brown dwarf atmospheres also results in linear polarization.

Linear polarization in ultra-cool dwarfs is not uncommon, and is primarily due to dust scattering (Sengupta & Krishan, 2001; Sengupta & Kwok, 2005), but can also be due to magnetic fields (Kuzmychov & Berdyugina, 2013). The degree of polarization can be a useful tool for probing the physical properties of, and studying the presence of dust cloud decks in ultra-cool dwarf and gas giant exoplanet atmospheres (Marley & Sengupta, 2011).

1.2 Rotation and Variability

As a consequence of contraction, both stars and brown dwarfs “spin-up” (increase their angular velocity) to conserve angular momentum from early in their lives. In low-mass stars, rotation is later slowed, primarily through magnetic braking, but also through interactions with disks and other effects. Brown dwarfs, however, continue to cool, contract, and spin-up as they age and do not undergo the same braking effects as stars. For example, due to their thick, neutral atmospheres, brown dwarfs lack strong magnetic fields (Meyer & Meyer-Hofmeister, 1999), which are required for magnetic braking. All brown dwarfs have at least some rotation, and most brown dwarfs, except for the very youngest ones, are considered “fast rotators” (rotation periods $\lesssim 1$ day; Scholz et al. 2015). The rate of rotation is heavily dependent on the internal and external processes during the formation of a brown dwarf. The internal processes include the rate of core collapse, and the external conditions depend on how turbulent the giant molecular clouds are, and if there is angular momentum exchange with the surrounding medium (Bouvier et al., 2014).

It is useful to gather statistics on the occurrence of rotating brown dwarfs and their rotation rates since rotation is an important parameter in stellar evolution; rotation is linked to binary formation, magnetic field generation, and other internal processes such as mixing and energy transport (Bouvier et al., 2014).

But how do we determine the rotation rates of brown dwarfs? One method is to measure the line broadening in spectroscopic observations, but this would yield the projected rotation velocity, and not the true equatorial velocity or the rotation period (which would require the radius and inclination of the object).

Since the surfaces of brown dwarfs are not uniform, neither is the radiation emitted from them. Patchy clouds and other surface features such as banding, like what is seen on Jupiter, result in varying flux across the surfaces of brown dwarfs. As brown dwarfs rotate, the photometric and spectroscopic signatures we observe will change as these surface inhomogeneities rotate in and out of view. If any variability detected is found to be periodic, the rotation period can be determined.

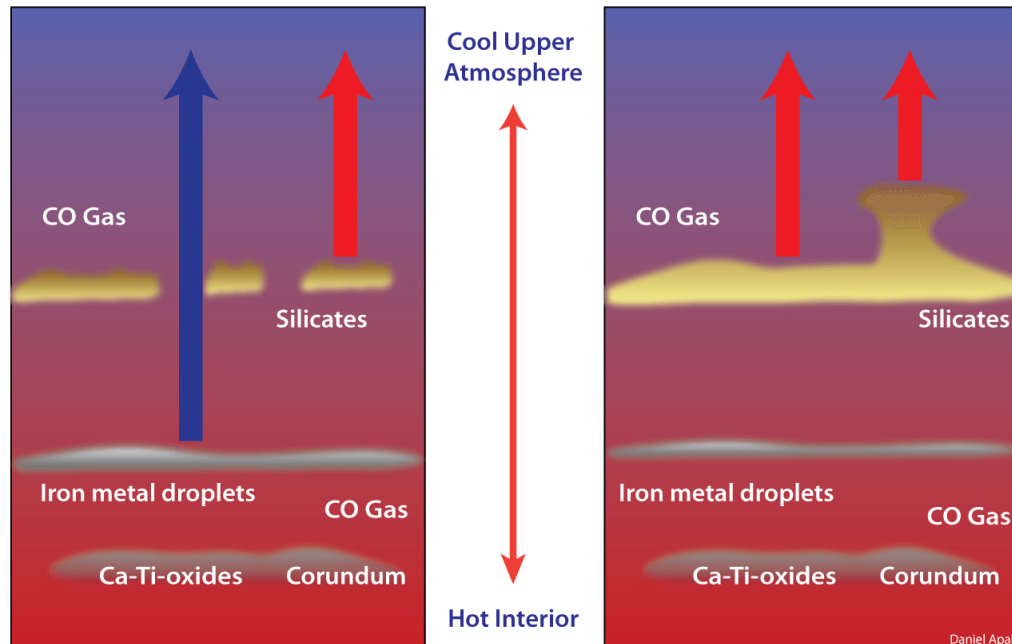


Figure 1.10: This cartoon illustrates the observational effects of patchy clouds with holes in a brown dwarf atmosphere. The bottom of the image is deeper in the atmosphere (lower atmospheric altitudes), and the top of the image is shallower in the atmosphere (higher atmospheric altitudes). Interior layers are hotter and emit shorter wavelength radiation (blue arrows) than the cooler, outer layers (red arrows). This figure is from Daniel Apai's website (<http://distantearths.com/research/exoplanet-atmospheres/>).

1.2.1 Photometric Variability Due to Clouds

Recent surveys (e.g., Buzzi et al. 2014; Wilson et al. 2014; Radigan et al. 2014; Radigan 2014; Metchev et al. 2015; Apai et al. 2017; Vos et al. 2019; see Section 1.2.3 for descriptions of these studies) have found that many brown dwarfs have variable brightness with time. The widely accepted explanation for the variability is patchy clouds rotating in and out of view. Figure 1.10 shows a simple cartoon demonstrating the effect patchy clouds will have on the measured flux; when holes are present in the cloud layers (left panel of Figure 1.10), some of the observed flux will come from the deeper, hotter layers of the atmosphere. The measured flux will brighten at shorter wavelengths when the hole faces the observer. When a region with thicker clouds or taller cloud columns faces the observer (right panel of Figure 1.10), the flux comes from the cooler, higher altitude regions of the atmosphere, and will appear brighter at longer wavelengths. As the brown dwarf rotates, these patches go in and out of view, and photometric monitoring will reveal variability in the brightness over time.

When photometric monitoring reveals periodic variations in the light curves (a plot of the brightness as a function of time) of brown dwarfs, the period may be interpreted as the rotation

period of that object. Some caution must be given to whether this period is the true period or a false period: it could be a multiple of the true period, potentially caused by multiple surface spots. And if variability is not detected, it is not that the object is not rotating, but that the object is either rotating very slowly, the surface is uniform in brightness, the amplitude of the variations is below the sensitivity of the instrument, or some combination of these effects.

Multi-wavelength photometric monitoring can be used to study the physics of brown dwarf atmospheres, to understand the chemistry of clouds, and to detect atmospheric activity such as storms. For example, variations in the dominant gas absorption species in atmospheres can explain wavelength-dependent amplitude differences (e.g., [Metchev et al. 2015](#)). When molecular gas opacity is strong, clouds reside below the photosphere and so cloud inhomogeneities below are obscured. Cloud structures are detectable only in relatively transparent spectral regions, away from dominant molecular bands (e.g., [Ackerman & Marley 2001](#)). Surveys across many spectral types and wavelengths will give a more complete picture of sub-stellar rotation rates and cloud formation and dissipation in brown dwarf atmospheres.

If clouds are indeed responsible for the observed variability, the most effective way to search for variability in brown dwarfs is to monitor the photometric brightness in the infrared, as the flux at these wavelengths is sensitive to changes in cloud opacity. Contrast between clouds and the hotter gases deeper in the atmosphere is thought to be largest in the *J* band ($\sim 1.22 \mu\text{m}$), as flux originates deep in the atmospheres of brown dwarfs (at pressures of ~ 10 bar) and would be absorbed by opaque clouds ([Ackerman & Marley, 2001](#); [Marley et al., 2002](#); [Morley et al., 2014a](#); [Radigan et al., 2014](#)). Since cloud and gas opacities vary with wavelength, depending on the molecular species present, monitoring across many wavelengths probes various pressures and temperatures. Spectroscopic monitoring provides a yet more detailed picture of these variations (e.g., [Kellogg et al. 2017](#); [Schlawin et al. 2017](#)), but is observationally difficult with current instruments with limited sensitivity, as the changes in brightness tend to be on the order of a few percent, or less (e.g., [Buenzli et al. 2014](#); [Wilson et al. 2014](#); [Radigan et al. 2014](#); [Radigan 2014](#); [Metchev et al. 2015](#)).

Patchy clouds are expected to be most common at the L/T transition; during the switch from cloudy to cloud-less atmospheres, clouds do not uniformly drop deeper into the atmospheres of brown dwarfs. This results in patchy, multi-layer, cloudy atmospheres with varying thickness and compositions. The holes and thinner layers allow us to glimpse at the hotter interiors of the atmospheres which produce greater flux. The clouds also absorb and scatter radiation at wavelengths dependent on their composition and temperature. It is now known that rotationally modulated variability is common across brown dwarfs of all spectral types, not just at the L/T transition (e.g., [Metchev et al. 2015](#)).

While brown dwarf cloud structures are typically found to be constant over timescales of at

least a few rotations (e.g., [Radigan et al. 2014](#); [Radigan 2014](#); [Metchev et al. 2015](#)), some brown dwarfs also exhibit changes in the shapes of their light curves indicating cloud evolution and these light curve changes can occur on timescales of hours, days, or years (e.g., [Artigau et al. 2009](#); [Radigan et al. 2012](#)). Long-term photometric monitoring of brown dwarfs over many epochs will therefore be an important tool for understanding the evolution of their atmospheres. One such survey by [Apai et al. \(2017\)](#) using the Spitzer Space Telescope has revealed key information about the nature of the cloud patterns on brown dwarfs. They found that a simple spot pattern to represent holes and columns in a brown dwarf atmosphere is not sufficient for explaining the observed shapes of light curves. Planetary scale waves (banding with sinusoidal surface brightness) must also be present to fully explain the observed light curves. A single elliptical bright spot on the surface of a brown dwarf (i.e., a hole in a cloud layer) would result in a light curve that appears as a truncated sine wave (see the bottom of [Figure 1.11](#)), but brown dwarf light curves commonly appear sinusoidal, or as a combination of sinusoids (e.g., [Metchev et al. 2015](#); [Figure 1.12](#)). To display a sinusoidal modulation in a light curve, banding with sinusoidal surface brightness is required (see the top of [Figure 1.11](#)). [Apai et al. \(2017\)](#) find that to reproduce their observed light curves, they require models with both small, elliptical spots, as well as planetary-scale waves. Additional details on this survey are given in [Section 1.2.3](#).

1.2.2 Other Sources of Variability

Clouds are not the only mechanism which can cause variability in brown dwarfs. Magnetic fields, fingering convection, and atmospheric temperature fluctuations have also been suggested as possible sources for variability. These alternative mechanisms do not preclude the existence of clouds in brown dwarf atmospheres; it means that clouds may not be responsible, or entirely responsible, for the observed variability.

Magnetic fields are known to cause starspots (hot or cool spots on the surface of a star; [Strassmeier 1994](#)) which can result in detectable variability. Given that brown dwarfs rotate and their interiors are ionized, they must also have magnetic fields generated through a dynamo effect ([Mohanty et al., 2002](#)). Starspots on rotating brown dwarfs would produce similar variability signatures in brown dwarf light curves as holes in patchy cloud layers. Magnetic activity is common in late-M stars and early-L dwarfs (e.g., [Lane et al. 2007](#)), but towards later spectral types magnetic activity drops off ([Basri, 2004](#)). This drop off is due to the low temperatures and neutral atmospheres of brown dwarfs; conductivity drops off, and so large currents cannot be sustained beyond the ionized interiors of brown dwarfs. This both reduces starspots which could cause variability, and prevents magnetic braking, allowing brown dwarfs to remain as fast rotators even late in their lives ([Mohanty et al., 2002](#)).

Two key types of atmospheric features and their impact on the lightcurve

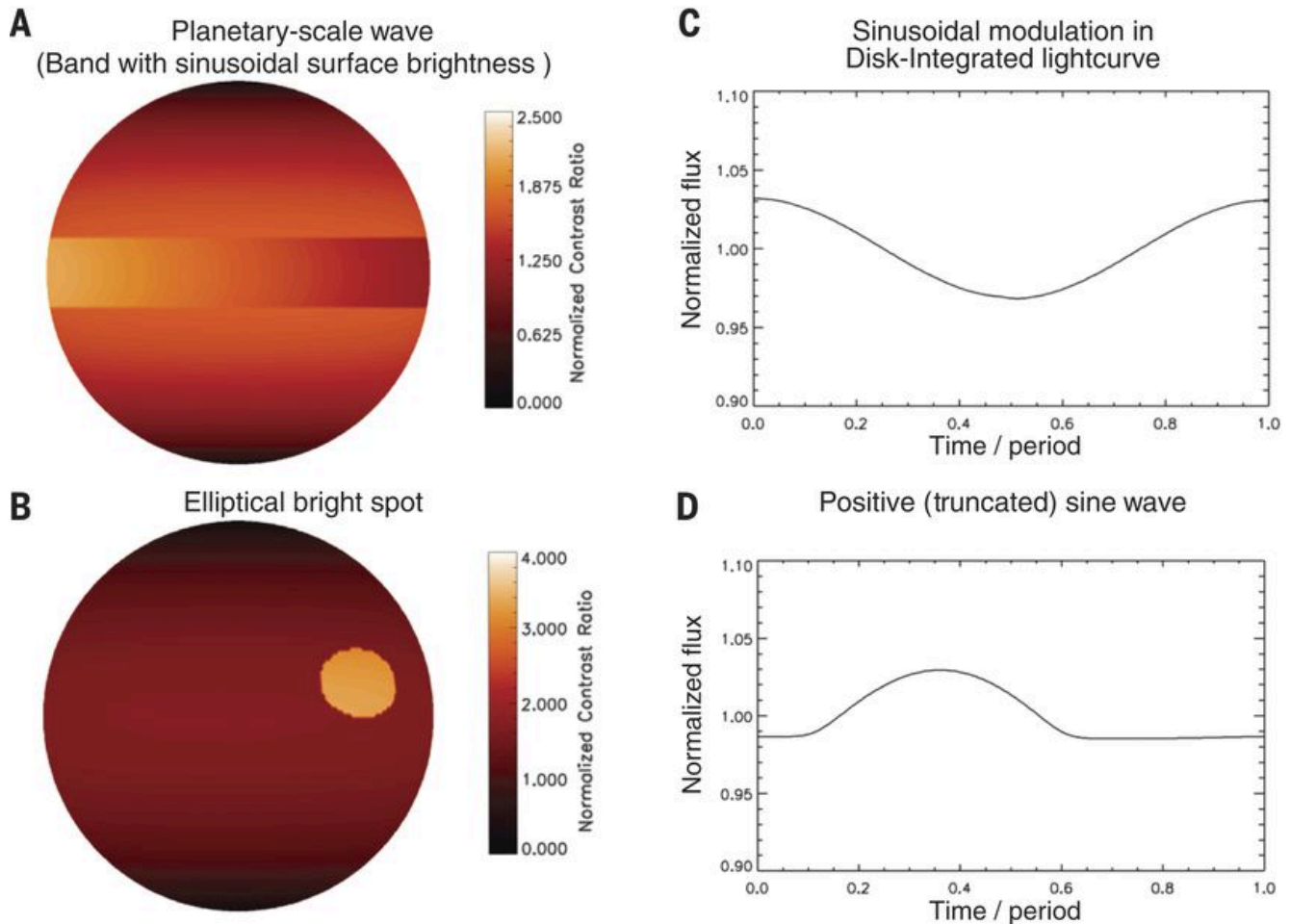


Figure 1.11: Panels A and B show simple illustrations of two of the main atmospheric features expected in brown dwarfs: bands and spots. Panels C and D show how these features would appear in a disk-integrated light curve (i.e., an observation where surface features on the brown dwarf are not resolved). The light curve plots flux as a function of time. Spots alone are not enough to recreate observed brown dwarf light curves; light curves can be well modelled by a combination of planetary-scale waves, similar to the banding on Jupiter (panels A and C, top of figure) and one or more elliptical spots (panels B and D, bottom of figure). This figure is from [Apai et al. \(2017\)](#).

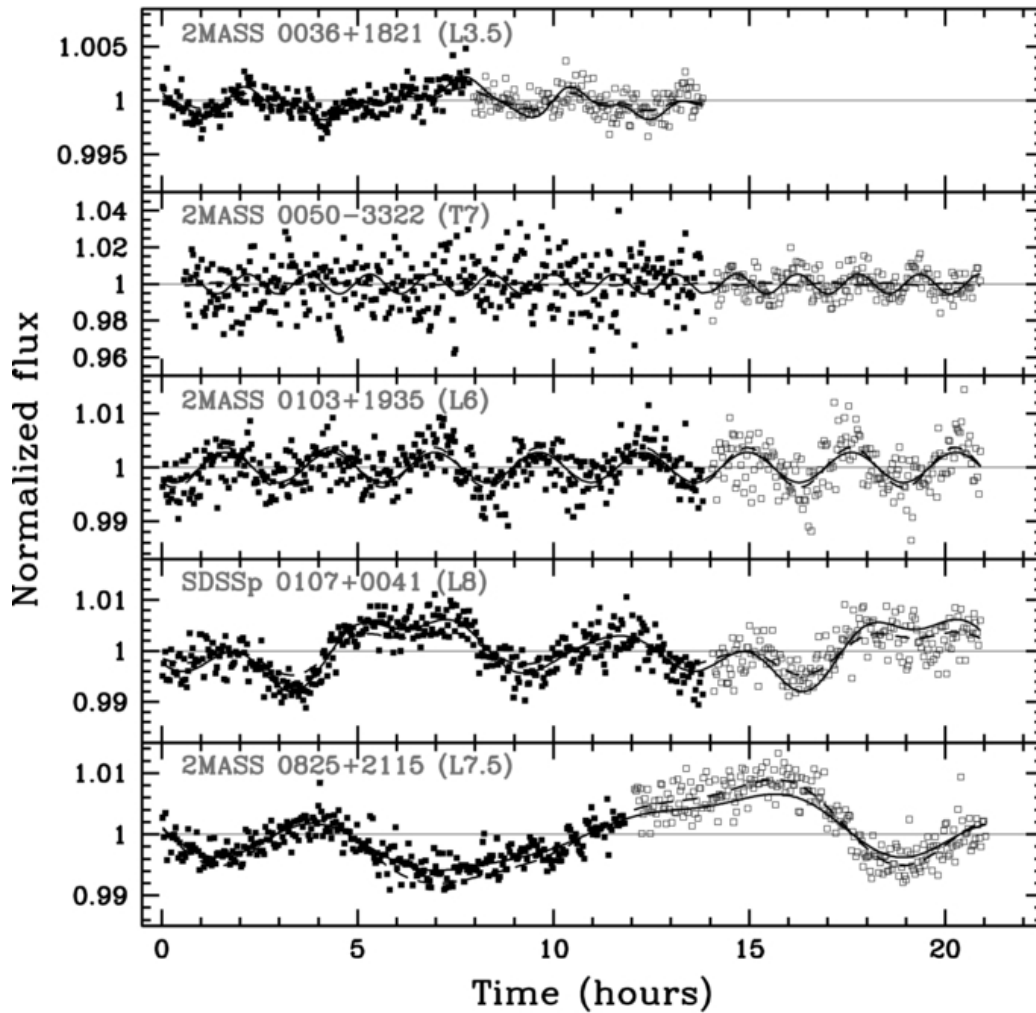


Figure 1.12: A sample of light curves for L and T dwarfs from the Weather on Other Worlds project by [Metchev et al. \(2015\)](#). Filled squares denote photometry at $3.6 \mu\text{m}$ and open squares denote photometry at $4.5 \mu\text{m}$. The solid and dashed lines are the variability models for the $3.6 \mu\text{m}$ and $4.5 \mu\text{m}$ photometry respectively. Some objects have simple sinusoidal and periodic light curves (e.g., the second and third panels from the top), while others have more complicated, yet still periodic light curves (top and fourth from the top). For others, periodicity cannot be confirmed on the time scale of the observations (bottom panel). All of the objects have variations on the timescales of hours, with confirmed or likely rotation periods of less than 20 hours, the duration of these observations. This figure is from [Metchev et al. \(2015\)](#). © AAS. Reproduced with permission.

It is possible that in the hottest brown dwarfs (early L-type), magnetic fields are responsible for variability through starspots, but this is not what is typically observed. [Miles-Páez et al. \(2017\)](#) tested for correlation between photometric variability and magnetic activity in previously-monitored brown dwarfs ranging in spectral type from L0–T8. They detected H α emission (a common tracer of magnetic activity; [Zarro & Rodgers 1983](#)) in only one of their targets and from a further investigation of the literature conclude that photometric variability and magnetic activity are not correlated, and that clouds typically drive photometric variability. This result is in agreement with other studies ([Bailer-Jones & Mundt, 2001](#); [Martín et al., 2001](#); [Gelino et al., 2002](#); [Richey-Yowell et al., 2020](#)), and so magnetic fields are unlikely to be the cause of photometric variability.

Atmospheric temperature fluctuations have been proposed as a potential cause of photometric variability, especially in cooler brown dwarfs (T-types). [Robinson & Marley \(2014\)](#) show that thermal fluctuations occurring deep in the atmosphere can cause surface brightness fluctuations at infrared wavelengths. However, these models produce variability on timescales of hundreds of hours, while observationally most brown dwarfs have variability on the scale of hours to tens of hours. These thermal fluctuations however, could be used to explain aperiodic flux variations.

[Tremblin et al. \(2015, 2016, 2017, 2020\)](#) show that fingering convection (so called for the columns or “fingers” of rising or sinking gas in the atmosphere) in a cloudless atmosphere can result in variability. They find that the slow conversion of CO to CH₄ (at the L/T transition) and N₂ to NH₃ (at the T/Y transition) causes surface inhomogeneities in molecular abundances and temperature. This added convection then warms the deep layers of the atmosphere, increasing the temperature gradient and causing a *J*-band brightening resulting in bluer colours for T dwarfs.

[Biller \(2017\)](#) argues that abundance inhomogeneities (like those described in the Tremblin et al. studies) should be observable through variability of individual spectral lines for rotating brown dwarfs. Studies by [Buenzli et al. \(2015b\)](#) and [Biller et al. \(2018\)](#) find no such variability in, for example, methane lines, compared to other spectral features, suggesting that fingering convection may not be responsible for variability. Furthermore, [Leconte \(2018\)](#) find that counter to the Tremblin et al. studies, turbulent transport would actually increase the thermal gradient, resulting in a *J*-band darkening for T dwarfs, which is the opposite of what is observed. They therefore conclude that fingering convection cannot be the source of observed variability in brown dwarfs.

1.2.3 Overview of Previous Variability Studies

Soon after brown dwarfs were first announced in 1995, searches for variability began. In this section I will review some of the key brown dwarf variability studies and their results, with a focus on the largest studies to date.

In one of the first searches for sub-stellar variability, [Tinney & Tolley \(1999\)](#) investigated an M9 dwarf and an L5.5 binary, finding variability in the latter, thought to indicate changes in cloud opacity. [Bailer-Jones & Mundt \(1999, 2001\)](#) performed a larger survey, investigating M and L dwarfs, and found variability in 12/27 of their targets. Later surveys by [Gelino et al. \(2002\)](#) and [Enoch et al. \(2003\)](#) also detected variability, finding 7/18 and 3/9 targets to be variable respectively. Both of these studies concluded that patchy cloud cover is likely responsible for the variability, as opposed to magnetic spots, like those seen in stars. These and other early variability searches were ground-based observations, primarily performed photometrically at red-optical wavelengths.

As described in Section 1.2.1, the highest contrast in brown dwarf variability is expected in the near-infrared. In more recent studies, [Wilson et al. \(2014\)](#) and [Radigan et al. \(2014\)](#) performed the largest ground-based surveys of brown dwarf variability to date, investigating 69 and 62 L and T dwarfs respectively, in the *J* band. Both studies aimed to improve the statistics of variable brown dwarfs, targeting the L/T transition where cloud dissipation and patchy atmospheres were expected to cause variability. While [Wilson et al. \(2014\)](#) found that the variable objects in their sample were not concentrated in any particular set of spectral types, [Radigan et al. \(2014\)](#) estimated that $\sim 80\%$ of brown dwarfs in the L/T transition would be variable if viewed equator-on, and $\sim 60\%$ are variable outside of the L/T transition. [Radigan et al. \(2014\)](#) also found that large-amplitude variables ($> 2\%$) are more common at the L/T transition. [Radigan \(2014\)](#) later performed an independent analysis of the targets from [Wilson et al. \(2014\)](#), and combining with the data of [Radigan et al. \(2014\)](#), they re-confirmed that strong (high-amplitude) variability occurs more frequently at the L/T transition. A recent study by [Eriksson et al. \(2019\)](#) targeting L/T transition objects found 4/10 targets to be strongly variable in the *J* band, with amplitudes $>2\%$, consistent with previous studies of L/T transition objects.

Despite the success of these studies, observing at infrared wavelengths from ground-based facilities is challenging; the Earth's atmosphere is bright in the near-infrared and introduces large amounts of correlated noise to the data (compared to optical observations). Moreover, water vapour, which is a major absorber in the near-infrared and is itself present in brown dwarf atmospheres, is variable in the Earth's atmosphere. This presents additional complications in detecting variability, especially over the timescales of brown dwarf variability (hours). So, many modern brown dwarf variability surveys take advantage of long-term monitoring programs and the stability of space telescopes.

[Buenzli et al. \(2014\)](#) used the Hubble Space Telescope to survey 22 L and T brown dwarfs in one of the first large space-based brown dwarf variability surveys. Observing each target for only 40 minutes, they found $\sim 30\%$ of their targets to be variable, noting that their survey was not sensitive to long-period variables. While ground-based studies are biased toward detections with the largest amplitudes, space-based surveys like this frequently detect variability with amplitudes $< 1\%$.

In the Weather on Other Worlds project, [Heinze et al. \(2013\)](#) and [Metchev et al. \(2015\)](#) performed one of the largest and most sensitive photometric variability surveys to date. Utilizing the unique stability of the Spitzer Space Telescope, this survey monitored 44 L3–L8 dwarfs continuously for 20 hours each in the mid-infrared. The long durations of the observations provided the means to detect long-period variables missed in previous surveys. This survey found $\sim 49\%$ of single objects (non-binaries) to be variable. Figure 1.12 shows a sample of the light curves from [Metchev et al. \(2015\)](#). This particular sample figure shows objects with variability on the order of 1% (though many in the sample show variability with amplitudes $< 1\%$), with some regular variables (the top four panels) and one irregular variable (i.e., it does not repeat on the timescales of this survey; the bottom panel). [Metchev et al. \(2015\)](#) also find large-amplitude variables near the L/T transition, similar to [Radigan et al. \(2014\)](#) and [Radigan \(2014\)](#), but they do not find increased fractions of variables in this spectral type region. The differences between these studies indicate that there may be differences in cloud structure appearance at different wavelengths (observations reported by [Radigan et al. 2014](#) and [Radigan 2014](#) were conducted at 1.1–1.7 μm , while [Metchev et al. 2015](#) was at 3–5 μm). [Metchev et al. \(2015\)](#) also find a tentative correlation between low-surface gravity and large-amplitude variability at 3–5 μm for L3–L5.5 dwarfs, as well as a tentative relationship between colour and variability (see Section 1.2.4).

A series of investigations by [Vos et al. \(2018, 2019, 2020\)](#) further investigated the tentative correlation between low gravity and high-amplitude variability in brown dwarfs found by [Metchev et al. \(2015\)](#). Using the Spitzer Space Telescope observations and ground-based *J*-band observations from the New Technology Telescope and the United Kingdom Infrared Telescope, they investigated a sample of L dwarfs and found that low-gravity L dwarfs are more likely to be variable than higher-mass field dwarfs.

Moving towards cooler brown dwarfs, [Heinze et al. \(2015\)](#) studied 12 T dwarfs for variability in the red optical wavelengths (0.70–0.95 μm). This work aimed to determine the occurrence rate of large amplitude variability in T dwarfs, in order to put into context one of the largest amplitude variable brown dwarfs, the T0.5 Luhman 16 B ([Luhman, 2013](#); [Gillon et al., 2013](#); [Biller et al., 2013](#); [Buenzli et al., 2015a,c](#); [Karalidi et al., 2016](#); [Apai et al., 2021](#)). Luhman 16 B has an amplitude of $\sim 11\%$ in the *I* + *z* filter (750 nm to 1100 nm; [Gillon et al. 2013](#)). [Heinze](#)

[et al. \(2015\)](#) found significant variability in two of their targets ($> 10\%$) and suggest that high-amplitude variability for T dwarfs is not uncommon. They also find that for cool brown dwarfs, variability amplitude may be anti-correlated with wavelength, finding that the amplitudes at $0.7\text{--}0.95\ \mu\text{m}$ are much larger than at $3.6\text{--}4.5\ \mu\text{m}$ (as measured in the [Metchev et al. 2015](#) study for the same targets).

Variability has also been detected in Y dwarfs. [Cushing et al. \(2016\)](#), [Esplin et al. \(2016\)](#), and [Leggett et al. \(2016\)](#) each report variability for single Y dwarfs using the Spitzer Space Telescope. [Leggett et al. \(2016\)](#) supplement their Spitzer Observations with ground-based near-infrared observations from Gemini Observatory, where they find tentative variability in the *Y* and *J* bands. The results of [Esplin et al. \(2016\)](#) are particularly exciting – they detect variability in the coldest known brown dwarf, WISE J085510.83+071442.5 ($T_{\text{eff}} \sim 250\ \text{K}$; [Luhman 2014](#)). This object is of spectral type Y2 ([Leggett et al., 2015](#)), is very low-mass ($3\text{--}10\ M_{\text{Jup}}$; [Luhman 2014](#)), and possesses the coldest atmosphere studied outside of our own solar system. These results indicate that variability (and therefore cloud evolution) is detectable on exoplanets, if the required sensitivity can be achieved for such faint targets. In fact, variability has already been detected in hotter planetary mass companions: [Zhou et al. \(2016, 2018, 2019, 2020\)](#) detect variability in five such objects with the Hubble Space Telescope, with spectral types from L1 to T2.5.

I have already briefly described the results of the study by [Apai et al. \(2017\)](#), but will describe the survey here for completeness. [Apai et al. \(2017\)](#) studies six brown dwarfs known to be variable with the Spitzer Space Telescope. Each target was observed for eight epochs over 1.5 years, totalling over 30 rotations for each target. This key study found that a simple combination of elliptical spots alone cannot reproduce brown dwarf light curves. A combination of spots and bands powered by planetary-scale waves is required.

The combined results of these surveys indicate that variability is ubiquitous in brown dwarfs. The majority of variability studies conclude that variability, particularly in the L/T transition, supports the hypothesis that brown dwarf atmospheres are composed of patchy, multi-layer clouds. Variability in brown dwarfs is driven by combinations of elliptical spots and bands. There is yet more exciting information that can be deduced from the variability and rotation of brown dwarfs, such as their viewing geometries.

1.2.4 Viewing Geometry

An intuitive consequence of rotation is that viewing geometry will have a large impact on what we observe: if either pole of a brown dwarf is directed towards us, even if it is rotating, the same parts of the atmospheric surface would always be visible to an observer on Earth. This means

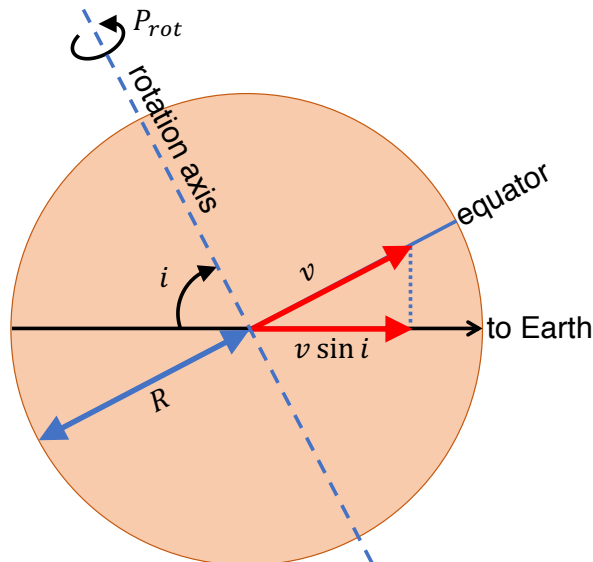


Figure 1.13: A schematic of how the viewing geometry can be measured for brown dwarfs with an estimate of the radius (R), and a measure of the projected rotation velocity ($v \sin i$) and the rotation period (P_{rot}). The calculation is shown in Equation 1.4.

that even if there are patchy clouds in the atmosphere, the brown dwarf would not appear to be variable. Viewing geometry is therefore an unavoidable bias in the detection of variability; the maximum amplitude variability will occur when a brown dwarf is viewed from the equator, and as inclination decreases to pole-on, the measured amplitude will decrease.

To constrain the viewing geometry of a rotating star or brown dwarf, three pieces of information are required: the equatorial rotational velocity (v), the projected rotational velocity ($v \sin i$), and the radius of the object (R). For ultra-cool dwarfs, the patchy atmospheres allow us to derive a relatively unbiased rotation period (P_{rot}), as discussed in Section 1.2.1, which, when combined with the radius, yields the equatorial rotational velocity. Thus, the inclination (i) of the object may be determined with the following equation:

$$\sin i = \frac{(v \sin i)}{v} = \frac{P_{\text{rot}}}{2\pi R} (v \sin i). \quad (1.4)$$

A schematic of this geometry is shown in Figure 1.13.

As discussed in Section 1.1.1, ultra-cool dwarfs older than ~ 500 Myr are conveniently predicted to have fairly constant radii ($0.8\text{--}1.0 R_{\text{Jup}}$; Chabrier et al. 2000). The radii are often the largest sources of uncertainty in determining the viewing geometry, as they are model-dependent. The projected rotational velocities, or $v \sin i$'s, are determined from the rotational broadening of spectral lines. The measurement and techniques for determining this parameter are similar across astronomy: for stars and brown dwarfs, a common approach is to broaden a

model spectrum with a suitable rotation profile (e.g., that of [Gray 1992](#)) and to compare to the observed spectrum. Alternatively, a template slow-rotator of the same spectral type can be used instead of a model, which are not always accurate (see Section 1.3.3). Observed templates are, however, subject to other sources of error, such as the rotation of the template itself (e.g., [Reid et al. 2002](#)).

[Kirkpatrick et al. \(2010\)](#) studied a set of L and T dwarfs containing several brown dwarfs redder and bluer in colour than the median. Based on kinematics, they determined that these targets were related, coming from the same relatively old population. Since the objects were related, they suggested that the viewing geometry was responsible for the differences in spectral appearance. They proposed that clouds distributed non-homogeneously across varying latitude could be the cause in variation of colours. Since fewer red objects were detected than blue, they suggest that redder colours may correspond to a pole-on viewing angle, which is statistically less likely than an equator-on viewing angle, which would subsequently correspond to bluer colours. They also suggest variations in cloud thickness and grain size could be dependent on latitude (and therefore viewing angle).

The extensive photometric variability survey by [Metchev et al. \(2015\)](#) also suggests that viewing angle affects spectral appearance and colour. Their study found a correlation between colour and high-amplitude variability, and that variable brown dwarfs tend to have colours redder than the median. Since variability effects appear larger when viewed equator-on, this may be interpreted as a latitudinal dependence where redder brown dwarfs are seen closer to equator-on, and bluer ones are closer to pole-on – the opposite of what was suggested by [Kirkpatrick et al. \(2010\)](#), perhaps due to the limited sample in this earlier study (less than 30 targets where the variability of the targets was not known). [Vos et al. \(2017\)](#) further investigated this effect, and found a statistically significant correlation between colour and inclination in their sample. Their findings suggest that equator-on (high inclination) objects in fact appear redder, while pole-on (low inclination) objects appear bluer. If this correlation between colour and viewing geometry is confirmed, it could provide insight into the long-standing questions about the L/T transition.

These studies show that viewing geometry is an important property in studies of brown dwarf atmospheres. Two objects may have very different colours, making us think we are studying two dissimilar objects with distinct atmospheric properties, when in reality, we are looking at two similar objects from two different angles. Our understanding of substellar atmospheres, their driving mechanisms, and low-mass stellar evolution depend on accurately modelling atmospheres to reproduce these observations.

1.3 Brown Dwarf Atmospheric Chemistry

Over the course of this introduction, we have established that brown dwarfs are complex and rich in molecules because of their cool atmospheres (relative to stars, which mostly contain neutral atoms and monatomic ions). Early L dwarfs have atmospheres and spectroscopic signatures similar to the lowest mass stars, while T and Y dwarfs are more similar to gas giant planets, with a whole sequence of subtle changes in the subtypes in between. In this section I will describe in more detail the molecules found in each of the brown dwarf spectral types (Section 1.3.1), and highlight some of the most important chemical reactions in brown dwarf atmospheres (Section 1.3.2). This section concludes with a summary of the different atmospheric models available, and a brief history of their development (Section 1.3.3).

1.3.1 Detailed Chemistry by Spectral Type

At effective temperatures less than ~ 5000 K, metal hydrides and oxides (e.g., CH, OH, FeH, CaH, MgH, SiH, and in particular, TiO and VO), as well as water gas (H_2O) and carbon monoxide gas (CO) are prominent in the atmospheres of K and M stars.

Below ~ 2600 K, these hydrides and oxides condense into micron-sized grains, or “dust,” such as perovskite (CaTiO_3), and silicates (e.g., MgSiO_3 , Mg_2SiO_4 , CaSiO_3 , and Ca_2SiO_4) in the atmospheres of late M and the earliest L dwarfs (e.g., [Allard et al. 2001](#)). Neutral atomic lines of Na, Fe, K, Al, and Ca are also prominent ([Kirkpatrick, 2005](#)). As we move cooler through the L dwarf sequence, Al and Ca lines and CaH bands disappear and these elements instead form corundum (Al_2O_3) and calcium aluminates ([McLean et al., 2003](#); [Kirkpatrick et al., 1999](#); [Martín et al., 1999](#)). Iron hydride (FeH) gas condenses into metallic iron clouds. In L dwarfs, the distinguishing spectral features are H_2O , and CO, with CO strengthening up to the mid-L types ([Noll et al., 2000](#); [Cushing et al., 2005](#); [Kirkpatrick, 2005](#)). Alkali lines, like the K I lines in the *J* band remain strong through all L-types and the early T-types.

At effective temperatures less than ~ 1800 K (mid-L and later), oxides continue to weaken, and the majority of the carbon is in the form of methane (CH_4) gas, weakening the CO signature ([Fegley & Lodders, 1996](#)). This change in the main carbon-bearing molecule marks the change from L-type to T-type. For effective temperatures less than 1400 K (late L, T and Y dwarfs), sulfides like Na_2S , MnS , and ZnS , as well as potassium chloride (KCl) and atomic chromium are expected to condense to liquids ([Lodders, 1999](#); [Marley, 2000](#); [Burrows et al., 2001](#); [Lodders & Fegley, 2006](#); [Visscher et al., 2006](#); [Morley et al., 2012](#)).

In T dwarfs, H_2O and CH_4 gas signatures strengthen, and alkali lines weaken. In late T-types and Y dwarfs ($\lesssim 600$ K), ammonia (NH_3) gas signatures appear in the near-infrared ([Burrows & Volobuyev, 2003](#); [Kirkpatrick, 2005](#); [Cushing et al., 2011](#)). In Y dwarfs, at the

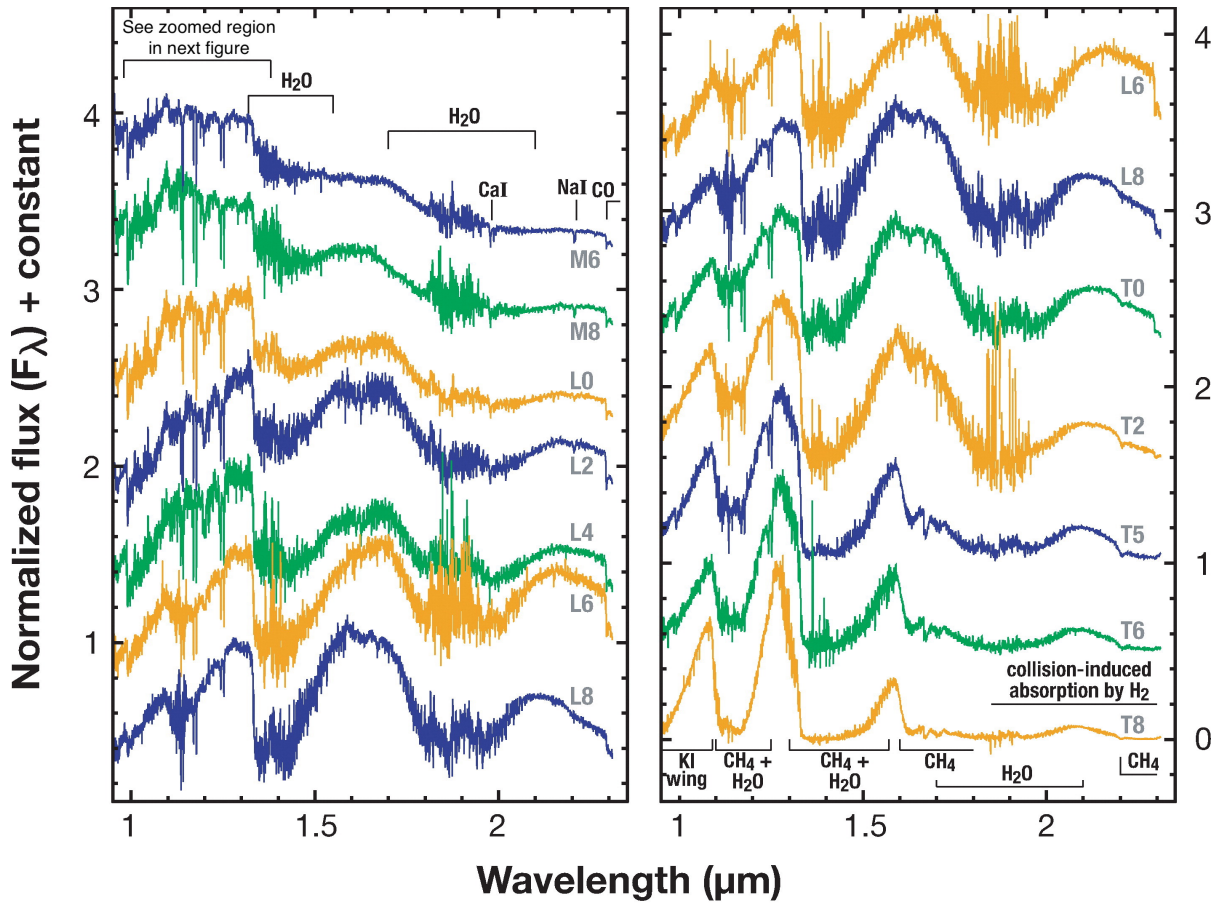


Figure 1.14: A near-infrared (0.95–2.3 μm) spectral sequence from late M dwarfs to late T dwarfs, in steps of two spectral subtypes. The spectra are offset by constants for clarity. Major absorption features are indicated, notably the H_2O and CH_4 bands (indicated on the figure) which significantly reduce the flux. This figure is from [Kirkpatrick \(2005\)](#).

lowest temperatures (less than 500 K), H_2O and CH_4 gas signatures remain prominent, and NH_3 begins to dominate. Phosphine (PH_3) may be present, and hydrogen sulfide (H_2S) also becomes the key sulfur-bearing molecule ([Lodders & Fegley, 2002](#)).

A more detailed near-infrared spectroscopic sequence than the one shown in Figure 1.6 is shown in Figures 1.14 and 1.15. Several of the molecules and atomic lines described above are marked on these figures. We can see how some opacity sources like the water and methane bands become stronger, and how atomic lines become weaker, as the effective temperatures drop through the spectral sequence.

In Figure 1.16, pressure-temperature profiles for cloud-free model brown dwarfs of various effective temperatures are shown. These profiles can be used to determine the interior temperature of the brown dwarf at a particular pressure (which corresponds to altitude in the atmosphere: higher pressures are deeper in the atmosphere, and lower pressures are higher).

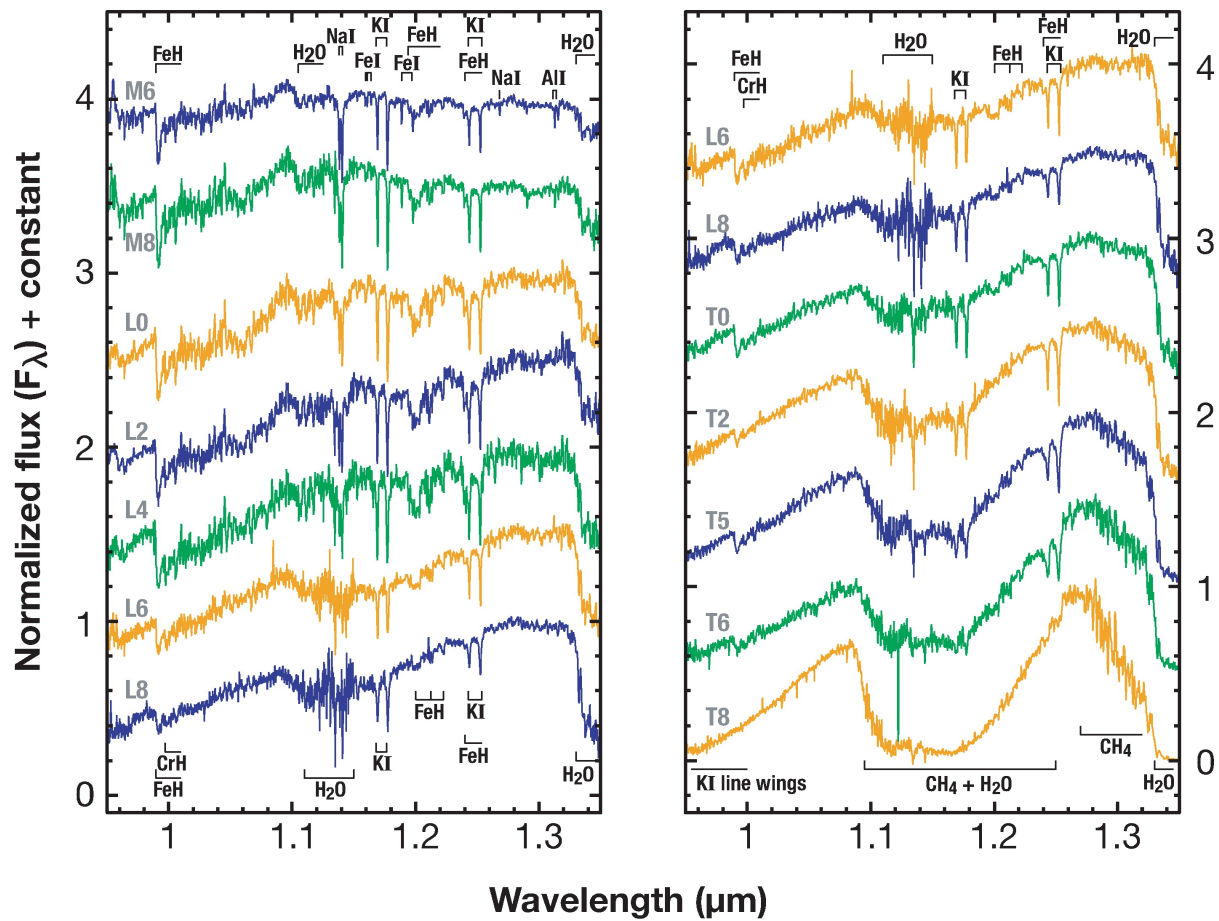


Figure 1.15: This figure is an expanded view of the $0.95\text{--}1.35\ \mu\text{m}$ region (the z and J bands) in Figure 1.14. Major absorption features are indicated, notably the K I potassium doublet that persists through to the mid-T dwarfs. This figure is from Kirkpatrick (2005).

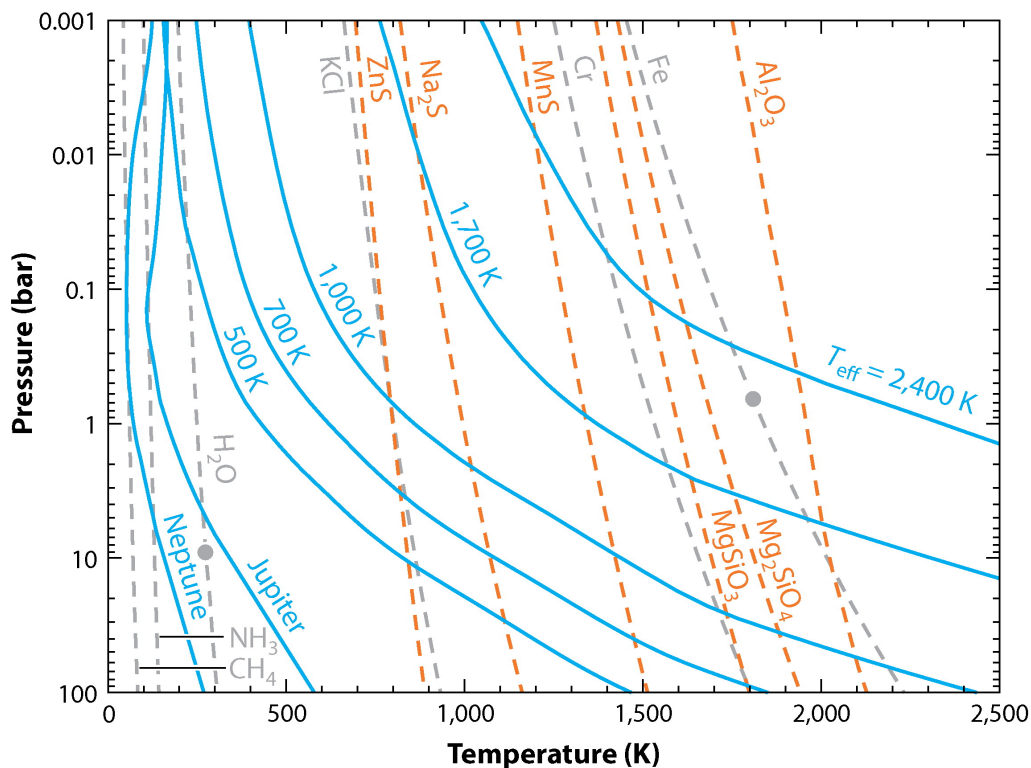


Figure 1.16: Pressure-temperature profiles shown with various condensation curves. Pressure-temperature profiles are shown in blue for cloud-free models with effective temperatures covering the ranges of brown dwarfs (2400 K to 500 K). Empirical thermal profiles Jupiter and Neptune also shown. Condensation curves are shown in grey for direct condensation and in orange for condensates that form from chemical reactions. Liquid to solid transitions are indicated with solid circles. This figure is from [Marley & Robinson \(2015\)](#).

This is helpful for determining where in the atmosphere particular gases and condensates might exist. This figure also shows the condensation curves for many of the molecules mentioned above. This allows us to see where in the atmosphere liquid or solids are forming from these molecules as opaque clouds. Note that gases are not indicated on this plot; for example, we see that H_2O will condense as a liquid in atmospheres with effective temperatures less than ~ 600 K, but water still exists as a gas in the atmospheres of warmer brown dwarfs.

1.3.2 Challenges in Understanding Brown Dwarf Chemistry

Identifying the aforementioned molecules and atoms in observed brown dwarf spectra, especially in cold brown dwarfs, has on occasion proven to be difficult (e.g., [Bochanski et al. 2011](#); [Leggett et al. 2012, 2019](#); [Beichman et al. 2014](#); [Canty et al. 2015](#); [Schneider et al. 2015](#);

Luhman & Esplin 2016; Miles et al. 2020). Blended lines present one such difficulty: lines from different molecular species may be blended due to rapid rotation or simply due to the limitations on instrument resolution. Inaccurate experimental and theoretical line lists can also prevent the identification of particular spectroscopic features. Additionally, there are gaps in our understanding and expectations of brown dwarf atmospheres. For instance, the temperature ranges discussed in the previous section for the various molecules and atoms are approximate; abundances, disequilibrium chemistry, and surface gravity can all affect what molecules form in brown dwarf atmospheres.

The overall abundance of elements in the entire brown dwarf is of course a key factor in determining which molecules may form. The carbon and oxygen abundances are the most important, as CO, H₂O, and CH₄ are the main absorbers across all brown dwarf spectral types. Therefore, the C/O ratio is a very important parameter for understanding brown dwarf atmospheres (Marley & Robinson, 2015). Local abundances matter as well; as condensates rainout in the atmosphere, it may limit the availability of particular elements elsewhere, like in the cooler, higher altitude layers.

Model atmospheres typically assume that the brown dwarf is in chemical equilibrium. When the atmosphere is in chemical equilibrium it implies no further reactions are taking place over time, and the abundances of any species can be computed for a given pressure and temperature using model pressure-temperature profiles, like the ones shown in Figure 1.16. However, many studies have shown that departures from chemical equilibrium (chemical disequilibrium) are common, especially for cold brown dwarfs (e.g., Noll et al. 1997; Oppenheimer et al. 1998; Golimowski et al. 2004; Geballe et al. 2009; Leggett et al. 2012; Sorahana & Yamamura 2012; Miles et al. 2020), and also in Jupiter’s atmosphere (Prinn & Barshay, 1977).

Chemical disequilibrium can occur when vertical mixing (convection) occurs in the atmosphere (Lodders & Fegley, 2002). If material is being brought from deeper, hotter layers to the upper atmosphere faster than chemical reactions can convert it to the next material and to settle into chemical equilibrium, there will be more of the parent material in the upper layers of the atmosphere than predicted from chemical equilibrium.

Consider, for example, the conversion of CO to CH₄: there are many chemical pathways to forming CH₄ (Zahnle & Marley, 2014), but the net reaction to convert CO to CH₄ is:



(e.g., Saumon et al. 2006). This is a relatively slow reaction as CO is particularly hard to break up due to its strong triple bond (Zahnle & Marley, 2014; Marley & Robinson, 2015). As such, an excess of CO is commonly observed in cold brown dwarf spectra (e.g., Noll et al. 1997;

[Oppenheimer et al. 1998](#); [Golimowski et al. 2004](#); [Geballe et al. 2009](#); [Leggett et al. 2012](#); [Sorahana & Yamamura 2012](#); [Miles et al. 2020](#)).

Carbon monoxide is not the only species which can be in chemical disequilibrium; the conversion of N_2 to NH_3 is similarly slowed by the strong bonds in N_2 :



(e.g., [Saumon et al. 2006](#)), and observations have found NH_3 abundances below the expectations for chemical equilibrium in late-T dwarfs ([Saumon et al., 2006](#)). Phosphine is also predicted to be an indicator of disequilibrium chemistry and vertical mixing ([Prinn & Lewis, 1975](#); [Visscher et al., 2006](#); [Miles et al., 2020](#)). [Zahnle & Marley \(2014\)](#) additionally find that the efficiency of the atmospheric mixing related to disequilibrium chemistry can be dependent on surface gravity.

Modern high-resolution spectrographs are allowing us to see deeper in to the jungle of molecular features in brown dwarf spectra. We are entering an era where the accuracy of molecular line lists can be rigorously tested, and molecular absorption can be identified even in cases with very low signal-to-noise ratios (such as in cross-correlation analysis of exoplanets, where the planet itself cannot be spatially resolved and the planet's flux is mixed in with the star's). Many of the outstanding questions related to brown dwarf atmospheres will be resolved as we develop models that reliably match observed data. The following section outlines some of the history of brown dwarf atmospheric models and highlights the most popular models available to date.

1.3.3 Atmospheric Models

Model spectra predict spectral and evolutionary properties, and are typically provided on grids of effective temperature and surface gravity. Some models may include additional parameters related to cloud formation or metallicity. These model grids can be compared to observations to derive the physical properties of brown dwarfs.

Model spectra are generated by constructing an atmospheric structure model that converts a given internal heat flux to the radiation that would be measured at the top of the atmosphere. This type of model is called a “radiative-convective equilibrium model” ([Marley & Robinson, 2015](#)), and involves solving radiative transfer, radiative equilibrium, and hydrostatic equilibrium equations. A convection model, a cloud model, and an opacity database for the molecular and atomic ingredients of a brown dwarf atmosphere are also required ([Burrows et al., 2003](#)). I will not discuss the methods for solving the radiative transfer, radiative equilibrium, and hydrostatic equilibrium equations here. I will instead focus on the features, parameters, and physics unique

to modelling brown dwarf atmospheres in each successive generation of models.

In even the earliest models (e.g., [Lunine et al. 1986](#); [Burrows et al. 1989](#)) it was recognized that cloud and dust opacities would be required to correctly model brown dwarf atmospheres. The [Tsuji \(2001, 2002\)](#) models allowed for clouds to form layers which become thicker and sink deeper for cooler atmospheres (as we expect for spectral types later than the L/T transition). These and subsequent models placed constraints on cloud particle sizes and dust grain sizes to prevent gravitational settling deeper in the atmospheres, in order to maintain cloud layers. To further avoid this problem, these models assumed that grains were constantly forming and evaporating. [Tsuji \(2002\)](#) were able to retrieve the L/T transition CO to CH₄ conversion and colour reversal, but over a much broader temperature range (~600 K instead of the observed 100 – 200 K).

[Ackerman & Marley \(2001\)](#) and [Marley et al. \(2002\)](#) introduced a parameter called the sedimentation efficiency (f_{sed}) to give an indication of how optically thick or thin the cloud layers are. Sedimentation efficiency determines how quickly particles settle out of clouds relative to turbulent mixing in the atmospheres of brown dwarfs. High f_{sed} results in clouds with larger particle sizes which tend to be thinner, and low f_{sed} results in clouds with smaller particle sizes which tend to be more vertically extended. These models were able to simulate atmospheres with varied mixing but were still unable to match the observational colour reversal at the L/T transition.

[Ackerman & Marley \(2001\)](#) and [Burgasser et al. \(2002b\)](#) suggested that holes in the cloud layers allow flux from the hotter interiors to come through, like those illustrated in [Figure 1.10](#). Such holes can help explain the colour reversal at the L/T transition in colour-magnitude diagrams; if there are fewer holes, brown dwarfs appear to be cooler overall (brighter at longer wavelengths, and thus “redder” in colour), and if there are more holes, brown dwarfs appear to be hotter overall (brighter at shorter wavelengths, and thus “bluer” in colour; [Ackerman & Marley 2001](#); [Burgasser et al. 2002a](#); [Kostov & Apai 2013](#)).

Building on the [Ackerman & Marley \(2001\)](#) and [Marley et al. \(2002\)](#) models and the ideas for “patchy clouds,” [Saumon & Marley \(2008\)](#)’s models for late-T and Y dwarfs simulated patchy clouds and hot spots, by perturbing the temperature structure at various depths in the atmospheres, combining separate cloudy and cloudless models. [Marley et al. \(2010\)](#) improved upon this further by generating single models which included patchy clouds, with parameters for cloud thickness and coverage. [Morley et al. \(2012\)](#) further included optically thin clouds which were neglected in previous models by considering higher and cooler regions of brown dwarf atmospheres, finding better matches to the observed colours of T dwarfs.

The most recent set of models built upon the Ackerman and Marley framework is known as “Sonora” ([Marley et al., 2021](#)). Several model grids are planned for the Sonora collection,

and these models include updated molecular line lists (notably for water and methane) and atmospheric chemistry. Currently available are the “Sonora Bobcat” models (Marley et al., 2021) and the “Sonora Cholla” models (Karalidi et al., 2021). The Sonora Bobcat models are for cloudless atmospheres in chemical equilibrium, covering effective temperatures from 200 K to 2400 K and are suitable for L, T, and Y dwarfs. The Sonora Cholla models are for cloudless atmospheres with solar metallicity in chemical disequilibrium, and focus on lower effective temperatures (500–1300 K), suitable for T dwarfs and wide-separation giant planets. A third grid of Sonora models which will include cloud processes is planned for release in the coming year (Morley et al., in prep.).

Under the PHOENIX framework (Allard & Hauschildt, 1995; Hauschildt et al., 1999), several grids of models have been generated since the late '90s. Unlike the Ackerman and Marley models, which use pre-tabulated chemistry and opacities, models based on PHOENIX compute chemistry and opacities concurrently with their radiative-convective equilibrium model. Allard et al. (2001) determined the cloud base for each condensate individually to develop two sets of models: one which includes condensation, but ignores dust opacities, titled “COND” and another which includes both condensation and dust opacities, titled “DUSTY.” Allard et al. (2012a, 2014) expand upon these models with the “BT-Settl” model grids, which include an updated water line list (Barber et al., 2006), and include the condensation, sedimentation, coagulation, and convection of grains by investigating gravitational settling within the atmosphere.

More recently, Phillips et al. (2020) generated three grids of model spectra for T and Y dwarfs titled “ATMO2020” based on the PHOENIX framework. One grid was generated for equilibrium chemistry, and two for variations on non-equilibrium chemistry due to vertical mixing. Notably these models make use of a new H-He equation of state (Chabrier et al., 2019) that improves the theoretical masses determined by their models, and alters the cooling tracks related to hydrogen and deuterium burning masses.

As stated in Section 1.3.2, even the most up-to-date models do not reproduce all observed features in brown dwarf spectra. However with the advances in cloud physics and the updated line lists for the dominant absorbers in brown dwarf spectra (e.g., H₂O, CH₄, NH₃) the accuracy of brown dwarf model spectra are improving rapidly. The fact that there are multiple groups working independently on modelling brown dwarf spectra with their own radiative-convective equilibrium models is a boon to the brown dwarf field; complementary models are necessary for confirming the accuracy and importance of physical and chemical assumptions in atmospheric models.

1.4 What This Thesis Addresses and Project Motivation

It has only been in recent years that sufficient data has been collected on the rotation periods of brown dwarfs that meaningful statistics can be calculated. One important result of modern large brown dwarf variability surveys is that it is now known that brown dwarfs tend to be “fast-rotators” with typical rotation periods on the order of hours to tens of hours. But how fast can brown dwarfs rotate? Since brown dwarfs lack the braking mechanisms often seen in stars, is there a limit on brown dwarf rotation speed? In Chapter 2 of this thesis, I present three brown dwarfs with the shortest rotation periods ever observed. I present Spitzer Space Telescope photometry at $3.6\ \mu\text{m}$ and $4.5\ \mu\text{m}$ and my precise measurements of rotation periods of $1.080_{-0.005}^{+0.004}$ h, $1.14_{-0.01}^{+0.03}$ h, and $1.23_{-0.01}^{+0.01}$ h for a T7, an L8, and an L3.5, respectively. These “ultra-fast rotators” span spectral types from mid-L to mid-T, and the clustering of the shortest rotation periods near 1 h suggests that brown dwarfs are unlikely to spin much faster. A limit on brown dwarf rotation may help to set meaningful limits on breakup speeds or angular momentum limits, and to help us understand the structure of brown dwarf interiors and the rotation evolution in brown dwarfs.

In the second part of Chapter 2 I investigate the effects of the rapid rotation on the near-infrared spectra of the three ultra-fast rotators. I compared the observations from Magellan/FIRE and Gemini/GNIRS to the atmospheric model spectra of [Saumon & Marley \(2008\)](#), [Allard et al. \(2012b; BT-Settl\)](#), [Morley et al. \(2012\)](#), and [Marley et al. \(2021; Sonora Bobcat\)](#) to determine the physical properties of these objects. I find the highest degrees of rotational broadening ever measured for brown dwarfs ($103.5 \pm 7.4\ \text{km s}^{-1}$, $79.0 \pm 3.4\ \text{km s}^{-1}$, and $82.6 \pm 0.2\ \text{km s}^{-1}$ for the T7, L8, and L3.5, respectively, which all correspond to equatorial velocities of $\geq 100\ \text{km s}^{-1}$), and confirm the rotation periods determined from the rapid variability seen in the photometry. I additionally measure the viewing geometries of all three of these brown dwarfs.

The paper presented in Chapter 2 of this thesis represents a significant contribution to the literature. This work was originally designed to be presented in two separate publications, but was combined into a single work at the request of the co-authors of [Tannock et al. \(2021\)](#).

In Chapter 3 of this thesis I delve into the complicated domain of brown dwarf atmospheric chemistry. I present one of the highest resolution ($R=45,000$), highest signal-to-noise ($\text{SNR}>200$) near-infrared spectra of a late-T dwarf ever observed. This T6 spectrum, observed with Gemini/IGRINS, presents a unique opportunity to test the most up-to-date model photospheres and to determine the accuracy of the available molecular line lists for water, methane, and ammonia. I perform a careful comparison to the models of [Allard et al. \(2012b; BT-Settl\)](#), [Morley et al. \(2012\)](#), [Marley et al. \(2021; Sonora Bobcat\)](#), and a special revised version of the Sonora Bobcat models with molecular line lists never before included in a publicly-released

model atmosphere grid (Hood et al., in prep.). I report the first unambiguous detection of hydrogen sulfide in an extra-solar atmosphere, find that this T6 dwarf demonstrates CO disequilibrium chemistry, and identify several absorption features in the observed spectrum that do not appear in any of the photospheric models. I find that the updated line lists for water, methane, and ammonia allow for precise empirical determinations of physical parameters, and are highly promising for the detection and characterization of exoplanets with high-dispersion spectroscopy. Finally, I present the most detailed atlas of spectroscopic lines in a cold brown dwarf to date.

I would also like to provide some motivation for the aforementioned works, and describe briefly my PhD project journey.

A substantial sample of L and T dwarfs were observed with the Spitzer Space Telescope as a follow-up to the Weather on Other Worlds study (Heinze et al., 2013; Metchev et al., 2015). Using the methods described in the Weather on Other Worlds publications, I analyzed these data and identified variable brown dwarfs. I determined the rotation periods and generated light curves for each of the variable brown dwarfs in this sample. Three of those brown dwarfs are the ultra-fast rotators presented in Chapter 2. Given the remarkable rotation periods of this trio, we felt that they merited their own paper, separate from the rest of the sample.

Over the course of my graduate studies I led an ambitious spectroscopic follow-up of the variable objects in Metchev et al. (2015) and the follow-up Spitzer program. I aimed to confirm the rotation periods of the variables by examining their rotation broadening and to determine their viewing geometries to further test the colour trends found by Metchev et al. (2015) and Vos et al. (2017). However, as the analysis progressed, again I found myself in the possession of a particularly exceptional data set warranting its own solo publication: the Gemini South/IGRINS T6 data that is featured in Chapter 3. In addition to the projected rotational velocity and viewing geometry I sought, it was also clear that this observation could greatly benefit the brown dwarf and exoplanet community by acting as an important benchmark and high resolution atlas of molecular absorption features for cold brown dwarfs.

The data I collected through my follow-up spectroscopic survey alone could fill another PhD project, and, personally, I think one PhD is enough. I will discuss some of the potential uses for this data in Chapter 4. On a journey to investigate brown dwarf variability, rotation rates, viewing geometries, and the L/T transition I found myself going in a totally different direction and chasing discoveries I hadn't even dreamt of. But I guess that is what science is all about, right?

Bibliography

- Ackerman, A. S., & Marley, M. S. 2001, *ApJ*, 556, 872, doi: [10.1086/321540](https://doi.org/10.1086/321540)
- Allard, F., & Hauschildt, P. H. 1995, *ApJ*, 445, 433, doi: [10.1086/175708](https://doi.org/10.1086/175708)
- Allard, F., Hauschildt, P. H., Alexander, D. R., Tamanai, A., & Schweitzer, A. 2001, *ApJ*, 556, 357, doi: [10.1086/321547](https://doi.org/10.1086/321547)
- Allard, F., Homeier, D., & Freytag, B. 2012a, *Philosophical Transactions of the Royal Society of London Series A*, 370, 2765, doi: [10.1098/rsta.2011.0269](https://doi.org/10.1098/rsta.2011.0269)
- Allard, F., Homeier, D., & Freytag, B. 2012b, in *IAU Symposium*, Vol. 282, *From Interacting Binaries to Exoplanets: Essential Modeling Tools*, ed. M. T. Richards & I. Hubeny, 235–242, doi: [10.1017/S1743921311027438](https://doi.org/10.1017/S1743921311027438)
- Allard, F., Homeier, D., & Freytag, B. 2014, in *Astronomical Society of India Conference Series*, Vol. 11, *Astronomical Society of India Conference Series*, 33–45
- Apai, D., Nardiello, D., & Bedin, L. R. 2021, *ApJ*, 906, 64, doi: [10.3847/1538-4357/abcb97](https://doi.org/10.3847/1538-4357/abcb97)
- Apai, D., Karalidi, T., Marley, M. S., et al. 2017, *Science*, 357, 683, doi: [10.1126/science.aam9848](https://doi.org/10.1126/science.aam9848)
- Artigau, É., Bouchard, S., Doyon, R., & Lafrenière, D. 2009, *ApJ*, 701, 1534, doi: [10.1088/0004-637X/701/2/1534](https://doi.org/10.1088/0004-637X/701/2/1534)
- Bailer-Jones, C. A. L., & Mundt, R. 1999, *A&A*, 348, 800
- . 2001, *A&A*, 367, 218, doi: [10.1051/0004-6361:20000416](https://doi.org/10.1051/0004-6361:20000416)
- Barber, R. J., Tennyson, J., Harris, G. J., & Tolchenov, R. N. 2006, *MNRAS*, 368, 1087, doi: [10.1111/j.1365-2966.2006.10184.x](https://doi.org/10.1111/j.1365-2966.2006.10184.x)
- Basri, G. 2004, in *IAU Symposium*, Vol. 215, *Stellar Rotation*, ed. A. Maeder & P. Eenens, 248

- Basri, G., & Brown, M. E. 2006, *Annual Review of Earth and Planetary Sciences*, 34, 193, doi: [10.1146/annurev.earth.34.031405.125058](https://doi.org/10.1146/annurev.earth.34.031405.125058)
- Beichman, C., Gelino, C. R., Kirkpatrick, J. D., et al. 2014, *ApJ*, 783, 68, doi: [10.1088/0004-637X/783/2/68](https://doi.org/10.1088/0004-637X/783/2/68)
- Biller, B. 2017, *The Astronomical Review*, 13, 1, doi: [10.1080/21672857.2017.1303105](https://doi.org/10.1080/21672857.2017.1303105)
- Biller, B. A., Crossfield, I. J. M., Mancini, L., et al. 2013, *ApJ Letters*, 778, L10, doi: [10.1088/2041-8205/778/1/L10](https://doi.org/10.1088/2041-8205/778/1/L10)
- Biller, B. A., Vos, J., Buenzli, E., et al. 2018, *AJ*, 155, 95, doi: [10.3847/1538-3881/aaa5a6](https://doi.org/10.3847/1538-3881/aaa5a6)
- Bochanski, J. J., Burgasser, A. J., Simcoe, R. A., & West, A. A. 2011, *AJ*, 142, 169, doi: [10.1088/0004-6256/142/5/169](https://doi.org/10.1088/0004-6256/142/5/169)
- Boss, A. P., Butler, R. P., Hubbard, W. B., et al. 2007, *Transactions of the International Astronomical Union, Series A*, 26, 183, doi: [10.1017/S1743921306004509](https://doi.org/10.1017/S1743921306004509)
- Bouvier, J., Matt, S. P., Mohanty, S., et al. 2014, *Protostars and Planets VI*, 433, doi: [10.2458/azu_uapress_9780816531240-ch019](https://doi.org/10.2458/azu_uapress_9780816531240-ch019)
- Buenzli, E., Apai, D., Radigan, J., Reid, I. N., & Flateau, D. 2014, *ApJ*, 782, 77, doi: [10.1088/0004-637X/782/2/77](https://doi.org/10.1088/0004-637X/782/2/77)
- Buenzli, E., Marley, M. S., Apai, D., et al. 2015a, *ApJ*, 812, 163, doi: [10.1088/0004-637X/812/2/163](https://doi.org/10.1088/0004-637X/812/2/163)
- Buenzli, E., Saumon, D., Marley, M. S., et al. 2015b, *ApJ*, 798, 127, doi: [10.1088/0004-637X/798/2/127](https://doi.org/10.1088/0004-637X/798/2/127)
- . 2015c, *ApJ*, 798, 127, doi: [10.1088/0004-637X/798/2/127](https://doi.org/10.1088/0004-637X/798/2/127)
- Burgasser, A. J., Marley, M. S., Ackerman, A. S., et al. 2002a, *ApJ Letters*, 571, L151, doi: [10.1086/341343](https://doi.org/10.1086/341343)
- Burgasser, A. J., Kirkpatrick, J. D., Brown, M. E., et al. 2002b, *ApJ*, 564, 421, doi: [10.1086/324033](https://doi.org/10.1086/324033)
- Burrows, A., Hubbard, W. B., & Lunine, J. I. 1989, *ApJ*, 345, 939, doi: [10.1086/167964](https://doi.org/10.1086/167964)
- Burrows, A., Hubbard, W. B., Lunine, J. I., & Liebert, J. 2001, *Reviews of Modern Physics*, 73, 719, doi: [10.1103/RevModPhys.73.719](https://doi.org/10.1103/RevModPhys.73.719)

- Burrows, A., & Liebert, J. 1993, *Reviews of Modern Physics*, 65, 301, doi: [10.1103/RevModPhys.65.301](https://doi.org/10.1103/RevModPhys.65.301)
- Burrows, A., & Sharp, C. M. 1999, *ApJ*, 512, 843, doi: [10.1086/306811](https://doi.org/10.1086/306811)
- Burrows, A., Sudarsky, D., & Lunine, J. I. 2003, *ApJ*, 596, 587, doi: [10.1086/377709](https://doi.org/10.1086/377709)
- Burrows, A., & Volobuyev, M. 2003, *ApJ*, 583, 985, doi: [10.1086/345412](https://doi.org/10.1086/345412)
- Burrows, A., Marley, M., Hubbard, W. B., et al. 1997, *ApJ*, 491, 856, doi: [10.1086/305002](https://doi.org/10.1086/305002)
- Canty, J. I., Lucas, P. W., Yurchenko, S. N., et al. 2015, *MNRAS*, 450, 454, doi: [10.1093/mnras/stv586](https://doi.org/10.1093/mnras/stv586)
- Chabrier, G., Baraffe, I., Allard, F., & Hauschildt, P. 2000, *ApJ*, 542, 464, doi: [10.1086/309513](https://doi.org/10.1086/309513)
- Chabrier, G., Baraffe, I., Allard, F., & Hauschildt, P. H. 2005, *ArXiv Astrophysics e-prints*
- Chabrier, G., & Baraffe, I. v. 2000, *Annu. Rev. Astron. Astrophys.*, 38, 337, doi: [10.1146/annurev.astro.38.1.337](https://doi.org/10.1146/annurev.astro.38.1.337)
- Chabrier, G., Mazevet, S., & Soubiran, F. 2019, *ApJ*, 872, 51, doi: [10.3847/1538-4357/aaf99f](https://doi.org/10.3847/1538-4357/aaf99f)
- Cushing, M. C., Rayner, J. T., & Vacca, W. D. 2005, *ApJ*, 623, 1115, doi: [10.1086/428040](https://doi.org/10.1086/428040)
- Cushing, M. C., Roellig, T. L., Marley, M. S., et al. 2006, *ApJ*, 648, 614, doi: [10.1086/505637](https://doi.org/10.1086/505637)
- Cushing, M. C., Kirkpatrick, J. D., Gelino, C. R., et al. 2011, *ApJ*, 743, 50, doi: [10.1088/0004-637X/743/1/50](https://doi.org/10.1088/0004-637X/743/1/50)
- Cushing, M. C., Hardegree-Ullman, K. K., Trucks, J. L., et al. 2016, *ApJ*, 823, 152, doi: [10.3847/0004-637X/823/2/152](https://doi.org/10.3847/0004-637X/823/2/152)
- Dantona, F., & Mazzitelli, I. 1985, *ApJ*, 296, 502, doi: [10.1086/163470](https://doi.org/10.1086/163470)
- Enoch, M. L., Brown, M. E., & Burgasser, A. J. 2003, *AJ*, 126, 1006, doi: [10.1086/376598](https://doi.org/10.1086/376598)
- Eriksson, S. C., Janson, M., & Calissendorff, P. 2019, *A&A*, 629, A145, doi: [10.1051/0004-6361/201935671](https://doi.org/10.1051/0004-6361/201935671)
- Esplin, T. L., Luhman, K. L., Cushing, M. C., et al. 2016, *ApJ*, 832, 58, doi: [10.3847/0004-637X/832/1/58](https://doi.org/10.3847/0004-637X/832/1/58)

- Fegley, Jr., B., & Lodders, K. 1996, *ApJ Letters*, 472, L37, doi: [10.1086/310356](https://doi.org/10.1086/310356)
- Filippazzo, J. C., Rice, E. L., Faherty, J., et al. 2015, *ApJ*, 810, 158, doi: [10.1088/0004-637X/810/2/158](https://doi.org/10.1088/0004-637X/810/2/158)
- Geballe, T. R., Saumon, D., Golimowski, D. A., et al. 2009, *ApJ*, 695, 844, doi: [10.1088/0004-637X/695/2/844](https://doi.org/10.1088/0004-637X/695/2/844)
- Gelino, C. R., Marley, M. S., Holtzman, J. A., Ackerman, A. S., & Lodders, K. 2002, *ApJ*, 577, 433, doi: [10.1086/342150](https://doi.org/10.1086/342150)
- Gillon, M., Triaud, A. H. M. J., Jehin, E., et al. 2013, *A&A*, 555, L5, doi: [10.1051/0004-6361/201321620](https://doi.org/10.1051/0004-6361/201321620)
- Golimowski, D. A., Leggett, S. K., Marley, M. S., et al. 2004, *AJ*, 127, 3516, doi: [10.1086/420709](https://doi.org/10.1086/420709)
- Gray, D. F. 1992, *The observation and analysis of stellar photospheres*. (Cambridge University Press). <http://adsabs.harvard.edu/abs/1992oasp.book.....G>
- Hauschildt, P. H., Allard, F., & Baron, E. 1999, *ApJ*, 512, 377, doi: [10.1086/306745](https://doi.org/10.1086/306745)
- Hayashi, C., & Nakano, T. 1963, *Progress of Theoretical Physics*, 30, 460, doi: [10.1143/PTP.30.460](https://doi.org/10.1143/PTP.30.460)
- Heinze, A. N., Metchev, S., & Kellogg, K. 2015, *ApJ*, 801, 104, doi: [10.1088/0004-637X/801/2/104](https://doi.org/10.1088/0004-637X/801/2/104)
- Heinze, A. N., Metchev, S., Apai, D., et al. 2013, *ApJ*, 767, 173, doi: [10.1088/0004-637X/767/2/173](https://doi.org/10.1088/0004-637X/767/2/173)
- Karalidi, T., Apai, D., Marley, M. S., & Buenzli, E. 2016, *ApJ*, 825, 90, doi: [10.3847/0004-637X/825/2/90](https://doi.org/10.3847/0004-637X/825/2/90)
- Karalidi, T., Marley, M., Fortney, J. J., et al. 2021, arXiv e-prints, arXiv:2110.11824. <https://arxiv.org/abs/2110.11824>
- Kellogg, K., Metchev, S., Heinze, A., Gagné, J., & Kurtev, R. 2017, *ApJ*, 849, 72, doi: [10.3847/1538-4357/aa8e4f](https://doi.org/10.3847/1538-4357/aa8e4f)
- Kirkpatrick, J. D. 1998, in *Astronomical Society of the Pacific Conference Series*, Vol. 134, *Brown Dwarfs and Extrasolar Planets*, ed. R. Rebolo, E. L. Martin, & M. R. Zapatero Osorio, 405

- Kirkpatrick, J. D. 2005, *Annu. Rev. Astron. Astrophys.*, 43, 195, doi: [10.1146/annurev.astro.42.053102.134017](https://doi.org/10.1146/annurev.astro.42.053102.134017)
- Kirkpatrick, J. D., Henry, T. J., & Irwin, M. J. 1997, *AJ*, 113, 1421, doi: [10.1086/118357](https://doi.org/10.1086/118357)
- Kirkpatrick, J. D., Reid, I. N., Liebert, J., et al. 1999, *ApJ*, 519, 802, doi: [10.1086/307414](https://doi.org/10.1086/307414)
- Kirkpatrick, J. D., Looper, D. L., Burgasser, A. J., et al. 2010, *ApJS*, 190, 100, doi: [10.1088/0067-0049/190/1/100](https://doi.org/10.1088/0067-0049/190/1/100)
- Knapp, G. R., Leggett, S. K., Fan, X., et al. 2004, *AJ*, 127, 3553, doi: [10.1086/420707](https://doi.org/10.1086/420707)
- Kostov, V., & Apai, D. 2013, *ApJ*, 762, 47, doi: [10.1088/0004-637X/762/1/47](https://doi.org/10.1088/0004-637X/762/1/47)
- Kuzmychov, O., & Berdyugina, S. V. 2013, *A&A*, 558, A120, doi: [10.1051/0004-6361/201220041](https://doi.org/10.1051/0004-6361/201220041)
- Lane, C., Hallinan, G., Zavala, R. T., et al. 2007, *ApJ Letters*, 668, L163, doi: [10.1086/523041](https://doi.org/10.1086/523041)
- Leconte, J. 2018, *ApJ Letters*, 853, L30, doi: [10.3847/2041-8213/aaaa61](https://doi.org/10.3847/2041-8213/aaaa61)
- Leggett, S. K., Morley, C. V., Marley, M. S., & Saumon, D. 2015, *ApJ*, 799, 37, doi: [10.1088/0004-637X/799/1/37](https://doi.org/10.1088/0004-637X/799/1/37)
- Leggett, S. K., Saumon, D., Marley, M. S., et al. 2012, *ApJ*, 748, 74, doi: [10.1088/0004-637X/748/2/74](https://doi.org/10.1088/0004-637X/748/2/74)
- Leggett, S. K., Cushing, M. C., Hardegree-Ullman, K. K., et al. 2016, *ApJ*, 830, 141, doi: [10.3847/0004-637X/830/2/141](https://doi.org/10.3847/0004-637X/830/2/141)
- Leggett, S. K., Dupuy, T. J., Morley, C. V., et al. 2019, *ApJ*, 882, 117, doi: [10.3847/1538-4357/ab3393](https://doi.org/10.3847/1538-4357/ab3393)
- Liu, M. C., Delorme, P., Dupuy, T. J., et al. 2011, *ApJ*, 740, 108, doi: [10.1088/0004-637X/740/2/108](https://doi.org/10.1088/0004-637X/740/2/108)
- Lodders, K. 1999, *ApJ*, 519, 793, doi: [10.1086/307387](https://doi.org/10.1086/307387)
- Lodders, K. 2004, *Science*, 303, 323, doi: [10.1126/science.1092865](https://doi.org/10.1126/science.1092865)
- Lodders, K., & Fegley, B. 2002, *Icarus*, 155, 393, doi: [10.1006/icar.2001.6740](https://doi.org/10.1006/icar.2001.6740)
- Lodders, K., & Fegley, Jr., B. 2006, *Chemistry of Low Mass Substellar Objects*, ed. J. W. Mason, 1, doi: [10.1007/3-540-30313-8_1](https://doi.org/10.1007/3-540-30313-8_1)

- Luhman, K. L. 2013, *ApJ Letters*, 767, L1, doi: [10.1088/2041-8205/767/1/L1](https://doi.org/10.1088/2041-8205/767/1/L1)
- . 2014, *ApJ Letters*, 786, L18, doi: [10.1088/2041-8205/786/2/L18](https://doi.org/10.1088/2041-8205/786/2/L18)
- Luhman, K. L., & Esplin, T. L. 2016, *AJ*, 152, 78, doi: [10.3847/0004-6256/152/3/78](https://doi.org/10.3847/0004-6256/152/3/78)
- Lunine, J. I., Hubbard, W. B., & Marley, M. S. 1986, *ApJ*, 310, 238, doi: [10.1086/164678](https://doi.org/10.1086/164678)
- Marley, M. 2000, in *Astronomical Society of the Pacific Conference Series*, Vol. 212, From Giant Planets to Cool Stars, ed. C. A. Griffith & M. S. Marley, 152
- Marley, M. S., & Leggett, S. K. 2009, in *Astrophysics and Space Science Proceedings*, Vol. 10, Astrophysics in the Next Decade, 101, doi: [10.1007/978-1-4020-9457-6_4](https://doi.org/10.1007/978-1-4020-9457-6_4)
- Marley, M. S., & Robinson, T. D. 2015, *Annu. Rev. Astron. Astrophys*, 53, 279, doi: [10.1146/annurev-astro-082214-122522](https://doi.org/10.1146/annurev-astro-082214-122522)
- Marley, M. S., Saumon, D., & Goldblatt, C. 2010, *ApJ Letters*, 723, L117, doi: [10.1088/2041-8205/723/1/L117](https://doi.org/10.1088/2041-8205/723/1/L117)
- Marley, M. S., Seager, S., Saumon, D., et al. 2002, *ApJ*, 568, 335, doi: [10.1086/338800](https://doi.org/10.1086/338800)
- Marley, M. S., & Sengupta, S. 2011, *MNRAS*, 417, 2874, doi: [10.1111/j.1365-2966.2011.19448.x](https://doi.org/10.1111/j.1365-2966.2011.19448.x)
- Marley, M. S., Saumon, D., Visscher, C., et al. 2021, *ApJ*, 920, 85, doi: [10.3847/1538-4357/ac141d](https://doi.org/10.3847/1538-4357/ac141d)
- Martín, E. L., Delfosse, X., Basri, G., et al. 1999, *AJ*, 118, 2466, doi: [10.1086/301107](https://doi.org/10.1086/301107)
- Martín, E. L., Zapatero Osorio, M. R., & Lehto, H. J. 2001, *ApJ*, 557, 822, doi: [10.1086/321685](https://doi.org/10.1086/321685)
- McLean, I. S., McGovern, M. R., Burgasser, A. J., et al. 2003, *ApJ*, 596, 561, doi: [10.1086/377636](https://doi.org/10.1086/377636)
- Metchev, S. A., Heinze, A., Apai, D., et al. 2015, *ApJ*, 799, 154, doi: [10.1088/0004-637X/799/2/154](https://doi.org/10.1088/0004-637X/799/2/154)
- Meyer, F., & Meyer-Hofmeister, E. 1999, *A&A*, 341, L23. <https://arxiv.org/abs/astro-ph/9901232>
- Miles, B. E., Skemer, A. J. I., Morley, C. V., et al. 2020, *AJ*, 160, 63, doi: [10.3847/1538-3881/ab9114](https://doi.org/10.3847/1538-3881/ab9114)

- Miles-Páez, P. A., Metchev, S. A., Heinze, A., & Apai, D. 2017, *ApJ*, 840, 83, doi: [10.3847/1538-4357/aa6f11](https://doi.org/10.3847/1538-4357/aa6f11)
- Mohanty, S., Basri, G., Shu, F., Allard, F., & Chabrier, G. 2002, *ApJ*, 571, 469, doi: [10.1086/339911](https://doi.org/10.1086/339911)
- Morley, C. V., Fortney, J. J., Marley, M. S., et al. 2012, *ApJ*, 756, 172, doi: [10.1088/0004-637X/756/2/172](https://doi.org/10.1088/0004-637X/756/2/172)
- Morley, C. V., Marley, M. S., Fortney, J. J., & Lupu, R. 2014a, *ApJ Letters*, 789, L14, doi: [10.1088/2041-8205/789/1/L14](https://doi.org/10.1088/2041-8205/789/1/L14)
- Morley, C. V., Marley, M. S., Fortney, J. J., et al. 2014b, *ApJ*, 787, 78, doi: [10.1088/0004-637X/787/1/78](https://doi.org/10.1088/0004-637X/787/1/78)
- Mužić, K., Schödel, R., Scholz, A., et al. 2017, *MNRAS*, 471, 3699, doi: [10.1093/mnras/stx1906](https://doi.org/10.1093/mnras/stx1906)
- Noll, K. S., Geballe, T. R., Leggett, S. K., & Marley, M. S. 2000, *ApJ Letters*, 541, L75, doi: [10.1086/312906](https://doi.org/10.1086/312906)
- Noll, K. S., Geballe, T. R., & Marley, M. S. 1997, *ApJ Letters*, 489, L87, doi: [10.1086/310954](https://doi.org/10.1086/310954)
- Oppenheimer, B. R., Kulkarni, S. R., Matthews, K., & Nakajima, T. 1995, *Science*, 270, 1478, doi: [10.1126/science.270.5241.1478](https://doi.org/10.1126/science.270.5241.1478)
- Oppenheimer, B. R., Kulkarni, S. R., Matthews, K., & van Kerkwijk, M. H. 1998, *ApJ*, 502, 932, doi: [10.1086/305928](https://doi.org/10.1086/305928)
- Phillips, M. W., Tremblin, P., Baraffe, I., et al. 2020, *A&A*, 637, A38, doi: [10.1051/0004-6361/201937381](https://doi.org/10.1051/0004-6361/201937381)
- Prinn, R. G., & Barshay, S. S. 1977, *Science*, 198, 1031, doi: [10.1126/science.198.4321.1031](https://doi.org/10.1126/science.198.4321.1031)
- Prinn, R. G., & Lewis, J. S. 1975, *Science*, 190, 274
- Radigan, J. 2014, *ApJ*, 797, 120, doi: [10.1088/0004-637X/797/2/120](https://doi.org/10.1088/0004-637X/797/2/120)
- Radigan, J., Jayawardhana, R., Lafrenière, D., et al. 2012, *ApJ*, 750, 105, doi: [10.1088/0004-637X/750/2/105](https://doi.org/10.1088/0004-637X/750/2/105)

- Radigan, J., Lafrenière, D., Jayawardhana, R., & Artigau, E. 2014, *ApJ*, 793, 75, doi: [10.1088/0004-637X/793/2/75](https://doi.org/10.1088/0004-637X/793/2/75)
- Rebolo, R., Zapatero Osorio, M. R., & Martín, E. L. 1995, *Nature*, 377, 129, doi: [10.1038/377129a0](https://doi.org/10.1038/377129a0)
- Reid, I. N., Kirkpatrick, J. D., Liebert, J., et al. 2002, *AJ*, 124, 519, doi: [10.1086/340805](https://doi.org/10.1086/340805)
- Richey-Yowell, T., Kao, M. M., Pineda, J. S., Shkolnik, E. L., & Hallinan, G. 2020, *ApJ*, 903, 74, doi: [10.3847/1538-4357/abb826](https://doi.org/10.3847/1538-4357/abb826)
- Robinson, T. D., & Marley, M. S. 2014, *ApJ*, 785, 158, doi: [10.1088/0004-637X/785/2/158](https://doi.org/10.1088/0004-637X/785/2/158)
- Saumon, D., & Marley, M. S. 2008, *ApJ*, 689, 1327, doi: [10.1086/592734](https://doi.org/10.1086/592734)
- Saumon, D., Marley, M. S., Cushing, M. C., et al. 2006, *ApJ*, 647, 552, doi: [10.1086/505419](https://doi.org/10.1086/505419)
- Schlawin, E., Burgasser, A. J., Karalidi, T., Gizis, J. E., & Teske, J. 2017, *ApJ*, 849, 163, doi: [10.3847/1538-4357/aa90b8](https://doi.org/10.3847/1538-4357/aa90b8)
- Schneider, A. C., Cushing, M. C., Kirkpatrick, J. D., et al. 2015, *ApJ*, 804, 92, doi: [10.1088/0004-637X/804/2/92](https://doi.org/10.1088/0004-637X/804/2/92)
- Scholz, A., Kostov, V., Jayawardhana, R., & Mužić, K. 2015, *ApJ Letters*, 809, L29, doi: [10.1088/2041-8205/809/2/L29](https://doi.org/10.1088/2041-8205/809/2/L29)
- Sengupta, S., & Krishan, V. 2001, *ApJ Letters*, 561, L123, doi: [10.1086/324559](https://doi.org/10.1086/324559)
- Sengupta, S., & Kwok, S. 2005, *ApJ*, 625, 996, doi: [10.1086/429659](https://doi.org/10.1086/429659)
- Sorahana, S., & Yamamura, I. 2012, *ApJ*, 760, 151, doi: [10.1088/0004-637X/760/2/151](https://doi.org/10.1088/0004-637X/760/2/151)
- Spiegel, D. S., Burrows, A., & Milsom, J. A. 2011, *ApJ*, 727, 57, doi: [10.1088/0004-637X/727/1/57](https://doi.org/10.1088/0004-637X/727/1/57)
- Strassmeier, K. G. 1994, *A&A*, 281, 395
- Tannock, M. E., Metchev, S., Heinze, A., et al. 2021, *AJ*, 161, 224, doi: [10.3847/1538-3881/abeb67](https://doi.org/10.3847/1538-3881/abeb67)
- Tinney, C. G., & Tolley, A. J. 1999, *MNRAS*, 304, 119, doi: [10.1046/j.1365-8711.1999.02297.x](https://doi.org/10.1046/j.1365-8711.1999.02297.x)

- Tremblin, P., Amundsen, D. S., Chabrier, G., et al. 2016, *ApJ Letters*, 817, L19, doi: [10.3847/2041-8205/817/2/L19](https://doi.org/10.3847/2041-8205/817/2/L19)
- Tremblin, P., Amundsen, D. S., Mourier, P., et al. 2015, *ApJ Letters*, 804, L17, doi: [10.1088/2041-8205/804/1/L17](https://doi.org/10.1088/2041-8205/804/1/L17)
- Tremblin, P., Phillips, M. W., Emery, A., et al. 2020, *A&A*, 643, A23, doi: [10.1051/0004-6361/202038771](https://doi.org/10.1051/0004-6361/202038771)
- Tremblin, P., Chabrier, G., Baraffe, I., et al. 2017, *ApJ*, 850, 46, doi: [10.3847/1538-4357/aa9214](https://doi.org/10.3847/1538-4357/aa9214)
- Tsuji, T. 2001, in *Ultracool Dwarfs: New Spectral Types L and T*, ed. H. R. A. Jones & I. A. Steele, 9
- Tsuji, T. 2002, *ApJ*, 575, 264, doi: [10.1086/341262](https://doi.org/10.1086/341262)
- Tsuji, T., Ohnaka, K., & Aoki, W. 1996, *A&A*, 305, L1
- Visscher, C., Lodders, K., & Fegley, Jr., B. 2006, *ApJ*, 648, 1181, doi: [10.1086/506245](https://doi.org/10.1086/506245)
- Vos, J. M., Allers, K. N., & Biller, B. A. 2017, *ApJ*, 842, 78, doi: [10.3847/1538-4357/aa73cf](https://doi.org/10.3847/1538-4357/aa73cf)
- Vos, J. M., Allers, K. N., Biller, B. A., et al. 2018, *MNRAS*, 474, 1041, doi: [10.1093/mnras/stx2752](https://doi.org/10.1093/mnras/stx2752)
- Vos, J. M., Biller, B. A., Bonavita, M., et al. 2019, *MNRAS*, 483, 480, doi: [10.1093/mnras/sty3123](https://doi.org/10.1093/mnras/sty3123)
- Vos, J. M., Biller, B. A., Allers, K. N., et al. 2020, *AJ*, 160, 38, doi: [10.3847/1538-3881/ab9642](https://doi.org/10.3847/1538-3881/ab9642)
- Wilson, P. A., Rajan, A., & Patience, J. 2014, *A&A*, 566, A111, doi: [10.1051/0004-6361/201322995](https://doi.org/10.1051/0004-6361/201322995)
- Zahnle, K. J., & Marley, M. S. 2014, *ApJ*, 797, 41, doi: [10.1088/0004-637X/797/1/41](https://doi.org/10.1088/0004-637X/797/1/41)
- Zarro, D. M., & Rodgers, A. W. 1983, *ApJS*, 53, 815, doi: [10.1086/190911](https://doi.org/10.1086/190911)
- Zhou, Y., Apai, D., Schneider, G. H., Marley, M. S., & Showman, A. P. 2016, *ApJ*, 818, 176, doi: [10.3847/0004-637X/818/2/176](https://doi.org/10.3847/0004-637X/818/2/176)
- Zhou, Y., Apai, D., Metchev, S., et al. 2018, *AJ*, 155, 132, doi: [10.3847/1538-3881/aaabbd](https://doi.org/10.3847/1538-3881/aaabbd)

Zhou, Y., Apai, D., Lew, B. W. P., et al. 2019, AJ, 157, 128, doi: [10.3847/1538-3881/ab037f](https://doi.org/10.3847/1538-3881/ab037f)

Zhou, Y., Apai, D., Bedin, L. R., et al. 2020, AJ, 159, 140, doi: [10.3847/1538-3881/ab6f65](https://doi.org/10.3847/1538-3881/ab6f65)

Chapter 2

Weather on Other Worlds. V. The Three Most Rapidly Rotating Ultra-Cool Dwarfs

A version of this chapter has been published in the *Astronomical Journal* as Megan E. Tannock *et al.* 2021 *AJ* **161** 224. DOI: [10.3847/1538-3881/abeb67](https://doi.org/10.3847/1538-3881/abeb67).

2.1 Introduction

Variability in ultra-cool dwarfs (spectral types $> M7$; Kirkpatrick *et al.* 1997) is caused by large-scale atmospheric structures, such as spots or longitudinal bands (Artigau *et al.*, 2009; Radigan *et al.*, 2014; Apai *et al.*, 2017). As inhomogeneities rotate in and out of view, they change the object's observed flux on the time scale of the rotation period (Tinney & Tolley, 1999; Bailer-Jones, 2002). The largest and most sensitive ultra-cool dwarf monitoring surveys (e.g., Radigan *et al.* 2014; Radigan 2014; Buenzli *et al.* 2014; Metchev *et al.* 2015) have found that variability is common across L and T dwarfs. Metchev *et al.* (2015) estimate that $53\%_{-18\%}^{+16\%}$ of L3–L9.5 and $36\%_{-17\%}^{+26\%}$ of T0–T8 dwarfs are variable at $> 0.4\%$. The rotational periods inferred for L and T dwarfs range over at least an order of magnitude: from 1.4 h (Clarke *et al.*, 2008) to likely longer than 20 h (Metchev *et al.*, 2015). Spectroscopic observations have shown that many ultra-cool dwarfs have relatively large projected rotational velocities ($v \sin i \geq 10 \text{ km s}^{-1}$; Mohanty & Basri 2003; Basri *et al.* 2000; Zapatero Osorio *et al.* 2006; Reiners & Basri 2008, 2010; Blake *et al.* 2010; Konopacky *et al.* 2012), and in some cases rotate at $\sim 30\%$ of their break-up speed (e.g., Konopacky *et al.* 2012). Ultra-cool dwarfs with halo kinematics also exhibit rapid rotation (Reiners & Basri, 2006), indicating that they maintain relatively large rotational velocities during their entire lifetimes.

In this paper we present the discovery of three ultra-cool dwarfs with the shortest known

photometric—and likely rotational—periods. In Section 2.2 we present our photometric monitoring with the Spitzer Space Telescope (Spitzer) and the discovery of the short periodicities. In Section 2.3 we present moderate-resolution infrared spectroscopy to confirm the rapid rotation of each target. In Section 2.4 we fit photospheric models to the spectra to determine the objects’ projected rotational velocities and physical parameters, and find the highest $v \sin i$ value yet reported for ultra-cool dwarfs. We discuss the objects’ rapid spins and oblateness in Section 2.5. Our findings are summarized in Section 2.6.

2.2 Spitzer Photometry, Variability, and Periods

The photometric observations were obtained as part of the GO 11174 (PI: S. Metchev) Spitzer Exploration Science Program, “A Paradigm Shift in Substellar Classification: Understanding the Apparent Diversity of Substellar Atmospheres through Viewing Geometry.” The program targeted 25 of the brightest known L3–T8 dwarfs to complement our earlier sample of 44 photometrically monitored L and T dwarfs (Metchev et al., 2015) and to investigate viewing geometry effects on photometric variability and brown dwarf colours. A full description of the program will be presented in a later publication.

We focus on three variables from the GO 11174 Spitzer program with photometric periods shorter than the shortest previously known: the 1.41 ± 0.01 h period of 2MASS J22282889–4310262 (Clarke et al., 2008; Buenzli et al., 2012; Metchev et al., 2015). Our targets are: the L3.5 dwarf 2MASS J04070752+1546457 (Reid et al. 2008; herein 2MASS J0407+1546), the L8 dwarf 2MASS J12195156+3128497 (Chiu et al. 2006; herein 2MASS J1219+3128), and the T7 dwarf 2MASS J03480772–6022270 (Burgasser et al. 2003; herein 2MASS J0348–6022).

2.2.1 Warm Spitzer Observations

We observed the three objects in staring mode with Spitzer’s Infrared Array Camera’s (IRAC; Werner et al. 2004, Fazio et al. 2004) channels 1 ($3.6 \mu\text{m}$, [3.6]) and 2 ($4.5 \mu\text{m}$, [4.5]). The dates of the observations are given in Table 2.1. The observing sequence was a 10 h staring observation in channel 1, followed immediately by a 10 h staring observation in channel 2. All exposures were 12 s long, taken in full-array readout mode. At the beginning of each staring sequence an additional 0.5 h were used for pointing calibration with the Pointing Calibration and Reference Sensor (PCRS). The PCRS peak-up procedure is intended to correct telescope pointing over long staring observations. We used nearby bright stars for peak-up, as none of our targets were sufficiently bright to perform the peak-up on-target.

The Spitzer IRAC detector is subject to intrapixel sensitivity variations, known as the “pixel

phase effect” (Reach et al., 2005). Precise photometry requires correcting for an object’s positioning to sub-pixel precision. The pixel phase effect is well characterized in a 0.5×0.5 pixel ($0''.6 \times 0''.6$) “sweet spot” (Mighell et al., 2008) near a corner of the IRAC array, and flux correction routines are available at the Spitzer Science Centre IRAC High Precision Photometry website.¹

We sought to acquire our targets as closely as possible to the center of the IRAC sweet spot. We used observation epoch-dependent positional corrections for proper and parallactic motions derived from a 2MASS-AllWISE cross-correlation. However, we were not entirely successful. The average centroid position for each of our three targets was up to a pixel away from the center of the sweet spot: i.e., twice its half-width. We therefore used our own custom pixel phase correction code (Heinze et al., 2013) developed for the Spitzer Cycle 8 “Weather on Other Worlds” program (Metchev et al., 2015) and summarized in Section 2.2.2. Experiments with archival Spitzer GO 13067 data on TRAPPIST-1, which was acquired on the sweet spot, confirmed that for point sources at least as bright as TRAPPIST-1 (WISE W1 = 10.07 mag), our pixel phase correction approach is at least as accurate as the set of sweet spot pixel phase corrections on the IRAC High Precision Photometry website.

2.2.2 Photometry and Initial Variability Assessment

We conducted a two-stage photometric and variability assessment, using the Spitzer Basic Calibrated Data images. We first performed approximate [3.6]- and [4.5]-band photometry in 1.5 pixel-radius apertures with the IDL Astronomy User’s Library² task `APER`. We applied the corresponding aperture correction from the IRAC Instrument Handbook, and a custom pixel phase correction derived as a two-dimensional quadratic function of the centroid position on the detector.

We identified variable targets by Lomb-Scargle periodogram analysis (Scargle, 1982), sampling periods between 0.1 h and the full 20 h duration of our Spitzer observations. We use the p -value, a measure of the likelihood that any variations are caused by random noise, to determine the significance of the periodogram peaks. The p -value is Me^{-P} , where P is the periodogram power of the highest peak, and M is the number of independent periods considered (Scargle, 1982; Press et al., 1992). Relative to other non-variable field stars, a sinusoidal signal yields the lowest p -value at a given amplitude, making it ideal for detecting rotation-induced photometric variations. We determined a threshold to identify variables by calculating the p -value from pixel phase-corrected light curves of 469 field stars in the IRAC field of view for our full Spitzer sample, with obvious variables (e.g., eclipsing binaries) rejected by visual

¹<https://irachpp.spitzer.caltech.edu>

²<https://idlastro.gsfc.nasa.gov>

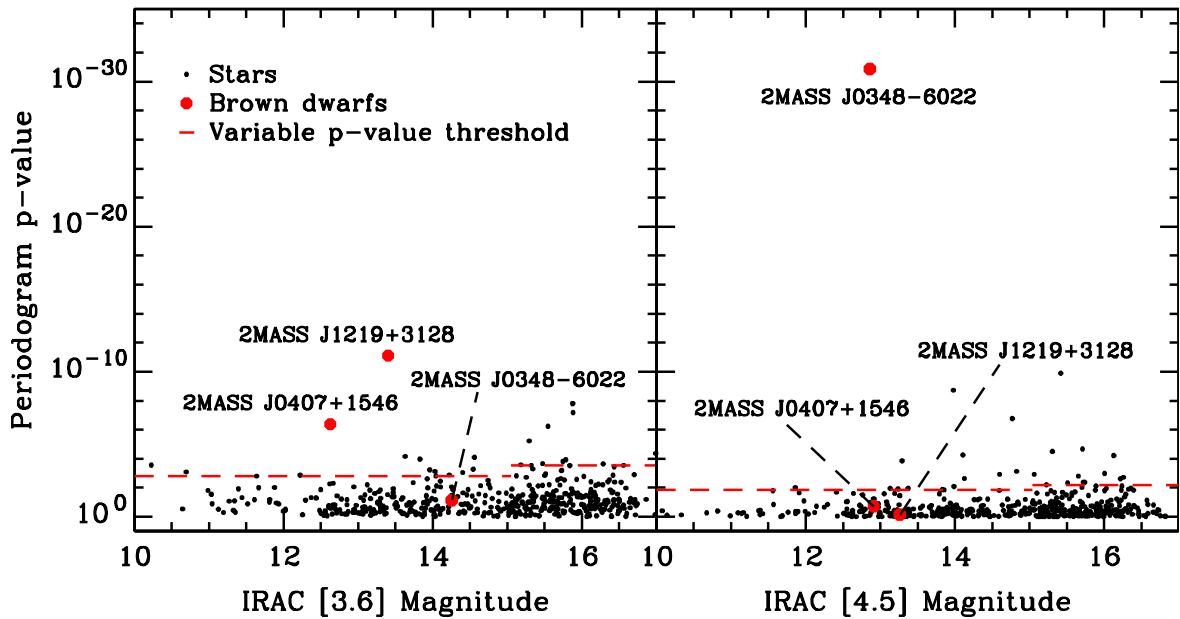


Figure 2.1: Results from the initial periodogram-based variability assessment on the three L and T dwarfs (red points) in the two Spitzer bands, compared to 469 other stars (black points) in the IRAC field of view for our full Spitzer sample. The horizontal dashed lines mark the p -value thresholds below which we claim variability (higher on the plot), with 95% of the comparison stars on the other side of this line (lower on the plot). We separately compute the 95% threshold for each IRAC channel for the brighter half of comparison stars ($\log(p\text{-value}) = -2.8$ and -1.9 in [3.6] and [4.5], respectively) and the fainter half of comparison stars ($\log(p\text{-value}) = -3.5$ and -2.2 in [3.6] and [4.5], respectively).

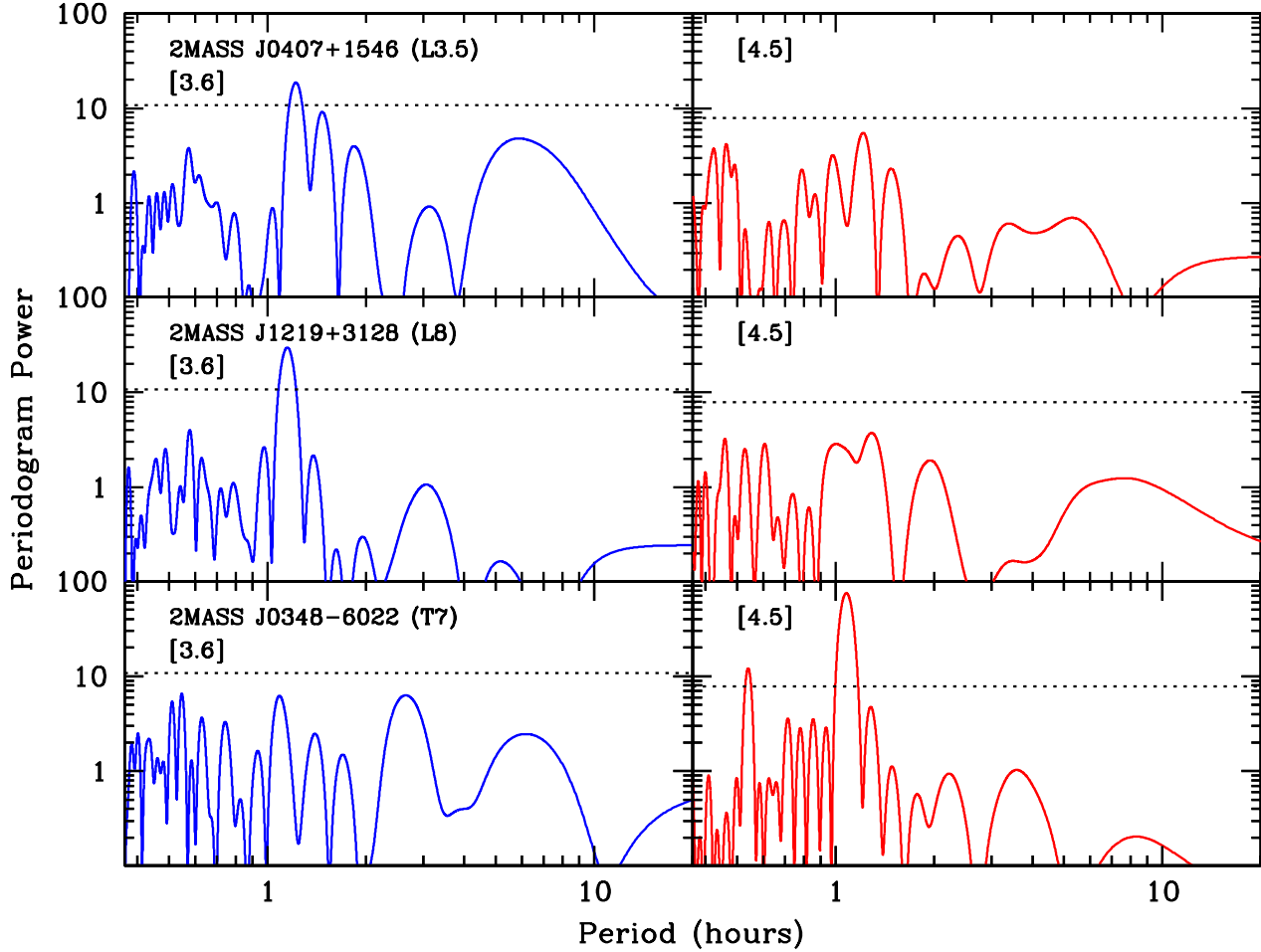


Figure 2.2: Lomb-Scargle periodogram power distributions of the light curves of our three targets for both Spitzer channels after the preliminary pixel phase correction (Sec. 2.2.2). We use the 95 percentile p -value thresholds determined from field stars (Fig. 2.1) to identify significant periodogram peaks. The relevant thresholds (dotted lines) at [3.6] and [4.5] are at periodogram powers of $P_{[3.6]} = 10.7$ and $P_{[4.5]} = 7.9$.

inspection. We split the field stars into two equal-sized groups based on their magnitudes. From the full Spitzer sample, we selected as candidate variables those L and T dwarfs for which the p -value was below that of 95% of field star p -values. The p -values of the current three L and T dwarfs and of the field stars are shown in Figure 2.1. The relevant thresholds are shown as dashed horizontal lines.

The most significant periodogram peaks above the p -value threshold for our three targets are in the 1.1–1.2 hour range (Fig. 2.2). In all three cases, significant periodicity is detected in only one of the two Spitzer IRAC channels: at [3.6] for the L dwarfs 2MASS J0407+1546 and 2MASS J1219+3128 and at [4.5] for the T dwarf 2MASS J0348–6022.

At this stage of our analysis, the applied pixel phase correction is not in the final form

presented in Section 2.2.3. The preliminary periodicities are potentially affected by Spitzer’s known pointing ‘wobble.’ The telescope’s boresight follows a small sawtooth quasi-periodic oscillation with a mostly sub-hour time scale: the result of heater cycling to maintain adequate battery temperature (Grillmair et al., 2012, 2014). The amplitude of the pointing oscillation, up to 0.4 pix, can be sufficiently high to impact photometric measurements because of the pixel phase effect. During 2015, when our observations were taken, the mean pointing oscillation period was 49 minutes, with an inner quartile range of 43 minutes to 54 minutes (Krick et al., 2018). However, a small fraction of year 2015 observations in the Spitzer archive have pointing oscillation periods up to 80 minutes, similar to the 1.1–1.2 hour-long periods identified in our periodograms (Fig. 2.2).

We do not believe that Spitzer’s pointing wobble is responsible for the detected 1.1–1.2 hour periodicities for three reasons. First, we expect roughly similar pixel phase-induced behavior of all point sources in our target fields. Therefore, by setting a global 95% p -value threshold in our preliminary analysis, we select for variability beyond what may be incurred by the pointing wobble. Second, in Section 2.2.3 we describe a more sophisticated photometric analysis that includes an astrophysical variability and a pointing oscillation model, and we clearly identify the wobble separately from the astrophysical periods. Finally, in Section 2.4 we confirm that the rapid rotations implied by such short periods are expressed as wide Doppler line broadening in moderate-dispersion spectra of our three science targets.

2.2.3 Simultaneous Fitting for Pixel Phase and Astrophysical Variability

Having identified candidate variables among the science targets with approximate photometry, we iterated our variability assessment with higher-precision photometry. We determined the optimal aperture for each object by seeking the lowest root-mean-square scatter in the measured fluxes. The optimal apertures in the [3.5]- and [4.5]-band data respectively were 1.4 and 2.1 pixels for 2MASS J0348–6022, 1.4 and 2.0 pixels for 2MASS J1219+3128, and 1.5 and 2.1 pixels for 2MASS J0407+1546. We binned the photometry in groups of 10 consecutive measurements to lower the random noise. Our binning interval of 120 s still ensures fast enough sampling to retain sensitivity to the hour-long timescales of interest. We incorporated the initial period estimates from Section 2.2.2 in an iterative least-squares method to simultaneously fit an astrophysical model (a truncated Fourier series) and a correction for the pixel phase effect in both channels (Heinze et al., 2013). We show the raw and corrected Spitzer light curves for our three targets in the left panel of Figure 2.3.

The raw photometry in Figure 2.3 shows the sawtooth pointing oscillation of Spitzer in the light curves of two of the three science targets. The effect is present mostly throughout the [3.6]-

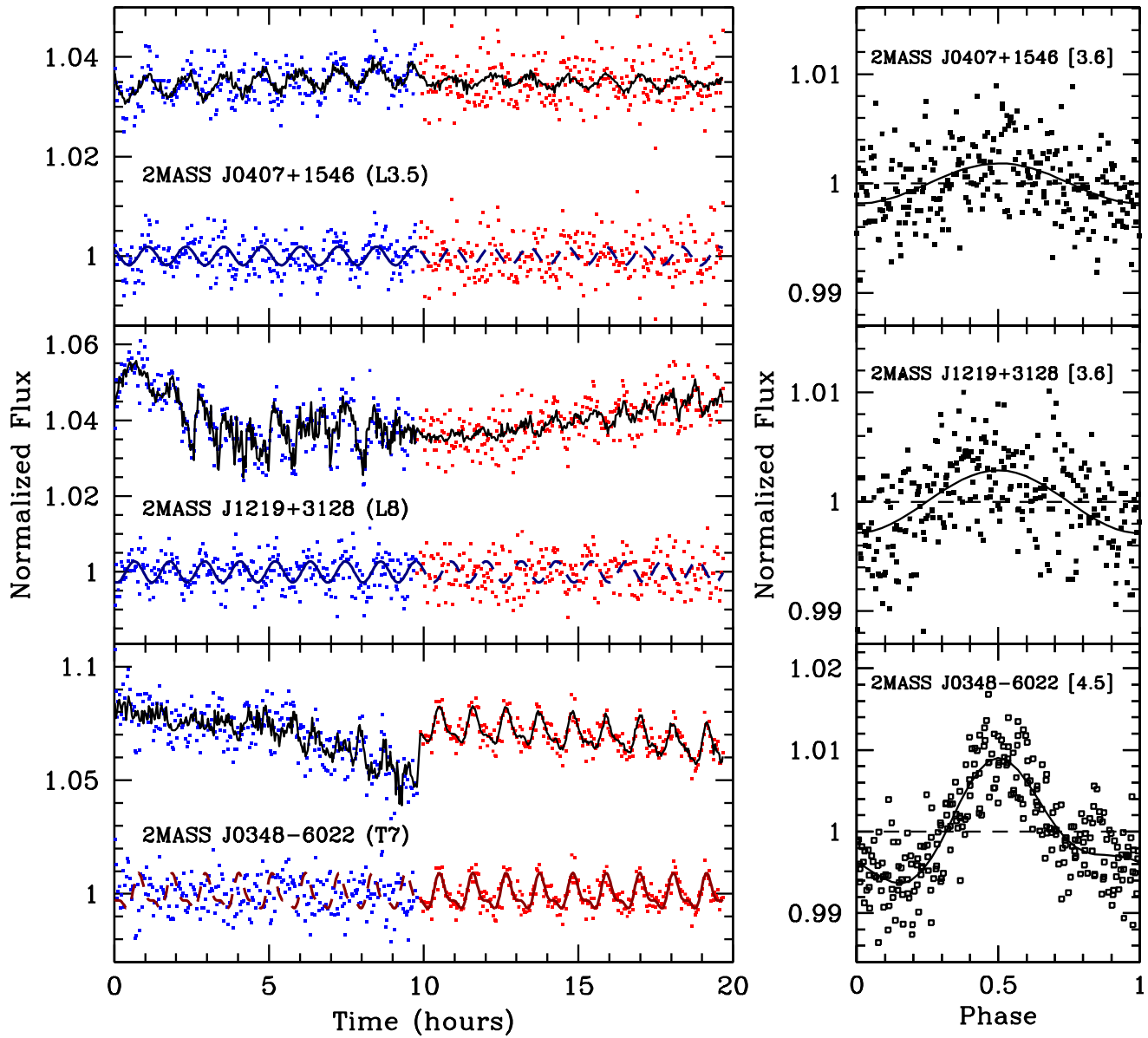


Figure 2.3: *Left:* Spitzer [3.6]- (blue) and [4.5]-band (red) light curves. Each target is shown in a separate panel, with the raw data on top. The bottom sequences show the final light curves after correcting for the pixel phase effect. All light curves are normalized to unity, and the raw data are offset by a constant for clarity. A combined astrophysical and pixel phase model fit (Sec. 2.2.3) to the raw data is shown in black. The astrophysical model fits to the corrected data are shown in blue for [3.6] and red for [4.5]. The models are shown with a solid line over the channel that exhibits significant variability and with a dashed line over the other channel that exhibits no significant variability. *Right:* Period-folded light curves in the channels with significant variability after the pixel phase correction. The mean flux level is represented as a horizontal dashed line at unity flux. The astrophysical model fit is shown as a solid line.

and [4.5]-band staring observation of 2MASS J1219+3128 (middle-left panel of Fig. 2.3), with a sawtooth-like pattern that repeats 10 times over 10 hours at [3.6]. The corresponding 60 minute time scale of the sawtooth pattern is distinct from the 68 minute astrophysical period seen in the corrected [3.6]-band light curve. The latter half of the [3.6]-band observation of 2MASS J0348–6022 also shows sawtooth variations on a 60 minute time scale. However, no astrophysical variability is detected in 2MASS J0348–6022 at [3.6]. This T7 dwarf is variable only at [4.5], where no effect of the sawtooth pattern is seen.

We further verified that there is no residual periodicity effect from the pointing wobble by confirming that there is no correlation between the flux and centroid position on the detector after correcting our photometry for pixel phase (Fig. 2.4). We computed Pearson correlation coefficients of $|r| \leq 0.04$ between flux and centroid position for each object and Spitzer channel. We conclude that Spitzer’s pointing oscillation is not the cause of the variability we observe.

We adopt the results from the simultaneous astrophysical and pixel phase model as the true periods and peak-to-trough amplitudes of our variables, rather than the preliminary results from the periodogram fitting shown in Figure 2.2. In all three cases the final and the preliminary periods agree to within 1%, and the periodogram power of the significant peaks increased for the final, corrected data. From our best-fit astrophysical model, the two L dwarfs require only a single Fourier term for an adequate light-curve fit. The T7 dwarf 2MASS J0348–6022 requires a two-term Fourier fit, and so both significant peaks seen in the [4.5]-periodogram (Fig. 2.2) are astrophysical in nature. However, the higher-frequency oscillation is less significant, and is a harmonic at half the period: 0.54 h versus 1.08 h. It may indicate a two-spot configuration on opposite hemispheres of the T dwarf.

We use a Markov chain Monte Carlo (MCMC) analysis, as described in Section 3.4 of Heinze et al. (2013), to determine the uncertainties on the periods and the amplitudes. We fit the [3.6] and [4.5] photometry simultaneously, by requiring the same period but different amplitudes for the two channels. Since in all cases only one of the channels shows significant variability, we set 2σ upper limits on the amplitude ratios of the “non-variable” channels to the variable channels.

The periods of the T7, L3.5, and L8 dwarfs range between 1.08 h and 1.23 h: faster than any measured before (see Section 2.5). We show the phase-folded light curves in the variable channel for each target in the right panel of Figure 2.3. The object names, spectral types, magnitudes, variable channels, and photometric periods, peak-to-trough amplitudes, and amplitude ratios are listed in Table 2.1.

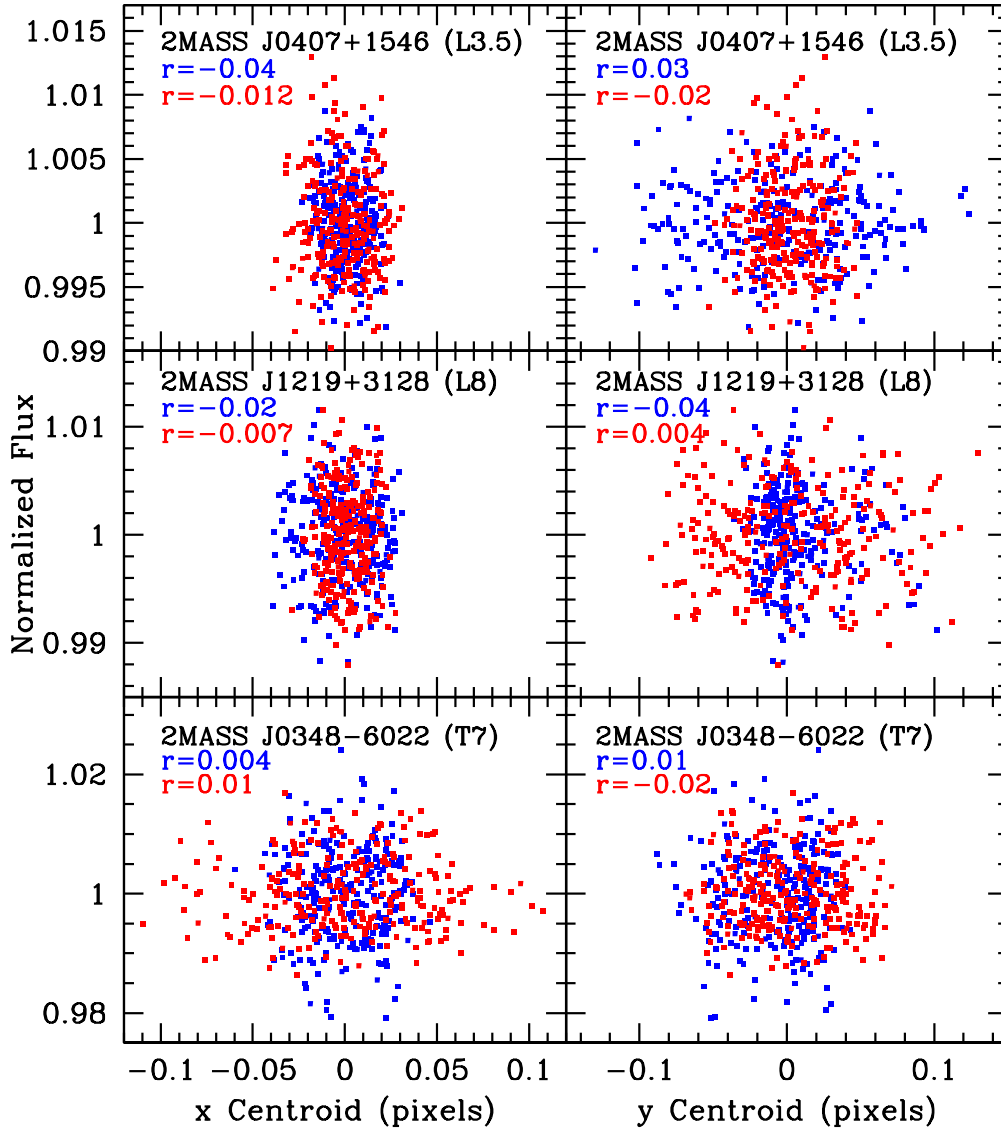


Figure 2.4: Pixel phase-corrected flux at [3.6] (blue) and [4.5] (red) as a function of centroid position in both the x - and y -directions. The centroids are measured relative to the average centroids across all exposures. The Pearson correlation coefficients (r) are given in each panel and we find that there is no correlation between the flux and centroid positions on the detector. We conclude that there is no residual periodic effect on the photometry after correcting for Spitzer’s pointing wobble.

Table 2.1. Spitzer photometry and results from Markov Chain Monte Carlo analysis of periods and peak-to-trough amplitudes

Object	Spectral Type ^a	Date Observed	[3.6] (mag)	[4.5] (mag)	Variable Channel ^b	Period ^c (h)	Amplitude in Variable Channel ^c (%)	Amplitude Ratio ^d
2MASS J04070752+1546457	L3.5	2015 Apr 26	12.83 ± 0.01	12.91 ± 0.01	[3.6]	1.23 [1.22, 1.24]	0.36 [0.24, 0.46]	<1.2
2MASS J12195156+3128497	L8	2015 Sep 16	13.40 ± 0.02	13.26 ± 0.02	[3.6]	1.14 [1.13, 1.17]	0.55 [0.42, 0.69]	<0.53
2MASS J03480772-6022270	T7	2015 Apr 22	14.36 ± 0.03	12.86 ± 0.02	[4.5]	1.080 [1.075, 1.084]	1.5 [1.4, 1.7]	<0.58

^aSpectral type references, in row order: Reid et al. (2008), Chiu et al. (2006), Burgasser et al. (2003).

^bEach target varies in only one of the two Spitzer IRAC channels.

^cSquare brackets denote the 2σ confidence intervals on the periods and amplitudes determined from our MCMC analysis (Sec. 2.2.3).

^dThis is the 2σ upper limit on the amplitude ratio between the two channels. The ratio is of the non-variable channel to the variable channel.

2.2.4 Discussion of Photometric Variability: Periods and Mechanisms

Two of our three targets have been previously reported as potential variables. For 2MASS J1219+3128 (L8), [Buenzli et al. \(2014\)](#) find a lower limit of 2% on the variability amplitude in a 1.12–1.20 μm subset of their 1.1–1.7 μm HST/WFC3 spectra, over a 36 minute sequence of nine spectroscopic exposures. However, the variability is not significant over any other part of their 1.1–1.7 μm spectra, and they classify the detection as tentative. For 2MASS J0348–6022 (T7), [Wilson et al. \(2014\)](#) report a *J*-band amplitude of $2.4\% \pm 0.5\%$ in a three hour long observation. However, a re-analysis of their NTT/SofI observations by [Radigan \(2014\)](#) shows that the reported variability is likely spurious, and related to residual detector and sky-background systematics. [Radigan \(2014\)](#) revised the *J*-band variability in the [Wilson et al. \(2014\)](#) observations to a $< 1.1\% \pm 0.4\%$ upper limit. Similarly, a 1% upper limit for 2MASS J0348–6022 is deduced from a prior six hour *J*-band monitoring observation by [Clarke et al. \(2008\)](#), also with NTT/SofI. No variability has been previously reported for 2MASS J0407+1546 (L3.5).

The small periodogram *p*-values and large periodogram powers (Figs. 2.1 and 2.2) of our Spitzer observations confidently establish that all three L and T dwarfs exhibit periodic variability. Each of our three targets varies in only one of the two IRAC channels within the photometric precision limits. The two L dwarfs vary only at [3.6], whereas the T7 dwarf varies only at [4.5]. Such behaviour is consistent with prior observations of infrared variability trends with spectral type. [Metchev et al. \(2015\)](#) found that five of their 19 variable L3–T8 dwarfs varied only at [3.6] (two L3s, two L4s, and a T2), and one (T7) dwarf varied only at [4.5]. Single-band [3.6] variations in an L dwarf have also been reported by [Gizis et al. \(2015\)](#), while [4.5]-only variations are seen in Y dwarfs ([Cushing et al., 2016](#); [Leggett et al., 2016](#)).

Wavelength-dependent amplitude differences are explained by the dominant gas absorption species in the atmosphere. In wavelength regions of strong molecular gas opacity, clouds reside below the photosphere and so cloud heterogeneities are obscured. Cloud structures are detectable only in relatively transparent spectral regions, away from dominant molecular bands (e.g., [Ackerman & Marley, 2001](#)). With CO being a dominant source of upper-atmosphere gas opacity in L dwarfs, cloud condensate-induced variability will be suppressed around the 4.5 μm fundamental CO band (i.e., in IRAC channel 2). Conversely, variability around the 3.3 μm CH₄ fundamental band (within IRAC channel 1) will be suppressed in T dwarfs.

Alternative variability mechanisms that do not require clouds have also been proposed. Such scenarios do not imply that clouds may not exist at all in the atmospheres of brown dwarfs, just that they are not responsible, or not entirely responsible, for the observed variability. For example, some variable brown dwarfs show radio emission that may be best explained as auroral in nature (e.g., [Antonova et al. 2008](#); [Hallinan et al. 2015](#); [Kao et al. 2018](#)). [Richey-Yowell et al. \(2020\)](#) correlate such auroral signatures with the presence of H α emission. One of our

three variables, the L3.5 dwarf 2MASS J0407+1546, is a strong H α emitter (equivalent width of 60Å; Reid et al., 2008). While Miles-Páez et al. (2017a) find no correlation between H α emission and large-amplitude ($\gtrsim 1\%$) variations (a result also confirmed by Richey-Yowell et al. 2020), the more subdued 0.36% variation in 2MASS J0407+1546 could well be magnetic in origin.

Robinson & Marley (2014) propose atmospheric temperature fluctuations as a potential cause of photometric variability. They show that thermal perturbations occurring deep in the atmosphere can cause surface brightness fluctuations at infrared wavelengths. Tremblin et al. (2015, 2020) show that fingering convection in a cloudless atmosphere can also result in variability. Ultimately, the observations that we present are not decisive of the variability mechanism, and our focus is instead on the short rotation periods.

The periodic regularity seen in the light curves of our three targets (Fig. 2.3) argues for one (2MASS J0407+1546, 2MASS J1219+3128) or two (2MASS J0348–6022) dominant photospheric spots. An alternative interpretation of these data is that we are seeing a repeating spot pattern extended along a band on a more slowly rotating object, e.g., as in the case for Jupiter (de Pater et al., 2016). Additionally, Apai et al. (2017) show that the variability of infrared brightness in T dwarfs can be dominated by planetary-scale waves. They find that the combined variability effect of multiple sets of planetary waves or spots may place the periodogram peak at half the true period, or that double peaks may occur near the true rotation period due to differential rotation.

To the sensitivity of our data, none of our objects show the kind of complex light modulations seen in the Apai et al. (2017) T dwarfs. However, Jupiter-like repeated spot patterns remain a possibility. In Sections 2.3 and 2.4 we use near-infrared spectroscopy to measure the projected rotation velocities ($v \sin i$) of our targets and confirm that all three rotate rapidly.

The rotation periods reported here are specifically the photometric rotation periods. It is possible that due to atmospheric motions, such as winds, the rotation periods of the interiors of these brown dwarfs may be different from the photometrically measured atmospheric rotation periods. Differences in these rotation periods have been detected previously, such for the T6.5 dwarf 2MASS J10475385+2124234 (Allers et al., 2020).

2.3 Spectroscopic Observations

If our objects are truly rapidly rotating, then their spectroscopic line profiles will be significantly Doppler-broadened, while more slowly rotating objects with repeating spot patterns will not show much line broadening. Herein we report $R = 6000 - 12,000$ near-infrared spectroscopy which we use to confirm the rapid rotations and in Section 2.4 to estimate the objects'

fundamental parameters.

We present a previously unpublished spectrum of the T7 dwarf 2MASS J0348–6022 and a new observation of the L8 dwarf 2MASS J1219+3128 at a resolution of 6000 over 0.91–2.41 μm with the Folded-port InfraRed Echellette (FIRE; Simcoe et al., 2008, 2013) at the Magellan Baade telescope. We also observed the L3.5 dwarf 2MASS J0407+1546 at a resolution of 12,000 over 2.275–2.332 μm with the Gemini Near-InfraRed Spectrograph (GNIRS; Elias et al. 2006) at the Gemini North Observatory. The spectroscopic observations are summarized in Table 2.2.

2.3.1 Magellan/FIRE Spectroscopy: 2MASS J0348-6022 (T7) and 2MASS J1219+3128 (L8)

For our FIRE observations we used the cross-dispersed echelle mode with the $0''.6$ (3.3 pixel) slit aligned to the parallactic angle to obtain $R \approx 6000$ spectra over 0.91–2.41 μm . We observed 2MASS J0348–6022 on 2012 January 3 (UT) under clear skies with $0''.7$ J -band seeing and airmass of 1.25–1.27. We obtained two 909 s exposures, dithered along the slit. We observed the A0 V star HD 28667 ($V = 6.87$ mag) in four 1 s dithered exposures following the 2MASS J0348–6022 observations at a similar airmass (1.28). We observed 2MASS J1219+3128 on 2017 February 16 (UT) under clear skies with $1''.2$ – $1''.4$ J -band seeing and airmass of 2.12–2.31. We obtained four 400 s exposures dithered pair-wise along the slit. We observed the A0 V star HD 96781 ($V = 10.2$ mag) in six 1 s dithered exposures at a similar airmass (1.96–2.05). For both sets of observations we obtained Thorium-Argon emission lamp spectra after each target. We obtained dome and sky flat-field observations at the beginning of each night for pixel response and slit illumination calibration.

The FIRE data were reduced using the Interactive Data Language (IDL) pipeline FIREHOSE v2 (Gagné et al., 2015a), which is based on the MASE (Bochanski et al., 2009) and SpeXTool (Vacca et al., 2003; Cushing et al., 2004) packages.³ Details for standard reduction of point-source data with FIREHOSE are described in Bochanski et al. (2011). The ThAr lamp images were used to trace the spectral orders and derive pixel response and illumination corrections which were applied to the science frames. A combination of OH telluric lines in the science frames and ThAr emission lamp lines were used to determine the wavelength solution along the centre of each order and the order tilt along the spatial direction, so as to construct a two-dimensional vacuum wavelength map. The typical uncertainty of the wavelength solution was 0.20 pixels, corresponding to a precision of 3.0 km s^{-1} . The sky background in each frame was fit with a two-dimensional sky model constructed using basis splines (Kelson, 2003), which

³https://github.com/jgagneastro/FireHose_v2/

Table 2.2. Magellan/FIRE and Gemini North/GNIRS spectroscopic observations

Target	K_s (mag)	Date Observed	Instrument	Resolution	Exposure Time (minutes)	S/N	Target Airmass	Telluric Standard	Telluric Standard Airmass
2MASS J03480772-6022270	15.60	2012 Jan 3	Magellan/FIRE	6000	30.3	36	1.25-1.27	HD 28667	1.28
2MASS J12195156+3128497	14.31	2017 Feb 16	Magellan/FIRE	6000	26.6	46	2.12-2.31	HD 96781	1.98
2MASS J04070752+1546457	13.56	2017 Oct 10	Gemini North/GNIRS	12,000	80.0	29	1.07-1.28	HD 17971	1.03

Note. — K_s magnitudes are from 2MASS (Cutri et al., 2003). The signal-to-noise ratio is the median around the K -band peaks of the FIRE spectra of for 2MASS J0348-6022 (between 2.05 and 2.15 μm) and 2MASS J1219+3128 (between 2.1 and 2.2 μm), and the median over the full range of the GNIRS spectrum of 2MASS J0407+1546.

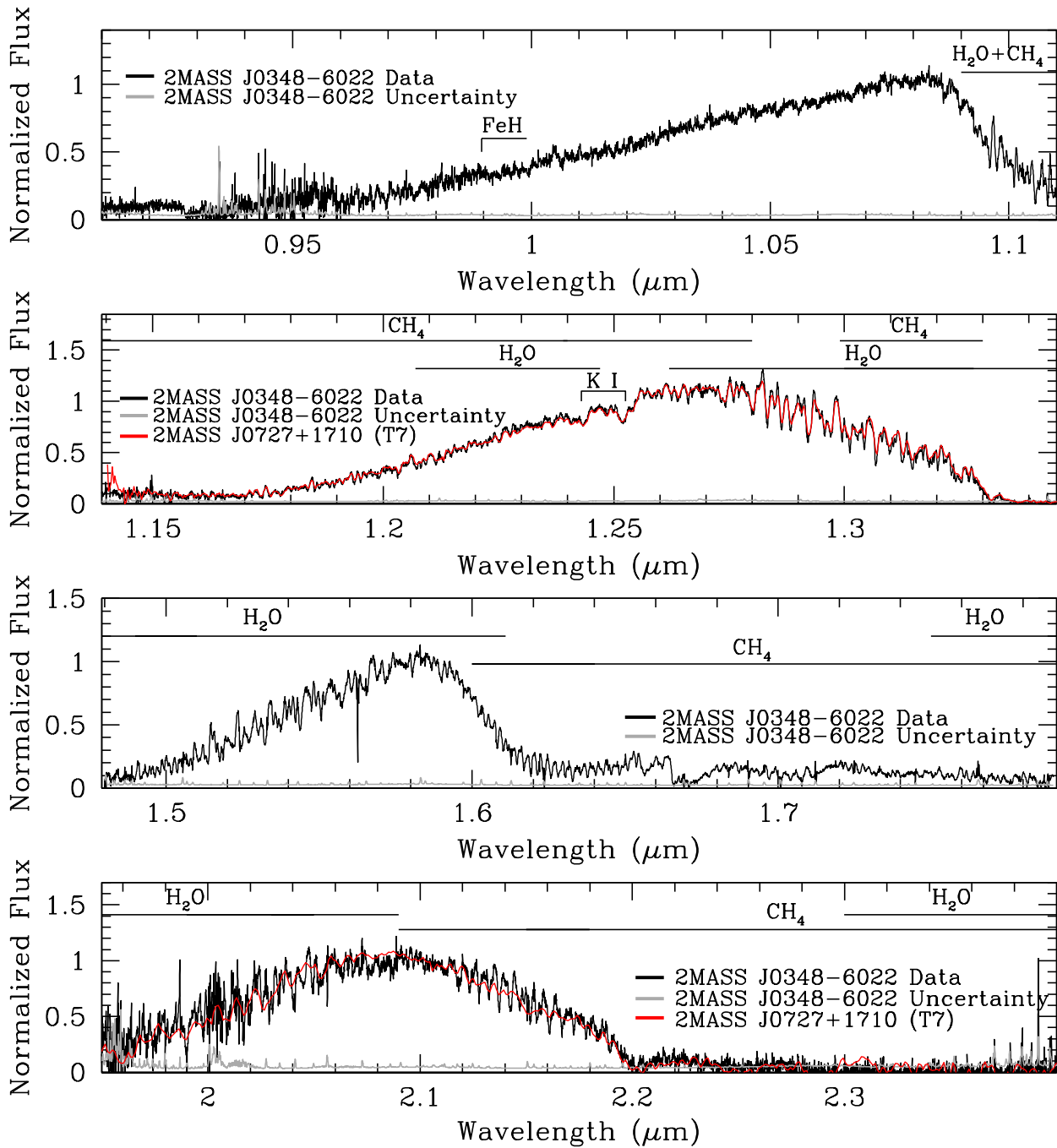


Figure 2.5: Magellan/Folded-port InfraRed Echellette (FIRE) *z*, *J*, *H*, and *K*-band spectra (from top to bottom) of 2MASS J0348-6022 (black), compared to template T7 spectra where available. The uncertainty on the FIRE spectrum is shown in grey along the bottom of each panel. The template spectrum of 2MASS J07271824+1710012 is from the Brown Dwarf Spectroscopic Survey (McLean et al., 2003). In the *J* band the template and our FIRE spectrum appear nearly identical; the template is not known to be a fast rotator, and is much lower resolution than our FIRE data. Major molecular features (McLean et al., 2003; Cushing et al., 2006; Bochanski et al., 2011) are indicated.

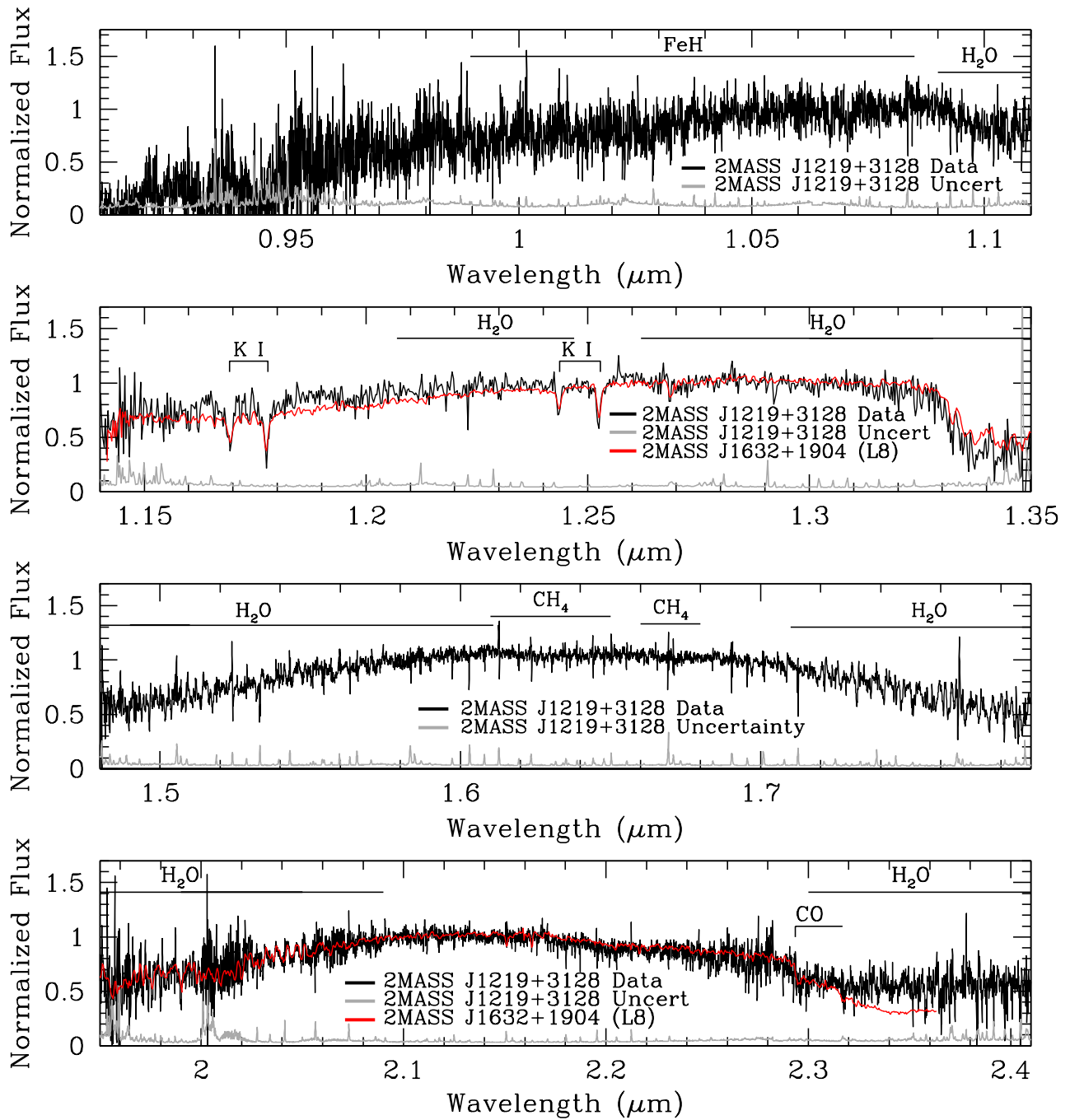


Figure 2.6: Magellan/FIRE z -, J -, H -, and K -band spectra (from top to bottom) of 2MASS J1219+3128 (black), compared to template L8 spectra where available. The uncertainty on the FIRE spectrum is shown in grey along the bottom of each panel. The template spectrum of 2MASS J16322911+1904407 is from the Brown Dwarf Spectroscopic Survey (McLean et al., 2003). Major molecular features (McLean et al., 2003; Cushing et al., 2006) are indicated.

was then subtracted from the frame. One-dimensional spectra were optimally extracted (Horne, 1986) in each order onto a heliocentric wavelength frame. Correction for telluric absorption and overall flux calibration was determined from the A0 V star spectra using a modified version of `xtellcor` from SpeXtool (Vacca et al., 2003; Cushing et al., 2004). Spectra from the individual frames of the FIRE data were combined for each target after relative flux normalization, and the individual orders were merged into one-dimensional spectra. The resulting reduced spectra are shown in Figure 2.5 for 2MASS J0348–6022 and in Figure 2.6 for 2MASS J1219+3128, along with comparison spectra, where data at similar resolution of other objects of the same spectral types were available from the literature.

2.3.2 Gemini/GNIRS Spectroscopy: 2MASS J0407+1546 (L3)

Our GNIRS observations of the L3.5 dwarf 2MASS J0407+1546 took place on 2017 October 10 (UT). We followed the same procedure and instrument settings as used by Allers et al. (2016) for radial and rotation velocity measurements of an L dwarf. We used the 111 lines mm^{-1} grating with the $0'.15$ (3.0 pixels) slit aligned to the parallactic angle to obtain $R \approx 12,000$ $2.27\text{--}2.33 \mu\text{m}$ spectra at an airmass of 1.07–1.28. We obtained eight 600 s exposures, dithered between two positions on the slit. We observed the A0 V star HD 17971 ($V = 8.78$ mag) for telluric absorption correction in eight 60 s dithered exposures at a similar airmass (1.03) using the same instrument setup. ThAr emission lamp observations were obtained immediately after the 2MASS J0407+1546 observations. The 2MASS J0407+1546 data were reduced using a combination of general and Gemini-specific IRAF⁴ routines. Data were prepared, sky-subtracted, and flat-fielded using the Gemini tasks `nsprepare`, `nsreduce`, and `nsflat`. Individual spectra were extracted using `apall`. The XeAr lamp spectrum was extracted once for each of the science spectra, using the science extraction traces as references, and `identify` and `dispcor` were used to identify calibration lines and generate a wavelength solution for each science spectrum. A Legendre polynomial was used with `identify`, typically of second order. The typical uncertainty in the wavelength calibration was 0.25 pixels, which corresponds to a precision of 2.0 km s^{-1} . The individual wavelength-calibrated spectra were median-combined, and the standard deviation was adopted as the uncertainty. The same reduction steps were repeated for the standard star, and the science spectrum was divided by the standard spectrum to remove telluric lines, and multiplied by a $T_{\text{eff}} = 9600 \text{ K}$ blackbody. The resulting spectrum is shown in Figure 2.7, along with a comparison spectrum of another L3.5 dwarf.

⁴Image Reduction and Analysis Facility, distributed by the National Optical Astronomy Observatories.

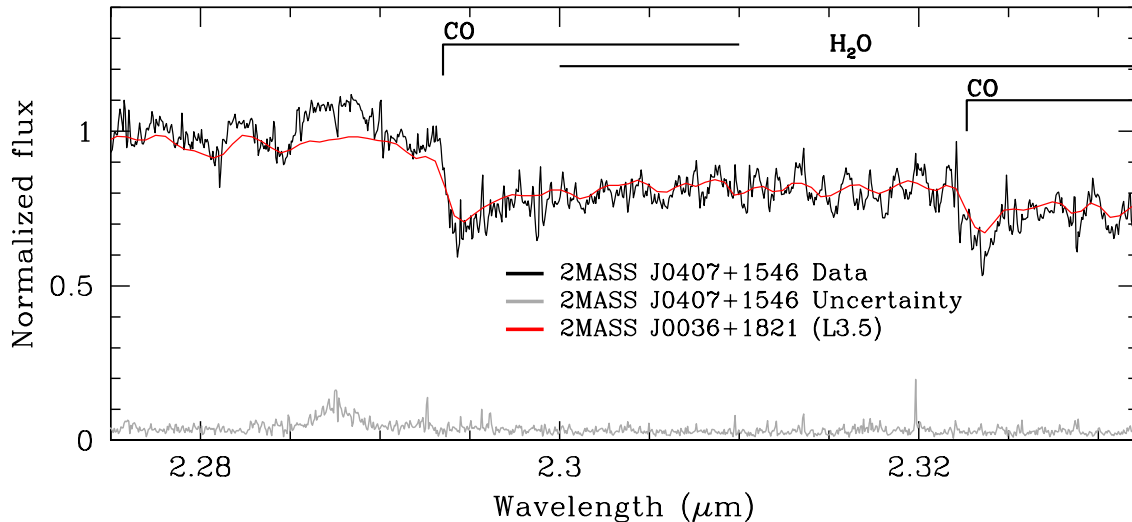


Figure 2.7: Gemini/Gemini Near-InfraRed Spectrograph (GNIRS) *K*-band spectrum of 2MASS J0407+1546 (black), compared to a template L3.5 spectrum (2MASS J00361617+1821104 from IRTF/SpEx; Rayner et al., 2009). The uncertainty on the GNIRS spectrum is shown in gray along the bottom of the panel. Major molecular features (Cushing et al., 2006) are indicated.

2.4 Confirmation of Rapid Rotations and Determination of Physical Parameters

We compared our spectra to the photosphere models of Saumon & Marley (2008; SM08), Allard et al. (2012; BT-Settl), Morley et al. (2012; Morley), and Marley et al. (2018; Sonora) to determine the physical properties of our objects. These models all assume solar metallicity. All but the BT-Settl models are based on the Ackerman & Marley (2001) cloud model. The model photospheres are provided on fixed grids of effective temperature (T_{eff}) and surface gravity ($\log g$). The SM08 and Morley models also have a sedimentation efficiency (f_{sed}) parameter, in integer steps from 2 to 5. The T_{eff} grids are in steps of 100 K for all except the BT-Settl models, which are in 50 K steps, and the $\log g$ grids are in steps of 0.5 dex for all except the Sonora models, which are in steps of 0.25 dex.

We also implemented grids for radial velocity (RV) and $v \sin i$ in steps of 0.1 km s^{-1} . For the RV we applied a simple Doppler shift to the wavelength of the models. For $v \sin i$ we simulated rotational broadening by convolving the model spectra with the standard rotation kernel from Gray (1992) using the `lsf_rotate` task in the IDL Astronomy User’s Library.⁵

We first verified the spectral types of our targets by overlaying the spectra of other well-studied L and T dwarfs (Figs. 2.5–2.7). For each object we restricted the effective temperature

⁵https://idlastro.gsfc.nasa.gov/ftp/pro/astro/lsf_rotate.pro

grids to 300 K above and below the expected values for each spectral type based on [Filippazzo et al. \(2015\)](#). We did not restrict the $\log g$ and f_{sed} (where available) grids.

The quality of the model fits to the full-band FIRE spectra is dominated by the low-order continuum which is mostly affected by the effective temperature and, when using the SM08 and Morley models, the sedimentation efficiency. Instrument systematics may also affect the continuum shape of our Magellan/FIRE spectra that cover a wide (0.91–2.41 μm) wavelength range. Broadband model fits thus preclude us from obtaining accurate information about the RV and $v \sin i$, both of which do not depend on the continuum but entirely on the positioning and profiles of spectral lines. The pressure-broadening effect of surface gravity is also well reflected in the theoretical line profiles, even though surface gravity does affect the continuum of model ultra-cool photospheres.

To extract accurate estimates of RV, $v \sin i$, and $\log g$, we fit models to select narrow-wavelength sub-regions of the FIRE spectra that are dominated by dense sequences of H_2O , FeH, or CH_4 absorption lines, as marked in Figures 2.5 to 2.7. It is likely that in doing so we may still be affected by wavelength systematics among the theoretical line lists for the different molecules. In addition, the different wavelength sub-regions probe different atmospheric depths and pressures. Hence, a wavelength region where flux originates deeper in the atmosphere could exhibit greater pressure broadening compared to a region where the flux originates higher up. We account for these effects by selecting several different narrow-wavelength regions from the Magellan/FIRE spectra (see Table 2.3) and, as much as possible, different molecular absorbers. Overall, we find that the values for RV, $v \sin i$, and $\log g$ obtained from the narrow-wavelength regions are more self-consistent, with uncertainties 1.5–3 times smaller, than those from the full bands.

Our approach was first to fit each of the narrow regions to determine RV, $v \sin i$, and $\log g$ and then to fit the full bands (z : 0.91 – 1.11 μm , J : 1.14 – 1.345 μm , H : 1.48 – 1.79 μm , and K : 1.96 – 2.35 μm) to determine T_{eff} and f_{sed} . We adopt the RV, $v \sin i$, and $\log g$ values determined from the narrow regions of the FIRE spectra of 2MASS J0348–6022 (T7) and 2MASS J1219+3128 (L8) as the fiducial values for these objects (Table 2.3). While the narrow-band fits also produce estimates for T_{eff} , the full-band spectra are likely more sensitive to it. Then, in re-applying the models to the full-band spectra, we allow RV and $v \sin i$ to vary only within 2σ of the values adopted from the narrow regions. That is, we constrain RV and $v \sin i$ within a small range, as they should not effect the determinations of T_{eff} and (where applicable) f_{sed} . We still allow $\log g$ to be a free parameter in the full-band fitting because of its stronger effect on the continuum. This mirrors our approach for fitting the narrow regions, where we allow T_{eff} to be a free parameter, even if we adopt the results from the broad regions. In this manner we probe the full parameter space for both $\log g$ and T_{eff} in each case, and obtain a

more reliable estimate for each. Ultimately, the two sets of determinations for T_{eff} are consistent with each other (Tables 2.3–2.5). Estimates for $\log g$ tend to be 0.5–1.0 dex higher based on the line profile fits compared to the continuum fits in all models. We favour the former, as they are closer to the fundamental radiative transfer calculations for each species. The latter involve additional considerations of convection and relative chemical abundances.

The spectral range of our Gemini/GNIRS observation of 2MASS J0407+1546 is much narrower, so we consider it only in its entirety.

In terms of specific steps to fit models to the data, we started by normalizing the data to unity. In the narrow regions we divided by the median flux value, and for the full-band data, we divided by a constant such that the peak flux was unity. We shifted the model for radial velocity, broadened for $v \sin i$, and then smoothed the model to the resolution of the data. We also determined a flux zero-point to be added to the data and a multiplicative factor to scale the model which minimized the χ^2 statistic ($\chi^2 = \sum_{i=1}^N [(O_i - M_i)^2 / \sigma_i^2]$, where O_i is the observed flux, M_i is the flux of the model, and σ_i is the uncertainty of the data). We computed the offset, multiplicative factor, and χ^2 statistic for every model on the grid of T_{eff} , $\log g$, RV, $v \sin i$, and f_{sed} (where available).

The probability of a given χ^2 value is $p \propto e^{-\chi^2/2}$ (e.g., Wall & Jenkins 2003). We computed the probabilities for every model on our grid, normalized the sum of the p -values to unity, then marginalized over each of the parameters (summed the probabilities over all other parameters) to obtain the probability distributions for each parameter. The distributions for RV and $v \sin i$ were Gaussian in shape, and we report the mean values and 1σ error bars in Table 2.3. For the other parameters the model grid spacing was coarse, and the probability of values other than the values presented in Tables 2.3 and 2.4 is negligible. We report the results for these parameters with error bars corresponding to the grid-spacing. Tables 2.3 and 2.4 give the most probable values for each family of models in each wavelength region.

We find that the best-fit parameter values can vary significantly between model families and between different wavelength regions, while giving comparable reduced χ^2 statistics. Understanding the subtle differences between the families of models is related to the molecular line lists and opacities used to compute these models, and is beyond the scope of this paper.

To determine the final values of the parameters, we take a weighted average of the values from each model family and region fit. For the FIRE data, we determine the RV, $v \sin i$, and $\log g$ from our narrow-region fits (Table 2.3), and the T_{eff} and f_{sed} from our full-band fits (Table 2.4). For the GNIRS data we determine all parameters from the full wavelength coverage available. We assign the weights in the weighted average as $e^{-\chi_{\text{reduced}}^2}$, where the χ_{reduced}^2 for each best-fit model is given in Tables 2.3 and 2.4. We report the final values from the weighted averages in Table 2.5, with the unbiased weighted sample standard deviation as our uncertainties.

We describe the outcomes of our model fitting and χ^2 analysis in detail for each target in Sections 2.4.1–2.4.3.

2.4.1 2MASS J0348-6022 (T7)

Based on its T7 spectral type, 2MASS J0348–6022 is expected to have an effective temperature $T_{\text{eff}} \lesssim 1000$ K (e.g., Stephens et al. 2009; Filippazzo et al. 2015). Its photosphere should be governed by gas opacity, with a cloud layer buried deeply ($f_{\text{sed}} \geq 3$; Ackerman & Marley, 2001; Marley et al., 2002) within the atmosphere. Thus we expect the atmosphere of this object to be relatively clear and cloudless. So, the cloud-free Sonora models are appropriate for fitting this object’s spectra. A cloudless atmosphere does not imply a completely homogeneous surface, and it is possible that one of the alternative mechanisms presented in Section 2.2.4 (e.g., temperature variations; Robinson & Marley 2014) is responsible for the observed variability. We also compared this target to the BT-Settl and Morley models. The effective temperature grid of the available SM08 models does not extend to the low temperatures expected for a T7 spectral type.

We selected a grid of parameters ranging from $T_{\text{eff}} = 700$ to 1000 K, $\log g = 4.0$ to 5.5 dex in steps of 0.5 dex (0.25 for the Sonora models), and, for the Morley models, condensate sedimentation efficiencies from $f_{\text{sed}} = 2$ to 5 in unit steps. We selected our $\log g$ grid based on the range in surface gravities predicted by the SM08 evolutionary models for brown dwarfs. We selected the RV and $v \sin i$ grids by first testing a wide, coarse grid to determine approximate RV and $v \sin i$ values. We then narrowed it down to between -5 km s^{-1} and -30 km s^{-1} for RV and between 75 km s^{-1} and 115 km s^{-1} for $v \sin i$, both in steps of 0.1 km s^{-1} .

We find that a wide range in parameters fit the z band equally well, and it is therefore not diagnostic for our study. We exclude the z band from our analysis, and only consider the J –, H –, and K – band spectra for this target. To reliably determine $\log g$, RV, and $v \sin i$, we selected narrow regions dominated by molecular lines within each band: the 1.26 – $1.30 \mu\text{m}$ J -band region dominated by H_2O and CH_4 (Fig. 2.8, top left), the 1.520 – $1.562 \mu\text{m}$ H -band region dominated by H_2O (Fig. 2.8, top right), and the 2.11 – $2.19 \mu\text{m}$ K -band region containing primarily CH_4 lines (Fig. 2.8, bottom). The best-fit photospheric models for the narrow wavelength regions are shown in Figure 2.8 and for the full bands in Figure 2.9. The high f_{sed} values of the Morley et al. (2012) models in all of the full band fits indicate an optically thin, relatively cloudless atmosphere, as expected for a late-T type brown dwarf.

We adopt the weighted average and unbiased weighted sample standard deviation (Sec. 2.4) of the values in Table 2.3 as our estimates for $\log g$, $v \sin i$, and RV. For $v \sin i$ in particular, we find a very high degree of rotational broadening: $v \sin i = 103.5 \pm 7.4 \text{ km s}^{-1}$. This is consistent

Table 2.3. Best-fit photospheric model parameters for the narrow-wavelength regions

Model	Region	Wavelength (μm)	T_{eff} (K)	f_{sed}	$\log g$ (dex)	$v \sin i$ (km s^{-1})	RV (km s^{-1})	χ^2_{reduced}
2MASS J03480772–6022270 (T7, FIRE data)								
BT-Settl	<i>J</i> narrow	1.260 – 1.300	950 ± 25	...	5.50 ± 0.25	102.4 ± 3.9	-11.8 ± 0.8	1.2
BT-Settl	<i>H</i> narrow	1.520 – 1.562	950 ± 25	...	5.00 ± 0.25	94.9 ± 1.5	-14.1 ± 0.9	0.9
BT-Settl	<i>K</i> narrow	2.110 – 2.190	700 ± 25	...	4.50 ± 0.25	115.4 ± 2.2	-17.1 ± 1.3	2.0
Morley	<i>J</i> narrow	1.260 – 1.300	900 ± 50	4	5.50 ± 0.25	105.7 ± 1.8	-15.1 ± 0.9	1.6
Morley	<i>H</i> narrow	1.520 – 1.562	1000 ± 50	5	5.50 ± 0.25	114.3 ± 2.2	-18.0 ± 1.0	2.1
Morley	<i>K</i> narrow	2.110 – 2.190	800 ± 50	5	5.00 ± 0.25	103.2 ± 1.9	-16.5 ± 1.3	2.1
Sonora	<i>J</i> narrow	1.260 – 1.300	1000 ± 50	...	5.00 ± 0.13	96.5 ± 1.5	-12.6 ± 0.8	1.6
Sonora	<i>H</i> narrow	1.520 – 1.562	1000 ± 50	...	5.00 ± 0.13	110.7 ± 1.5	-14.2 ± 0.9	1.1
Sonora	<i>K</i> narrow	2.110 – 2.190	800 ± 50	...	4.75 ± 0.13	99.6 ± 2.6	-11.2 ± 1.4	2.0
Adopted values		5.1 ± 0.3	103.5 ± 7.4	-14.1 ± 3.7	...
2MASS J12195156+3128497 (L8, FIRE data)								
BT-Settl	<i>H</i> narrow 1	1.500 – 1.550	1250 ± 25	...	5.00 ± 0.25	77.4 ± 2.6	-17.2 ± 1.6	1.3
BT-Settl	<i>H</i> narrow 2	1.720 – 1.780	1150 ± 25	...	4.00 ± 0.25	85.7 ± 1.4	-19.0 ± 0.9	2.6
BT-Settl	<i>K</i> narrow	1.970 – 2.055	1400 ± 25	...	5.00 ± 0.25	76.8 ± 1.4	-16.6 ± 1.1	2.7
SM08	<i>H</i> narrow 1	1.500 – 1.550	1400 ± 50	4	5.50 ± 0.25	78.1 ± 2.4	-19.6 ± 1.4	1.4
SM08	<i>H</i> narrow 2	1.720 – 1.780	1500 ± 50	4	5.00 ± 0.25	84.3 ± 1.3	-25.9 ± 0.9	2.6
SM08	<i>K</i> narrow	1.970 – 2.055	1400 ± 50	2	5.50 ± 0.25	77.1 ± 1.5	-20.0 ± 1.1	2.7
Adopted values		5.1 ± 0.5	79.0 ± 3.4	-19.0 ± 4.2	...
2MASS J04070752+1546457 (L3.5, GNIRS data)								
BT-Settl	<i>K</i>	2.275 – 2.332	1700 ± 25	...	5.00 ± 0.25	82.7 ± 0.9	43.7 ± 0.9	1.0
SM08	<i>K</i>	2.275 – 2.332	2000 ± 50	4	5.50 ± 0.25	82.4 ± 0.9	43.1 ± 0.8	1.1
Adopted values		...	1840 ± 210	4	5.2 ± 0.4	82.6 ± 0.2	43.4 ± 2.1	...

Note. — Best-fit photospheric model parameters for our three L and T dwarfs over the narrow regions within each FIRE band, and over the entirety of the GNIRS spectrum. We fit each wavelength region independently. We adopt the $\log g$, $v \sin i$, and RV values determined from the narrow wavelength regions of the FIRE spectra of the T7 and L8 dwarfs. The T_{eff} and f_{sed} estimates are adopted from the full-band fits (Table 2.4), although we include the findings T_{eff} and f_{sed} from the narrow region fitting for completeness. For the GNIRS data of the L3.5 dwarf we adopt all parameters from the wavelength region shown here. The f_{sed} parameter is only applicable to the SM08 and Morley models. The adopted values are the weighted averages for each object, where the weights are $e^{-\chi^2_{\text{reduced}}}$, and the uncertainties are the unbiased weighted sample standard deviations (as described in Section 2.4). The adopted RVs include systematic uncertainties of $\pm 3.0 \text{ km s}^{-1}$ (for the T7 and L8 dwarfs) or $\pm 2.0 \text{ km s}^{-1}$ (for the L3.5 dwarf) added in quadrature to account for the wavelength calibration uncertainties of the FIRE and GNIRS spectra, respectively (Sec. 2.3).

Table 2.4. Best-fit photospheric model parameters for the full bands

Model	Band	Wavelength (μm)	T_{eff} (K)	f_{sed}	$\log g^{\text{a}}$ (dex)	$v \sin i^{\text{a}}$ (km s^{-1})	RV^{a} (km s^{-1})	χ^2_{reduced}
2MASS J03480772–6022270 (T7, FIRE data)								
BT-Settl	<i>J</i>	1.140 – 1.345	900 ± 25	...	5.0 ± 0.25	118.3	-14.2	7.4
BT-Settl	<i>H</i>	1.480 – 1.790	750 ± 25	...	4.5 ± 0.25	118.3	-11.3	11
BT-Settl	<i>K</i>	1.960 – 2.350	700 ± 25	...	4.0 ± 0.25	107.9	-13.7	2.8
Morley	<i>J</i>	1.140 – 1.345	800 ± 50	5	4.0 ± 0.25	118.3	-15.1	10
Morley	<i>H</i>	1.480 – 1.790	700 ± 50	5	4.0 ± 0.25	118.3	-10.0	28
Morley	<i>K</i>	1.960 – 2.350	900 ± 50	5	4.0 ± 0.25	107.2	-19.5	2.5
Sonora	<i>J</i>	1.140 – 1.345	900 ± 50	...	5.25 ± 0.13	94.0	-16.8	4.2
Sonora	<i>H</i>	1.480 – 1.790	850 ± 50	...	4.25 ± 0.13	118.3	-21.5	2.0
Sonora	<i>K</i>	1.960 – 2.350	1000 ± 50	...	4.50 ± 0.13	104.5	-15.5	2.3
Adopted values		...	880 ± 110	5
2MASS J12195156+3128497 (L8, FIRE data)								
BT-Settl	<i>J</i>	1.140 – 1.345	1400 ± 25	...	5.50 ± 0.25	72.2	-24.5	2.3
BT-Settl	<i>H</i>	1.480 – 1.790	1200 ± 25	...	4.50 ± 0.25	85.8	-18.9	2.0
BT-Settl	<i>K</i>	1.960 – 2.350	1250 ± 25	...	4.50 ± 0.25	85.8	-17.8	2.1
SM08	<i>J</i>	1.140 – 1.345	1200 ± 50	3	5.50 ± 0.25	72.2	-14.6	2.0
SM08	<i>H</i>	1.480 – 1.790	1500 ± 50	3	5.00 ± 0.25	83.2	-23.2	1.9
SM08	<i>K</i>	1.960 – 2.350	1500 ± 50	3	4.50 ± 0.25	85.8	-18.6	2.4
Adopted values		...	1330 ± 140	3

Note. — Best-fit photospheric model parameters for the FIRE data of the T7 and L8 dwarfs, fit over each of the full *J*, *H*, and *K* bands. We use these fits to inform our final T_{eff} and f_{sed} determinations. The adopted values are the weighted averages (as described in Section 2.4). The GNIRS data for the L3.5 dwarf are not shown here as they only cover a narrow-wavelength region, and so the fitting results for that object are shown in their entirety in Table 2.3.

^aWe adopt the $\log g$, RV and $v \sin i$ values from the narrow-wavelength regions (Table 2.3). To better determine T_{eff} and f_{sed} , we still allow $\log g$ to vary unconstrained in the full-band fitting, while RV and $v \sin i$ are allowed to probe within 2σ of the adopted values. In some cases the best-fitting RVs and $v \sin i$ values correspond to the extremes of their allowed range, so we do not include uncertainties for them here.

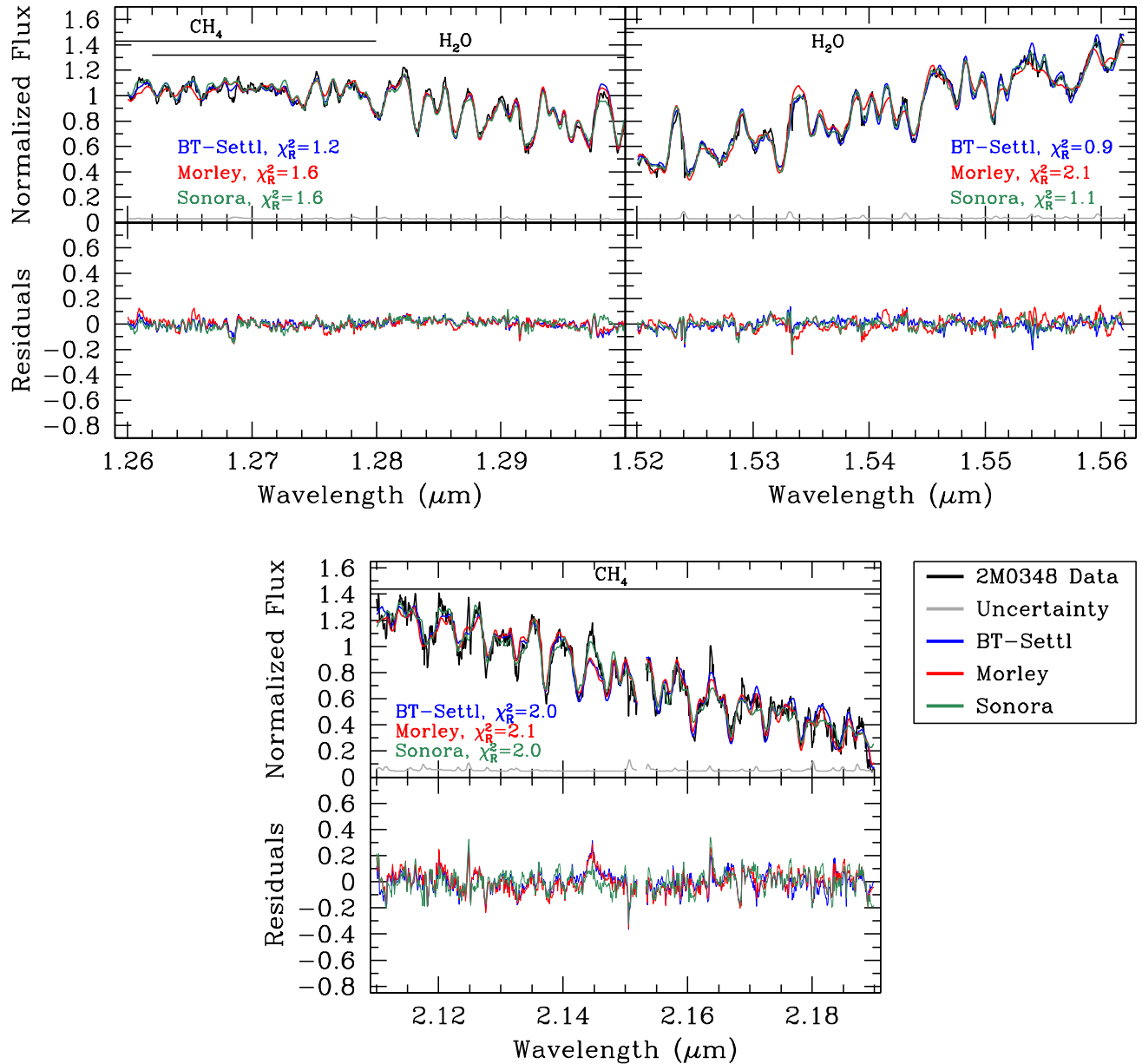


Figure 2.8: Three narrow regions within the *J* (top left), *H* (top right), and *K* (bottom) bands of our $R \approx 6000$ FIRE spectra of 2MASS J0348–6022 (T7), with the best-fitting BT-Settl, Morley, and Sonora models. The parameters of the best-fit models shown here are listed in Table 2.3. These regions were selected for their density of H_2O and CH_4 absorption lines (McLean et al., 2003; Cushing et al., 2006; Bochanski et al., 2011) to allow precise RV, $v \sin i$, and $\log g$ determinations. The reduced χ^2 statistic is shown for each model (χ^2_R). The residuals are shown in the lower section of each panel, where the colours match those of the corresponding models.

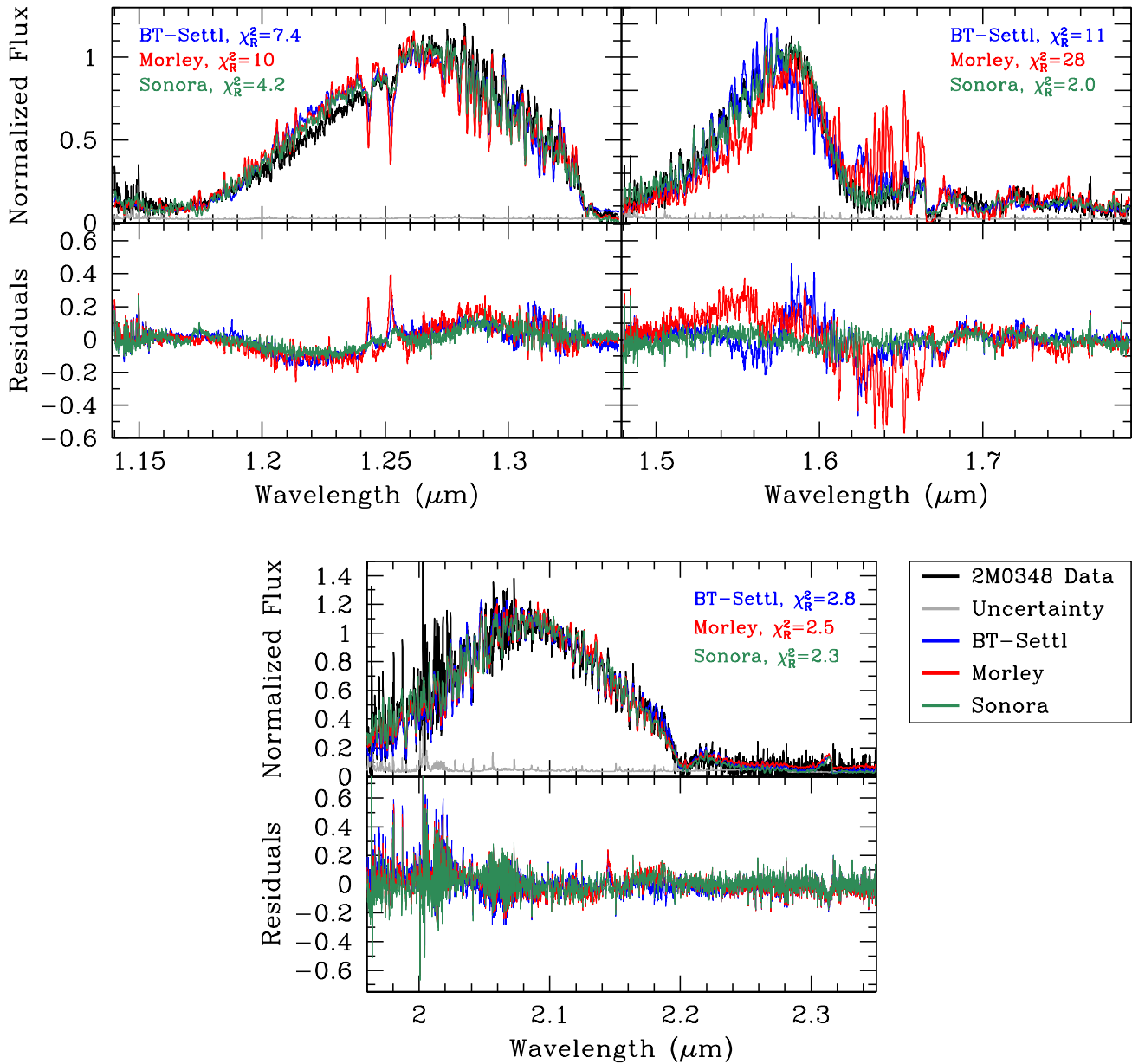


Figure 2.9: FIRE $R \approx 6000$ J- (top left), H- (top right), and K-band (bottom) spectra of 2MASS J0348-6022 (T7) with the best-fitting BT-Settl, Morley, and Sonora models for each band. The parameters of the best-fit models shown here are listed in Table 2.4. The reduced χ^2 statistic is shown for each model. The residuals are shown in the lower sections of each panel, where the colours match those of the corresponding models.

with the short rotational period (Sec. 2.2.4), and will be discussed further in Section 2.5. The adopted parameters from the spectroscopic fitting are shown in Table 2.5.

2.4.2 2MASS J1219+3128 (L8)

Based on its L8 spectral type, we expect 2MASS J1219+3128 to have an effective temperature of $T_{\text{eff}} \sim 1400$ K (e.g., Stephens et al. 2009; Filippazzo et al. 2015). The Morley models are not suitable for this target, as that model grid extends to a maximum of $T_{\text{eff}} = 1300$ K. The Sonora models are also not appropriate, as they are cloud-free, while late-L dwarfs are very dusty and are expected to have thick, patchy clouds. Therefore, we instead adopt only the SM08 and BT-Settl models as they cover sufficiently high temperatures for this spectral type and include treatments of dust. We selected a grid of parameters ranging from $T_{\text{eff}} = 1100$ K to 1700 K, $\log g = 4.0$ to 5.5 dex, and for the SM08 models, condensate sedimentation efficiencies from $f_{\text{sed}} = 1$ to 4 in unit steps. We selected the RV and $v \sin i$ grids using the same method as before (Sec. 2.4.1): by first testing a large, coarse grid to determine the approximate RV and $v \sin i$ values. The final grid was between -5 km s^{-1} and -30 km s^{-1} for RV and between 70 km s^{-1} and 110 km s^{-1} for $v \sin i$, both in steps of 0.1 km s^{-1} .

As for 2MASS J0348–6022 (Sec. 2.4.1), we find that a wide range in parameters fit the z band equally well. It is not diagnostic for our study, and we exclude the z band from our analysis. The J -band data had fairly low signal-to-noise ratio and had no regions with clearly defined lines from which we could measure $v \sin i$. We instead selected two narrow regions in the H band, along with a narrow region in the K band. In the H band we selected $1.50\text{--}1.55 \mu\text{m}$ and $1.72\text{--}1.78 \mu\text{m}$, where the first region is dominated by H_2O , and the second is dominated by FeH, H_2O , and potentially some CH_4 . The best lines in our data set for measuring $v \sin i$ in the K band are H_2O lines between $1.970 \mu\text{m}$ and $2.055 \mu\text{m}$, located on either side of a major telluric feature where our data have very low quality. We opted to mask out this region ($2.00\text{--}2.02 \mu\text{m}$) before fitting the models. We show the narrow band fits in Figure 2.10, and the full-band fits in Figure 2.11.

We also find a high degree of rotational broadening for 2MASS J1219+3128, with $v \sin i = 79.0 \pm 3.4 \text{ km s}^{-1}$ (Table 2.3). This is consistent with the short photometric period for this object. The adopted parameters from the spectroscopic fitting are shown in Table 2.5.

2.4.3 2MASS J0407+1546 (L3.5)

Based on its L3.5 spectral type, 2MASS J0407+1546 is expected to have an effective temperature of ~ 1800 K (e.g., Stephens et al., 2009; Filippazzo et al., 2015), with a fairly cloudy atmosphere. We therefore select the SM08 and BT-Settl models. We do not include the Sonora models as

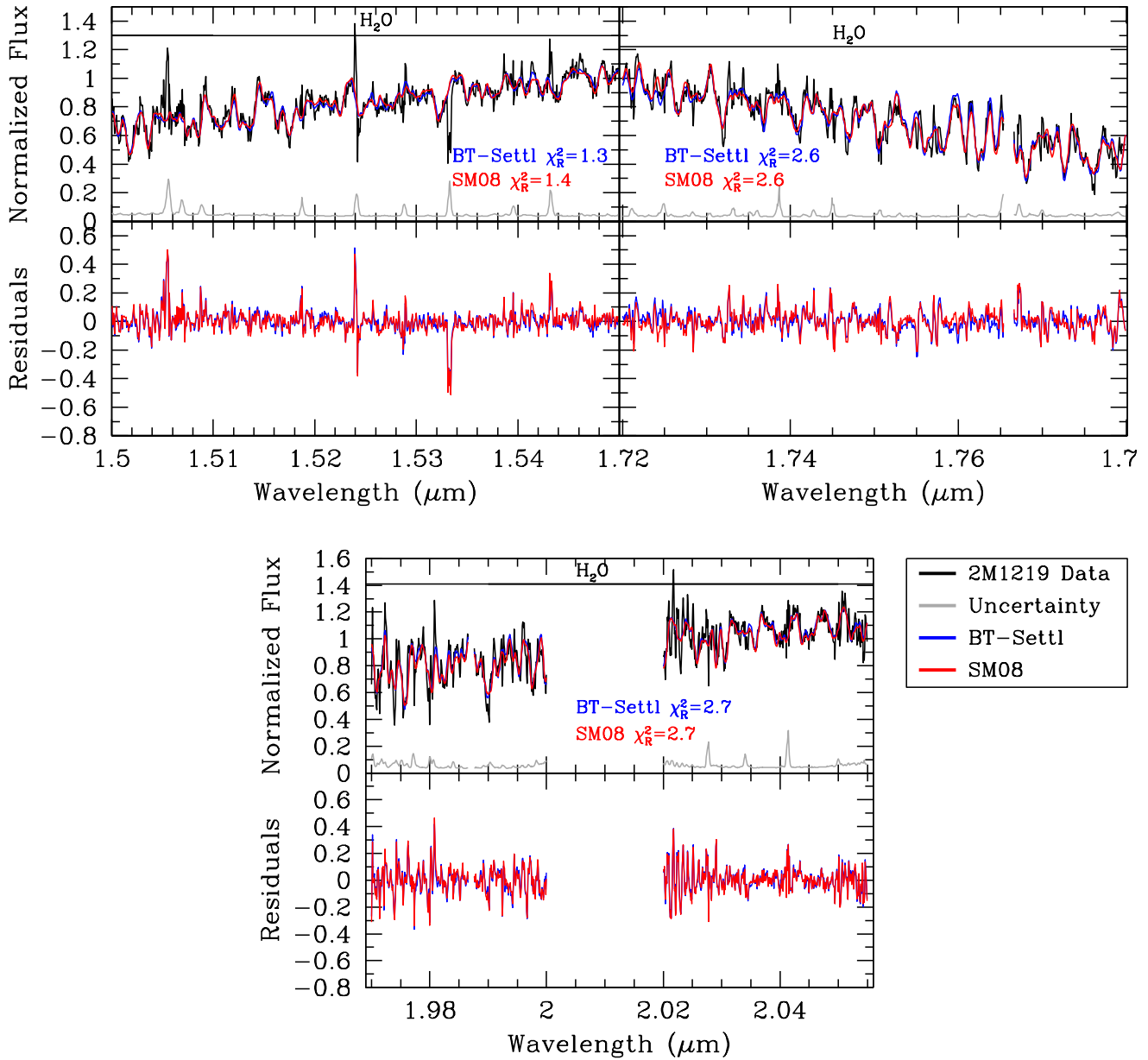


Figure 2.10: Three narrow regions within the H (top left and right) and K (bottom) bands of our $R \approx 6000$ FIRE spectrum of 2MASS J1219+3128 (L8), with the best-fitting BT-Settl, and SM08 models. These regions were selected for their density of H_2O absorption lines (McLean et al., 2003; Cushing et al., 2006) to allow precise $v \sin i$, RV, and $\log g$ determinations. The parameters of the models shown here are listed in Table 2.3. The reduced χ^2 statistic is shown for each model. The residuals are shown in the lower sections of each panel, where the colours match those of the corresponding models. A strong telluric feature has been masked between 2.00 and 2.02 μm in the K band.

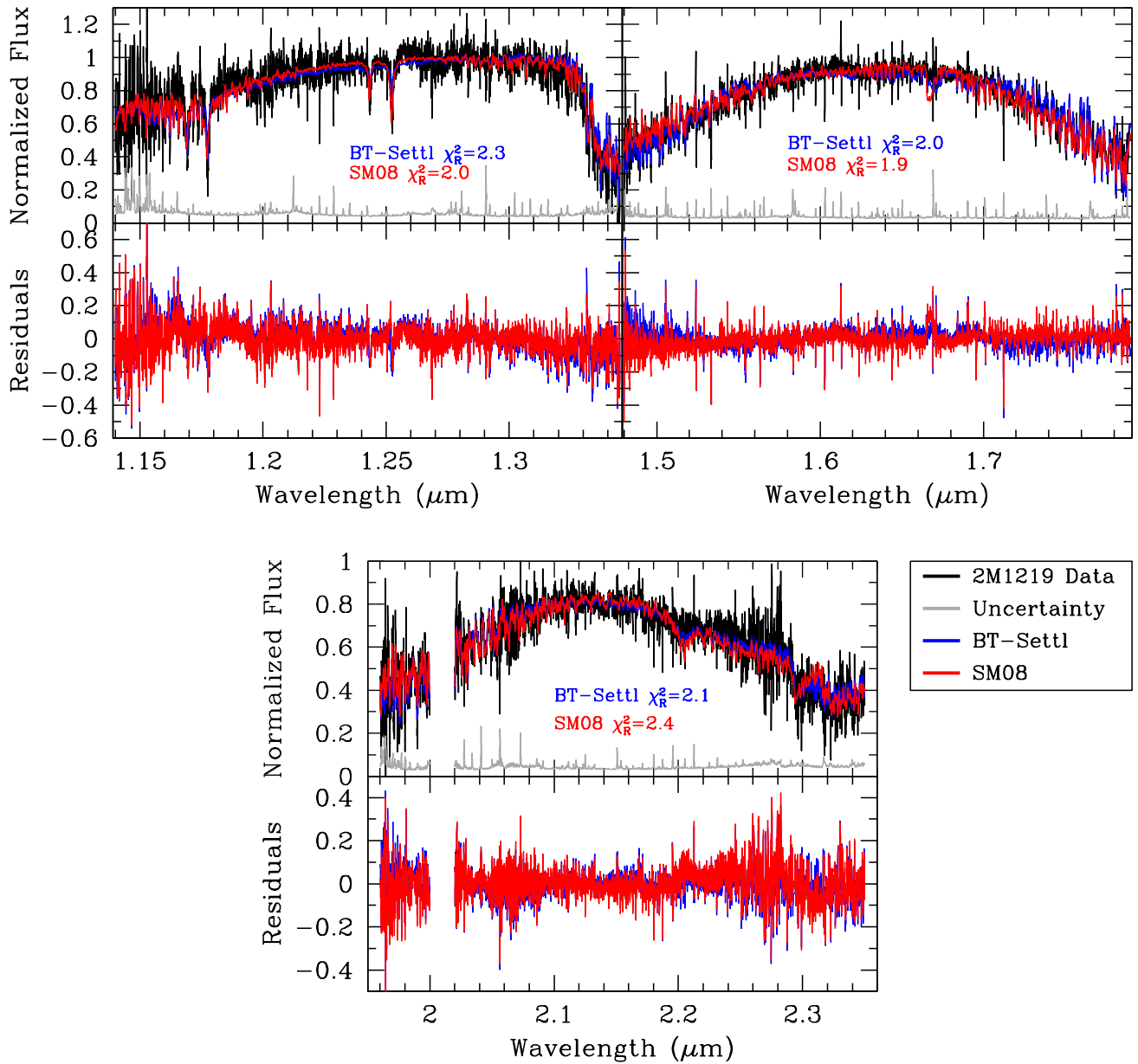


Figure 2.11: FIRE $R \approx 6000$ J - (top left), H - (top right), and K -band (bottom) spectra of 2MASS 1219+3128 (L8) with the best-fitting BT-Settl and SM08 models for the entire bands. The parameters of the models shown here are listed in Table 2.4. The reduced χ^2 statistic is shown for each model. The residuals are shown in the lower sections of each panel, where the colours match those of the corresponding models. The best-fitting SM08 model has $T_{\text{eff}} = 1500$ K and $\log g = 5.0$ and shows a methane feature at $1.665 \mu\text{m}$. Despite the presence of this feature in the model and its absence in the data, the shown photospheric model offers the best overall fit to the H -band spectrum. The appearance of the methane feature in the photospheric model may suggest that this L8 dwarf is close to transitioning to a T-type atmosphere. A strong telluric feature has been masked between 2.00 and $2.02 \mu\text{m}$ in the K band.

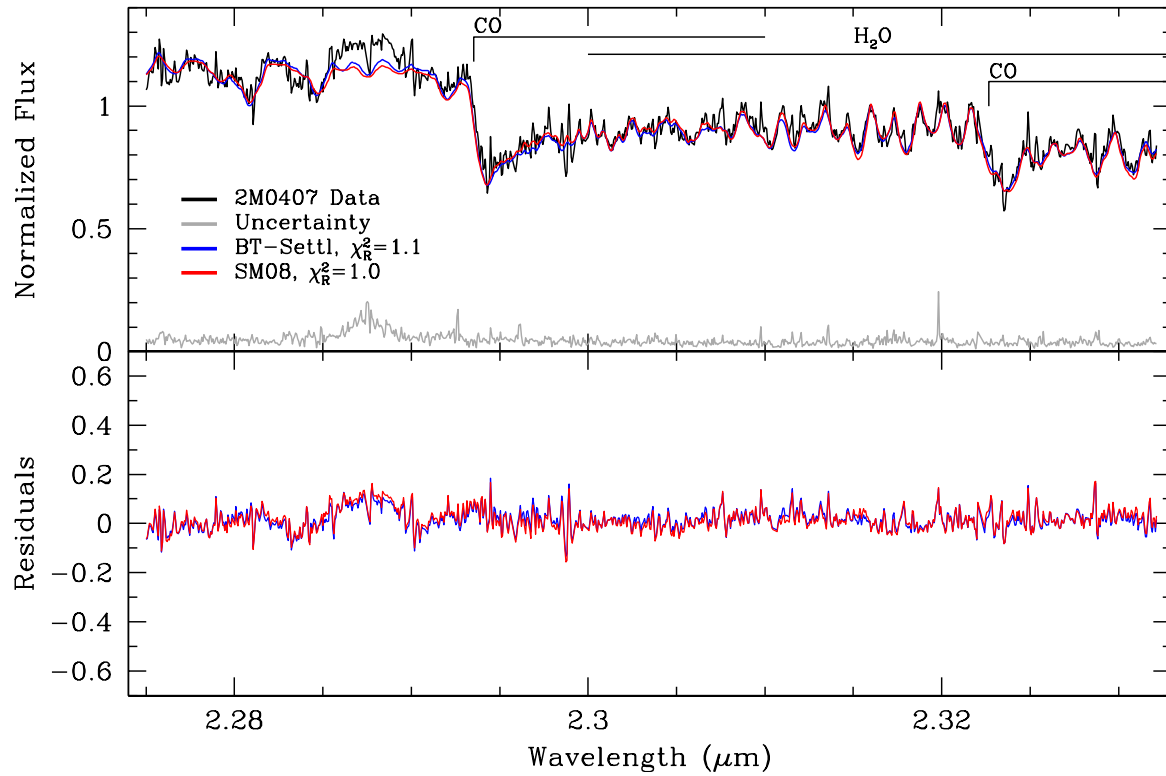


Figure 2.12: GNIRS 2.275–2.332 μm $R \approx 12,000$ spectrum of 2MASS J0407+1546, with the best-fitting SM08 and BT-Settl models overlaid. The parameters of the models shown here are listed in Table 2.3. The reduced χ^2 statistic is shown for each model. Major molecular features (Cushing et al., 2006) are indicated. The residuals are shown in the lower panel, where the colours match those of the corresponding models.

they are cloudless, or the Morley models as they are for temperatures below 1300 K. We selected the following parameter grid for fitting: $T_{\text{eff}} = 1500$ K to 2100 K in steps of 100 K, $\log g = 4.0$ dex to 5.5 dex in steps of 0.5 dex, and condensate sedimentation efficiency $f_{\text{sed}} = 1$ to 4 in unit steps. We selected 30 km s^{-1} to 60 km s^{-1} for RV and 75 km s^{-1} to 100 km s^{-1} for $v \sin i$, both in steps of 0.1 km s^{-1} . Our GNIRS observations cover the narrow region from $2.275 \mu\text{m}$ to $2.332 \mu\text{m}$, which contains primarily H_2O and CO lines. We show the best-fitting models in Figure 2.12.

The narrower-wavelength coverage of our GNIRS data means we have limited effective temperature and sedimentation efficiency information compared to the full-band spectra of the two other objects. Although we cannot place a high confidence on the results for these two parameters, we find that the effective temperature is consistent with expectations for an L3.5 dwarf, with $T_{\text{eff}} = 1840 \pm 210$ K. We find a high degree of rotational broadening, at $v \sin i = 82.6 \pm 0.2 \text{ km s}^{-1}$, consistent with the short rotational period. Table 2.5 lists all of the physical parameters determined from the spectroscopic fits.

2.5 Discussion

2.5.1 The Three Most Rapidly Rotating Ultra-cool Dwarfs: Possibility for Auroral Emissions

The $1.080_{-0.005}^{+0.004}$ h, $1.14_{-0.01}^{+0.03}$ h, and $1.23_{-0.01}^{+0.01}$ h photometric periods of our three L and T dwarfs are shorter than any others yet observed (Fig. 2.13; Table 2.6). The previously reported shortest photometric period for an ultra-cool dwarf was 1.41 ± 0.01 h for the T6 2MASS J22282889–4310262 (Clarke et al., 2008; Buenzli et al., 2012; Metchev et al., 2015). Route & Wolszczan (2016) have reported an even shorter possible period, 0.288 h for the T6 dwarf WISEPC J112254.73+255021.5, based on radio flare observations from the Arecibo Observatory radio telescope. However, they indicate that the 0.288 h period may be a harmonic of a longer period, or that the flares may in fact not have been periodic. They base their period on five flaring events with the first and last separated by ~ 240 days. When analyzing the data with the flares removed, they do not find any indication of variability. A later study by Williams et al. (2017) using the Very Large Array confirmed the same object to have variable polarized emission, but with a longer period of 1.93 h. They also observed the target photometrically in the z band using Gemini/GMOS-N, and did not find any indication of variability. We therefore do not consider WISEPC J112254.73+255021.5 as an ultra-fast rotator, leaving the three objects reported here as the fastest known L or T dwarf rotators.

We find a high degree of rotational line broadening for all three targets, consistent with the

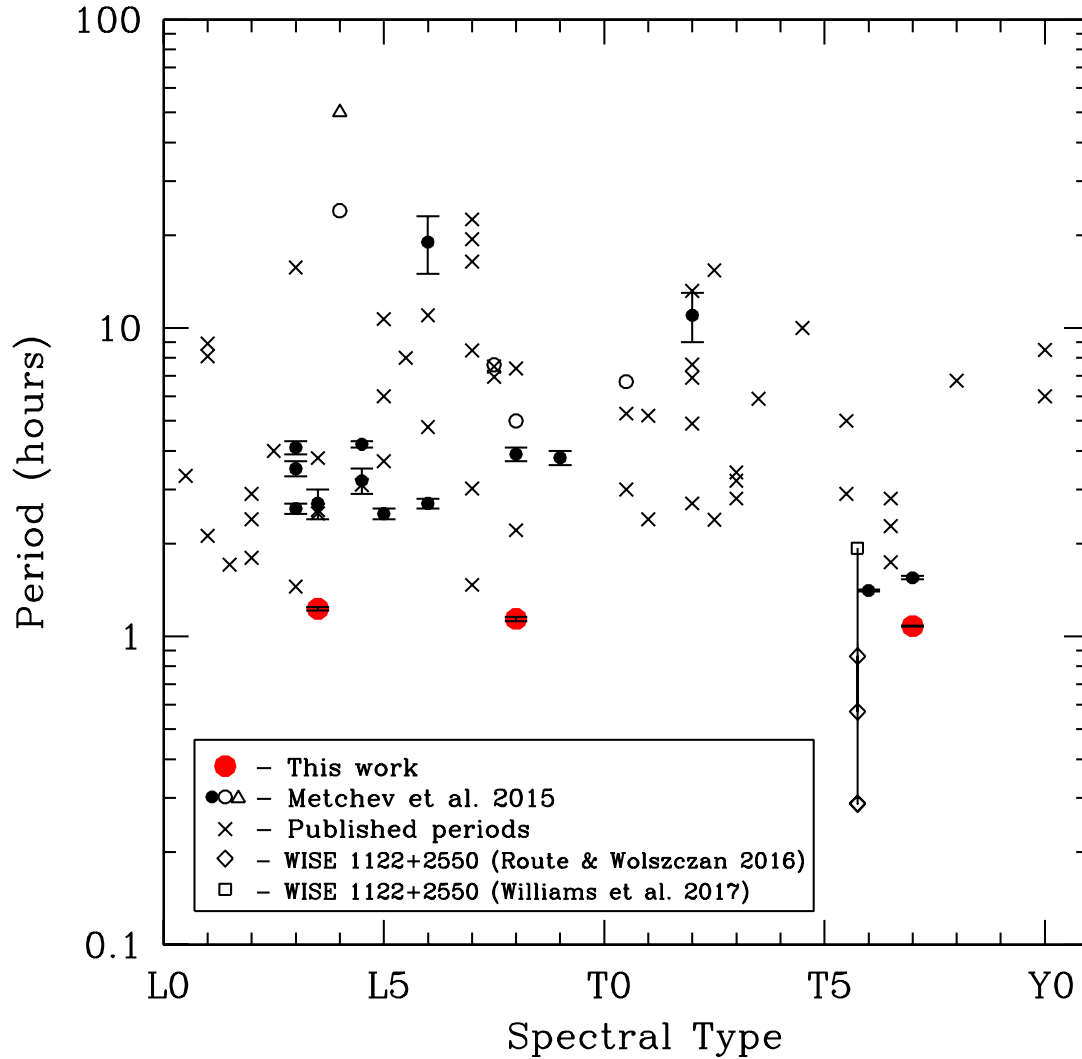


Figure 2.13: Rotation period as a function of spectral type for all 78 periodically variable L0–Y0 dwarfs known as of this writing. The full list of rotation periods is given in the Appendix in Table 2.6 with references. The “ultra-fast rotators” of this work are shown in red. Black circles are periods from Metchev et al. (2015), where solid circles denote variables with well-determined periodicities and open circles denote variables with uncertainties of $\geq 50\%$. An upward-facing triangle denotes the 50 hour lower limit on the periodicity of 2MASS 1753–6559. Open diamonds denote the possible period harmonics of WISEPC J1122+2550 (Route & Wolszczan, 2016), while an open square denotes the revised rotational period for this target from Williams et al. (2017). The points for WISEPC J1122+2550 are offset slightly to the left to avoid ambiguity with another T6 dwarf. Other previously published periods are denoted by the “x” symbol.

short photometric periods. At projected rotation velocities of 103.5 km s^{-1} for 2MASS J0348–6022 (T7), 79.0 km s^{-1} for 2MASS J1219+3128 (L8) and 82.6 km s^{-1} for 2MASS J0407+1546 (L3.5), these are among the most rapidly spinning ultra-cool dwarfs known to date. In the comprehensive compilation of ultra-cool dwarf rotation measurements by Crossfield (2014), he lists only two other ultra-cool dwarfs with $v \sin i > 80 \text{ km s}^{-1}$: HD 130948C (86 km s^{-1} , L4) and LP 349–45B (83 km s^{-1} , M9), both from Konopacky et al. (2012). HD 130948C has no reported photometric variability. Harding et al. (2013a) report optical photometric variability for LP 349–45B with a rotation period of $1.86 \pm 0.02 \text{ h}$.

The rapid projected rotational velocities of our targets confirm that the $\sim 1 \text{ h}$ periodicities of their light curves correspond to their true rotation periods, and that they are not more slowly rotating brown dwarfs with multiple spots at semi-regular longitudinal intervals, as seen on Jupiter (de Pater et al., 2016), or beat patterns arising from planetary-scale waves (Apai et al., 2017).

The $v \sin i$ measurements give lower limits on the true rotational velocities and may so be used to constrain the spin-axis inclinations of our targets. We assume that these brown dwarfs rotate as rigid spheres so that the equatorial rotation velocity is $v = 2\pi R/P$, where P is the photometric rotation period, and R is the radius. We estimate the radii, masses, and ages by comparing our findings for surface gravities and effective temperatures to the $\log g$ - T_{eff} grid in the evolutionary models of SM08. Oblateness due to the rapid rotation (see Section 2.5.2; notes in Table 2.5) and the corresponding increase in equatorial radius produce a second-order effect, which we have ignored in these calculations. Combining the radii (R), the photometric periods (P_{rot}), and the spectroscopically determined projected rotational velocities ($v \sin i$), we calculate the inclinations (i) and the equatorial rotation velocities (v_{eq}) of our targets (Table 2.5). All three L and T dwarfs have equatorial velocities $\gtrsim 100 \text{ km s}^{-1}$, and 2MASS J0348–6022 (T7) is seen near equator-on.

All three objects are also likely substellar. At a spectral type of L3.5, 2MASS J0407+1546 is the warmest and potentially most massive among our three L and T dwarfs. Its evolutionary model-dependent mass estimate is $0.037\text{--}0.073 M_{\odot}$ (Table 2.5). Optical spectroscopy from Reid et al. (2008) does not reveal lithium absorption, so it must be $> 0.060 M_{\odot}$ (e.g., Burrows et al., 1997). This still leaves the estimated $0.060\text{--}0.073 M_{\odot}$ mass of 2MASS J0407+1546 mostly in the substellar ($< 0.072 M_{\odot}$) domain.

The L3.5 dwarf 2MASS J0407+1546 is also known to be chromospherically active based on the strong (60 \AA equivalent width) $\text{H}\alpha$ emission reported by Reid et al. (2008). Its rapid rotation and $\text{H}\alpha$ emission may well indicate the presence of an aurora. Based on radio detections of three L and T dwarfs with short ($1.5\text{--}2.2 \text{ h}$) rotation periods, Kao et al. (2018) conclude that rapid rotation is key to powering auroral emissions via the electron cyclotron maser instability

Table 2.5. Physical parameters for the three L and T dwarfs

Parameter	2MASS J0348-6022	2MASS J1219+3128	2MASS J0407+1546
Spectral Type	T7	L8	L3.5
P_{rot} (h)	$1.080^{+0.004}_{-0.005}$	$1.14^{+0.03}_{-0.01}$	$1.23^{+0.01}_{-0.01}$
T_{eff} (K)	880 ± 110	1330 ± 140	1840 ± 210
$\log g$	5.1 ± 0.3	5.1 ± 0.5	5.2 ± 0.4
$v \sin i$ (km s^{-1})	103.5 ± 7.4	79.0 ± 3.4	82.6 ± 0.2
RV (km s^{-1})	-14.1 ± 3.7	-19.0 ± 4.2	43.4 ± 2.1
R (R_{\odot})	$0.093^{+0.016}_{-0.010}$	$0.100^{+0.027}_{-0.013}$	$0.100^{+0.024}_{-0.008}$
M (M_{\odot})	$0.041^{+0.021}_{-0.017}$	$0.047^{+0.022}_{-0.025}$	$0.064^{+0.009}_{-0.027}$
Age (Gyr)	$3.5^{+11.5}_{-2.9}$	$0.9^{+12.8}_{-0.8}$	$0.8^{+11.2}_{-0.65}$
v_{eq} (km s^{-1})	105^{+18}_{-12}	107^{+29}_{-15}	99^{+24}_{-8}
Inclination ($^{\circ}$)	81^{+9}_{-27}	47^{+9}_{-17}	57^{+7}_{-21}
Oblateness	0.08	0.08	0.05

Note. — P_{rot} is determined from our photometric data. T_{eff} , $\log g$, $v \sin i$, and RV are determined from our spectra by comparing to model photospheres. R , M , and the ages are determined by interpolation of the $\log g$ - T_{eff} grid in the evolutionary models of SM08. The equatorial velocities (v_{eq}) and spin-axis inclinations (i) are computed using the aforementioned values.

The evolutionary model radii listed are assumed to be the equatorial radii. With oblateness factors between 0.05 and 0.08, the difference between the polar and equatorial radii is 5%–8%. In reality, the evolutionary models (which ignore rotation) likely produce “mean” radii that are in between the equatorial and the polar radii. Hence, any difference between the “mean” and the equatorial radii would be 3%–4%. This would revise our estimates for the equatorial velocities up by $\sim 3\%$ – 4% , but such systematic offsets would still be ~ 3 times smaller than the quoted uncertainties. The effect on the inclination estimates would be negligible.

(Hallinan et al., 2007, 2015). Kao et al. (2016); Pineda et al. (2017) and Richey-Yowell et al. (2020) further demonstrate that brown dwarf $H\alpha$ and radio luminosities and radio aurorae are correlated. It is possible that all three of our rapidly rotating brown dwarfs have strong dipole fields that power auroral emission (Kao et al., 2018). In particular, the near equator-on view of the T7 dwarf 2MASS J0348–6022 makes it an excellent candidate for seeking pulses of circularly polarized electron cyclotron maser emission. This is already known from other rapidly rotating ultra-cool dwarfs seen at their equators (Berger et al., 2001; Hallinan et al., 2007).

2.5.2 Proximity to Rotational Break-up and Oblateness

An upper limit on the spin rate of brown dwarfs exists from simple arguments of rotational stability. Konopacky et al. (2012) estimate that their two most rapidly rotating ultra-cool dwarfs, HD 130948C ($v \sin i = 86 \text{ km s}^{-1}$) and LP 349–45B ($v \sin i = 83 \text{ km s}^{-1}$) rotate at approximately 30% of break-up speed. The break-up periods for typical >1 Gyr-aged field brown dwarfs are in the tens of minutes. For example, a massive $0.07 M_{\odot}$, $0.09 R_{\odot}$ brown dwarf has $P_{\text{breakup}} = 2\pi(R^3/GM)^{1/2} = 17 \text{ min}$, while a low-mass $0.02 R_{\odot}$, $0.12 R_{\odot}$ brown dwarf has $P_{\text{breakup}} = 49 \text{ min}$. These are approximately consistent with extrapolations from the shortest known (5 h) brown dwarf rotation period at 5 Myr (Scholz et al., 2015), assuming that the fastest rotators at ~ 5 Myr remain the fastest when they contract and age. Using the evolutionary models of (non-accreting) brown dwarfs from Baraffe et al. (2015), by 3 Gyr conservation of angular momentum, dictates periods in the 10–70 min range (e.g., Schneider et al., 2018a).

The 65–74 min periods of our three fast rotators are at the long end of this range. They would be near break-up only if they all had very low masses and large radii, i.e., were young brown dwarfs with low surface gravities. This is highly unlikely, given the wide range in spectral types (L3.5–T7) of our three rapid rotators, and the fact that their moderate-to-high surface gravities ($\log g \gtrsim 5.0$; Table 2.5) point to >0.1 Gyr ages. Using our measured RVs and precise proper motions and parallaxes determined from the Hawaii Infrared Parallax Program (Liu et al., 2016; Best et al., 2020) or from Spitzer (Kirkpatrick et al., 2019), the BANYAN Σ young moving group tool (Gagné et al., 2018) reports that the space motions of all three L and T dwarfs are $\geq 99\%$ consistent with field-dwarf kinematics. Only for 2MASS J0407+1546 (L3.5) is there a 1% chance of membership in the 40–50 Myr Argus association (Zuckerman, 2019), and Gagné et al. (2015b) independently discuss that this object may either be ~ 200 Myr old or have peculiar metallicity, based on weaker FeH and slightly weaker alkali line widths. Thus, 2MASS J0407+1546 may indeed be moderately young, even if it is not a member of any of the

known young stellar moving groups.

To assess the proximity to break-up spin-velocity, we consider the effect of the centrifugal acceleration on surface gravity. Rapid rotation decreases the surface gravity near the equator, and may make the object appear younger. We can determine the surface gravity decrement due to the centrifugal acceleration using the inferred radii and equatorial velocities (Table 2.5). For our potentially fastest and largest rotator, the L8 dwarf 2MASS J1219+3128, the centrifugal acceleration is $a_c = v^2/R = 1.6 \times 10^4 \text{ cm s}^{-2}$ ($\log a_c = 4.2$), where $v_{\text{eq}} = 107 \text{ km s}^{-1}$ and $R = 0.100 R_{\odot}$. The centrifugal acceleration thus reduces the surface gravity at the equator by about 13%, when compared to the $\log g = 5.1 \pm 0.5$ surface gravity inferred from the photospheric model fitting (Table 2.5). While this does indicate that the rotation speed amounts to a significant fraction (35%) of the break-up speed, we note that it has a minor effect on our ability to assess the surface gravity spectroscopically.

The rotational stability limit for brown dwarfs may not necessarily be set by the centrifugal levitation argument above. The stability limit for the oblateness f (fractional difference between polar and equatorial radii) of axisymmetric rotating polytropes for brown dwarf-like structures ($n \sim 1$ to 1.5) is about 0.4 (James, 1964). The Darwin-Radau relationship (e.g., Barnes & Fortney 2003) connects the oblateness, mass, radius, rotation, and moment of inertia for objects with smoothly varying interiors. Using the central values from Table 2.5, we compute oblateness factors of 0.08, 0.08 and 0.05 for the most (2MASS J0348–6022, 2MASS J1219+3128) and least (2MASS J0407+1546) oblate objects. This places the spin rates of both 2MASS J0348–6022 and 2MASS J1219+3128 at about 45% of their rotational stability limits: closer to instability than indicated by the rigid-body rotation break-up velocity estimates. For comparison, Saturn, the most oblate planet in the solar system, has an oblateness of 0.1. The brown dwarfs have surface gravities about 100 times greater than Saturn but rotation rates 10 times faster. Since oblateness scales as Ω^2/g (where Ω is the rotation rate), it is not surprising the oblateness of these objects are comparable to that of Saturn.

Finally, the preceding discussion ignores the effect of any magnetic dynamo from the metallic hydrogen interior, which may be an important contributor to the energy balance in such rapid rotators, and may further limit the maximum spin velocity. So these three objects may be even closer to instability than indicated by estimates that ignore magnetic fields.

From an observational standpoint, the three rapid rotators delineate a clear lower boundary to the envelope of all 78 L-, T-, and Y-dwarf rotation periods measured to date (Fig. 2.13). This limit holds over a broad range of spectral types, for objects that presumably have different ages. Hence, ~ 1 h may be close to a physical lower limit to the spin period of field-aged Jupiter-sized brown dwarfs.

Because of their significant oblateness, the three rapid rotators are potentially good targets

for searches for polarized thermal emission (e.g., [Marley & Sengupta 2011](#); [de Kok et al. 2011](#); [Stolker et al. 2017](#)). Several surveys have been successful in detecting polarized thermal emission from brown dwarfs (e.g., [Ménard et al. 2002](#); [Zapatero Osorio et al. 2005](#); [Miles-Páez et al. 2013, 2017c](#); [Millar-Blanchaer et al. 2020](#)), which could be attributed to inhomogeneous cloud cover or oblateness. Intriguingly, [Miles-Páez et al. \(2013\)](#) find that ultra-cool dwarfs with the fastest rotation ($v \sin i \geq 60 \text{ km s}^{-1}$) are more likely to exhibit linear polarization and at a larger degree than slower rotators.

2.6 Conclusions

We present a T7, L3.5, and an L8 dwarf with the shortest photometric periodicities measured to date: 1.08 h, 1.14 h, and 1.23 h. We confirm these extremely short rotation periods with moderate-dispersion spectroscopy and comparisons to Doppler-broadened model photospheres. The inferred $v \sin i$ value of the T7 dwarf 2MASS J0348–6022 is the highest known to date for an ultra-cool dwarf. Combining the projected rotation velocities of our targets with their photometric periods and photospheric model-dependent radii, we determine their equatorial velocities. All three L and T dwarfs spin at $\gtrsim 100 \text{ km s}^{-1}$ at their equators, and are the most rapidly spinning field ultra-cool dwarfs known to date. As such, they are excellent candidates for seeking auroral radio emission, which has been linked to rapid rotation in ultra-cool dwarfs. We consider the role of the centrifugal acceleration on surface gravity, and find that, while the effect can be significant, at $\lesssim 0.1$ dex in surface gravity it can be difficult to discern with current photospheric models. We find that the objects have oblateness factors of between 5% and 8%, which ranks them among the best targets for seeking net optical or infrared polarization. Given that the three rapid rotators presented in this paper appear to lie near a short-period limit of approximately 1 h across all brown dwarf spectral types, we consider it unlikely that rotation periods much shorter than 1 h exist for brown dwarfs.

2.7 Appendix: All Known Brown Dwarf Rotation Periods

The full list of rotation periods shown in [Figure 2.13](#) is given in [Table 2.6](#) with references.

Table 2.6. Known L-, T-, and Y-dwarf rotation periods

Object	RA	DEC	Spectral Type	Period (h)	Period Uncertainty (h)	Reference
2MASS J00132229-1143006	00 13 22.2	-11 43 00.6	T3	2.8	...	(1)
LSPM J0036+1821	00 36 16.1	+18 21 10.2	L3.5	2.7	0.3	(2), (3), (4), (5)
2MASS J00452143+1634446	00 45 21.4	+16 34 44.7	L2 β	2.4	0.1	(6), (7)
2MASS J00470038+6803543	00 47 00.3	+68 03 54.3	L7	16.4	0.2	(8), (9)
2MASS J00501994-3322402	00 50 19.9	-33 22 40.2	T7	1.55	0.02	(2)
2MASS J0103320+193536	01 03 32.0	+19 35 36.1	L6	2.7	0.1	(2)
2MASS J01075242+0041563	01 07 52.4	+00 41 56.3	L8	5	...	(2)
GU Psc B	01 12 36.5	+17 04 29.9	T3.5	5.9	0.7	(10), (11)
2MASS 0122-2439 b	01 22 50.8	-24 39 51.6	L5	6	...	(12)
SIMP J013656.5+093347.3	01 36 56.6	+09 33 47.3	T2.5	2.3895	0.0005	(13), (14), (5), (15), (16), (17), (1)
2MASS J01383648-0322181	01 38 36.4	-03 22 18.1	T3	3.2	...	(1)
DENIS J025503.3-470049	02 55 03.6	-47 00 51.3	L8	7.4	...	(18), (19), (20)
2MASS J03480772-6022270	03 48 07.7	-60 22 27.0	T7	1.08	0.005	(21), (22)
2MASS J04070752+1546457	04 07 07.5	+15 46 45.5	L3.5	1.23	0.01	(21)
2MASS J0423485-041403	04 23 48.5	-04 14 03.2	L7	1.47	0.13	(17), (23)
2MASS J05012406-0010452	05 01 24.0	-00 10 45.5	L3	15.7	0.2	(6), (7)
Beta Pic b	05 47 17.0	-51 03 59.4	L1	8.1	1.0	(24)
2MASS J05591914-1404488	05 59 19.1	-14 04 49.2	T4.5	10	...	(14)
AB Pic B	06 19 12.9	-58 03 20.9	L1	2.12	...	(12)
2MASS J07003664+3157266	07 00 36.7	+31 57 25.5	L3.5	3.79	1.3	(25)
2MASS J07464256+2000321A	07 46 42.4	+20 00 32.6	L0.5	3.32	0.15	(4)
2MASS J07584037+3247245	07 58 40.3	+32 47 24.5	T2	4.9	0.2	(14)
2MASS J08173001-6155158	08 17 29.9	-61 55 15.6	T6.5	2.8	0.2	(14)
2MASS J0825196+211552	08 25 19.6	+21 15 51.5	L7.5	7.6	...	(2), (26)
2MASS J08283419-1309198	08 28 34.1	-13 09 19.8	L2	2.9	...	(27)
2MASS J08354256-0819237	08 35 42.5	-08 19 23.3	L4.5	3.1	...	(27), (22)
LP 261-75 B	09 51 05.4	+35 58 02.1	L6	4.78	0.95	(28)
2MASS J1043075+222523	10 43 07.5	+22 25 23.6	L8	2.21	0.14	(17)
2MASS J10433508+1213149	10 43 35.0	+12 13 14.9	L9	3.8	0.2	(2)
2MASSW J1047539+212423	10 47 53.8	+21 24 23.4	T6.5	1.741	0.007	(29), (30), (17)
Luhman 16A	10 49 19.0	-53 19 10	L7.5	6.94	...	(31), (32), (33), (34), (35)
Luhman 16B	10 49 18.9	-53 19 09	T0.5	5.28	...	(31), (32), (36), (33), (34), (35)
2MASS J10521350+4422559	10 52 13.5	+44 22 55.9	T0.5	3	...	(37)
DENIS J1058.7-1548	10 58 47.8	-15 48 17.2	L3	4.1	0.2	(2), (38)
2MASS J11193254-1137466	11 19 32.5	-11 37 46.6	L7	3.02	0.04	(39)
2MASS J11225550+2550250	11 22 55.5	+25 50 25.0	T6	1.93	0.12	(40), (41)
DENIS J112639.9-500355	11 26 39.8	-50 03 54.8	L4.5	3.2	0.3	(2), (14)
WISEA J114724.10-204021.3	11 47 24.2	-20 40 20.4	L7	19.39	0.33	(39)
2MASSW J1207334-393254 b	12 07 33.5	-39 32 54.4	L5	10.7	1.2	(42), (12)
HD 106906 B	12 17 52.6	-55 58 26.6	L2.5	4	...	(43)
2MASS J12195156+3128497	12 19 51.5	+31 28 49.7	L8	1.14	0.03	(21), (26)
2MASS J12373919+6526148	12 37 39.1	+65 26 14.8	T6.5	2.28	0.1	(17)
VHS J1256-1257B	12 56 01.8	-12 57 27.6	L7	22.5	0.4	(44)
Ross 458 C	13 00 42.0	+12 21 15.0	T8	6.75	1.58	(45)
Kelu-1	13 05 40.1	-25 41 05.8	L2	1.8	...	(46), (47)

Table 2.6 (cont'd)

Object	RA	DEC	Spectral Type	Period (h)	Period Uncertainty (h)	Reference
2MASS J13243553+6358281	13 24 35.5	+63 58 28.1	T2	13.2	...	(16), (2)
WISE J140518.39+553421.3	14 05 18.3	+55 34 21.3	Y0	8.5	...	(48)
2MASS J14252798-3650229	14 25 27.9	-36 50 23.2	L5	3.7	0.8	(14), (7), (6)
DENIS J145407.8-660447	14 54 07.9	-66 04 47.4	L3.5	2.57	0.002	(47)
2MASSW J1507476-162738	15 07 47.6	-16 27 40.1	L5	2.5	0.1	(2), (15)
SDSS J151114.65+060742.9	15 11 14.6	+06 07 43.1	T2	11	2	(2)
2MASS J15164306+3053443	15 16 43.0	+30 53 44.3	T0.5	6.7	...	(2)
2MASS J15394189-0520428	15 39 41.9	-05 20 42.7	L3.5	2.51	1.6	(25), (49)
2MASS J16154255+4953211	16 15 42.5	+49 53 21.1	L4 β	24	...	(2)
2MASS J16291840+0335371	16 29 18.4	+03 35 37.1	T2	6.9	2.4	(14)
2MASS J16322911+1904407	16 32 29.1	+19 04 40.7	L8	3.9	0.2	(2)
2MASSI J1721039+334415	17 21 03.6	+33 44 16.9	L3	2.6	0.1	(2)
JWISE J173835.53+273259.0	17 38 35.5	+27 32 59.0	Y0	6	0.1	(50)
2MASS J17502385+4222373	17 50 23.8	+42 22 37.3	T2	2.7	0.2	(14)
2MASS J17534518-6559559	17 53 45.1	-65 59 55.6	L4	≥ 50	...	(2)
2MASS J18071593+5015316	18 07 15.9	+50 15 31.6	L1.5	1.71	0.3	(25)
2MASS J18212815+1414010	18 21 28.1	+14 14 00.8	L4.5	4.2	0.1	(2), (15)
2MASS J18283572-4849046	18 28 35.7	-48 49 04.6	T5.5	5	0.6	(14)
2MASS J19064801+4011089	19 06 48.0	+40 11 08.5	L1	8.9	...	(51)
2MASSI J2002507-052152	20 02 50.7	-05 21 52.5	L5.5	8	2	(7)
2MASS J20360316+1051295	20 36 03.1	+10 51 29.5	L3	1.45	0.55	(25)
PSO J318.5338-22.8603	21 14 08.0	-22 51 35.8	L7	8.45	0.05	(7), (52), (53), (54)
HD 203030B	21 18 58.9	+26 13 46.1	L7.5	7.5	0.6	(55)
2MASS J21392676+0220226	21 39 26.7	+02 20 22.6	T2	7.614	0.178	(15), (56), (14), (16)
HN Peg B	21 44 28.4	+14 46 07.7	T2.5	15.4	0.5	(57), (2)
2MASSW J2148162+400359	21 48 16.2	+40 03 59.3	L6	19	4	(2)
2MASS J21483578+2239427	21 48 35.7	+22 39 42.7	T1	2.4	0.4	(1)
2MASSW J2208136+292121	22 08 13.6	+29 21 21.5	L3 γ	3.5	0.2	(2)
2MASS J22153705+2110554	22 15 37.0	+21 10 55.4	T1	5.2	0.5	(1)
2MASS J22282889-4310262	22 28 28.8	-43 10 26.2	T6	1.41	0.01	(2), (23), (58), (14), (15)
2MASS J22393718+1617127	22 39 37.1	+16 17 12.7	T3	3.4	...	(1)
2MASS J22443167+2043433	22 44 31.6	+20 43 43.3	L6	11	2	(8), (18), (7)
2MASS J23312378-4718274	23 31 23.7	-47 18 27.4	T5.5	2.9	0.9	(23)

Note. — Where multiple references are given, we have adopted the spectral type and period value from the first reference. Additional L3–T8 periods compiled in [Crossfield \(2014\)](#) that have not withstood independent confirmation so we do not include them here.

References. — (1) [Eriksson et al. \(2019\)](#); (2) [Metchev et al. \(2015\)](#); (3) [Berger et al. \(2005\)](#); (4) [Harding et al. \(2013b\)](#); (5) [Croll et al. \(2016\)](#); (6) [Vos et al. \(2020\)](#); (7) [Vos et al. \(2019\)](#); (8) [Vos et al. \(2018\)](#); (9) [Lew et al. \(2016\)](#); (10) [Naud et al. \(2017\)](#); (11) [Lew et al. \(2020\)](#); (12) [Zhou et al. \(2019\)](#); (13) [Artigau et al. \(2009\)](#); (14) [Radigan et al. \(2014\)](#); (15) [Yang et al. \(2016\)](#); (16) [Apai et al. \(2017\)](#); (17) [Kao et al. \(2018\)](#); (18) [Morales-Calderón et al. \(2006\)](#); (19) [Koen \(2005\)](#); (20) [Koen et al. \(2005\)](#); (21) This work; (22) [Wilson et al. \(2014\)](#); (23) [Clarke et al. \(2008\)](#); (24) [Snellen et al. \(2014\)](#); (25) [Miles-Páez et al. \(2017b\)](#); (26) [Buenzli et al. \(2014\)](#); (27) [Koen \(2004\)](#); (28) [Manjavacas et al. \(2018\)](#); (29) [Allers et al. \(2020\)](#); (30) [Williams & Berger \(2015\)](#); (31) [Apai et al. \(2021\)](#); (32) [Biller et al. \(2013\)](#); (33) [Buenzli et al. \(2015b\)](#); (34) [Buenzli et al. \(2015a\)](#); (35) [Karlidi et al. \(2016\)](#); (36) [Gillon et al. \(2013\)](#); (37) [Girardin et al. \(2013\)](#); (38) [Heinze et al. \(2013\)](#); (39) [Schneider et al. \(2018b\)](#); (40) [Williams et al. \(2017\)](#); (41) [Route & Wolszczan \(2016\)](#); (42) [Zhou et al. \(2016\)](#); (43) [Zhou et al. \(2020\)](#); (44) [Bowler et al. \(2020\)](#); (45) [Manjavacas et al. \(2019\)](#); (46) [Clarke et al. \(2002\)](#); (47) [Koen \(2013\)](#); (48) [Cushing et al. \(2016\)](#); (49) [Koen \(2013\)](#); (50) [Leggett et al. \(2016\)](#); (51) [Gizis et al. \(2015\)](#); (52) [Biller et al. \(2015\)](#); (53) [Allers et al. \(2016\)](#); (54) [Biller et al. \(2018\)](#); (55) [Miles-Páez et al. \(2019\)](#); (56) [Radigan et al. \(2012\)](#); (57) [Zhou et al. \(2018\)](#); (58) [Buenzli et al. \(2012\)](#).

Bibliography

- Ackerman, A. S., & Marley, M. S. 2001, *ApJ*, 556, 872, doi: [10.1086/321540](https://doi.org/10.1086/321540)
- Allard, F., Homeier, D., & Freytag, B. 2012, *Philosophical Transactions of the Royal Society of London Series A*, 370, 2765, doi: [10.1098/rsta.2011.0269](https://doi.org/10.1098/rsta.2011.0269)
- Allers, K. N., Gallimore, J. F., Liu, M. C., & Dupuy, T. J. 2016, *ApJ*, 819, 133, doi: [10.3847/0004-637X/819/2/133](https://doi.org/10.3847/0004-637X/819/2/133)
- Allers, K. N., Vos, J. M., Biller, B. A., & Williams, P. K. G. 2020, *Science*, 368, 169, doi: [10.1126/science.aaz2856](https://doi.org/10.1126/science.aaz2856)
- Antonova, A., Doyle, J. G., Hallinan, G., Bourke, S., & Golden, A. 2008, *A&A*, 487, 317, doi: [10.1051/0004-6361:20079275](https://doi.org/10.1051/0004-6361:20079275)
- Apai, D., Nardiello, D., & Bedin, L. R. 2021, *ApJ*, 906, 64, doi: [10.3847/1538-4357/abcb97](https://doi.org/10.3847/1538-4357/abcb97)
- Apai, D., Karalidi, T., Marley, M. S., et al. 2017, *Science*, 357, 683, doi: [10.1126/science.aam9848](https://doi.org/10.1126/science.aam9848)
- Artigau, É., Bouchard, S., Doyon, R., & Lafrenière, D. 2009, *ApJ*, 701, 1534, doi: [10.1088/0004-637X/701/2/1534](https://doi.org/10.1088/0004-637X/701/2/1534)
- Bailer-Jones, C. A. L. 2002, *A&A*, 389, 963, doi: [10.1051/0004-6361:20020730](https://doi.org/10.1051/0004-6361:20020730)
- Baraffe, I., Homeier, D., Allard, F., & Chabrier, G. 2015, *A&A*, 577, A42, doi: [10.1051/0004-6361/201425481](https://doi.org/10.1051/0004-6361/201425481)
- Barnes, J. W., & Fortney, J. J. 2003, *ApJ*, 588, 545, doi: [10.1086/373893](https://doi.org/10.1086/373893)
- Basri, G., Mohanty, S., Allard, F., et al. 2000, *ApJ*, 538, 363, doi: [10.1086/309095](https://doi.org/10.1086/309095)
- Berger, E., Ball, S., Becker, K. M., et al. 2001, *Nature*, 410, 338. <https://arxiv.org/abs/astro-ph/0102301>

- Berger, E., Rutledge, R. E., Reid, I. N., et al. 2005, *ApJ*, 627, 960, doi: [10.1086/430343](https://doi.org/10.1086/430343)
- Best, W. M. J., Liu, M. C., Magnier, E. A., & Dupuy, T. J. 2020, *AJ*, 159, 257, doi: [10.3847/1538-3881/ab84f4](https://doi.org/10.3847/1538-3881/ab84f4)
- Biller, B. A., Crossfield, I. J. M., Mancini, L., et al. 2013, *ApJ Letters*, 778, L10, doi: [10.1088/2041-8205/778/1/L10](https://doi.org/10.1088/2041-8205/778/1/L10)
- Biller, B. A., Vos, J., Bonavita, M., et al. 2015, *ApJ Letters*, 813, L23, doi: [10.1088/2041-8205/813/2/L23](https://doi.org/10.1088/2041-8205/813/2/L23)
- Biller, B. A., Vos, J., Buenzli, E., et al. 2018, *AJ*, 155, 95, doi: [10.3847/1538-3881/aaa5a6](https://doi.org/10.3847/1538-3881/aaa5a6)
- Blake, C. H., Charbonneau, D., & White, R. J. 2010, *ApJ*, 723, 684, doi: [10.1088/0004-637X/723/1/684](https://doi.org/10.1088/0004-637X/723/1/684)
- Bochanski, J. J., Burgasser, A. J., Simcoe, R. A., & West, A. A. 2011, *AJ*, 142, 169, doi: [10.1088/0004-6256/142/5/169](https://doi.org/10.1088/0004-6256/142/5/169)
- Bochanski, J. J., Hennawi, J. F., Simcoe, R. A., et al. 2009, *PASP*, 121, 1409, doi: [10.1086/648597](https://doi.org/10.1086/648597)
- Bowler, B. P., Zhou, Y., Morley, C. V., et al. 2020, *ApJ Letters*, 893, L30, doi: [10.3847/2041-8213/ab8197](https://doi.org/10.3847/2041-8213/ab8197)
- Buenzli, E., Apai, D., Radigan, J., Reid, I. N., & Fplateau, D. 2014, *ApJ*, 782, 77, doi: [10.1088/0004-637X/782/2/77](https://doi.org/10.1088/0004-637X/782/2/77)
- Buenzli, E., Marley, M. S., Apai, D., et al. 2015a, *ApJ*, 812, 163, doi: [10.1088/0004-637X/812/2/163](https://doi.org/10.1088/0004-637X/812/2/163)
- Buenzli, E., Saumon, D., Marley, M. S., et al. 2015b, *ApJ*, 798, 127, doi: [10.1088/0004-637X/798/2/127](https://doi.org/10.1088/0004-637X/798/2/127)
- Buenzli, E., Apai, D., Morley, C. V., et al. 2012, *ApJ Letters*, 760, L31, doi: [10.1088/2041-8205/760/2/L31](https://doi.org/10.1088/2041-8205/760/2/L31)
- Burgasser, A. J., McElwain, M. W., & Kirkpatrick, J. D. 2003, *AJ*, 126, 2487, doi: [10.1086/378608](https://doi.org/10.1086/378608)
- Burrows, A., Marley, M., Hubbard, W. B., et al. 1997, *ApJ*, 491, 856, doi: [10.1086/305002](https://doi.org/10.1086/305002)
- Chiu, K., Fan, X., Leggett, S. K., et al. 2006, *AJ*, 131, 2722, doi: [10.1086/501431](https://doi.org/10.1086/501431)

- Clarke, F. J., Hodgkin, S. T., Oppenheimer, B. R., Robertson, J., & Haubois, X. 2008, MNRAS, 386, 2009, doi: [10.1111/j.1365-2966.2008.13135.x](https://doi.org/10.1111/j.1365-2966.2008.13135.x)
- Clarke, F. J., Tinney, C. G., & Covey, K. R. 2002, MNRAS, 332, 361, doi: [10.1046/j.1365-8711.2002.05308.x](https://doi.org/10.1046/j.1365-8711.2002.05308.x)
- Croll, B., Muirhead, P. S., Han, E., et al. 2016, arXiv e-prints, arXiv:1609.03586. <https://arxiv.org/abs/1609.03586>
- Crossfield, I. J. M. 2014, A&A, 566, A130, doi: [10.1051/0004-6361/201423750](https://doi.org/10.1051/0004-6361/201423750)
- Cushing, M. C., Vacca, W. D., & Rayner, J. T. 2004, PASP, 116, 362, doi: [10.1086/382907](https://doi.org/10.1086/382907)
- Cushing, M. C., Roellig, T. L., Marley, M. S., et al. 2006, ApJ, 648, 614, doi: [10.1086/505637](https://doi.org/10.1086/505637)
- Cushing, M. C., Hardegree-Ullman, K. K., Trucks, J. L., et al. 2016, ApJ, 823, 152, doi: [10.3847/0004-637X/823/2/152](https://doi.org/10.3847/0004-637X/823/2/152)
- Cutri, R. M., Skrutskie, M. F., van Dyk, S., et al. 2003, VizieR Online Data Catalog, II/246
- de Kok, R. J., Stam, D. M., & Karalidi, T. 2011, ApJ, 741, 59, doi: [10.1088/0004-637X/741/1/59](https://doi.org/10.1088/0004-637X/741/1/59)
- de Pater, I., Sault, R. J., Butler, B., DeBoer, D., & Wong, M. H. 2016, Science, 352, 1198, doi: [10.1126/science.aaf2210](https://doi.org/10.1126/science.aaf2210)
- Elias, J. H., Joyce, R. R., Liang, M., et al. 2006, in Proc. SPIE, Vol. 6269, Society of Photo-Optical Instrumentation Engineers (SPIE) Conference Series, 62694C, doi: [10.1117/12.671817](https://doi.org/10.1117/12.671817)
- Eriksson, S. C., Janson, M., & Calissendorff, P. 2019, A&A, 629, A145, doi: [10.1051/0004-6361/201935671](https://doi.org/10.1051/0004-6361/201935671)
- Fazio, G. G., Hora, J. L., Allen, L. E., et al. 2004, ApJS, 154, 10, doi: [10.1086/422843](https://doi.org/10.1086/422843)
- Filippazzo, J. C., Rice, E. L., Faherty, J., et al. 2015, ApJ, 810, 158, doi: [10.1088/0004-637X/810/2/158](https://doi.org/10.1088/0004-637X/810/2/158)
- Gagné, J., Lambrides, E., Faherty, J. K., & Simcoe, R. 2015a, Firehose v2.0, Zenodo
- Gagné, J., Faherty, J. K., Cruz, K. L., et al. 2015b, ApJS, 219, 33, doi: [10.1088/0067-0049/219/2/33](https://doi.org/10.1088/0067-0049/219/2/33)

- Gagné, J., Mamajek, E. E., Malo, L., et al. 2018, *ApJ*, 856, 23, doi: [10.3847/1538-4357/aaae09](https://doi.org/10.3847/1538-4357/aaae09)
- Gillon, M., Triaud, A. H. M. J., Jehin, E., et al. 2013, *A&A*, 555, L5, doi: [10.1051/0004-6361/201321620](https://doi.org/10.1051/0004-6361/201321620)
- Girardin, F., Artigau, É., & Doyon, R. 2013, *ApJ*, 767, 61, doi: [10.1088/0004-637X/767/1/61](https://doi.org/10.1088/0004-637X/767/1/61)
- Gizis, J. E., Dettman, K. G., Burgasser, A. J., et al. 2015, *ApJ*, 813, 104, doi: [10.1088/0004-637X/813/2/104](https://doi.org/10.1088/0004-637X/813/2/104)
- Gray, D. F. 1992, *The observation and analysis of stellar photospheres*. (Cambridge University Press). <http://adsabs.harvard.edu/abs/1992oasp.book.....G>
- Grillmair, C. J., Carey, S. J., Stauffer, J. R., & Ingalls, J. G. 2014, in *Proc. SPIE*, Vol. 9143, *Space Telescopes and Instrumentation 2014: Optical, Infrared, and Millimeter Wave*, 914359, doi: [10.1117/12.2057238](https://doi.org/10.1117/12.2057238)
- Grillmair, C. J., Carey, S. J., Stauffer, J. R., et al. 2012, in *Proc. SPIE*, Vol. 8448, *Observatory Operations: Strategies, Processes, and Systems IV*, 84481I, doi: [10.1117/12.927191](https://doi.org/10.1117/12.927191)
- Hallinan, G., Bourke, S., Lane, C., et al. 2007, *ApJ Letters*, 663, L25, doi: [10.1086/519790](https://doi.org/10.1086/519790)
- Hallinan, G., Littlefair, S. P., Cotter, G., et al. 2015, *Nature*, 523, 568, doi: [10.1038/nature14619](https://doi.org/10.1038/nature14619)
- Harding, L. K., Hallinan, G., Boyle, R. P., et al. 2013a, *ApJ*, 779, 101, doi: [10.1088/0004-637X/779/2/101](https://doi.org/10.1088/0004-637X/779/2/101)
- Harding, L. K., Hallinan, G., Konopacky, Q. M., et al. 2013b, *A&A*, 554, A113, doi: [10.1051/0004-6361/201220865](https://doi.org/10.1051/0004-6361/201220865)
- Heinze, A. N., Metchev, S., Apai, D., et al. 2013, *ApJ*, 767, 173, doi: [10.1088/0004-637X/767/2/173](https://doi.org/10.1088/0004-637X/767/2/173)
- Horne, K. 1986, *PASP*, 98, 609, doi: [10.1086/131801](https://doi.org/10.1086/131801)
- James, R. A. 1964, *ApJ*, 140, 552, doi: [10.1086/147949](https://doi.org/10.1086/147949)
- Kao, M. M., Hallinan, G., Pineda, J. S., et al. 2016, *ApJ*, 818, 24, doi: [10.3847/0004-637X/818/1/24](https://doi.org/10.3847/0004-637X/818/1/24)

- Kao, M. M., Hallinan, G., Pineda, J. S., Stevenson, D., & Burgasser, A. 2018, *ApJS*, 237, 25, doi: [10.3847/1538-4365/aac2d5](https://doi.org/10.3847/1538-4365/aac2d5)
- Karalidi, T., Apai, D., Marley, M. S., & Buenzli, E. 2016, *ApJ*, 825, 90, doi: [10.3847/0004-637X/825/2/90](https://doi.org/10.3847/0004-637X/825/2/90)
- Kelson, D. D. 2003, *PASP*, 115, 688, doi: [10.1086/375502](https://doi.org/10.1086/375502)
- Kirkpatrick, J. D., Henry, T. J., & Irwin, M. J. 1997, *AJ*, 113, 1421, doi: [10.1086/118357](https://doi.org/10.1086/118357)
- Kirkpatrick, J. D., Martin, E. C., Smart, R. L., et al. 2019, *ApJS*, 240, 19, doi: [10.3847/1538-4365/aaf6af](https://doi.org/10.3847/1538-4365/aaf6af)
- Koen, C. 2004, *MNRAS*, 354, 378, doi: [10.1111/j.1365-2966.2004.08192.x](https://doi.org/10.1111/j.1365-2966.2004.08192.x)
- . 2005, *MNRAS*, 360, 1132, doi: [10.1111/j.1365-2966.2005.09119.x](https://doi.org/10.1111/j.1365-2966.2005.09119.x)
- Koen, C. 2013, *MNRAS*, 429, 652, doi: [10.1093/mnras/sts370](https://doi.org/10.1093/mnras/sts370)
- Koen, C. 2013, *MNRAS*, 428, 2824, doi: [10.1093/mnras/sts208](https://doi.org/10.1093/mnras/sts208)
- Koen, C., Tanabé, T., Tamura, M., & Kusakabe, N. 2005, *MNRAS*, 362, 727, doi: [10.1111/j.1365-2966.2005.09280.x](https://doi.org/10.1111/j.1365-2966.2005.09280.x)
- Konopacky, Q. M., Ghez, A. M., Fabrycky, D. C., et al. 2012, *ApJ*, 750, 79, doi: [10.1088/0004-637X/750/1/79](https://doi.org/10.1088/0004-637X/750/1/79)
- Krick, J., Ingalls, J., Lowrance, P., et al. 2018, in *Society of Photo-Optical Instrumentation Engineers (SPIE) Conference Series*, Vol. 10698, *Space Telescopes and Instrumentation 2018: Optical, Infrared, and Millimeter Wave*, 106985Y, doi: [10.1117/12.2310185](https://doi.org/10.1117/12.2310185)
- Leggett, S. K., Cushing, M. C., Hardegree-Ullman, K. K., et al. 2016, *ApJ*, 830, 141, doi: [10.3847/0004-637X/830/2/141](https://doi.org/10.3847/0004-637X/830/2/141)
- Lew, B. W. P., Apai, D., Zhou, Y., et al. 2016, *ApJ Letters*, 829, L32, doi: [10.3847/2041-8205/829/2/L32](https://doi.org/10.3847/2041-8205/829/2/L32)
- Lew, B. W. P., Apai, D., Zhou, Y., et al. 2020, *AJ*, 159, 125, doi: [10.3847/1538-3881/ab5f59](https://doi.org/10.3847/1538-3881/ab5f59)
- Liu, M. C., Dupuy, T. J., & Allers, K. N. 2016, *ApJ*, 833, 96, doi: [10.3847/1538-4357/833/1/96](https://doi.org/10.3847/1538-4357/833/1/96)
- Manjavacas, E., Apai, D., Zhou, Y., et al. 2018, *AJ*, 155, 11, doi: [10.3847/1538-3881/aa984f](https://doi.org/10.3847/1538-3881/aa984f)

- Manjavacas, E., Apai, D., Lew, B. W. P., et al. 2019, *ApJ Letters*, 875, L15, doi: [10.3847/2041-8213/ab13b9](https://doi.org/10.3847/2041-8213/ab13b9)
- Marley, M., Saumon, D., Morley, C., & Fortney, J. 2018, *Sonora 2018: Cloud-free, solar composition, solar C/O substellar atmosphere models and spectra*, nc_m+0.0_co1.0_v1.0, Zenodo, doi: [10.5281/zenodo.1309035](https://doi.org/10.5281/zenodo.1309035)
- Marley, M. S., Seager, S., Saumon, D., et al. 2002, *ApJ*, 568, 335, doi: [10.1086/338800](https://doi.org/10.1086/338800)
- Marley, M. S., & Sengupta, S. 2011, *MNRAS*, 417, 2874, doi: [10.1111/j.1365-2966.2011.19448.x](https://doi.org/10.1111/j.1365-2966.2011.19448.x)
- McLean, I. S., McGovern, M. R., Burgasser, A. J., et al. 2003, *ApJ*, 596, 561, doi: [10.1086/377636](https://doi.org/10.1086/377636)
- Ménard, F., Delfosse, X., & Monin, J. L. 2002, *A&A*, 396, L35, doi: [10.1051/0004-6361:20021657](https://doi.org/10.1051/0004-6361:20021657)
- Metchev, S. A., Heinze, A., Apai, D., et al. 2015, *ApJ*, 799, 154, doi: [10.1088/0004-637X/799/2/154](https://doi.org/10.1088/0004-637X/799/2/154)
- Mighell, K. J., Glaccum, W., & Hoffmann, W. 2008, in *Proc. SPIE, Vol. 7010, Space Telescopes and Instrumentation 2008: Optical, Infrared, and Millimeter*, 70102W, doi: [10.1117/12.789801](https://doi.org/10.1117/12.789801)
- Miles-Páez, P. A., Metchev, S. A., Heinze, A., & Apai, D. 2017a, *ApJ*, 840, 83, doi: [10.3847/1538-4357/aa6f11](https://doi.org/10.3847/1538-4357/aa6f11)
- Miles-Páez, P. A., Pallé, E., & Zapatero Osorio, M. R. 2017b, *MNRAS*, 472, 2297, doi: [10.1093/mnras/stx2191](https://doi.org/10.1093/mnras/stx2191)
- Miles-Páez, P. A., Zapatero Osorio, M. R., Pallé, E., & Peña Ramírez, K. 2013, *A&A*, 556, A125, doi: [10.1051/0004-6361/201321851](https://doi.org/10.1051/0004-6361/201321851)
- Miles-Páez, P. A., Zapatero Osorio, M. R., Pallé, E., & Peña Ramírez, K. 2017c, *MNRAS*, 466, 3184, doi: [10.1093/mnras/stw3278](https://doi.org/10.1093/mnras/stw3278)
- Miles-Páez, P. A., Metchev, S., Apai, D., et al. 2019, *ApJ*, 883, 181, doi: [10.3847/1538-4357/ab3d25](https://doi.org/10.3847/1538-4357/ab3d25)
- Millar-Blanchaer, M. A., Girard, J. H., Karalidi, T., et al. 2020, *ApJ*, 894, 42, doi: [10.3847/1538-4357/ab6ef2](https://doi.org/10.3847/1538-4357/ab6ef2)

- Mohanty, S., & Basri, G. 2003, *ApJ*, 583, 451, doi: [10.1086/345097](https://doi.org/10.1086/345097)
- Morales-Calderón, M., Stauffer, J. R., Kirkpatrick, J. D., et al. 2006, *ApJ*, 653, 1454, doi: [10.1086/507866](https://doi.org/10.1086/507866)
- Morley, C. V., Fortney, J. J., Marley, M. S., et al. 2012, *ApJ*, 756, 172, doi: [10.1088/0004-637X/756/2/172](https://doi.org/10.1088/0004-637X/756/2/172)
- Naud, M.-E., Artigau, É., Rowe, J. F., et al. 2017, *AJ*, 154, 138, doi: [10.3847/1538-3881/aa83b7](https://doi.org/10.3847/1538-3881/aa83b7)
- Pineda, J. S., Hallinan, G., & Kao, M. M. 2017, *ApJ*, 846, 75, doi: [10.3847/1538-4357/aa8596](https://doi.org/10.3847/1538-4357/aa8596)
- Press, W. H., Teukolsky, S. A., Vetterling, W. T., & Flannery, B. P. 1992, *Numerical recipes in C. The art of scientific computing* (Cambridge: University Press)
- Radigan, J. 2014, *ApJ*, 797, 120, doi: [10.1088/0004-637X/797/2/120](https://doi.org/10.1088/0004-637X/797/2/120)
- Radigan, J., Jayawardhana, R., Lafrenière, D., et al. 2012, *ApJ*, 750, 105, doi: [10.1088/0004-637X/750/2/105](https://doi.org/10.1088/0004-637X/750/2/105)
- Radigan, J., Lafrenière, D., Jayawardhana, R., & Artigau, E. 2014, *ApJ*, 793, 75, doi: [10.1088/0004-637X/793/2/75](https://doi.org/10.1088/0004-637X/793/2/75)
- Rayner, J. T., Cushing, M. C., & Vacca, W. D. 2009, *ApJS*, 185, 289, doi: [10.1088/0067-0049/185/2/289](https://doi.org/10.1088/0067-0049/185/2/289)
- Reach, W. T., Megeath, S. T., Cohen, M., et al. 2005, *PASP*, 117, 978, doi: [10.1086/432670](https://doi.org/10.1086/432670)
- Reid, I. N., Cruz, K. L., Kirkpatrick, J. D., et al. 2008, *AJ*, 136, 1290, doi: [10.1088/0004-6256/136/3/1290](https://doi.org/10.1088/0004-6256/136/3/1290)
- Reiners, A., & Basri, G. 2006, *AJ*, 131, 1806, doi: [10.1086/500298](https://doi.org/10.1086/500298)
- . 2008, *ApJ*, 684, 1390, doi: [10.1086/590073](https://doi.org/10.1086/590073)
- . 2010, *ApJ*, 710, 924, doi: [10.1088/0004-637X/710/2/924](https://doi.org/10.1088/0004-637X/710/2/924)
- Richey-Yowell, T., Kao, M. M., Pineda, J. S., Shkolnik, E. L., & Hallinan, G. 2020, *ApJ*, 903, 74, doi: [10.3847/1538-4357/abb826](https://doi.org/10.3847/1538-4357/abb826)
- Robinson, T. D., & Marley, M. S. 2014, *ApJ*, 785, 158, doi: [10.1088/0004-637X/785/2/158](https://doi.org/10.1088/0004-637X/785/2/158)

- Route, M., & Wolszczan, A. 2016, *ApJ Letters*, 821, L21, doi: [10.3847/2041-8205/821/2/L21](https://doi.org/10.3847/2041-8205/821/2/L21)
- Saumon, D., & Marley, M. S. 2008, *ApJ*, 689, 1327, doi: [10.1086/592734](https://doi.org/10.1086/592734)
- Scargle, J. D. 1982, *ApJ*, 263, 835, doi: [10.1086/160554](https://doi.org/10.1086/160554)
- Schneider, A. C., Hardegree-Ullman, K. K., Cushing, M. C., Kirkpatrick, J. D., & Shkolnik, E. L. 2018a, *AJ*, 155, 238, doi: [10.3847/1538-3881/aabfc2](https://doi.org/10.3847/1538-3881/aabfc2)
- . 2018b, *AJ*, 155, 238, doi: [10.3847/1538-3881/aabfc2](https://doi.org/10.3847/1538-3881/aabfc2)
- Scholz, A., Kostov, V., Jayawardhana, R., & Mužić, K. 2015, *ApJ Letters*, 809, L29, doi: [10.1088/2041-8205/809/2/L29](https://doi.org/10.1088/2041-8205/809/2/L29)
- Simcoe, R. A., Burgasser, A. J., Bernstein, R. A., et al. 2008, in *Proc. SPIE*, Vol. 7014, Ground-based and Airborne Instrumentation for Astronomy II, 70140U, doi: [10.1117/12.790414](https://doi.org/10.1117/12.790414)
- Simcoe, R. A., Burgasser, A. J., Schechter, P. L., et al. 2013, *PASP*, 125, 270, doi: [10.1086/670241](https://doi.org/10.1086/670241)
- Snellen, I. A. G., Brandl, B. R., de Kok, R. J., et al. 2014, *Nature*, 509, 63, doi: [10.1038/nature13253](https://doi.org/10.1038/nature13253)
- Stephens, D. C., Leggett, S. K., Cushing, M. C., et al. 2009, *ApJ*, 702, 154, doi: [10.1088/0004-637X/702/1/154](https://doi.org/10.1088/0004-637X/702/1/154)
- Stolker, T., Min, M., Stam, D. M., et al. 2017, *A&A*, 607, A42, doi: [10.1051/0004-6361/201730780](https://doi.org/10.1051/0004-6361/201730780)
- Tinney, C. G., & Tolley, A. J. 1999, *MNRAS*, 304, 119, doi: [10.1046/j.1365-8711.1999.02297.x](https://doi.org/10.1046/j.1365-8711.1999.02297.x)
- Tremblin, P., Amundsen, D. S., Mourier, P., et al. 2015, *ApJ Letters*, 804, L17, doi: [10.1088/2041-8205/804/1/L17](https://doi.org/10.1088/2041-8205/804/1/L17)
- Tremblin, P., Phillips, M. W., Emery, A., et al. 2020, *A&A*, 643, A23, doi: [10.1051/0004-6361/202038771](https://doi.org/10.1051/0004-6361/202038771)
- Vacca, W. D., Cushing, M. C., & Rayner, J. T. 2003, *PASP*, 115, 389, doi: [10.1086/346193](https://doi.org/10.1086/346193)
- Vos, J. M., Allers, K. N., Biller, B. A., et al. 2018, *MNRAS*, 474, 1041, doi: [10.1093/mnras/stx2752](https://doi.org/10.1093/mnras/stx2752)

- Vos, J. M., Biller, B. A., Bonavita, M., et al. 2019, MNRAS, 483, 480, doi: [10.1093/mnras/sty3123](https://doi.org/10.1093/mnras/sty3123)
- Vos, J. M., Biller, B. A., Allers, K. N., et al. 2020, AJ, 160, 38, doi: [10.3847/1538-3881/ab9642](https://doi.org/10.3847/1538-3881/ab9642)
- Wall, J. V., & Jenkins, C. R. 2003, Practical Statistics for Astronomers, Vol. 3 (Cambridge University Press), doi: [10.1017/CBO9780511536618](https://doi.org/10.1017/CBO9780511536618)
- Werner, M. W., Roellig, T. L., Low, F. J., et al. 2004, ApJS, 154, 1, doi: [10.1086/422992](https://doi.org/10.1086/422992)
- Williams, P. K. G., & Berger, E. 2015, ApJ, 808, 189, doi: [10.1088/0004-637X/808/2/189](https://doi.org/10.1088/0004-637X/808/2/189)
- Williams, P. K. G., Gizis, J. E., & Berger, E. 2017, ApJ, 834, 117, doi: [10.3847/1538-4357/834/2/117](https://doi.org/10.3847/1538-4357/834/2/117)
- Wilson, P. A., Rajan, A., & Patience, J. 2014, A&A, 566, A111, doi: [10.1051/0004-6361/201322995](https://doi.org/10.1051/0004-6361/201322995)
- Yang, H., Apai, D., Marley, M. S., et al. 2016, ApJ, 826, 8, doi: [10.3847/0004-637X/826/1/8](https://doi.org/10.3847/0004-637X/826/1/8)
- Zapatero Osorio, M. R., Caballero, J. A., & Béjar, V. J. S. 2005, ApJ, 621, 445, doi: [10.1086/427433](https://doi.org/10.1086/427433)
- Zapatero Osorio, M. R., Martín, E. L., Bouy, H., et al. 2006, ApJ, 647, 1405, doi: [10.1086/505484](https://doi.org/10.1086/505484)
- Zhou, Y., Apai, D., Schneider, G. H., Marley, M. S., & Showman, A. P. 2016, ApJ, 818, 176, doi: [10.3847/0004-637X/818/2/176](https://doi.org/10.3847/0004-637X/818/2/176)
- Zhou, Y., Apai, D., Metchev, S., et al. 2018, AJ, 155, 132, doi: [10.3847/1538-3881/aaabbd](https://doi.org/10.3847/1538-3881/aaabbd)
- Zhou, Y., Apai, D., Lew, B. W. P., et al. 2019, AJ, 157, 128, doi: [10.3847/1538-3881/ab037f](https://doi.org/10.3847/1538-3881/ab037f)
- Zhou, Y., Apai, D., Bedin, L. R., et al. 2020, AJ, 159, 140, doi: [10.3847/1538-3881/ab6f65](https://doi.org/10.3847/1538-3881/ab6f65)
- Zuckerman, B. 2019, ApJ, 870, 27, doi: [10.3847/1538-4357/aaee66](https://doi.org/10.3847/1538-4357/aaee66)

Chapter 3

IGRINS Spectroscopy of the T6 Dwarf 2MASS J08173001-6155158: Verification of Water, Methane, and Ammonia Line Lists and a Near-Infrared Spectroscopic Atlas of a Cold Brown Dwarf

3.1 Introduction

Reliable determinations of the effective temperatures, radii, and masses of self-luminous brown dwarfs and giant exoplanets are dependent on accurate modelling of their spectra. However, it is known that the laboratory-based experimental line lists used to generate model spectra are inconsistent with each other and are even missing lines for some molecular species (e.g., [Saumon et al. 2012](#); [Canty et al. 2015](#)). Even the most up-to date spectral models do not completely reproduce observed spectral features in cold brown dwarfs, limiting our ability to constrain their basic properties.

Methane and ammonia are of particular interest for T dwarfs. At the time of their discovery, the distinction between L and T dwarfs was based on whether methane lines were present in their spectra ([Oppenheimer et al., 1995](#); [Geballe et al., 1996](#)). Similarly, ammonia was used to mark the end of the T-sequence and is the distinguishing opacity source of Y dwarfs ([Cushing et al., 2011](#)). However, [Noll et al. \(2000\)](#) showed that the onset of methane absorption actually occurs earlier in the near-infrared spectral sequence, as early as L5, due to overlooked lines in wavelength- and resolution-limited data, and ammonia bands first appear at spectral types as

early as T2 in the mid-infrared (Cushing et al., 2006). In the latest T dwarfs (T8, T9), ammonia becomes a major opacity source (Cushing et al., 2006).

Previous spectroscopic studies of late-T and Y dwarfs with broad wavelength coverage have been limited to $R \sim 6000$ or less, making the identification of specific molecular absorption features difficult. Additionally, older generations of photospheric models have not been able to fit the available data well (e.g., Bochanski et al. 2011; Leggett et al. 2012, 2019; Beichman et al. 2014; Carty et al. 2015; Schneider et al. 2015; Luhman & Esplin 2016; Miles et al. 2020; Tannock et al. 2021).

A current hurdle in characterizing cold brown dwarfs and giant exoplanets are systematic uncertainties in the wavelengths and strengths of absorption lines in theoretical photospheres. Missing lines or inaccurate line lists make detections of molecules and determinations of radial velocities and spins difficult or impossible, especially in low signal-to-noise observations of exoplanet atmospheres. It is therefore necessary to confirm the accuracy of line lists by comparing to high signal-to-noise observations. Isolated brown dwarfs, free from the overwhelming light of a companion star, have atmospheres containing some of the key opacity sources in exoplanets, making them suitable laboratories for testing the accuracy of line lists. Improvements in the atmospheric opacity estimates for cold substellar atmospheres would also be invaluable for the characterization of potentially habitable exoplanets. Methane and ammonia have been suggested as biosignature gases in exoplanet atmospheres (e.g., Léger et al. 1996; Seager et al. 2013). Water, while not a biosignature gas, is also an important signature of habitability and is a major opacity source in brown dwarfs.

We present a high signal-to-noise ($\text{SNR} > 200$) spectrum of a T6 dwarf with unprecedented $R=45,000$ resolution and $1.45\text{--}2.48 \mu\text{m}$ coverage, observed with the Immersion GRating INfrared Spectrometer (IGRINS; Yuk et al. 2010; Park et al. 2014; Mace et al. 2016, 2018) on Gemini South. We study in detail absorption features due to water, methane, ammonia, carbon monoxide, and hydrogen sulfide. Our target, 2MASS J08173001–6155158 (also known as DENIS J081730.0-615520; herein 2M0817) was discovered by Artigau et al. (2010) through a photometric cross match between the Two Micron All Sky Survey (2MASS) and the DEep Near-Infrared Survey of the Southern sky (DENIS) point-source catalogues, and spectroscopically identified as a T6 dwarf. It is at a heliocentric distance of only 5.2211 ± 0.0165 pc (Gaia Collaboration, 2018), and is one of the brightest late-T dwarfs (K -band magnitude 13.52; Cutri et al. 2003). Radigan et al. (2014) find a rotation period of 2.8 ± 0.2 h from ground-based J -band observations for 2M0817, spanning four hours.

3.2 Spectroscopy with IGRINS on Gemini South

We observed 2M0817 with IGRINS on Gemini South under Gemini program ID GS-2018A-Q-304 (PI: M. Tannock). IGRINS is a high-resolution ($R = \lambda/\Delta\lambda = 45,000$), cross-dispersed spectrograph that simultaneously covers the H and K bands from 1.45 to 2.48 μm .

Observations took place over four nights in April and May 2018 while IGRINS was on Gemini South. The slit was oriented at a position angle of 90 degrees (east-west), and exposures were taken along an ABBA dither pattern. We observed an A0 V star before or after each observation of the target. We summarize these observations in Table 3.1.

3.2.1 Data Reduction

The data were reduced with the IGRINS Pipeline Package (PLP; Lee & Gullikson 2016) at each epoch individually. The PLP produces telluric-corrected, wavelength-calibrated fluxes and the signal-to-noise ratio (SNR) for each point in the spectrum.

We used a custom IDL code to combine the individual spectra. We first corrected for the barycentric velocity at each epoch. We then processed the H and K bands separately: we normalized the flux to peak at unity in each of the H and K bands, and then resampled the data to identical wavelength values. We computed the weights from the SNR values computed by the PLP ($w_i = (\text{SNR}_i/f_i)^2$, where f_i is the flux at each epoch) and computed the weighted average ($\bar{f} = \sum_{i=1}^N (f_i w_i / w_t)$ where w_t is the sum of the weights for N epochs) and uncertainties ($\sigma = w_t^{1/2}$) across all epochs.

We found that in some cases, the IGRINS PLP produced fluxes of ~ 0 , but with a disproportionately high SNR value, resulting in a large weight. This produced large downward spikes in the weighted average spectrum. We obtained the highest SNR combined spectrum free of such spikes when we combined the three highest SNR epochs: 2018 May 22 (both sequences) and 2018 May 23. In Figure 3.1 we show the data from each epoch in a region at the centre of the H band. Three epochs stand out with their higher SNR. We performed the remainder of our analysis with the weighted average of these three epochs. Our final combined spectrum (Figure 3.2) had a signal to noise of ~ 300 at the peak of the H band and ~ 200 at the peak of the K band.

There is some overlap between the diffraction orders in the spectrum (see Table 3.2 for a list of the order numbers, m , and their wavelength coverage). For our analysis, we analyzed each order individually. The instrument blaze profile results in the short-wavelength ends of the order having lower SNR than the long-wavelength ends (see the bottom panel of Figure 3.1). We also observed an instrumental effect resulting in an upward curving in the residuals when compared to models at the ends of the orders. To minimize this effect and analyze the highest

Table 3.1. Gemini/IGRINS spectroscopic observations of 2MASS J08173001-6155158

Date Observed	Exposure Time (s)	Exposure Sequence	Target Airmass	Telluric		H-band SNR (at 1.589 μm)	K-band SNR (at 2.101 μm)	FWHM of the Trace in the H band ($''$)
				AOV Standard	Airmass			
2018 Apr 5	1200	AB	1.18-1.20	HIP 40621	1.14	85	44	0.9
2018 Apr 5	600	ABBA	1.20-1.25	HIP 35393	1.28	63	34	0.9
2018 May 7	600	ABBA	1.22-1.28	HIP 36489	1.31	56	33	0.8
2018 May 22	518	ABBAAB	1.27-1.37	HIP 40621	1.36	174	112	0.6
2018 May 22	518	ABBAAB	1.40-1.58	HIP 40621	1.58	181	113	0.6
2018 May 23	518	ABBAAB	1.26-1.37	HIP 40621	1.35	184	119	0.6

Note. — These observations were taken under Gemini program ID GS-2018A-Q-304 (PI: M. Tannock). The given SNR values are for the final, combined spectra. The FWHM of the trace includes both atmospheric seeing and effects from telescope and instrument optics. Typical atmospheric seeing at Gemini South is 0.5''.

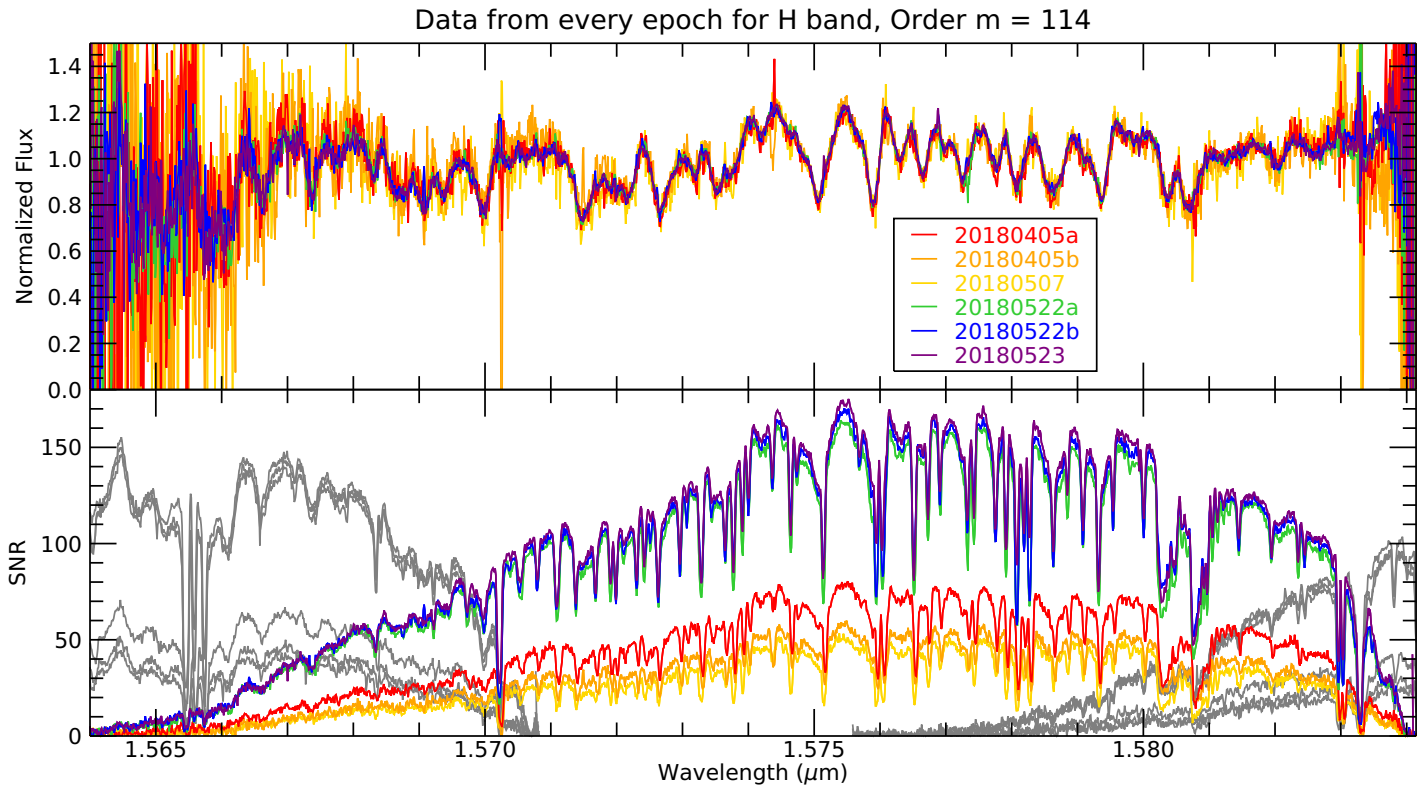


Figure 3.1: A sample order near the centre of the H band, showing spectra from each of the six observing epochs. The normalized flux is shown in the top panel, and the deep absorption features in this order are due to H_2O . The SNR is shown in the bottom panel. The SNR of the neighbouring orders are also shown in grey, to show that IGRINS has good SNR coverage at all wavelengths. The IGRINS instrument transmission profile (blaze) is clearly imprinted on the SNR spectrum, and is the reason for the fall-off in SNR at the edges of the order. The three highest-SNR spectra, obtained on 2018 May 22 and 23, were combined to create the final spectrum shown in Figure 3.2.

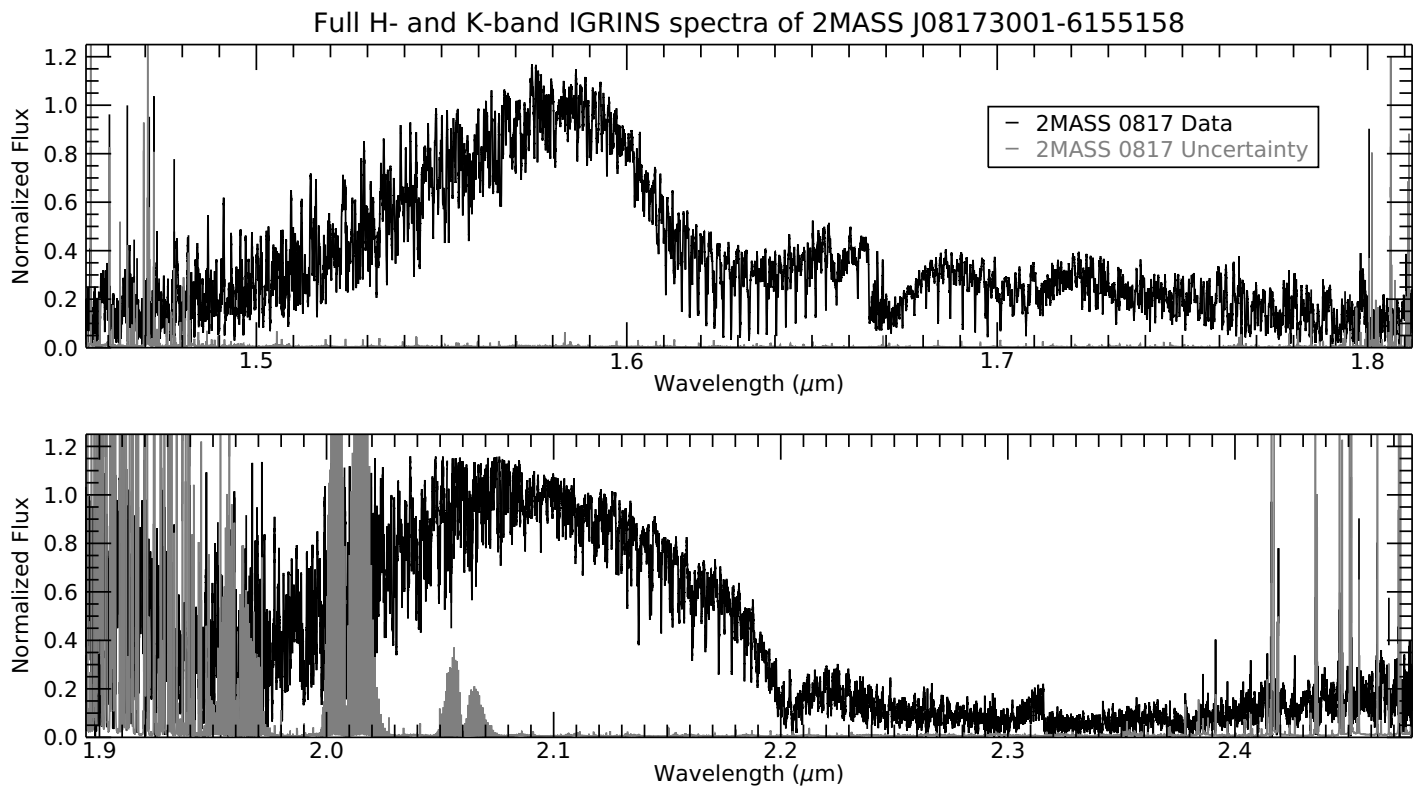


Figure 3.2: The full H - and K -band IGRINS spectra of 2MASS J08173001–6155158 with epochs combined and the orders stitched together. This figure does not include the quadratic correction described in Section 3.3.1. These data appear noisy but in fact have $\text{SNR} \approx 300$ at the peak of the H -band spectrum and $\text{SNR} \approx 200$ at the K -band peak. The apparent noise spikes are all absorption features, and can be seen in detail in the full set of figures in Appendix 3.7.

SNR regions of the data, we removed the ends of each order, leaving ~ 1 – 2 nm overlap between orders. We additionally divided out a quadratic function which minimized the chi square statistic (χ^2) between the data and a given model to further remove this instrumental effect (see Section 3.3). In each region of overlap, we averaged the fluxes from the two orders. We show the complete spectra with the orders stitched together in Figure 3.2.

3.2.2 Confirmation of Wavelength Calibration and Masking of Telluric Lines

We verified our wavelength calibration by comparing the telluric lines in the spectra of our A0V standard stars to an Earth’s transmittance spectrum from the Planetary Spectrum Generator (PSG; Villanueva et al. 2018). We used the Earth’s Transmittance template with the longitude,

latitude, and altitude of the Gemini South Observatory to generate spectra over the wavelength coverage of IGRINS at 1.5 times the resolution of IGRINS. We then compared the positions of the minima of the telluric lines in the PSG and in our data. We find an average offset of less than half an IGRINS pixel (0.110 \AA at the centre of the H band), confirming our wavelength calibration.

We found that masking strong telluric features improved the precision of our model photosphere fits (Section 3.3). To prepare our data for comparisons to model spectra, we masked out telluric absorption lines with greater than 35% absorption strengths in the PSG Earth transmittance spectrum. This threshold is shown as a horizontal dashed line in Figures 3.13 and 3.14. We also masked out wavelengths with strong OH emission features. These telluric features were otherwise found to drive the χ^2 values.

3.3 Model Fitting and Parameter Determination

We compared our observed spectra to the models of Allard et al. (2012, 2014; hereafter, BT-Settl), Morley et al. (2012; hereafter, Morley), Marley et al. (2021; hereafter, Sonora Bobcat), and an alternative version of the Sonora Bobcat models with updated molecular line lists Hood et al. (in prep.; hereafter, Bobcat Alternative A). The BT-Settl models are based on the PHOENIX code (Allard & Hauschildt, 1995; Hauschildt et al., 1999). The latter three model sets are all based on the same 1D radiative-convective equilibrium model atmosphere code (e.g., Marley et al. 1996; Fortney et al. 2008; Marley & Robinson 2015). The Morley models include the effect of clouds that may be relevant for T dwarf atmospheres by applying the Ackerman & Marley (2001) cloud model. In contrast, the Sonora Bobcat models assume a cloud-free atmosphere. In addition, the Sonora Bobcat models include post-2012 updates to the gas opacity database, described in Freedman et al. (2014), Lupu et al. (2014), and Marley et al. (2021). The Bobcat Alternative A models are thermal emission spectra generated from the Sonora Bobcat atmospheric structures with the code described in the Appendix of Morley et al. (2015). Only a selection of opacities are included, which dominate at near infrared wavelengths: H_2O , CH_4 , CO , NH_3 , H_2S , and collision-induced opacity of $\text{H}_2\text{-H}_2$, $\text{H}_2\text{-He}$, and $\text{H}_2\text{-CH}_4$. The opacity data for these sources are the same as the Sonora Bobcat models, with the notable exceptions of updated H_2O (Polyansky et al., 2018), CH_4 (Hargreaves et al., 2020), NH_3 (Coles et al., 2019) line lists.

3.3.1 Fitting of Photospheric Models

The models are provided on fixed grids of effective temperature (T_{eff}) and surface gravity ($\log g$), and we do not interpolate to intermediate values. We allowed our model fitting to explore T_{eff} grids between 700 K and 1300 K (the expected range of 900–1100 K in T_{eff} for a T6 dwarf, ± 200 K; [Filippazzo et al. 2015](#)), in steps of 50 K or 100 K, depending on the model family. For $\log g$ we explored grids between $\log g = 4.0$ and 5.5, in steps of 0.5 dex for all model families except the Sonora Bobcat models, which are in steps of 0.25 dex. The Morley models also have a sedimentation efficiency (f_{sed}) parameter on a grid from 2 to 5 in integer steps.

We also explored a radial velocity (RV) grid by applying a Doppler shift to the wavelength of the models. We also expect that our observed spectrum will have significant rotational broadening from its known axial rotation. We explored a grid of projected rotation velocities ($v \sin i$), by simulating rotational broadening in the model spectra. We convolved the model spectra with the standard rotation kernel from [Gray \(1992\)](#), as described in [Tannock et al. \(2021\)](#). For both RV and $v \sin i$ we first explored coarse grids with steps of 2 km s^{-1} over a broad range of values, then narrowed our grid and repeated the fitting with finer steps of 0.1 km s^{-1} .

For every model available at every point on these grids, we calculated the χ^2 statistic to determine the best fitting family of models. In [Tannock et al. \(2021\)](#) we included a flux zero-point offset as a free parameter added to the data in order to correct for instrumental effects and minimize the χ^2 statistic. We include the same correction here, and after our initial analysis found that the residuals exhibited a curve over each order, implying an additional unaccounted for instrumental effect. Thus we have included a quadratic correction for the data as well.

Following a similar process to [Suárez et al. \(2021\)](#), we designed a “goodness of fit” parameter G :

$$G = \sum_{i=1}^N \left(\frac{(O_i + d) - (a\lambda_i^2 + b\lambda_i + c)M_i}{\sigma_i} \right)^2 \quad (3.1)$$

where O_i is the observed flux, M_i is the flux of the model, σ_i is the uncertainty of the data, and λ_i is the wavelength of the corresponding data point. The coefficients of the quadratic correction are a , b , and c , and the additive flux zero-point is d . We set the partial derivatives of G to zero and solve the resulting system of equations to find the values of a , b , c , and d . We determine these parameters for every model on the model grid individually. We multiply the model by the quadratic correction in order to simplify solving the system of equations. We later divide the data by this quadratic, in order to present data that are free of instrumental systematics, rather than models that have been “bent” to fit these systematics.

Our final χ^2 statistic is given by:

$$\chi^2 = \sum_{i=1}^N \left(\frac{[(O_i + d)/(a\lambda^2 + b\lambda + c)] - M_i}{\sigma_i} \right)^2. \quad (3.2)$$

To account for uncertainty in the flux of the models, we identified the best-fit order of the entire spectrum (order $m = 85$ of the K band for the Bobcat Alternative A model) and determined a constant to be added to the uncertainty to give a reduced χ^2 statistic of 1.0 in that order. This value was then added to the uncertainty in every order. We used the same value in every order to represent the uncertainty on the model to allow for a comparison between orders. The total uncertainty, including this constant, is shown in grey in Figure 3.3 and all following figures, including the Appendix. The total uncertainty is small in most orders, but we believe this uncertainty to be accurate based on this χ^2 statistic analysis.

3.3.2 Determination of Physical Parameters

We show the results of the model fitting across all orders for all model families in Figures 3.3 and 3.4. In the top panel, a Bobcat Alternative A model is used to separate the contribution of each molecular species, in order to identify the dominant molecule or molecules in each order. These “single-molecule models” include a single molecule (e.g., water, methane), plus collision-induced absorption from molecular hydrogen and helium. To help identify particular features and molecules, a panel like this is included at the top of almost all of our figures.

We find that the Bobcat Alternative A models with the updated line lists provide the best fits to the data. These models are the most consistent across all orders, and give the smallest uncertainty on the measured parameters. Overall, all models do fairly well in regions dominated by water, while fits are poor in regions dominated by methane. The goodness of the fits under each molecule will be explored further in Section 3.4.

We adopt the values given by the Bobcat Alternative A models, and present the weighted average of each parameter across all H and K band orders in Table 3.3. As described in Tannock et al. (2021), we compute the weighted average and the unbiased weighted sample standard deviation, where the weight is $e^{-\chi^2_{\text{reduced}}}$, so that the better fits and more reliable orders are more heavily weighted. The values given in Figures 3.3 and 3.4 are computed in the same way, but for each order separately.

For the remainder of our analysis, we will focus on the results of the Bobcat Alternative A models, unless otherwise stated. We show the best fitting Bobcat Alternative A models for all orders of the H and K bands in Figures 3.13 and 3.14, and in the following sections we highlight a few notable orders and regions.

Table 3.2. Wavelengths of the IGRINS orders and the major molecular absorbers

Order Name	Wavelength Coverage (μm)	Major Absorbers	Order Name	Wavelength Coverage (μm)	Major Absorbers
<i>H</i> 124	1.454–1.460	H ₂ O	<i>K</i> 94	1.894–1.910	H ₂ O
<i>H</i> 123	1.459–1.470	H ₂ O	<i>K</i> 93	1.909–1.930	H ₂ O
<i>H</i> 122	1.469–1.483	H ₂ O	<i>K</i> 92	1.929–1.950	H ₂ O
<i>H</i> 121	1.482–1.494	H ₂ O	<i>K</i> 91	1.949–1.972	H ₂ O, NH ₃
<i>H</i> 120	1.493–1.506	H ₂ O	<i>K</i> 90	1.971–1.993	H ₂ O, NH ₃
<i>H</i> 119	1.504–1.519	H ₂ O, NH ₃	<i>K</i> 89	1.992–2.015	H ₂ O, NH ₃
<i>H</i> 118	1.517–1.531	H ₂ O	<i>K</i> 88	2.014–2.038	H ₂ O, NH ₃
<i>H</i> 117	1.529–1.543	H ₂ O	<i>K</i> 87	2.037–2.061	H ₂ O, NH ₃
<i>H</i> 116	1.541–1.556	H ₂ O	<i>K</i> 86	2.060–2.085	H ₂ O, CH ₄ , NH ₃
<i>H</i> 115	1.554–1.569	H ₂ O, CO	<i>K</i> 85	2.084–2.109	H ₂ O, CH ₄
<i>H</i> 114	1.567–1.583	H ₂ O	<i>K</i> 84	2.108–2.134	H ₂ O, CH ₄
<i>H</i> 113	1.581–1.596	H ₂ O, CH ₄ , H ₂ S	<i>K</i> 83	2.133–2.159	H ₂ O, CH ₄
<i>H</i> 112	1.594–1.610	H ₂ O, CH ₄	<i>K</i> 82	2.158–2.185	CH ₄
<i>H</i> 111	1.608–1.624	H ₂ O, CH ₄	<i>K</i> 81	2.184–2.212	CH ₄ , NH ₃
<i>H</i> 110	1.622–1.639	H ₂ O, CH ₄	<i>K</i> 80	2.211–2.239	CH ₄
<i>H</i> 109	1.637–1.653	H ₂ O, CH ₄	<i>K</i> 79	2.238–2.267	CH ₄
<i>H</i> 108	1.651–1.668	H ₂ O, CH ₄	<i>K</i> 78	2.266–2.295	H ₂ O, CH ₄
<i>H</i> 107	1.666–1.683	H ₂ O, CH ₄	<i>K</i> 77	2.294–2.326	H ₂ O, CH ₄ , CO
<i>H</i> 106	1.681–1.699	H ₂ O, CH ₄	<i>K</i> 76	2.325–2.355	H ₂ O, CH ₄ , CO
<i>H</i> 105	1.697–1.715	H ₂ O, CH ₄	<i>K</i> 75	2.354–2.383	H ₂ O, CH ₄ , CO
<i>H</i> 104	1.713–1.730	H ₂ O, CH ₄	<i>K</i> 74	2.389–2.414	H ₂ O, CH ₄ , CO
<i>H</i> 103	1.728–1.747	H ₂ O, CH ₄	<i>K</i> 73	2.420–2.445	H ₂ O, CH ₄ , CO
<i>H</i> 102	1.745–1.764	H ₂ O, CH ₄	<i>K</i> 72	2.452–2.478	H ₂ O, CH ₄
<i>H</i> 101	1.762–1.781	H ₂ O, CH ₄			
<i>H</i> 100	1.779–1.798	H ₂ O, CH ₄			
<i>H</i> 99	1.797–1.812	H ₂ O, CH ₄			

Note. — Diffraction order numbers, m , were extrapolated from [Stahl et al. \(2021\)](#).

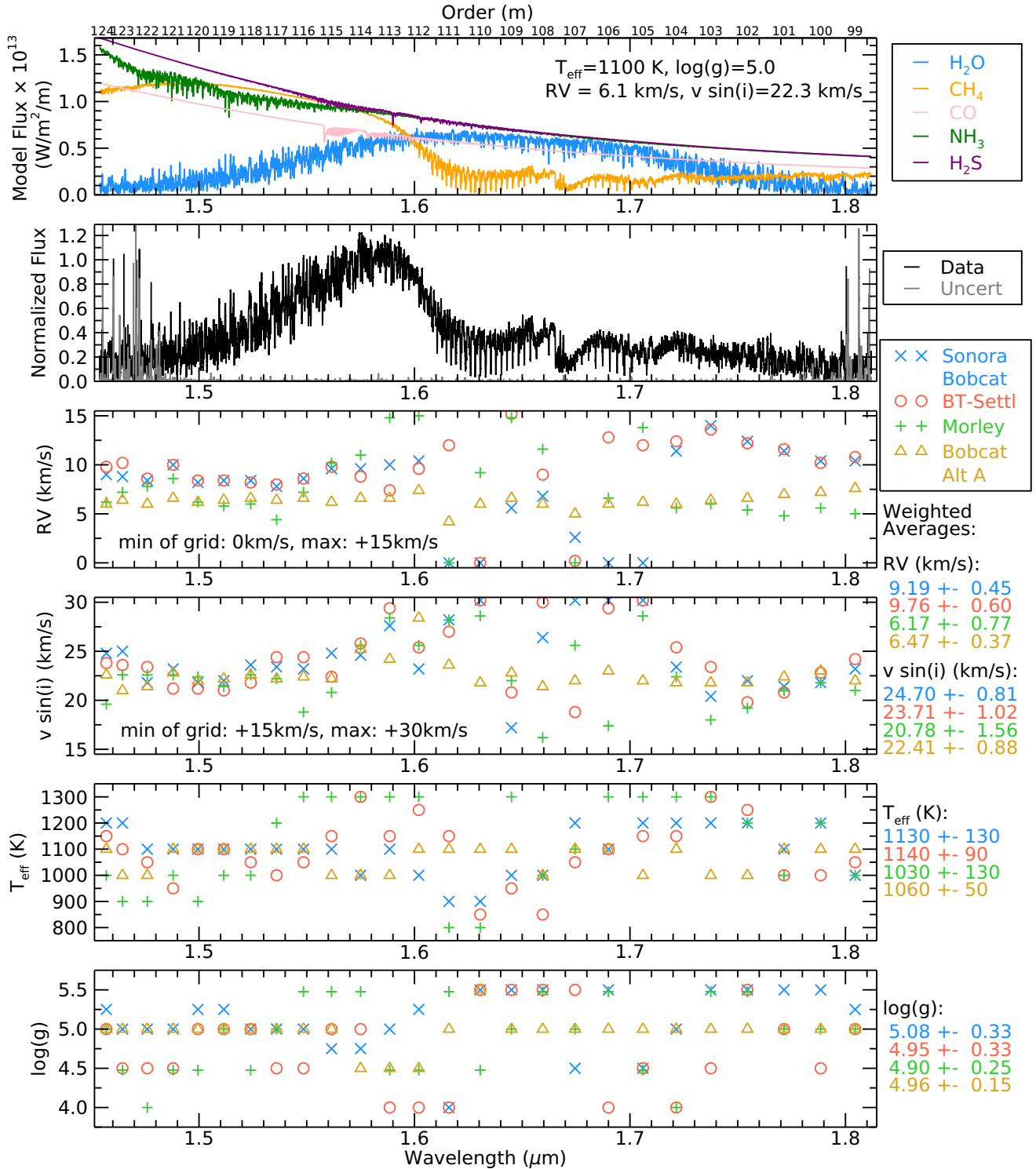


Figure 3.3: Results of the model fitting for the H band. Top panel: The spectra of each major molecule with collision-induced absorption from molecular hydrogen and helium included. The Model Flux is what would be measured at the surface of the object. The models shown in this panel have $T_{\text{eff}} = 1100 \text{ K}$, $\log g = 5.0$, $v \sin i = 22.3 \text{ km s}^{-1}$, and $RV = 6.1 \text{ km s}^{-1}$, and are also matched to the resolution of the IGRINS data. The IGRINS order names are given along the top horizontal axis. Second panel from the top: The full H -band IGRINS spectrum, with the orders stitched together. Bottom four panels: The parameters of the best-fit model for each order, from each family of models. From top to bottom the parameters are: RV , $v \sin i$, T_{eff} , and $\log g$. The weighted average of each parameter is given on the right side of the figure. In some cases the best-fitting models are at the maximum and minimum values of the allowed grid, which indicates that these models produce inadequate fits in the particular order. These values are still included in the weighted mean, but have very little χ^2 weight assigned to them due to their large χ^2 statistics.

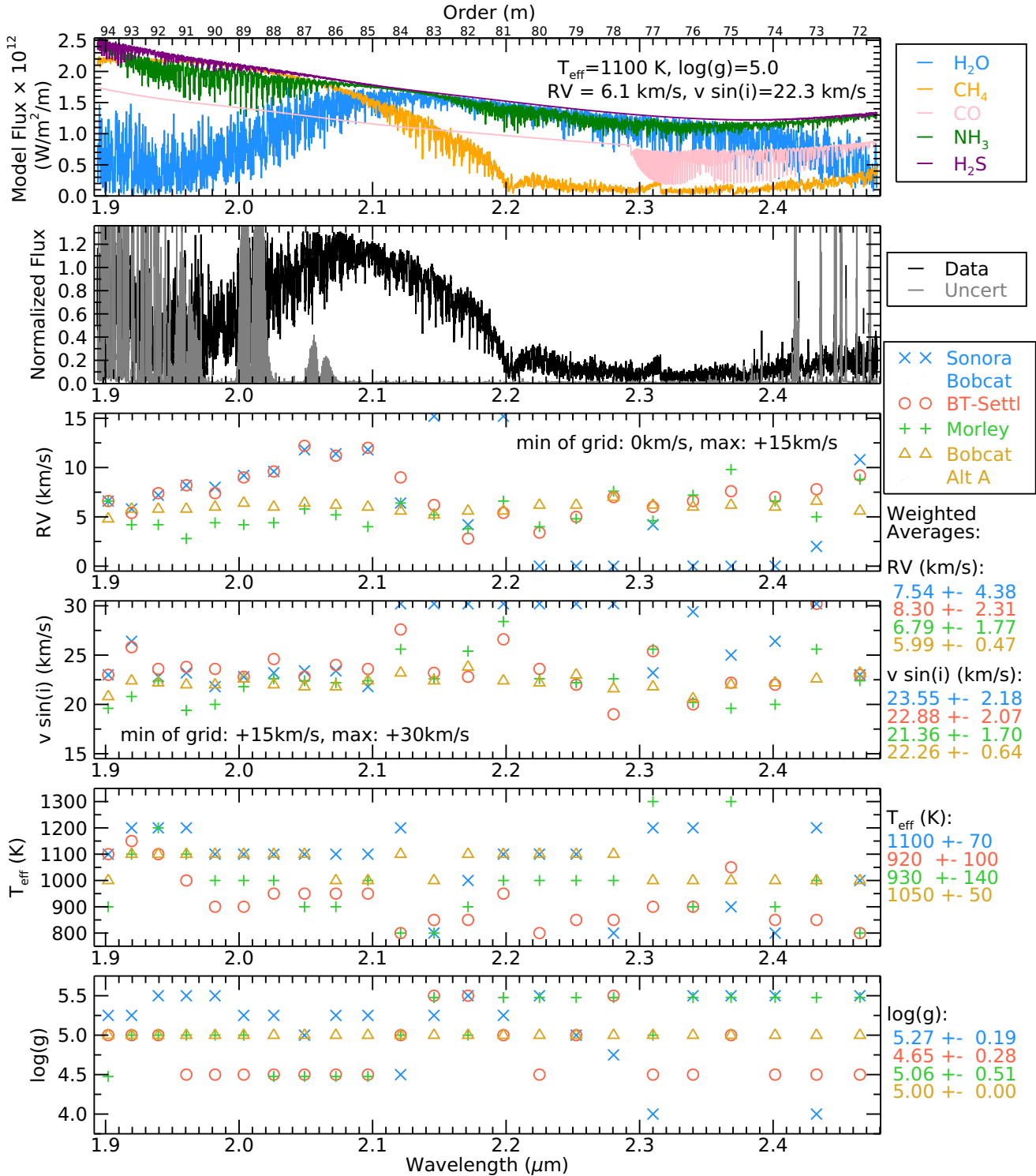


Figure 3.4: The same as Figure 3.3, but for the K band. The $\log g$ value is extremely consistent for the Bobcat Alternative A models, with $\log g=5.0$ in every order of the K band. The standard deviation on this weighted average is therefore zero (see Section 3.3.2 for details on this calculation). In Table 3.3 we compute the weighted average and standard deviation based on both the H and K bands, so the standard deviation is non-zero for the final adopted value.

Table 3.3. Physical parameters of 2MASS J08173001–6155158

Property	Value
Spectral Type	T6 ^a
Effective temperature (T_{eff})	1050 ± 50 K
Surface gravity ($\log g$)	5.0 ± 0.1
Projected rotation velocity ($v \sin i$)	22.3 ± 0.7 km s ⁻¹
Radial velocity (RV)	6.1 ± 0.5 km s ⁻¹

Note. — Parameters estimated from the spectra presented in this paper are based on all H and K band orders.

^a[Artigau et al. \(2010\)](#)

3.4 Molecule-by-Molecule Analysis of the Model Spectra

In this section we assess the quality of the fits from each family of models. We examine the parameters determined for each region of the spectrum and what the dominant absorbers are in each region. Water (H_2O) and methane (CH_4) are the most abundant absorbers in late-T dwarf spectra ([Burgasser et al., 2006](#)). Carbon monoxide (CO) and ammonia (NH_3) also play a major role, and hydrogen sulfide (H_2S) is the next most abundant absorber. The references for the line lists of the major molecules used in each family of models are listed in Table 3.4. As 2M0817 is a fairly rapid rotator ($v \sin i = 22.3 \pm 0.7$ km s⁻¹; Table 3.3), we see that most lines are in fact blends of the dominant absorbers, most often H_2O and CH_4 .

In Figure 3.5 we show order $m = 85$ of the K band: the order where the models most accurately represent the data. The dominant absorbers in this order are H_2O , and CH_4 . The Bobcat Alternative A model provides the best fit, and the residuals for this model are very flat. The other models also do a fair job in matching the major features. For comparison, in Figure 3.6, we show order $m = 111$ of the H band: one of the orders where all models provide poor fits. The major absorber in this order is CH_4 . We see that the locations of the strongest CH_4 features are matched in the Bobcat Alternative A model, which has the most up-to-date CH_4 line list (Table 3.4). In the following sections, we discuss each molecular absorber separately.

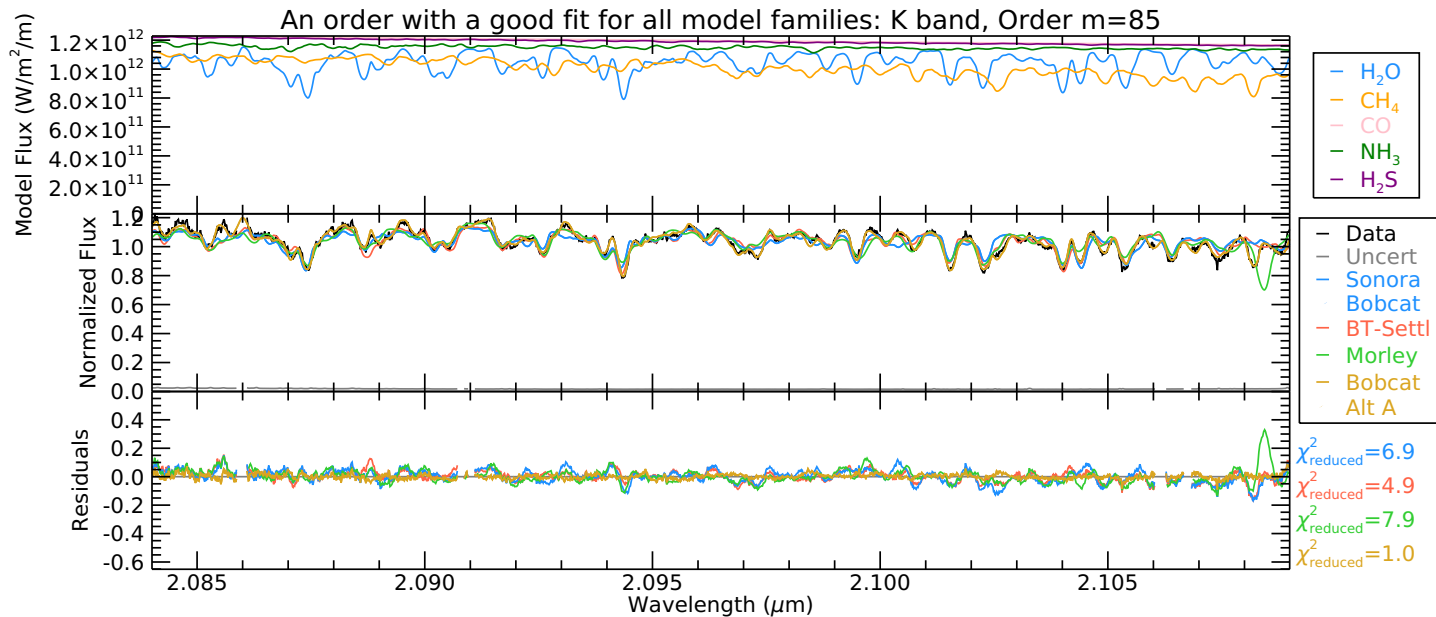


Figure 3.5: In order $m = 85$ of the K band all models are very well matched to the data. The dominant absorbers in this region are H_2O and CH_4 . The top panel shows the Bobcat Alternative A model spectra including opacity from one major molecule at a time, in addition to H_2/He collision-induced absorption. The middle panel shows the IGRINS data (black; uncertainty shown in grey) with the best fitting models from each model family. The Bobcat Alternative A model spectra in the top panel have the same T_{eff} and $\log g$ values as the best fitting Bobcat Alternative A model, are broadened to the same $\nu \sin i$, and have the same RV shift applied. The bottom panel shows the residuals (data - model) on the same vertical scale as the middle panel, with the same colour scheme. The data and residuals contain gaps in the plot where strong telluric lines have been masked out. The reduced chi square statistics (χ^2_{reduced}) for each model are also shown.

Table 3.4. Literature references for the line lists of each model photosphere family

Molecule	Bobcat Alternative A (Hood et al., in prep.)	Sonora Bobcat (Marley et al., 2021)	Morley (Morley et al., 2012)	BT-Settl (Allard et al., 2012, 2014)
H ₂ O	ExoMol/POKAZATEL (Polyan- sky et al., 2018); BT2 (Barber et al., 2006)	Tennyson & Yurchenko (2018); BT2 (Barber et al., 2006)	Partridge & Schwenke (1997); HI- TRAN'08 (Rothman et al., 2009)	BT2 (Barber et al., 2006)
CH ₄	HITEMP (Hargreaves et al., 2020)	Yurchenko et al. (2013); Exo- mol/10to10 (Yurchenko & Ten- nyson, 2014); Spherical Top Data System (Wenger & Champion, 1998)	Spherical Top Data System (Wenger & Champion, 1998); HITRAN'08 (Rothman et al., 2009); Strong et al. (1993)	Spherical Top Data System (Wenger & Champion, 1998)
CO	HITEMP 2010 (Rothman et al., 2010; Li et al. (2015)	HITEMP 2010 (Rothman et al., 2010; Li et al. (2015)	Goorvitch (1994); R. Tipping (1993, private communication); HITRAN'08 (Rothman et al., 2009)	Goorvitch (1994)
NH ₃	ExoMol/CoYuTe (Coles et al., 2019)	BYTe (Yurchenko et al., 2011)	BYTe (Yurchenko et al., 2011)	Sharp & Burrows (2007)
H ₂ S	ExoMol (Tennyson & Yurchenko, 2012); Azzam et al. (2015); HI- TRAN 2012 (Rothman et al., 2013)	ExoMol (Tennyson & Yurchenko, 2012); Azzam et al. (2015); HI- TRAN 2012 (Rothman et al., 2013)	R. Wattson (1996, private commu- nication); HITRAN'08 (Rothman 2005) et al., 2009)	HITRAN 2004 (Rothman et al., 2005)

Note. — For information about specific isotopologues, line widths, and how these sources are combined for each family of models please see the original works listed in the column headers.

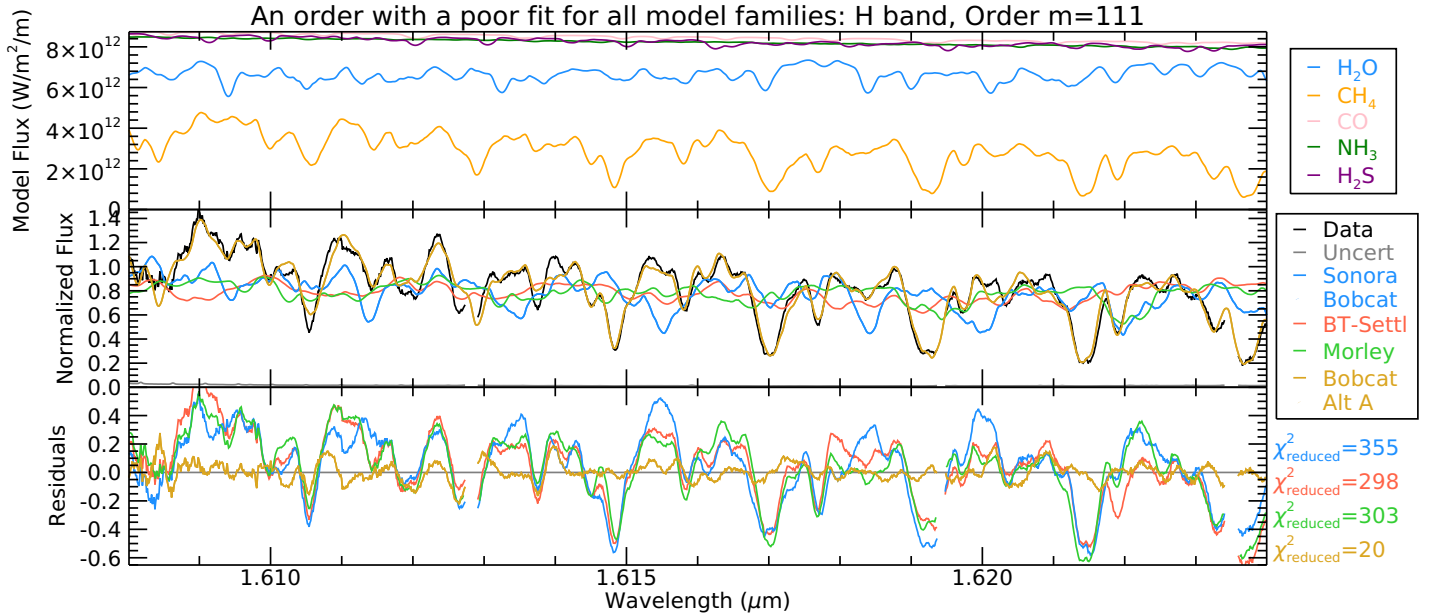


Figure 3.6: The same layout as Figure 3.5, but now showing order $m = 111$ of the H band, an order with a poor fit. The dominant absorber in this order is CH_4 . The most up-to-date line lists for CH_4 (Hargreaves et al. 2020, used in the Bobcat Alternative A model) provide accurate wavelengths for the deepest lines, but the weaker features in the continuum (likely CH_4 blended with H_2O) are poorly-fit.

3.4.1 Water

The water-dominated regions of the spectrum provide the most consistent results from fitting models to spectra across all model families (Figures 3.3 and 3.4). The short-wavelength end of the H band (1.454–1.580 μm) gives consistent results for each model family, and across the various families. The long-wavelength end of the H band (1.750–1.812 μm) and the short-wavelength end of the K band (1.894–2.100 μm) give consistent results within each family of models, but not necessarily across the various model families.

We note that the Sonora Bobcat and BT-Settl models give higher estimates of the RV, and there is a trend in RV where the RV increases with wavelength (the models are increasingly blue-shifted) in the short-wavelength end of the K band (1.894–2.060 μm ; Figure 3.4) for these two models. NH_3 is also an important absorber in this region but is likely not responsible for this trend in RV because Sonora Bobcat shares the same line lists for ammonia as the Morley models (Yurchenko et al., 2011; BYTe), and the Morley models do not show this trend. The behaviour for the BT-Settl models indicates that the BT2 (Barber et al., 2006) H_2O line lists, when used alone, are unreliable for RV determinations in this wavelength region. The similar behaviour from Sonora Bobcat indicates that BYTe (Yurchenko et al., 2011), supplemented with isotopologues from BT2, is also unreliable. The Bobcat Alternative

A models use ExoMol/POKAZATEL (Polyansky et al., 2018) as their main H₂O line list, and also use isotopologue data from BT2. However for this model, we obtain very consistent RV measurements in this wavelength region. The improved accuracy of ExoMol/POKAZATEL line lists appear to make up for any discrepancies in BT2. The HITRAN'08 (Rothman et al., 2009) and Partridge & Schwenke (1997) line lists used in the Morley models also give more self-consistent estimates of RV in this region.

Overall we consider water, specifically for the line list used in the Bobcat Alternative A models (ExoMol/POKAZATEL), to be the most reliable molecule for determining the physical parameters of cold brown dwarfs, producing values that we trust.

3.4.2 Methane

As seen in Figures 3.3 and 3.4, there is much greater variation in the parameters estimated in the methane-dominated regions (1.60–1.73 μm in the *H* band and 2.11–2.40 μm in the *K* band) compared to the water-dominated regions. The $v \sin i$ values are particularly discrepant in the methane-dominated regions, and we also see that where the dominant absorber switches from water to methane at the peaks of both the *H* and *K* bands the spectra are fairly featureless, and therefore not very sensitive to $v \sin i$.

Each family of models uses a different set of line lists for CH₄, though there is some overlap between the Sonora Bobcat, Morley, and BT-Settl models which use multiple sources for their CH₄ line lists (Table 3.4). Uncertainty has been reported for CH₄ band positions previously: Canty et al. (2015) report offsets between the absorption features in their observed data and the peaks of CH₄ opacity from the Exomol/10to10 line list (Yurchenko & Tennyson, 2014) between 1.615 and 1.710 μm .

In Figure 3.7 we show a Sonora Bobcat model and a Bobcat Alternative A model with identical physical parameters for an order in the methane region of the *H* band (order $m = 111$ of the *H* band, 1.608–1.624 μm). The CH₄ lines used in the Sonora Bobcat models (the same as examined by Canty et al. 2015; Table 3.4) do not match the data well, and appear to have a stretch, or misalignment, across this order compared to the updated Bobcat Alternative A model. The stretch in this order worsens further away from the 1.6355 μm feature, which has the best alignment at the given RV. Using this feature as a zero point, we find that the offset in the seven deepest absorption features of this order are misaligned by $\sim 3.5\%$ per unit wavelength. Both models also poorly fit the weaker lines and the continuum in this region.

Radial velocities estimated by the Sonora Bobcat models are particularly discrepant in the methane-dominated regions, due to these inaccurate line positions. We find significant improvement from the line lists used in the Bobcat Alternative A models (HITEMP, Hargreaves

et al. 2020) over older models in regions dominated by CH_4 , in particular in the H band. However, the regions dominated by CH_4 , even in the Bobcat Alternative A models, still have the most variation in the estimates of the physical parameters. We summarize these regions in Table 3.5, noted as “ CH_4 regions.” Models using older CH_4 line lists should therefore be used with caution.

Recent theoretical line lists are far more complete than the previously-used laboratory-measured line lists, which are designed to have very accurate line positions but capture fewer lines due to the limits on resolution in laboratory experiments. Therefore, theoretical line lists should improve accuracy in regions of the spectrum with weaker bands present, if those bands were unresolved in the laboratory lists. A recent improvement in the available line lists has been the combinations of theoretical line lists with laboratory measurements (e.g., Hargreaves et al. 2020). Such combination lists provide the best of both worlds, as we show here, where we find a dramatic improvement to high resolution spectroscopic fits.

In high-dispersion spectroscopic observations of exoplanets, where the planet itself cannot be spatially resolved, cross-correlation is a powerful technique for detecting and characterizing the planet. In addition to the identification of specific molecules, the velocity relative to the host star, information about planetary spin ($v \sin i$) and atmospheric wind speeds may be determined (Snellen et al., 2010, 2014). However, when a spectrum combines the star and planet, individual lines from the planet can have $\text{SNR} \ll 1$, and the ability to recover a planet is only as good as the model. If fitting an incorrect model to a low SNR spectrum, the planet may not be recovered, or even discovered. We have confirmed that the older CH_4 line lists are inaccurate in the 1.60–1.73 μm region, and the inaccurate line positions could result in a non-detection of the exoplanet. Snellen et al. (2010, 2014) were successful in this type of cross-correlation with CO, but fail to recover CH_4 in the K -band spectra of HD 209458 b and β Pictoris b, respectively. Inaccurate line lists could be responsible for these non-detections, as these studies use the older HITRAN’08 (Rothman et al., 2009) for their CH_4 line lists. More recently, Guilluy et al. (2019) and Giacobbe et al. (2021) had success detecting CH_4 for HD 102195 b and HD 209458 b, respectively, with more up-to-date line lists. Guilluy et al. (2019) used HITRAN2012 (Rothman et al., 2013), and Giacobbe et al. (2021) used Hargreaves et al. (2020), the same CH_4 line list we use here.

3.4.3 Carbon Monoxide

For effective temperatures $\lesssim 1300$ K (near the L/T transition), the dominant carbon-bearing molecule in the visible part of atmospheres of brown dwarfs switches from CO to CH_4 (Fegley & Lodders, 1996; Burrows et al., 1997). There are still signatures of CO in the spectra of

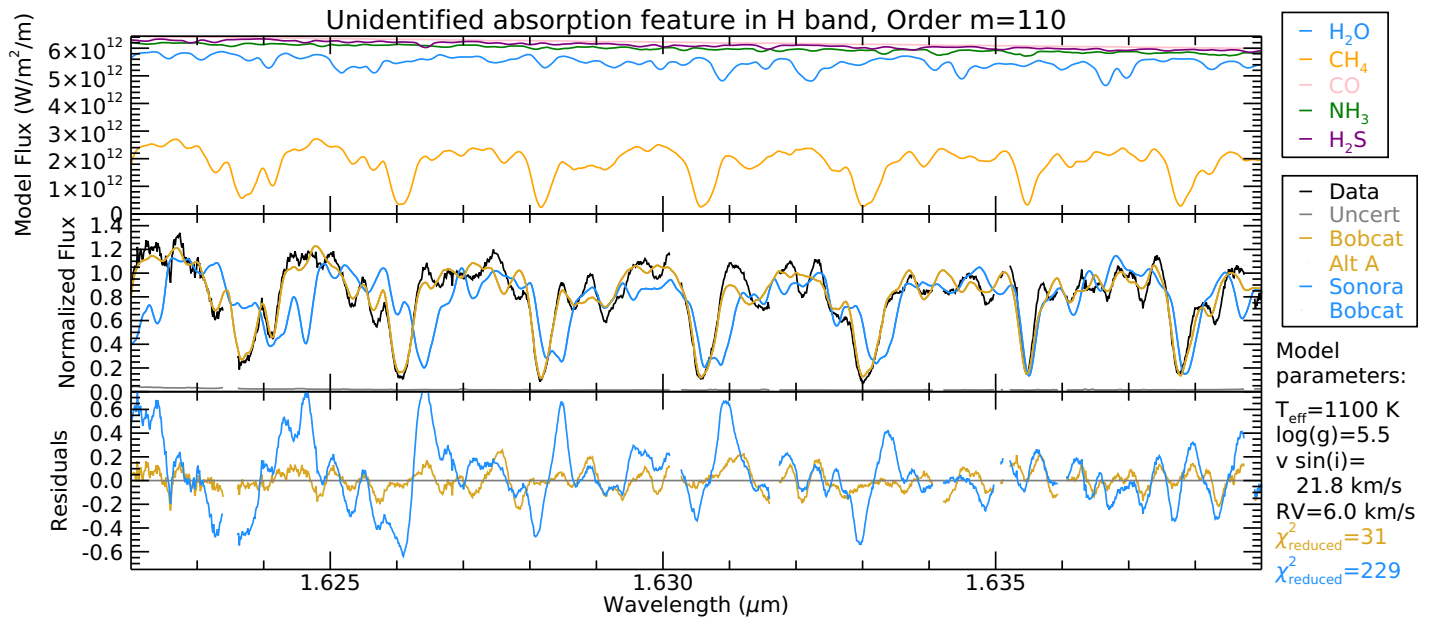


Figure 3.7: The improvement made with the newer CH_4 line lists is most apparent in order $m = 110$ of the H band. The top panel is similar to Figure 3.5: the Bobcat Alternative A model spectra of each major molecule with H_2/He collision-induced absorption are shown. Here the middle panel shows the IGRINS data (black), the Sonora Bobcat model (light blue), and the Bobcat Alternative A model (gold). The models have identical physical parameters, rotational broadening ($v \sin i$), and RV shift. The bottom panel shows the residuals (data - model) on the same vertical scale, with the same colour scheme. The deepest features are CH_4 , and the weaker features in the continuum are mainly CH_4 or CH_4 blended with H_2O . The Bobcat Alternative A model shows excellent agreement with the data in the major features, while the Sonora Bobcat model appears to have a stretch causing misalignment in the major features when compared to the IGRINS data.

cold brown dwarfs, and carbon exists abundantly as CO deeper in the atmosphere, where temperatures are higher.

We found that at the CO bands (1.554–1.569 μm in the *H* band and 2.29–2.45 μm in the *K* band), our model fitting selected higher effective temperatures ($T_{\text{eff}} \sim 1200$ K) compared to other orders. Accordingly, we observed several notable features in the residuals of orders $m = 77$ through $m = 73$ of the *K* band (2.294–2.445 μm), as well as in order $m = 115$ of the *H* band (1.554–1.569 μm), where a CO band head is present. The features in the residuals aligned with CO absorption features. We show an example of this in Figure 3.8, along with a model with increased CO abundance, providing an improved fit. The model with increased CO abundance is described in detail below.

This increased CO abundance implies disequilibrium chemistry, which can occur when vertical mixing (convection) occurs in the atmosphere (Lodders & Fegley, 2002). If CO is being brought from deeper, hotter layers to the upper atmosphere faster than the chemical reaction that converts CO to CH_4 , there will be more CO in the upper layers of the atmosphere than predicted from chemical equilibrium.

The Sonora Bobcat and Bobcat Alternative A models use the same cloudless, rainout chemical equilibrium structure models (Marley et al., 2021). These structure models assume chemical equilibrium and give the pressure, temperature, and chemical abundances throughout the atmosphere. To improve our fitting, we generated a small grid of Bobcat Alternative A models with varied amounts of CO, deviating from the chemical equilibrium assumptions used in the Sonora Bobcat structure models. We take a simple approach where we fix the volume mixing ratio (VMR) for CO to values of 10^{-6} , 3×10^{-5} , 10^{-5} , 3×10^{-4} , 10^{-4} , 3×10^{-3} , and 10^{-3} . This is a zeroth-order approximation, as 1) the CO VMR is not constant throughout the entire atmosphere, 2) other abundances like CH_4 and H_2O will also be affected by disequilibrium chemistry, and 3) we are using the temperature-pressure profile from the chemical equilibrium Sonora Bobcat models, but a much higher CO abundance could affect the temperature-pressure profile.

We found a CO VMR of 3×10^{-4} provided the best fits to our data. Figure 3.8 shows a comparison of the original equilibrium chemistry model to the model with this fixed CO VMR value. Figures 3.3 and 3.4, along with the figures for order $m = 115$ of the *H* band of the *H* band and orders $m = 77$ through $m = 72$ of the *K* band of the *K* band (orders where CO has a strong signature) shown in the Appendix (Section 3.7), show models with the fixed CO VMR of 3×10^{-4} . In equilibrium models, the CO VMR ranges from $10^{-3.6}$ to 10^{-7} for pressures probed by the *K* band. The increased CO VMR beyond the equilibrium range also explains why our initial fitting selected models with higher effective temperatures, as the CO abundance would be higher in the hotter models.

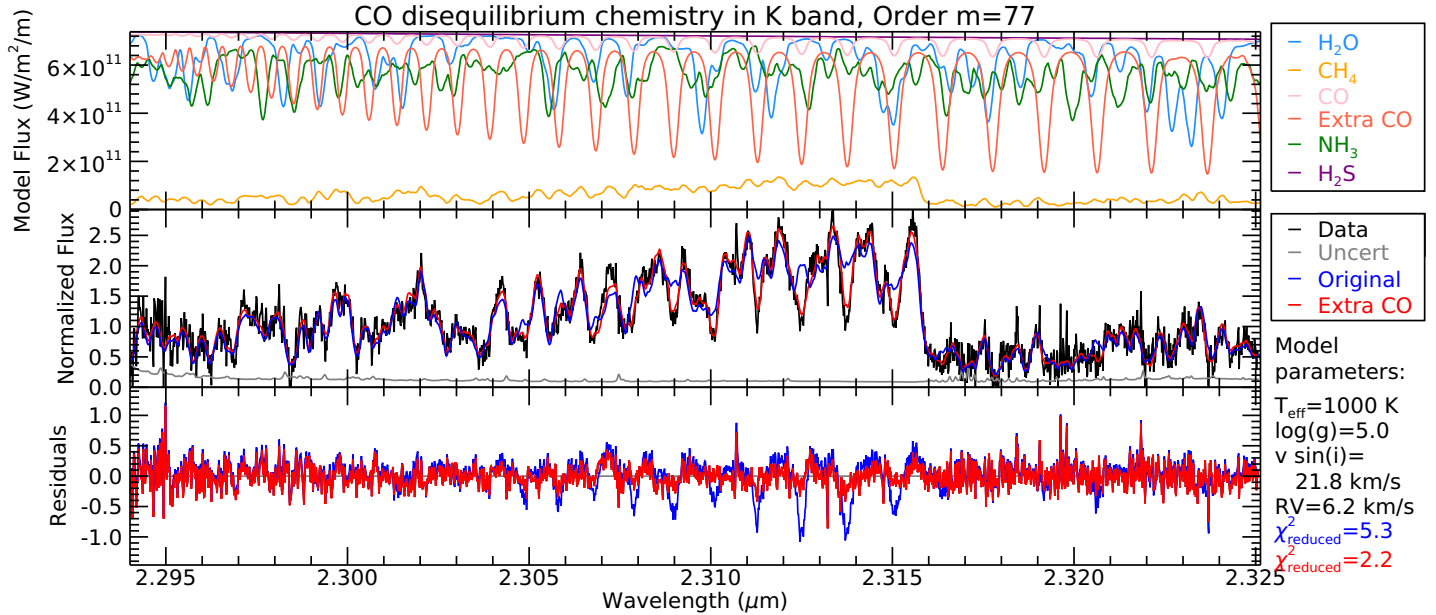


Figure 3.8: Order $m = 77$ of the K band is dominated by CH_4 , but CO and H_2O are also important absorbers. Here the top panel is similar to Figure 3.5, with an extra line for a model with an increased CO abundance (CO volume mixing ratio of 3×10^{-4} , labelled “Extra CO ”). The middle panel shows the observed spectrum with two versions of a Bobcat Alternative A model, one with the CO as estimated by chemical equilibrium (labelled “Original”) and one with an increased abundance of CO (labelled “Extra CO ”). The bottom panel shows the residuals for the two models. The CO strength in particular is important to improve the accuracy of the models in the long end of the K band. It is clear that the depth of the features in the “Original” model is too weak at the positions of the CO features, implying that vertical mixing must be taking place in this atmosphere.

Disequilibrium chemistry for CO has been observed spectroscopically and inferred photometrically in many other late-T dwarfs and Y dwarfs (e.g., Noll et al. 1997; Oppenheimer et al. 1998; Golimowski et al. 2004; Geballe et al. 2009; Leggett et al. 2012; Sorahana & Yamamura 2012; Miles et al. 2020), and has been known in Jupiter for decades (Prinn & Barshay, 1977; Noll et al., 1988). The growing number of T and Y dwarfs with evidence for CO disequilibrium chemistry indicates that vertical mixing is an important factor in accurately modelling brown dwarf spectra even at cold temperatures.

It is also possible that the increased CO abundance may be due to a larger primordial C/O ratio. Line et al. (2017) found super-solar C/O ratios for nine out of 11 late-T type ($\geq \text{T7}$) brown dwarfs.

3.4.4 Ammonia

Water and methane are the dominant absorbers in the spectra of late-T dwarfs, but ammonia is important too, especially at $T < 700$ K (the coldest T dwarfs and Y dwarfs), where it becomes the dominant nitrogen-bearing molecule (Lodders & Fegley, 2002). Ammonia is of special significance as it is the defining species in the spectra of Y dwarfs (Cushing et al., 2011).

The choice of an ammonia line list (among published lists) does not appear to significantly impact the physical parameters derived by comparing to models, but ammonia lines are clearly present in the observed spectrum and are important to include in the models. We are able to detect ammonia clearly in several regions of our spectrum.

This T6 dwarf joins the handful of T dwarfs with confirmed NH_3 detections in the near-infrared. Saumon et al. (2000) find evidence for NH_3 in the *H*- and *K*-band spectra of Gliese 229B (spectral type T6.5p, $T_{\text{eff}} \sim 950$ K) and Canty et al. (2015) report the detection of several NH_3 absorption features in the *H* and *K* bands in a T8 and T9 dwarf. Bochanski et al. (2011) additionally report detections of NH_3 in a T9 dwarf, however, Saumon et al. (2012) question whether some of those detections are indeed attributable to NH_3 . Saumon et al. (2012) do confirm the stronger NH_3 features at $\sim 2 \mu\text{m}$ in the spectrum of Bochanski et al. (2011). We re-confirm the strongest NH_3 identified in these works, but some of the weaker lines identified in these later spectral types do not appear in our warmer T6 dwarf.

Cushing et al. (2021) indicate NH_3 features should be present in the infrared at 1.03, 1.21, 1.31, 1.51, 1.66, 1.98, and $2.26 \mu\text{m}$, but would be blended with stronger H_2O and CH_4 lines making them difficult to detect. While the features at 1.03, 1.21, and $1.31 \mu\text{m}$ are outside of our wavelength coverage, we do have clear detections of NH_3 at 1.51, 1.98, and $2.26 \mu\text{m}$ using the Bobcat Alternative A models. The ammonia lines in our observed spectra are indeed blended with stronger H_2O lines, but we are able to detect them nonetheless. We compared Bobcat Alternative A models, with and without NH_3 , and the presence of the NH_3 is clear in the comb-like residuals of Figure 3.9. We also see significant improvement in the reduced χ^2 statistic when NH_3 is included in the model. We find that the NH_3 at $1.66 \mu\text{m}$ is far too weak to detect amongst the much stronger H_2O and CH_4 features in this region for an object of this temperature. While NH_3 has been detected in early T dwarfs in the mid-infrared (Roellig et al., 2004; Cushing et al., 2006), 2M0817 is the warmest brown dwarf with individual NH_3 lines detected in the near-infrared.

More recently, Line et al. (2015, 2017) and Zalesky et al. (2019) constrained the NH_3 abundance for multiple cold brown dwarfs (spectral types T7 and later, including several Y dwarfs) with low-resolution ($R < 300$ with IRTF/SpeX and HST/WFC3) retrievals. These studies are sensitive to how NH_3 opacities influence the spectroscopic appearance of cold brown dwarfs, but the low-resolution of the observations prevents identification of individual

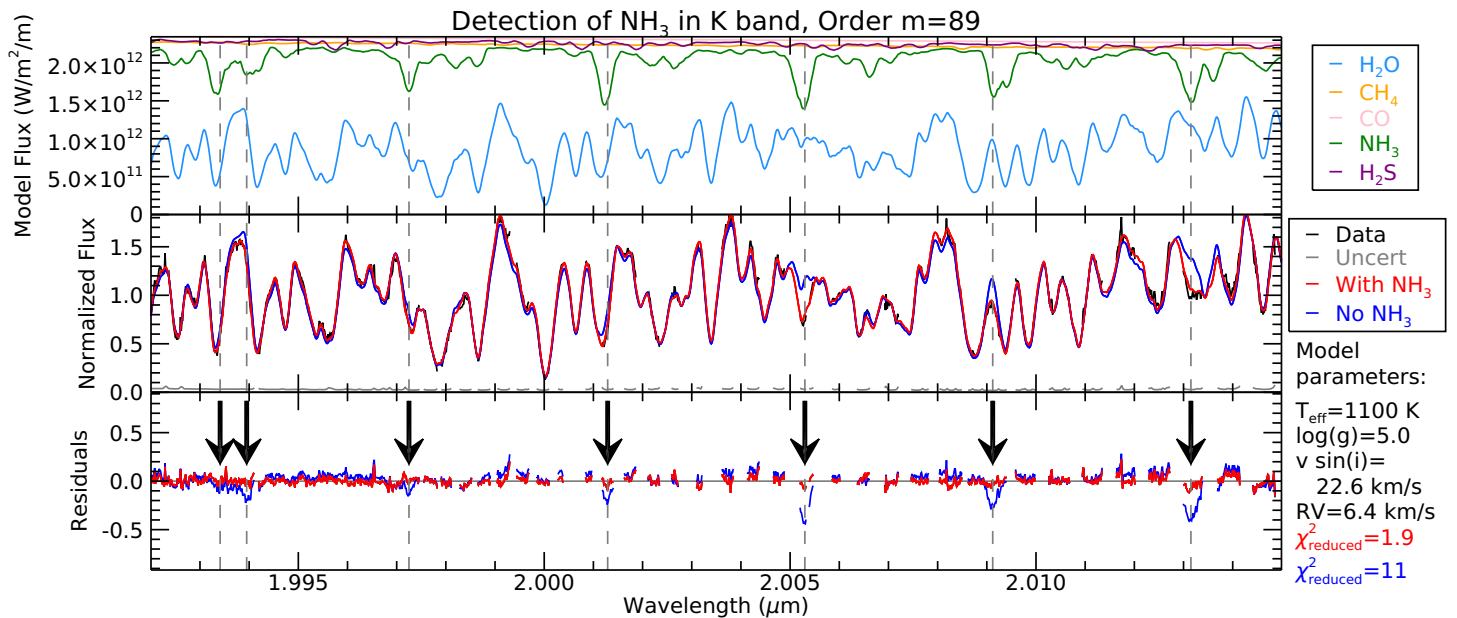


Figure 3.9: The same layout as Figure 3.8, but showing Bobcat Alternative A models with and without NH_3 . Arrows indicate where the model without NH_3 deviates from the data. The NH_3 lines are blended with stronger H_2O lines, but we see significant improvement in the χ^2_{reduced} values when NH_3 is included in the model. Order $m = 89$ of the K band has many strong telluric lines, but is still well fit by the models. It is difficult to discern the data from the model containing NH_3 , and the quality of the fit is reflected in the flat residuals and low χ^2_{reduced} value.

NH_3 lines in the spectra. Additionally, [Line et al. \(2021\)](#) recently determined the C/H, O/H, and C/O ratios of the hot Jupiter WASP-77AB using cross-correlation methods with IGRINS data. That work and our study of 2M0817 presented here have clear implications for exoplanetary studies like this in the future.

3.4.5 Hydrogen Sulfide

We present clear, unambiguous detections of H_2S in 2M0817. Our most notable detection is a feature at $1.590 \mu\text{m}$. This feature is blended with a weak H_2O line at the same position, so we show our data compared to Bobcat Alternative A models with and without H_2S in Figure 3.10. We see the clear signature of this H_2S line in the residuals, as well as the presence of other weaker H_2S lines nearby at $1.5906 \mu\text{m}$ and $1.5912 \mu\text{m}$.

There is only one other report of a possible H_2S detection in a brown dwarf in the literature. [Saumon et al. \(2000\)](#) note an H_2S absorption feature at $2.1084 \mu\text{m}$ in the spectrum of Gliese 229B (spectral type T6.5p), but we do not confirm this line in our data, nor do our updated models predict any H_2S lines at this position.

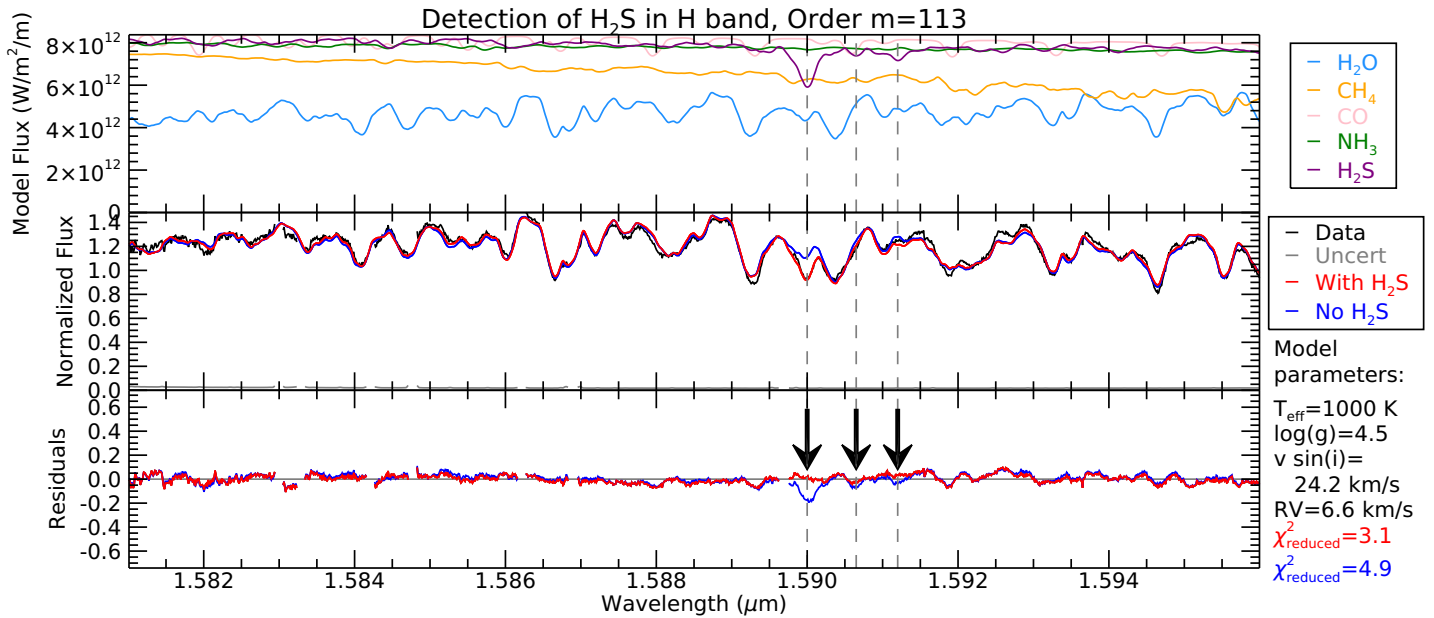


Figure 3.10: The same layout as Figure 3.9, but showing Bobcat Alternative A models with and without H_2S . This order shows a clear H_2S detection at $1.590 \mu\text{m}$. Order $m = 113$ of the H band is well fit by models. The H_2S line of interest is blended with an H_2O line, but we see improvement in the χ^2_{reduced} value for the model including H_2S .

H_2S has been identified in the giant planets of our Solar System: Irwin et al. (2018) detect H_2S in the atmosphere of Uranus and Irwin et al. (2019) present a tentative detection of H_2S in Neptune, both in the $1.57\text{--}1.59 \mu\text{m}$ region, the same region in which we have our clearest detection. Detections of H_2S in Jupiter have also been debated (Noll et al., 1995; Niemann et al., 1998). Our spectrum of 2M0817 exhibits the only convincing detection of H_2S in an extra-solar atmosphere to date.

3.4.6 Shortcomings of the Models and Unidentified Lines

A major goal of this work is to identify regions where the photospheric models do not completely reproduce the features in the observed spectra. To identify regions and specific absorption lines in the data which are not well reproduced with the models, we performed two checks. First, we measured the standard deviation, σ , of the residuals in each order, and then selected regions with at least five consecutive pixels more than 2σ away from zero. Second, we applied a matched filter to the residuals of each other, using a high SNR telluric line surrounded by a flat continuum as the template. We then identified regions in the spectra where both the pixel values were outside of two standard deviations, and the matched filter response was higher than the surrounding pixels. This helped to eliminate false detections due to noise. We perform these

checks only for the Bobcat Alternative A models, as they are the most up-to-date and the most accurate. We show an example of this analysis in Figure 3.11, and we summarize the regions of interest in Table 3.5, with a brief description of the potential issue affecting the model in each case. These discrepancies can be seen in Figures 3.13 and 3.14, indicated with black arrows.

Most notably, a line is clearly missing from the model in order $m = 84$ of the K band at $2.12187 \mu\text{m}$. We show this region in Figure 3.12. Another notable line missing from the data is at $2.20695 \mu\text{m}$ in order $m = 81$ of the K band, (Figure 3.14). None of the models includes a line at this wavelength, and we have not identified the element or molecule responsible for this feature. Additionally, we find no absorption or emission in the A0V stars at the wavelengths given in Table 3.5 which could introduce these unidentified features to our T6 spectrum. The feature in H band order $m=121$ does line up with a weak telluric H_2O feature, but given the difference in the line widths, we believe this discrepancy between the data and model is not caused by the telluric line.

The Bobcat Alternative A models we use to analyze our data are comprised of the five most abundant molecules (H_2O , CH_4 , CO , NH_3 , and H_2S), plus collision-induced absorption from molecular hydrogen and helium. The older Sonora Bobcat, Morley, and BT-Settl models consist of more complete sets of molecules. We have confirmed that the lines listed in Table 3.5 are indeed missing in all families of models. We cannot eliminate all molecules (such as C_2H_2 , C_2H_4 , C_2H_6 , etc.) that are included in the more complete Sonora Bobcat, Morley, and BT-Settl model families as being responsible for these missing lines, as the line lists could be incomplete or inaccurate, or there could be disequilibrium chemistry taking place, as we observed with CO (Section 3.4.3).

Disequilibrium chemistry could imply that other mixing-sensitive gases such as phosphine (PH_3 ; the next most abundant molecule in these cold atmospheres) could also be present at higher abundances than expected for chemical equilibrium (Fegley & Lodders, 1996). We generated a Bobcat Alternative A model with a greatly over-estimated abundance of PH_3 (VMR of 1×10^{-4} , which is more than 300 times the amount expected for equilibrium chemistry, and would require far more phosphorus than would be available in a solar-composition atmosphere) to compare to our spectra, intending to match the locations of the PH_3 features to the unidentified lines. We found that the PH_3 features did not match with any of the unidentified lines, and PH_3 is likely not responsible for these features. A recent study by Miles et al. (2020) searched for PH_3 in atmospheres of cold brown dwarfs displaying disequilibrium CO absorption. This study was performed in the L and M bands (centred at $3.45 \mu\text{m}$ and $4.75 \mu\text{m}$, respectively), where H_2O , CH_4 , and NH_3 absorb less strongly, but PH_3 absorbs much more strongly, and so should give the best chance at detecting PH_3 . Unfortunately, they were also unable to detect PH_3 .

Among the list of unidentified regions and lines in Table 3.5, we list nearly the full wavelength

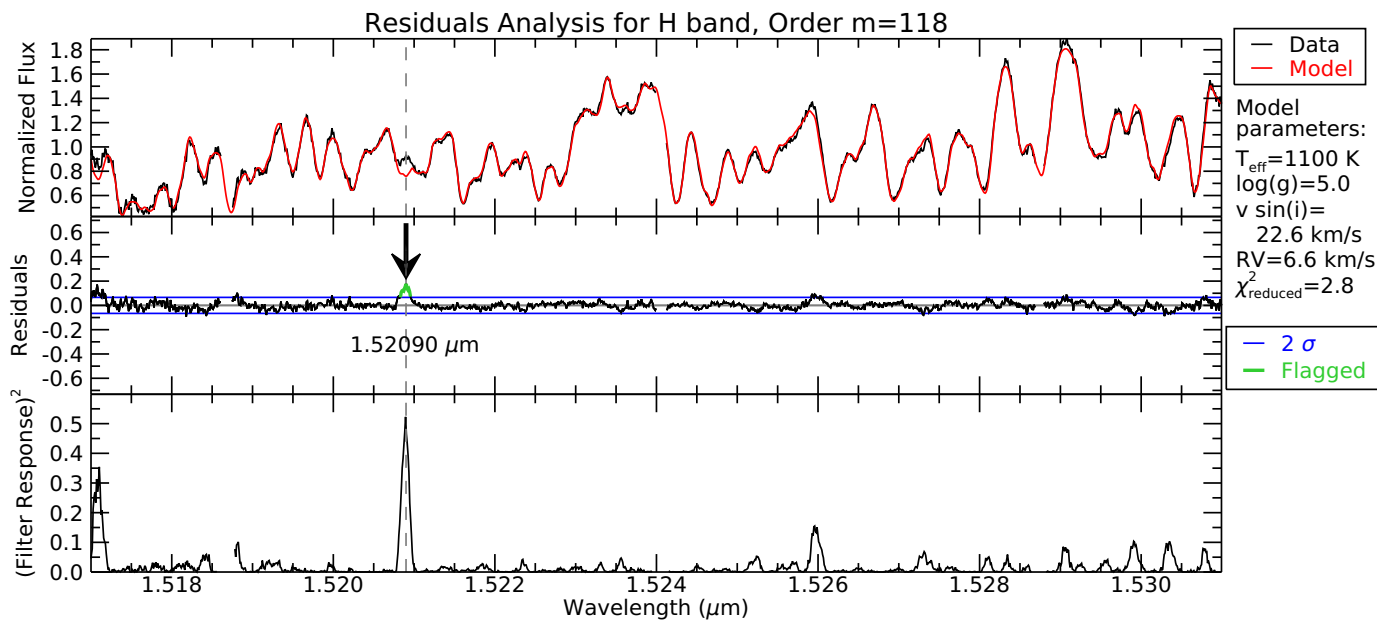


Figure 3.11: An example of the analysis done on the residuals to identify discrepancies between the models and data. The top panel shows the IGRINS spectrum with the best-fitting Bobcat Alternative A model for this order. The middle panel shows the residuals on the same y-scale as the top panel. Horizontal blue lines delineate 2σ threshold, and regions with more than five consecutive pixels beyond 2σ are highlighted with green. The filter response of a matched filter using a clean telluric line surrounded by a flat continuum is shown in the bottom panel. There is a clear outlier region at $1.52094 \mu\text{m}$ flagged by both the residuals analysis, and also giving a high filter response. Other regions with a high filter response (e.g., $1.51714 \mu\text{m}$ and $1.52602 \mu\text{m}$) don't meet our residuals criteria, and are therefore more likely due to noise in the data. The dominant absorber in order $m = 118$ of the H band is H_2O .

coverage of orders $m = 113$ through $m = 107$ of the H band. These orders cover $1.596\text{--}1.681 \mu\text{m}$ and the dominant absorber in these orders is CH_4 . As discussed in Section 3.4.2, while the strongest absorption features are very well modelled in the Bobcat Alternative A models, the weaker features and continua in the models deviate significantly from the observations.

3.5 Lessons Learned

We find that atmospheric models that use state-of-the-art line lists represent observations well. We are now able to extract more precise information from our data than merely detect the most abundant molecules: we can detect trace species that have never been seen before (like H_2S), see low abundance species, and more readily detect abundances of species (as we have done for CO here).

Table 3.5. Wavelengths of discrepancies in the models and unidentified lines

Band	Order	Wavelength (μm)	Notes
<i>H</i>	121	1.48463	Potential issue with blended line or something missing in the model
<i>H</i>	118	1.52090	A line appears in the model which is missing in the data. The model line appears to be a water/ammonia blend
<i>H</i>	116	1.55120	Potential issue with blended line (H_2O and NH_3 ?)
<i>H</i>	115	1.56396	Potential issue with blended line (H_2O and NH_3 or H_2O and H_2S ?)
<i>H</i>	113	1.5875–1.5960	CH_4 region ^a
<i>H</i>	112	1.598–1.609	CH_4 region ^a
<i>H</i>	111	1.608–1.624	CH_4 region ^a
<i>H</i>	110	1.6244–1.6390	CH_4 region ^a
<i>H</i>	109	1.6375–1.6510	CH_4 region ^a
<i>H</i>	108	1.6515–1.6650	CH_4 region ^a
<i>H</i>	108	1.65355	Potential issue with blended line (CH_4 and H_2O ?)
<i>H</i>	108	1.65446	Model over-estimates flux
<i>H</i>	108	1.66319	Model over-estimates flux
<i>H</i>	107	1.6675–1.6810	CH_4 region ^a
<i>H</i>	107	1.66960	Line too weak in model
<i>H</i>	107	1.67380	Model under-estimates flux
<i>H</i>	106	1.68443	Potential issue with blended line (CH_4 and H_2O ?)
<i>H</i>	106	1.68672	Potential issue with blended line (CH_4 and H_2O ?)
<i>H</i>	106	1.69600	Potential issue with blended line (CH_4 and H_2O ?)
<i>K</i>	87	2.04020	Model over-estimates flux
<i>K</i>	87	2.05478	Model under-estimates flux
<i>K</i>	84	2.12187	Line missing from model (see Figure 3.12)
<i>K</i>	81	2.20690	Line missing from model

Note. — The wavelengths of discrepancies in the models and unidentified lines. These regions are identified in Figures 3.13 and 3.14, with black arrows for lines, and black brackets for regions.

^aIn these CH_4 regions the model accurately represents the deepest features, but appears to be incorrect or incomplete in the weaker features and continuum. Given the accuracy of the H_2O lines elsewhere in the spectrum, we suspect these discrepancies are due to weak CH_4 lines, and not H_2O .

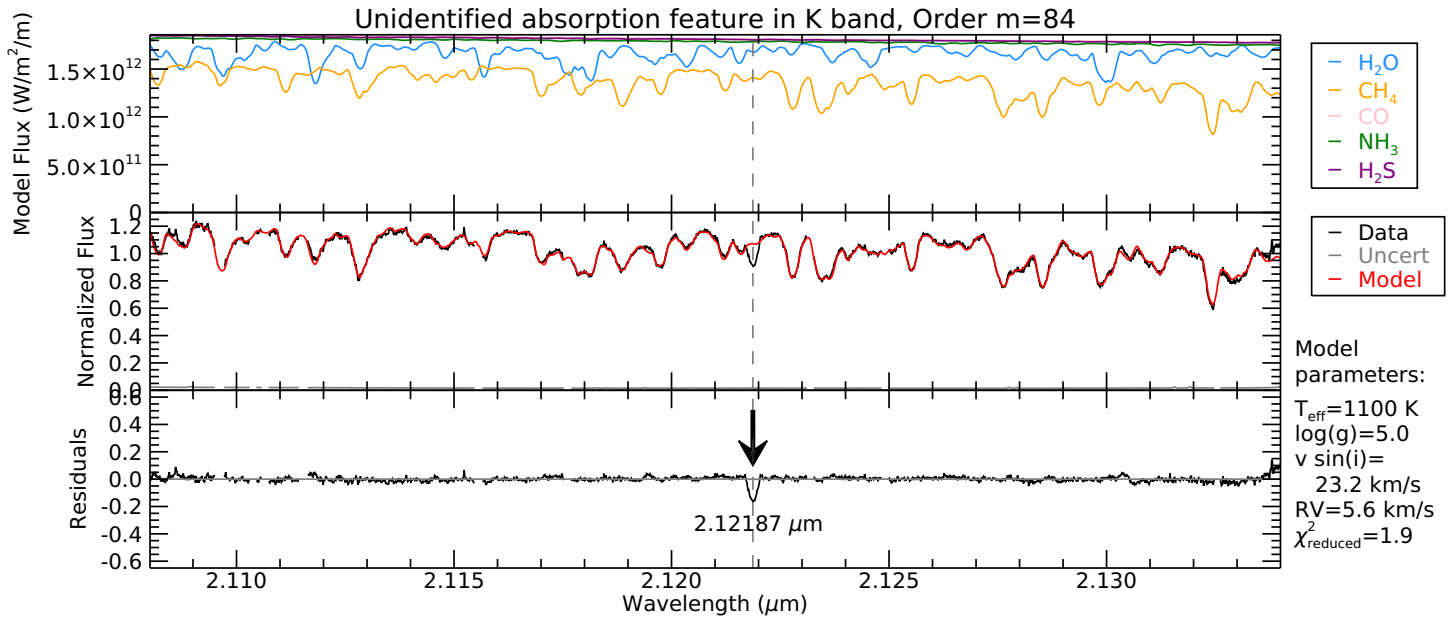


Figure 3.12: The same layout as Figure 3.8, but showing only the best-fitting Bobcat Alternative A model for this order. Order $m = 84$ of the K band is very well fit by models, and shows an unknown absorption feature that doesn't appear in any model of any family at $2.12187 \mu\text{m}$. This line is indicated with a black arrow.

In all cases we recommend using the most-up-to-date models available with the most recent molecular line lists. We have found that the line lists used in the Bobcat Alternative A models (Table 3.4) give the most reliable and consistent estimates of all physical parameters across all wavelength regions of this study. More generally, we have found that all models do an adequate job fitting the data in regions where H_2O is the dominant absorber.

We summarize our main recommendations and warnings, organized by the information of interest in the following two subsections.

3.5.1 Fitted Spectroscopic Parameters

Effective Temperature (T_{eff}) measurements are the most accurate and consistent in the K band, in regions where H_2O is the dominant opacity source. We recommend using the Bobcat Alternative A models for measuring T_{eff} anywhere in the H and K bands. The BT-Settl models under-estimate T_{eff} in the K band. If disequilibrium chemistry effects are not taken into consideration, T_{eff} may be over-estimated.

Surface gravity ($\log g$) measurements are the most accurate and consistent in regions where H_2O is the dominant opacity source in the H band. We recommend using the Bobcat Alternative A models for measuring $\log g$ anywhere in the H and K bands. The Sonora Bobcat models

over-estimate $\log g$ in the K band. $\log g$ may be over estimated in regions where the dominant molecule switches from H_2O to CH_4 , near the peaks of H and K bands ($1.6 \mu\text{m}$ and $2.1 \mu\text{m}$, respectively).

Projected Rotation Velocity ($v \sin i$) measurements are the most accurate and consistent in regions where H_2O is the dominant opacity source in both the H and K bands. We recommend using the Bobcat Alternative A models for measuring $v \sin i$ anywhere in the H and K bands. We recommend using the region from 1.45 to $1.57 \mu\text{m}$ in the H band, or 1.89 to $2.10 \mu\text{m}$ in the K band if measuring $v \sin i$ with any other model. $v \sin i$ may be over estimated in regions where the dominant molecule switches from H_2O to CH_4 , near the peaks of H and K bands ($1.6 \mu\text{m}$ and $2.1 \mu\text{m}$, respectively).

Radial Velocity (RV) measurements are the most accurate and consistent in regions where H_2O is the dominant opacity source in both the H and K bands. We recommend using the Bobcat Alternative A models for measuring RV anywhere in the H and K bands. We recommend using the region from 1.45 to $1.58 \mu\text{m}$ in the H band if measuring RV with any other model. RV measurements demonstrate a blueshift with wavelength when measured from the Sonora Bobcat and BT-Settl models between 1.894 and $2.060 \mu\text{m}$.

3.5.2 Specific Molecules

Water (H_2O) is the dominant opacity source between 1.45 and $1.58 \mu\text{m}$ in the H band, and between 1.89 and $2.10 \mu\text{m}$ in the K band. The H_2O -dominant region of the H band (1.45 – $1.58 \mu\text{m}$) gives consistent results for all parameters across all model families. We recommend using the ExoMol/POKAZATEL (Polyansky et al., 2018) line list when studying water.

Methane (CH_4) is the dominant opacity source between 1.60 and $1.73 \mu\text{m}$ in the H band, and between 2.10 and $2.48 \mu\text{m}$ in the K band. The CH_4 -dominant region of the K band (2.10 – $2.48 \mu\text{m}$) gives consistent results for all parameters for the Bobcat Alternative A models. Weak CH_4 lines between 1.59 and $1.67 \mu\text{m}$ are poorly matched to data in all model families and in all line lists. We recommend using the HITEMP (Hargreaves et al., 2020) line list when studying CH_4 .

Carbon monoxide (CO) bands occur between 1.55 and $1.57 \mu\text{m}$ in the H band, and 2.29 to $2.45 \mu\text{m}$ in the K band. To measure accurate and consistent parameters, especially T_{eff} , disequilibrium chemistry may need to be considered for CO. We recommend using the HITEMP 2010 (Rothman et al., 2010) line list when studying CO.

The strongest **ammonia (NH_3)** features occur between 1.50 and $1.52 \mu\text{m}$ in the H band, and 1.95 to $2.09 \mu\text{m}$ and 2.18 to $2.21 \mu\text{m}$ in the K band. The choice of NH_3 line list does not appear to significantly impact the measured parameters, and we recommend using the ExoMol/CoYuTe

(Coles et al., 2019) line list when studying NH_3 .

The strongest **hydrogen sulfide (H_2S)** features occur in the H band between 1.58 and 1.60 μm . The choice of H_2S line list does not appear to impact the measured parameters, and we recommend using the combinations of ExoMol (Tennyson & Yurchenko, 2012), Azzam et al. (2015), and HITRAN 2012 (Rothman et al., 2013) line lists when studying H_2S .

3.6 Conclusions

The data presented here are among the highest resolution spectra ever published for a cold brown dwarf. We find that model spectra with the most recent line lists show significant improvement in fitting the observed spectra of the T6 dwarf 2MASS J08173001–6155158, in particular in regions where methane is the dominant absorber. We determined the physical parameters of this brown dwarf, and identified the most reliable regions for measuring physical parameters of cold brown dwarfs by comparing to model spectra. We present the first unambiguous detection of H_2S in an extra-solar atmosphere. We also confirm that like many other late-T and Y dwarfs, 2MASS J08173001–6155158 demonstrates CO disequilibrium chemistry. Additionally, we identify several absorption features and regions which are missing from, or poorly fit by the models. The updated line lists for water, methane, and ammonia allow for very precise empirical determinations of physical parameters, and are highly promising for the detection and characterization of exoplanets with high-dispersion spectroscopy.

3.7 Appendix: The Full Suite of Model Fits for Every IGRINS Order

We show the best fitting Bobcat Alternative A models for all orders in the IGRINS spectrum in Figures 3.13 (H band) and 3.14 (K band).

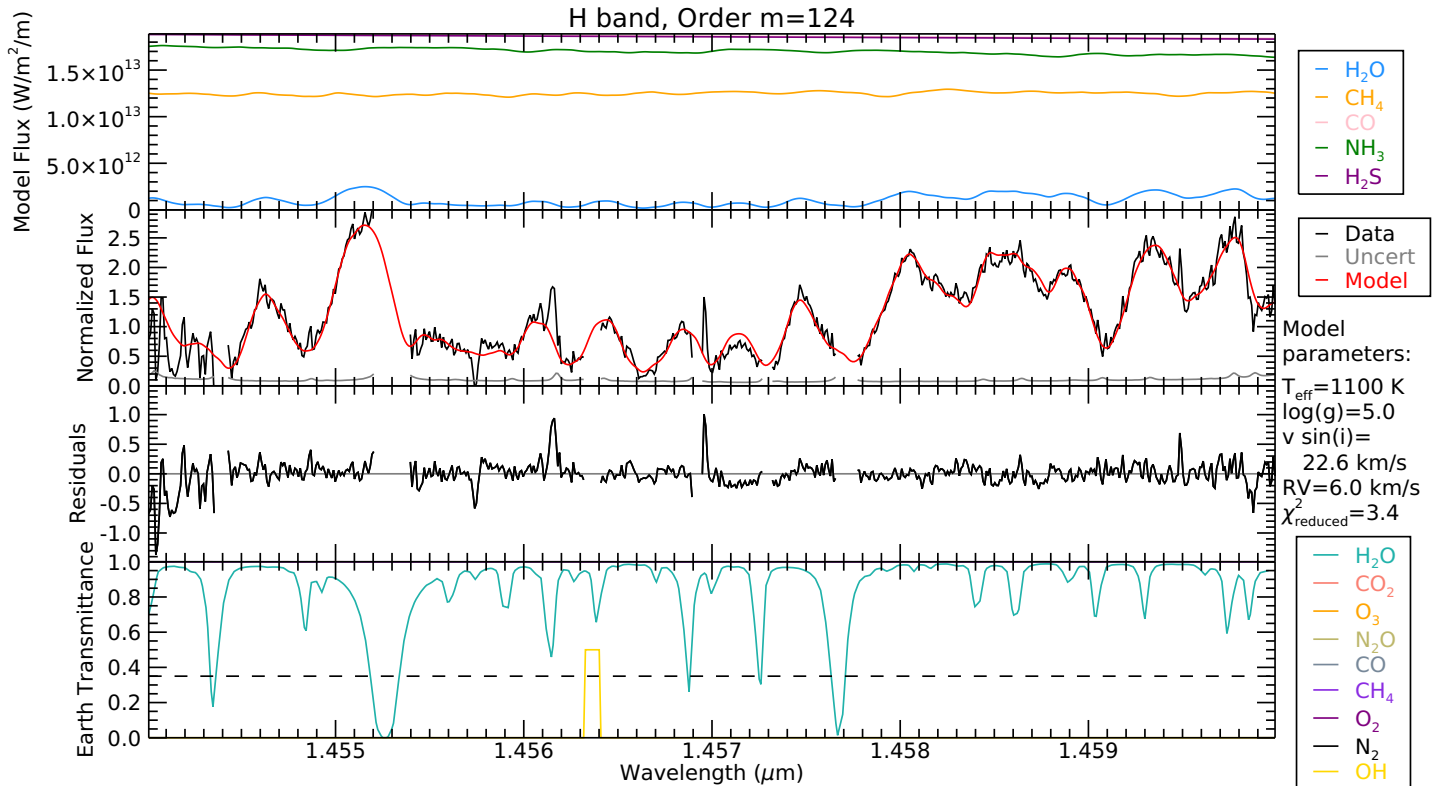


Figure 3.13: Every order of the H band. The model shown is the best fitting Bobcat Alternative A model for each order. Each order is fit independently (Section 3.3), so the physical parameters may differ between orders. The top panel shows the molecule-by-molecule breakdown of the model. The second panel from the top shows the IGRINS data with the full model. The second panel from the bottom shows the residuals on the same y-scale as the panel above it. The model discrepancies listed in Table 3.5 are indicated in these figures with black arrows for discrepant lines, and black brackets for discrepant regions. The bottom panel shows the PSG Earth’s transmittance to help assess the telluric lines in our spectra. The OH emission lines are also shown as boxes and indicate position only, not line strength. Wider boxes indicate blended OH emission lines. A dashed horizontal line indicates the 35% threshold used for our telluric mask. This figure continues for many pages, with two orders per page, to show all 26 orders of the H band.

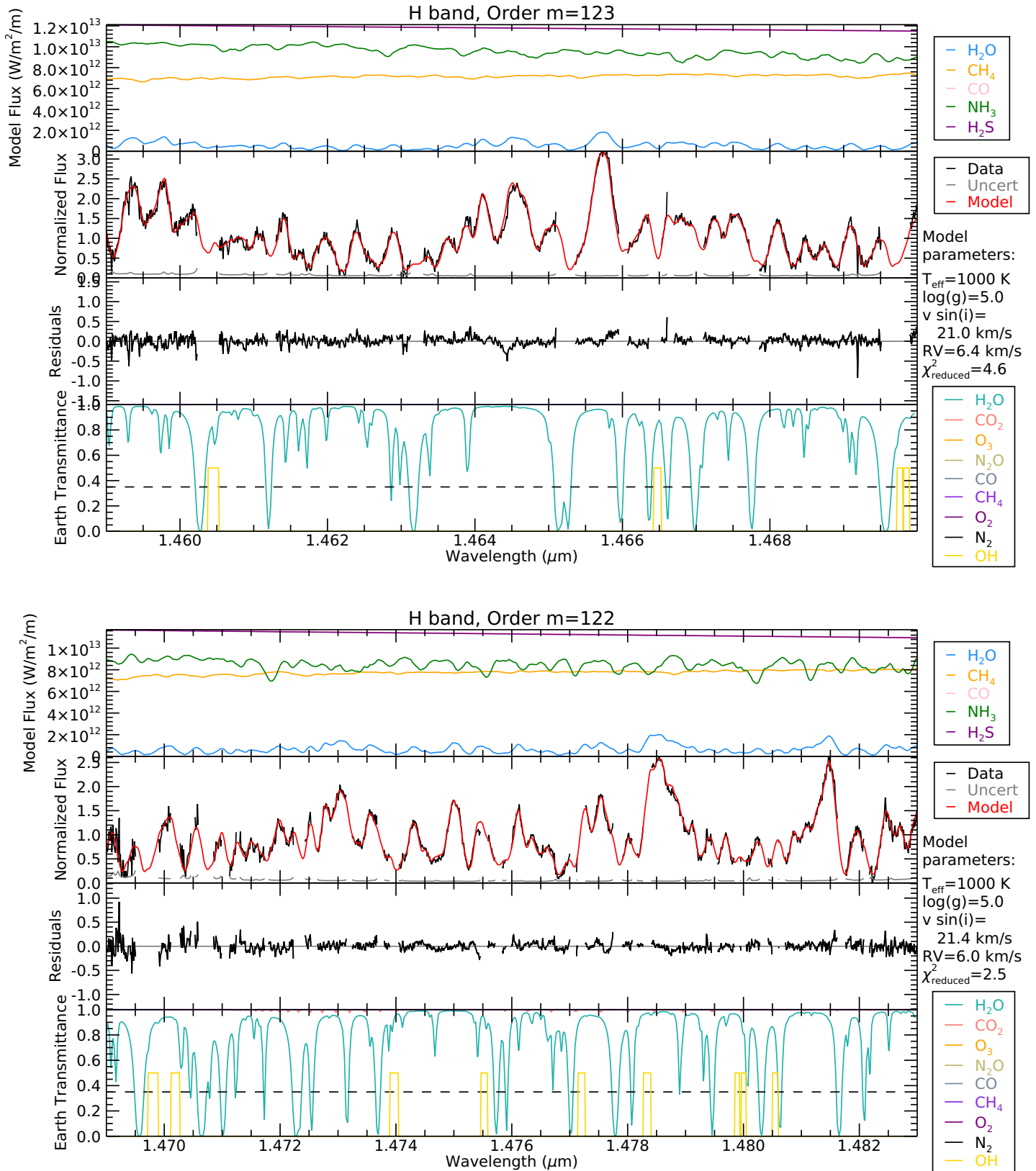


Figure 3.13: Continued.

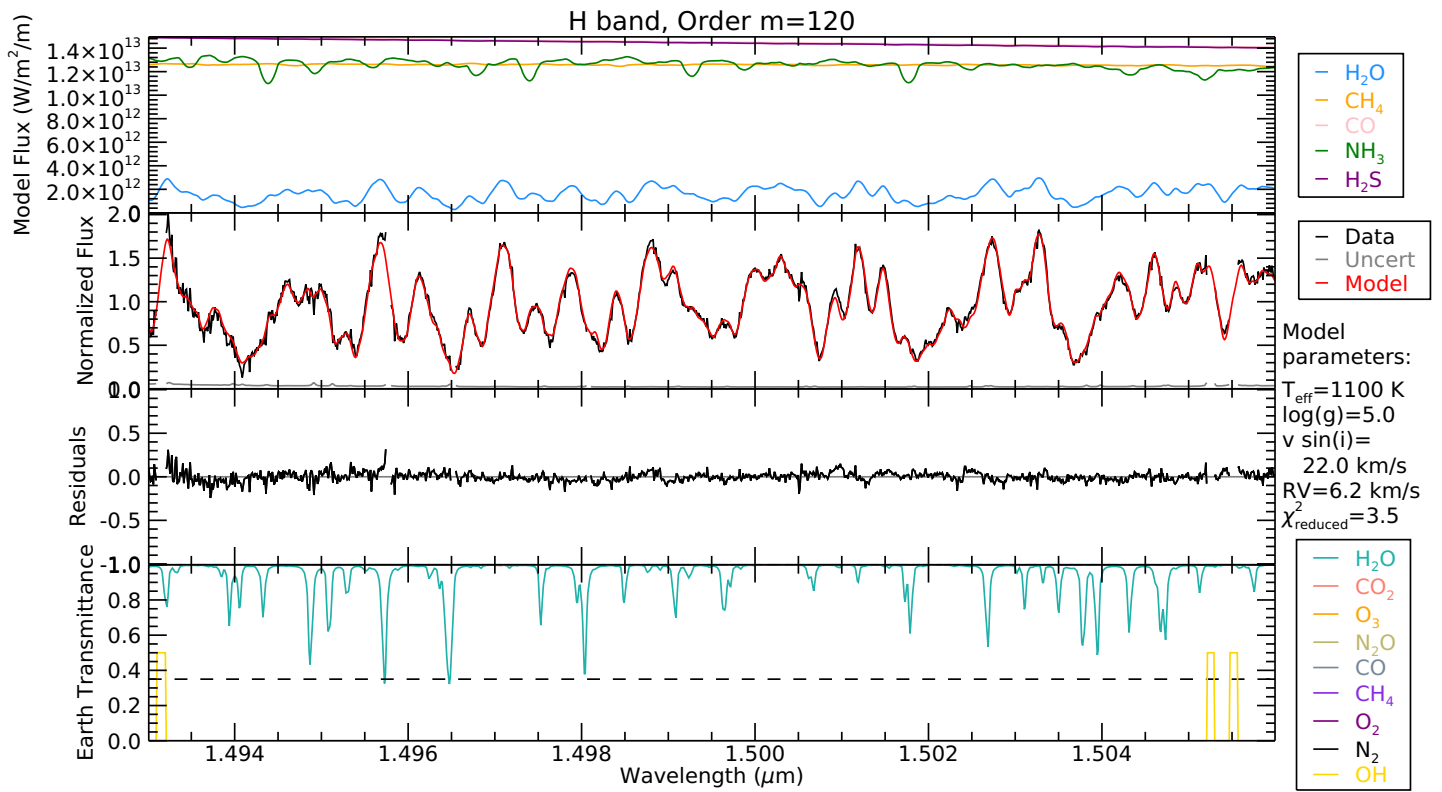
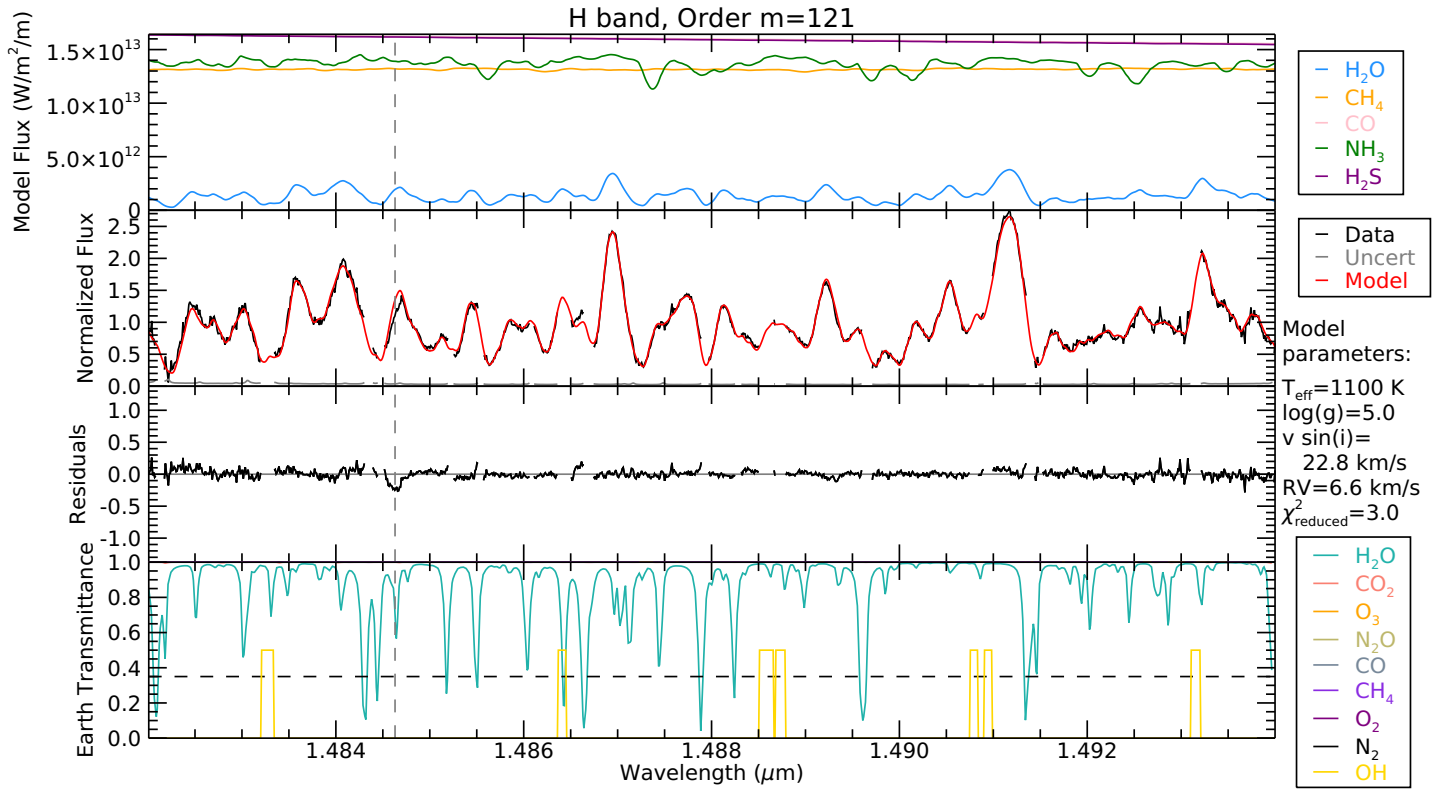


Figure 3.13: Continued.

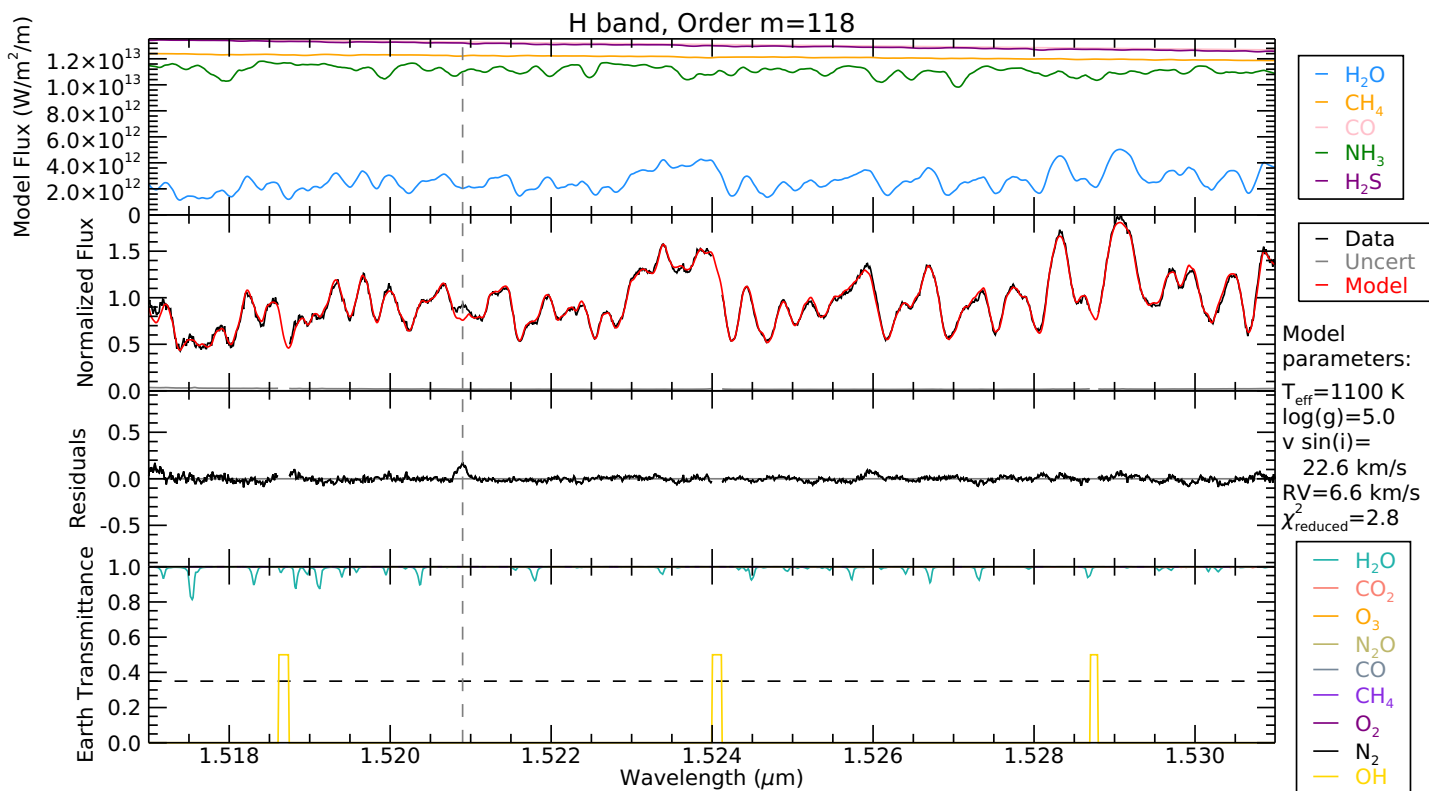
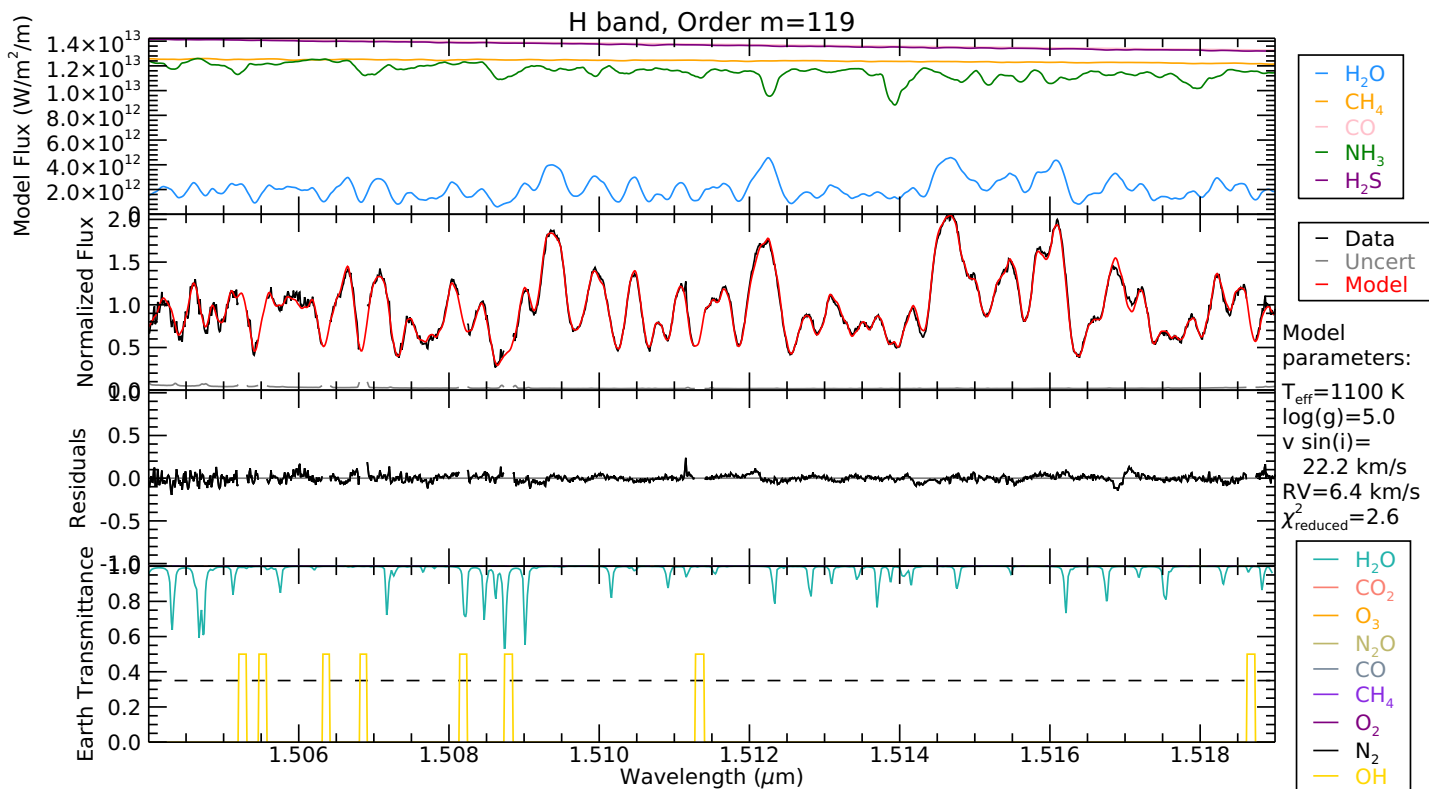


Figure 3.13: Continued.

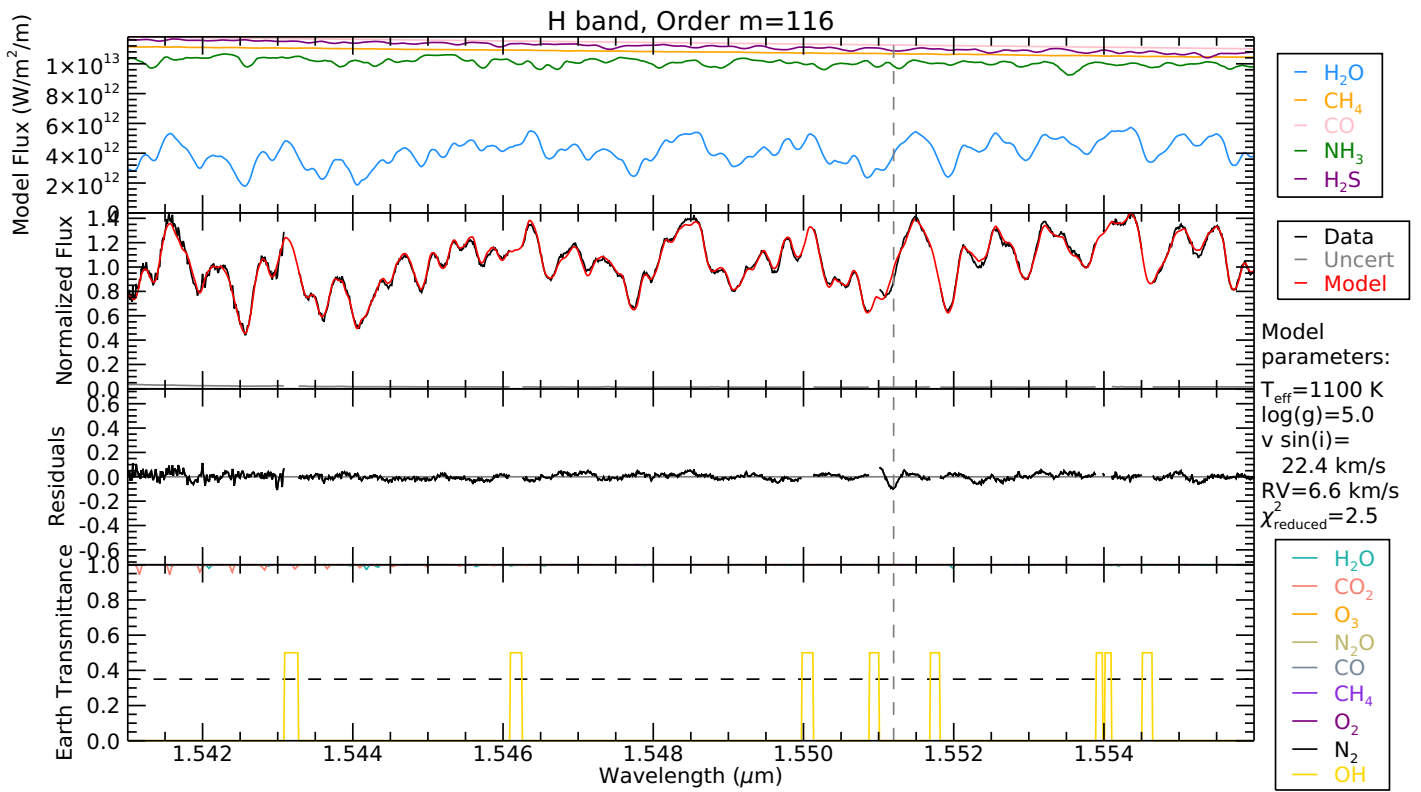
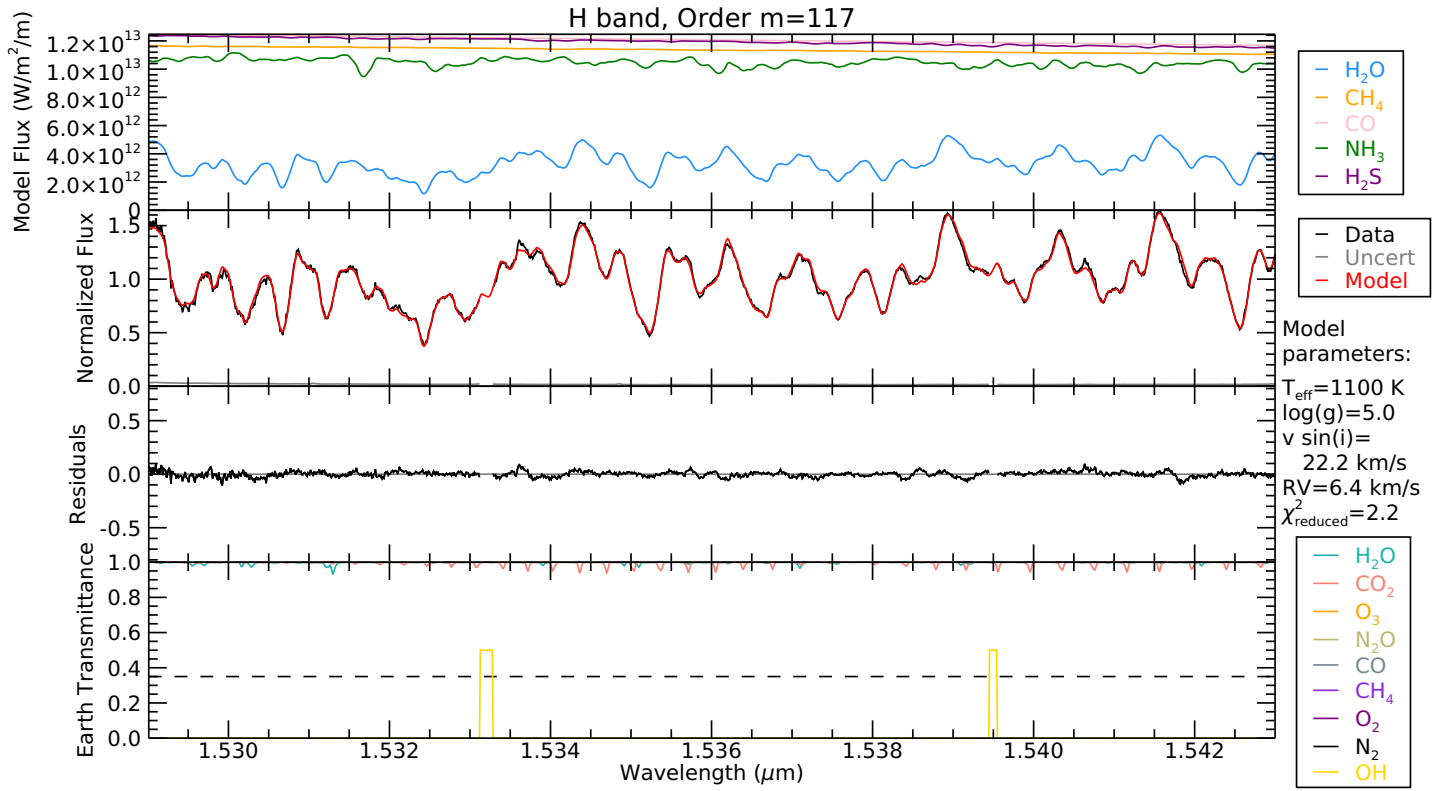


Figure 3.13: Continued.

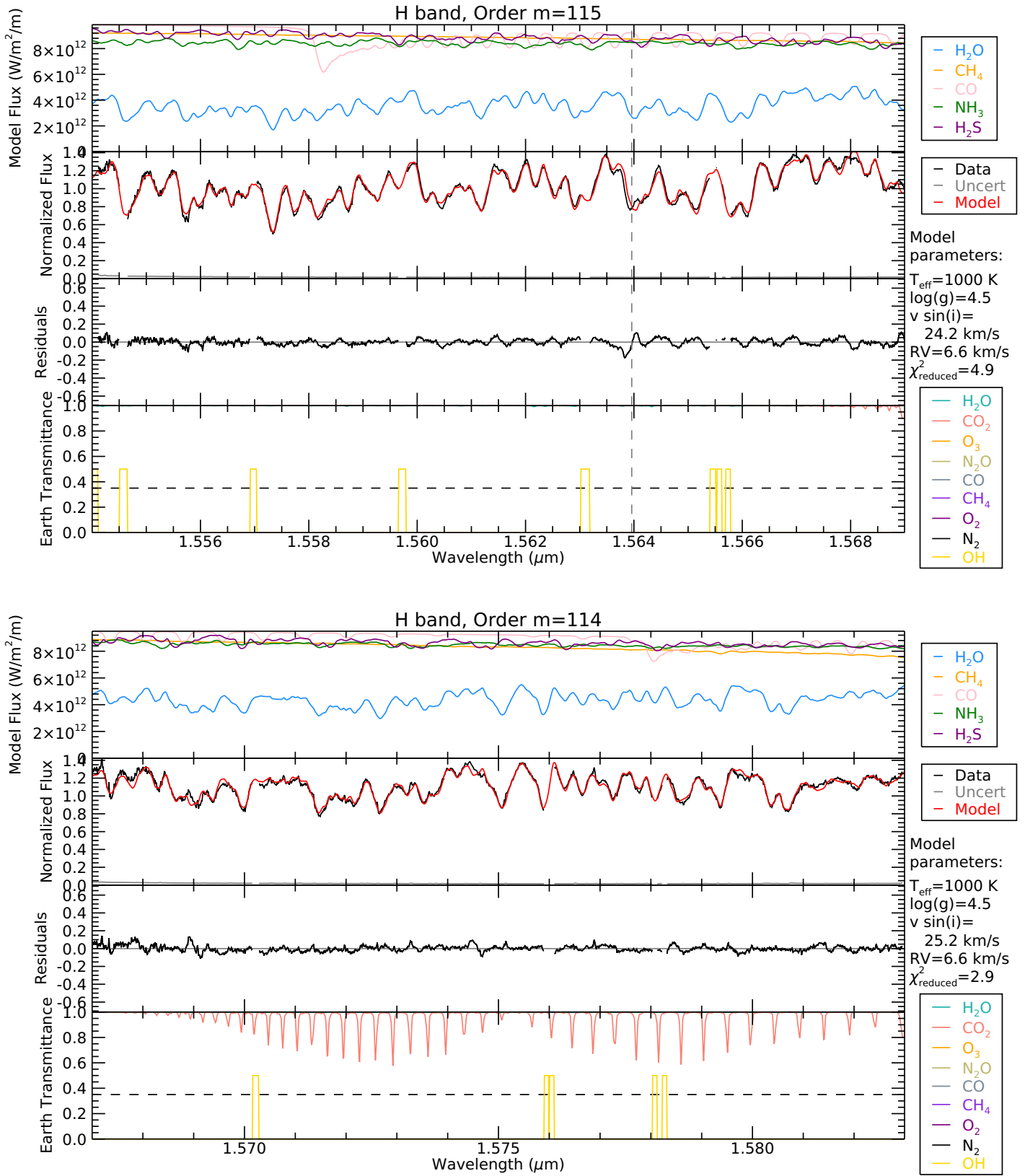


Figure 3.13: Continued.

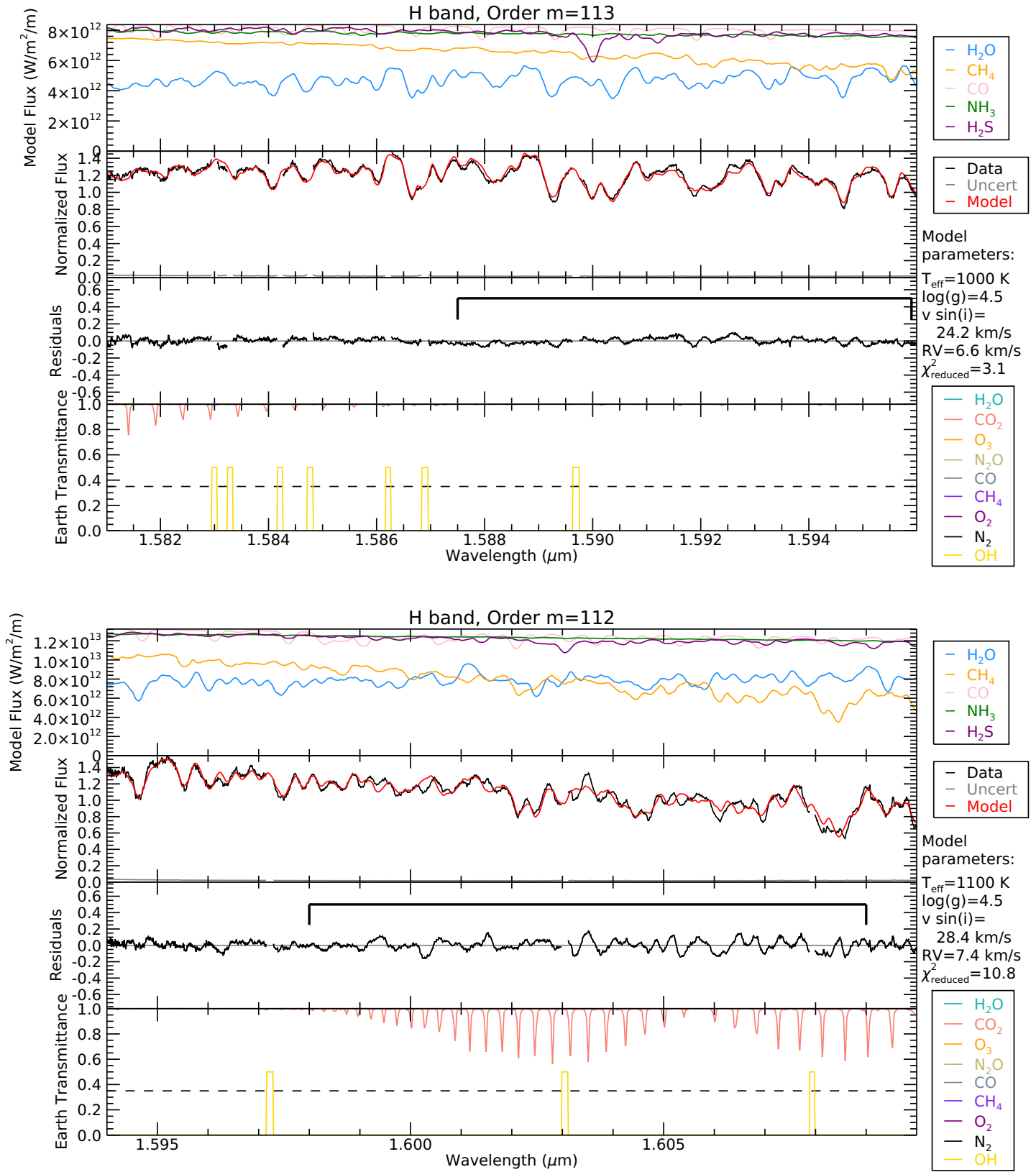


Figure 3.13: Continued.

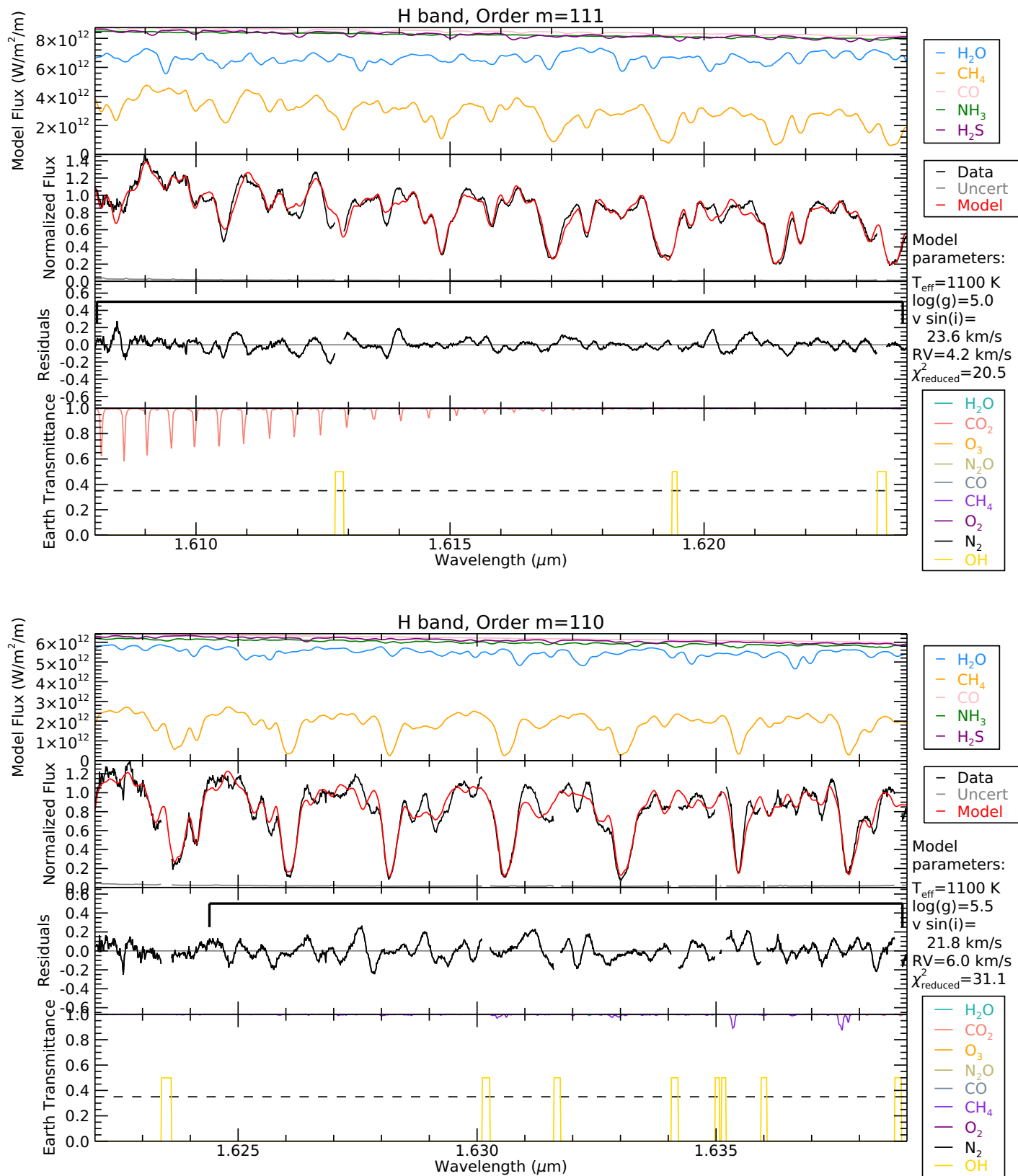


Figure 3.13: Continued.

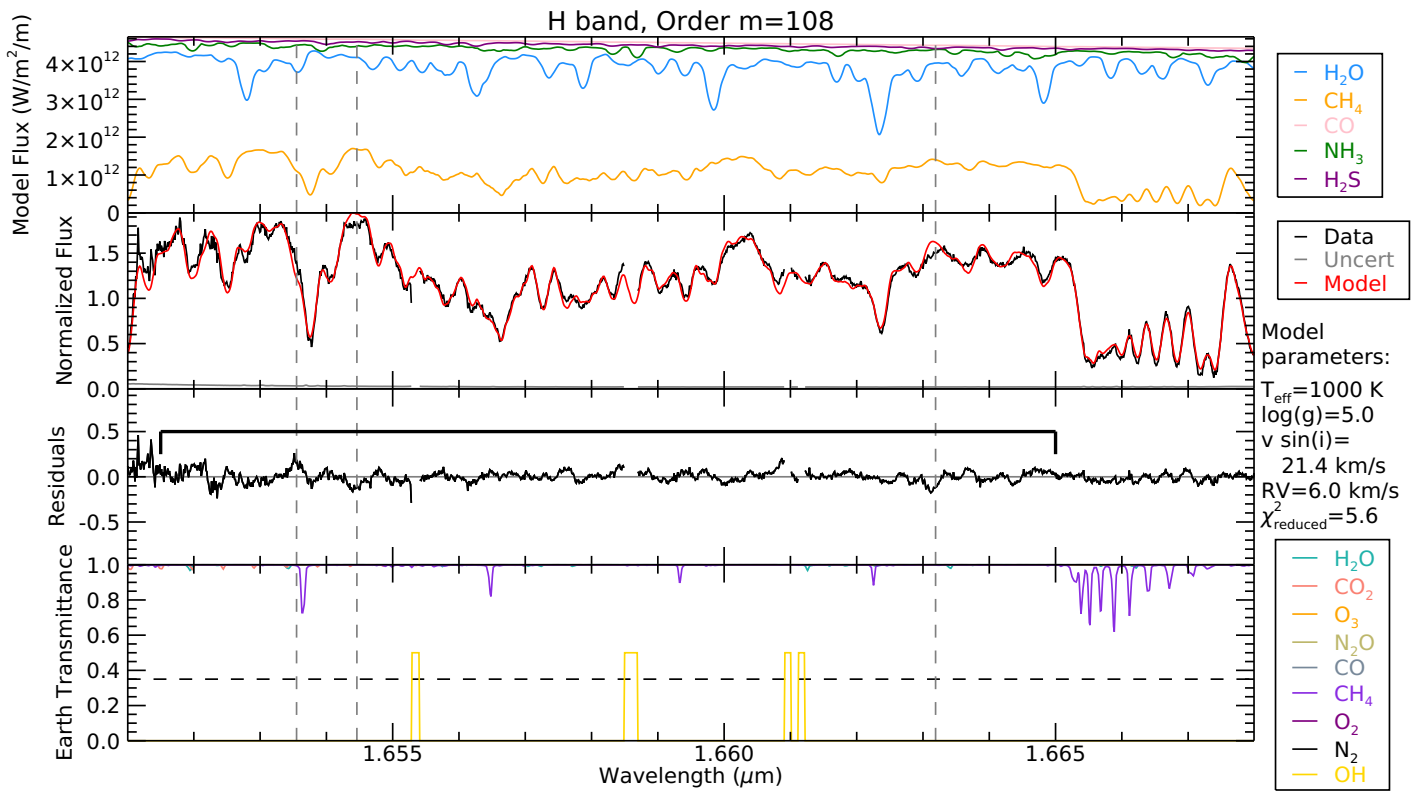
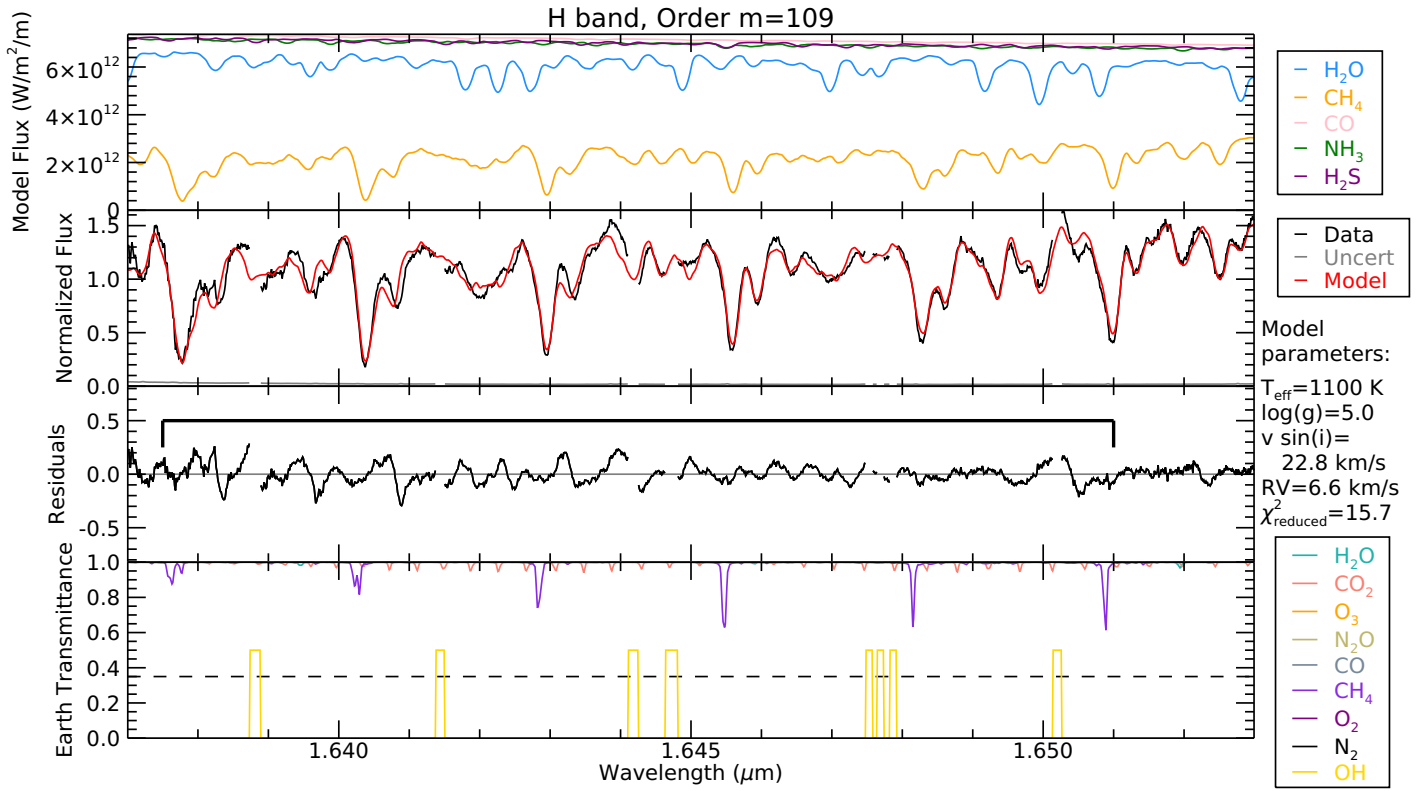


Figure 3.13: Continued.

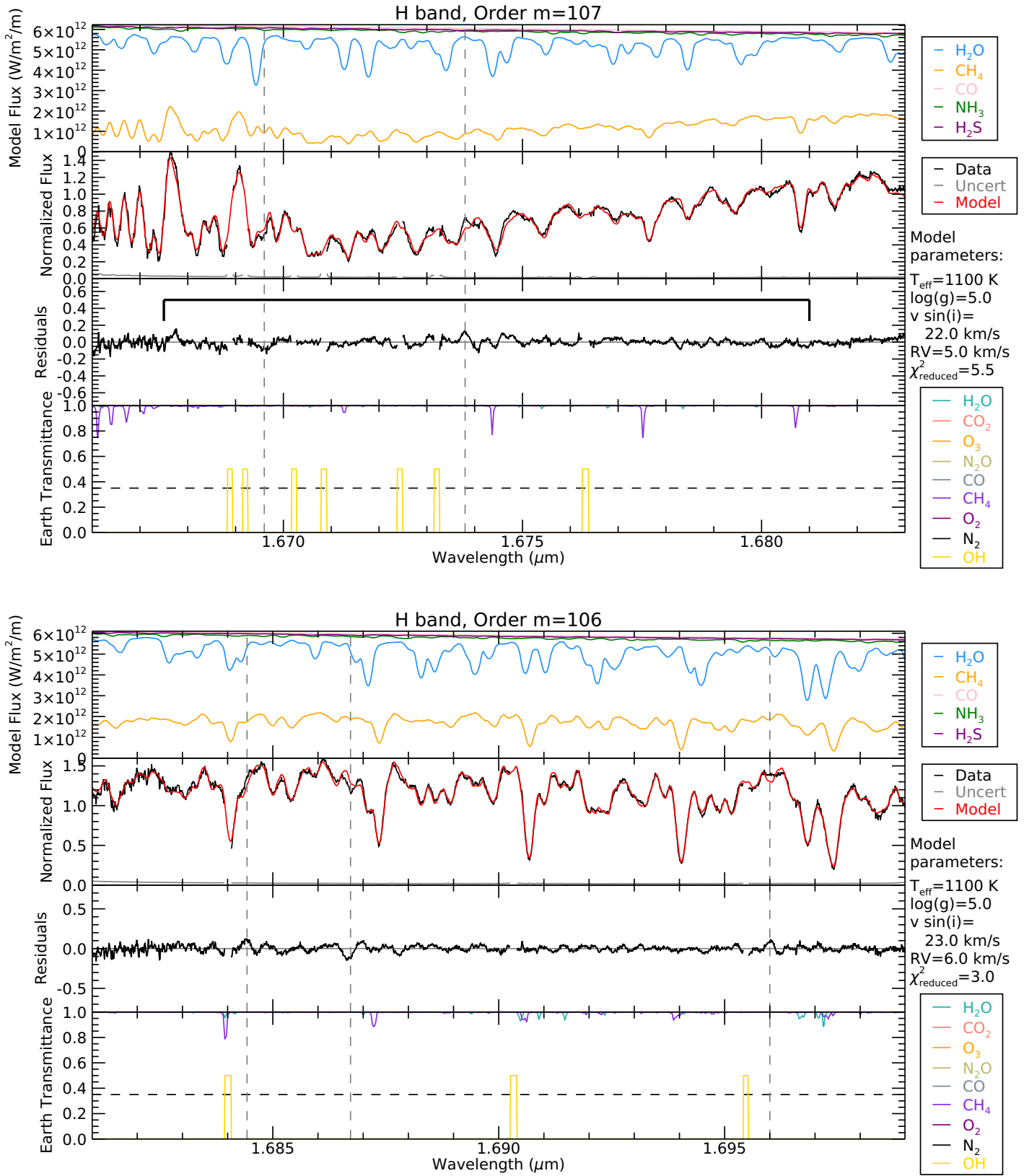


Figure 3.13: Continued.

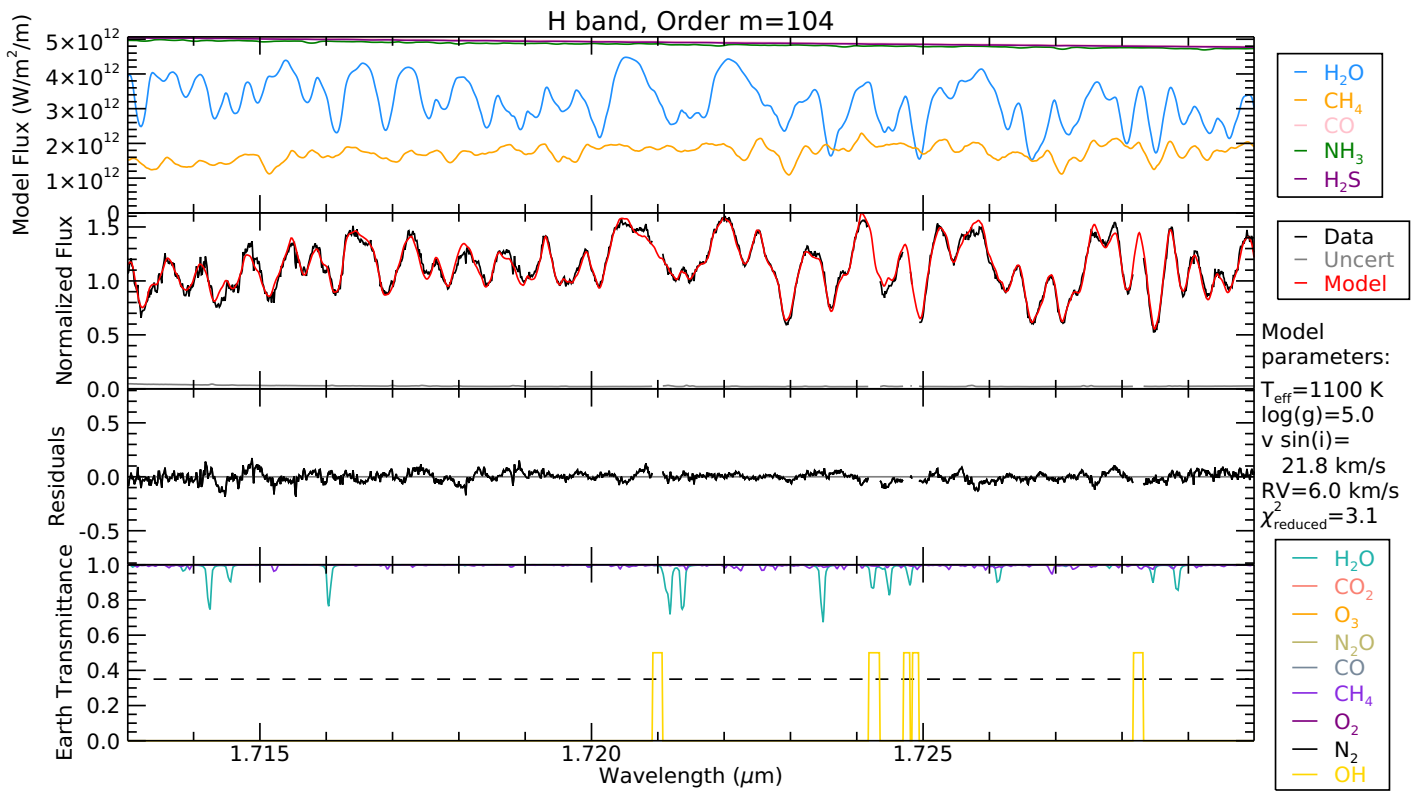
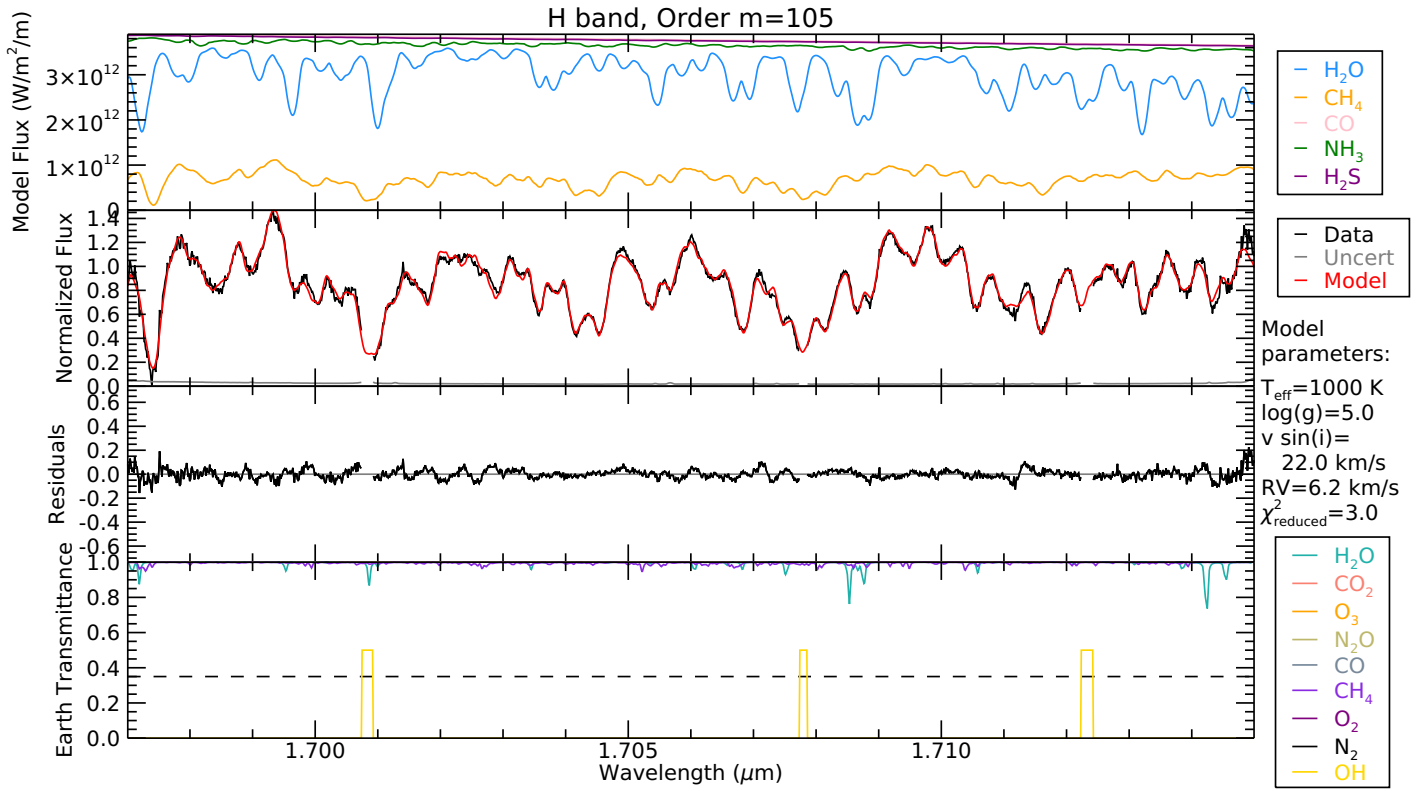


Figure 3.13: Continued.

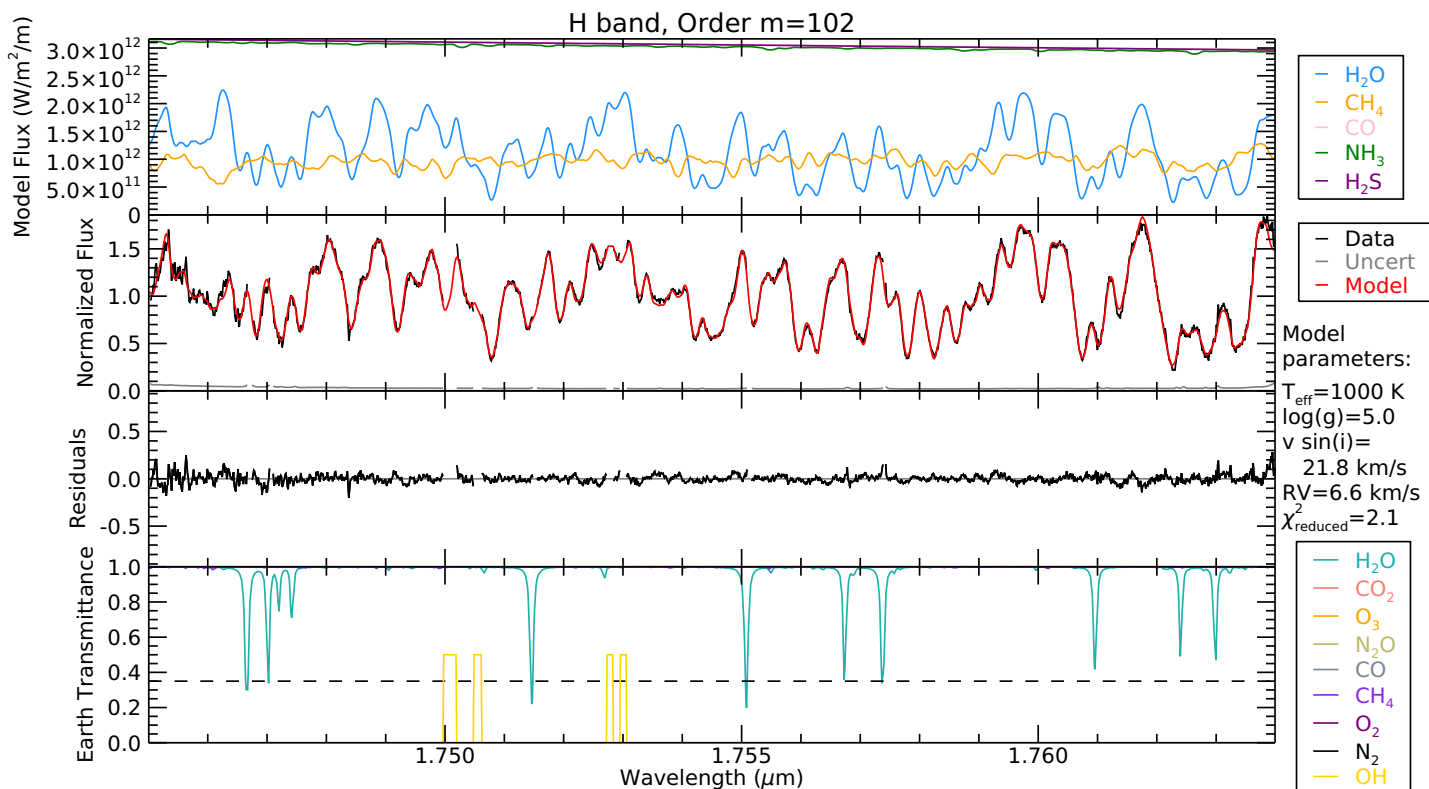
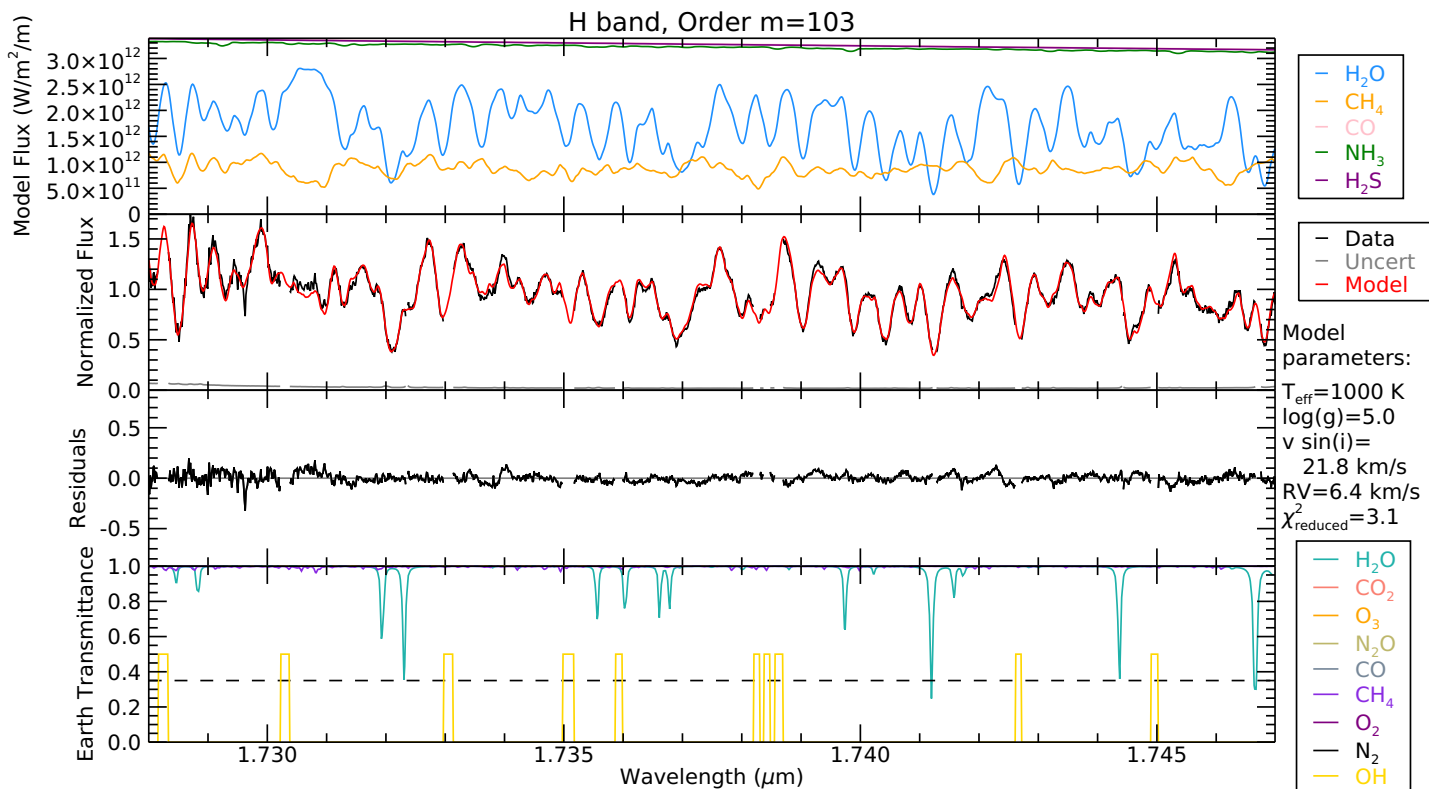


Figure 3.13: Continued.

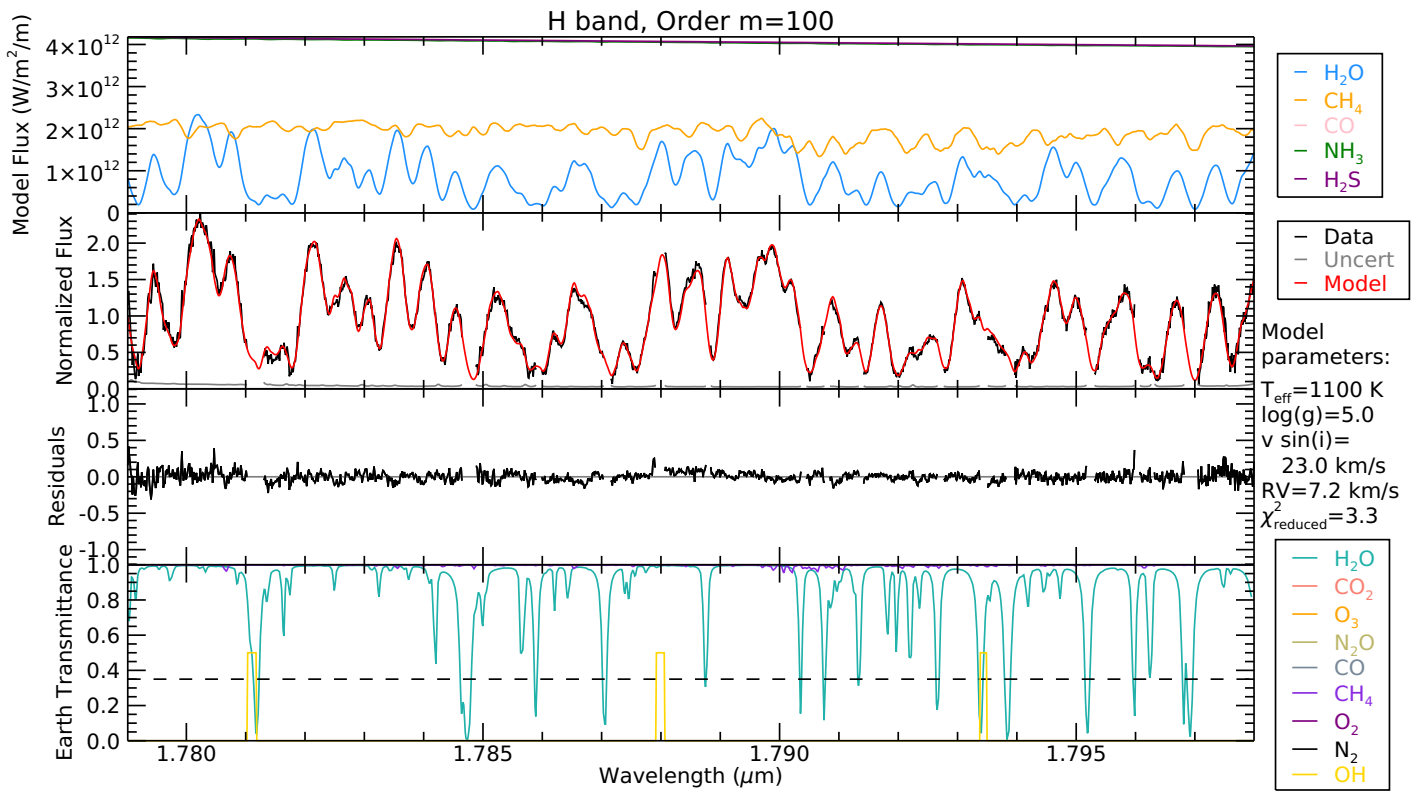
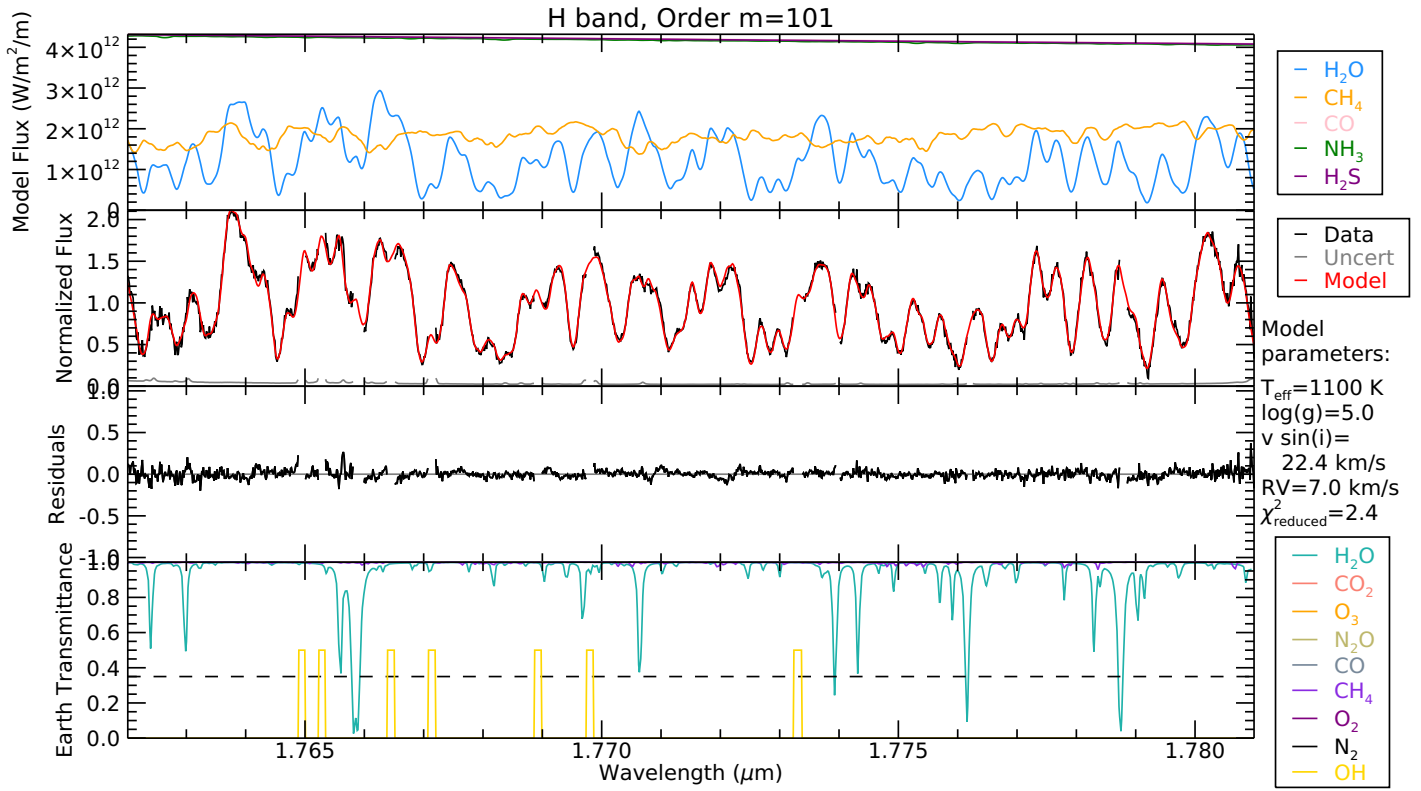


Figure 3.13: Continued.

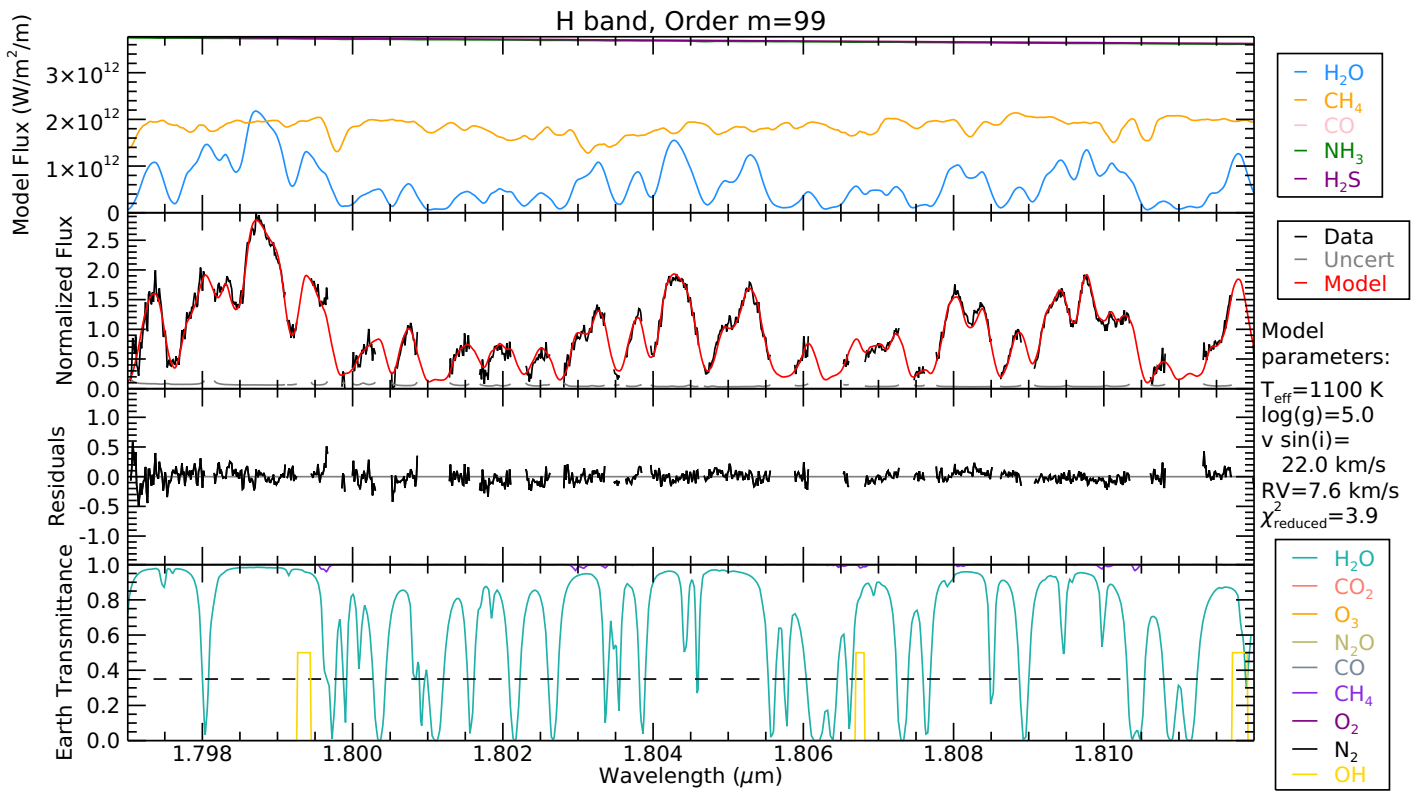


Figure 3.13: Continued.

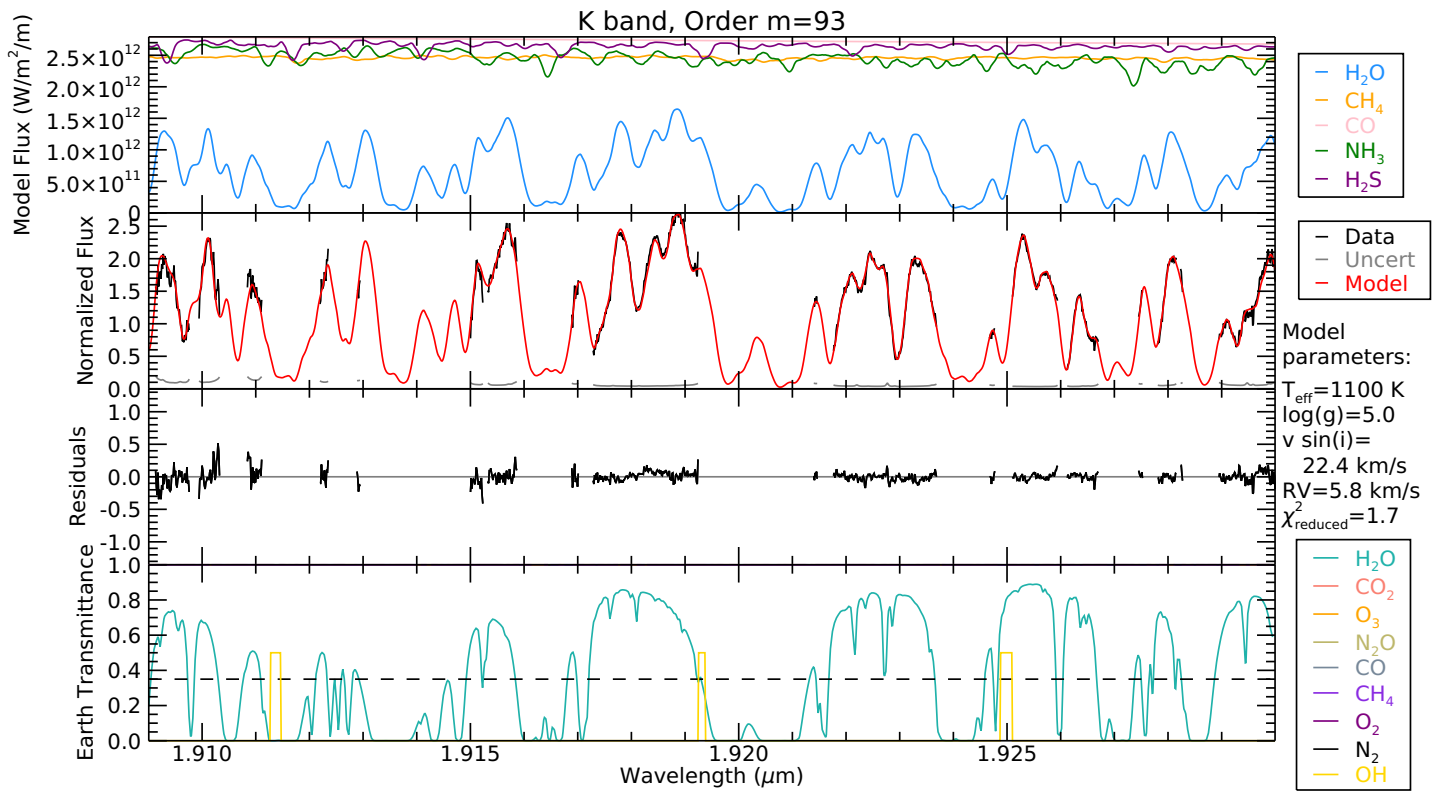
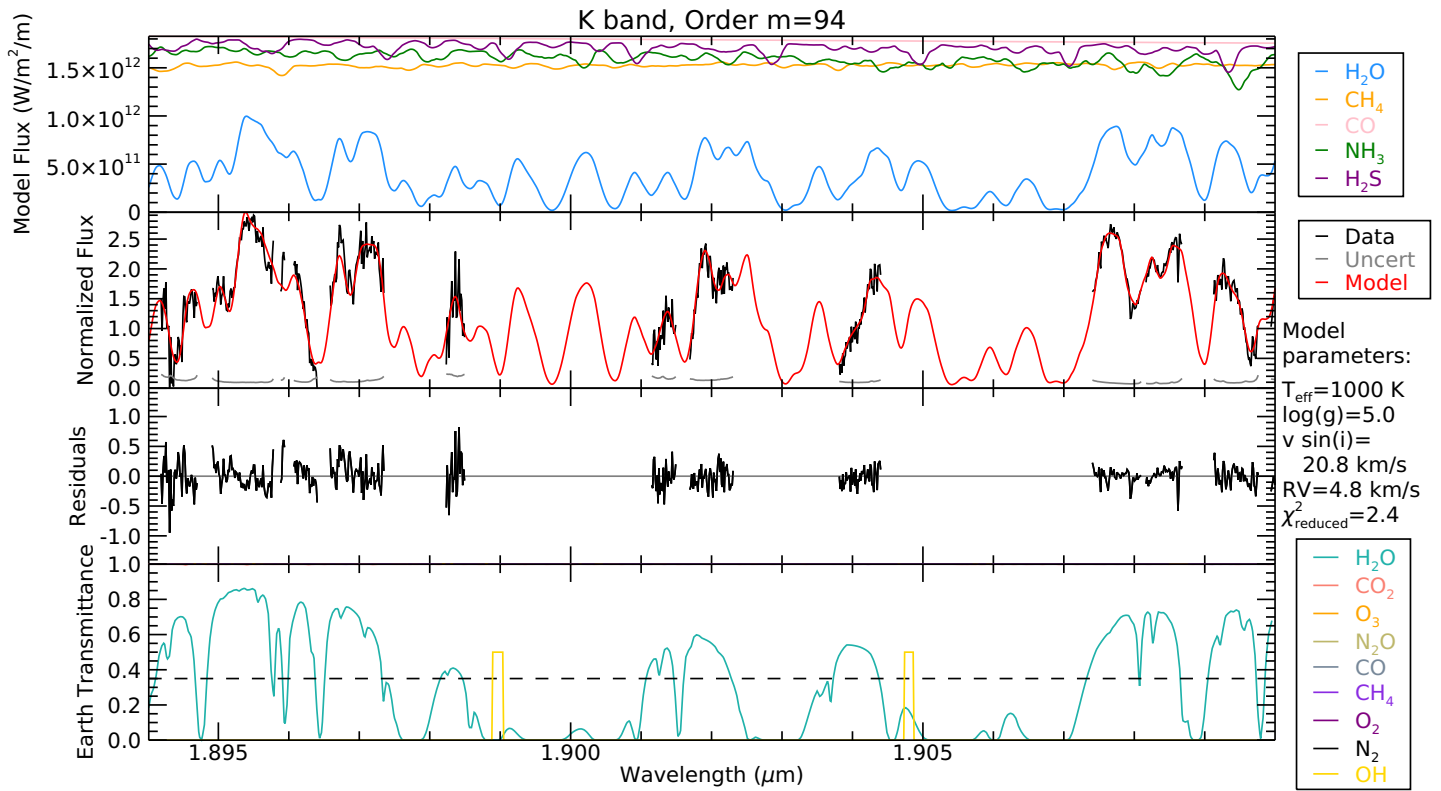


Figure 3.14: The same as Figure 3.13, but for the *K* band. This figure continues for many pages, with two orders per page, to show all 23 orders of the *K* band.

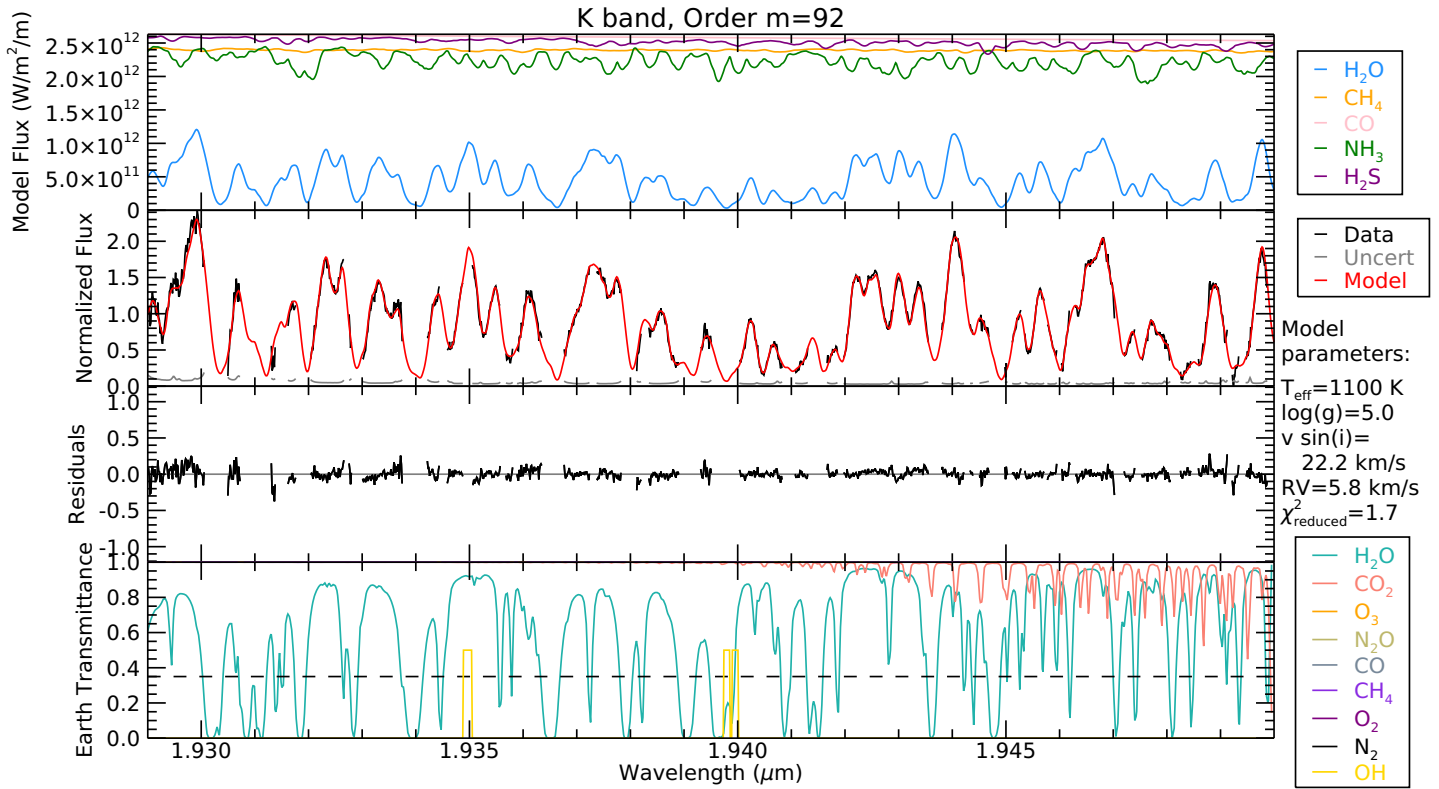


Figure 3.14: Continued.

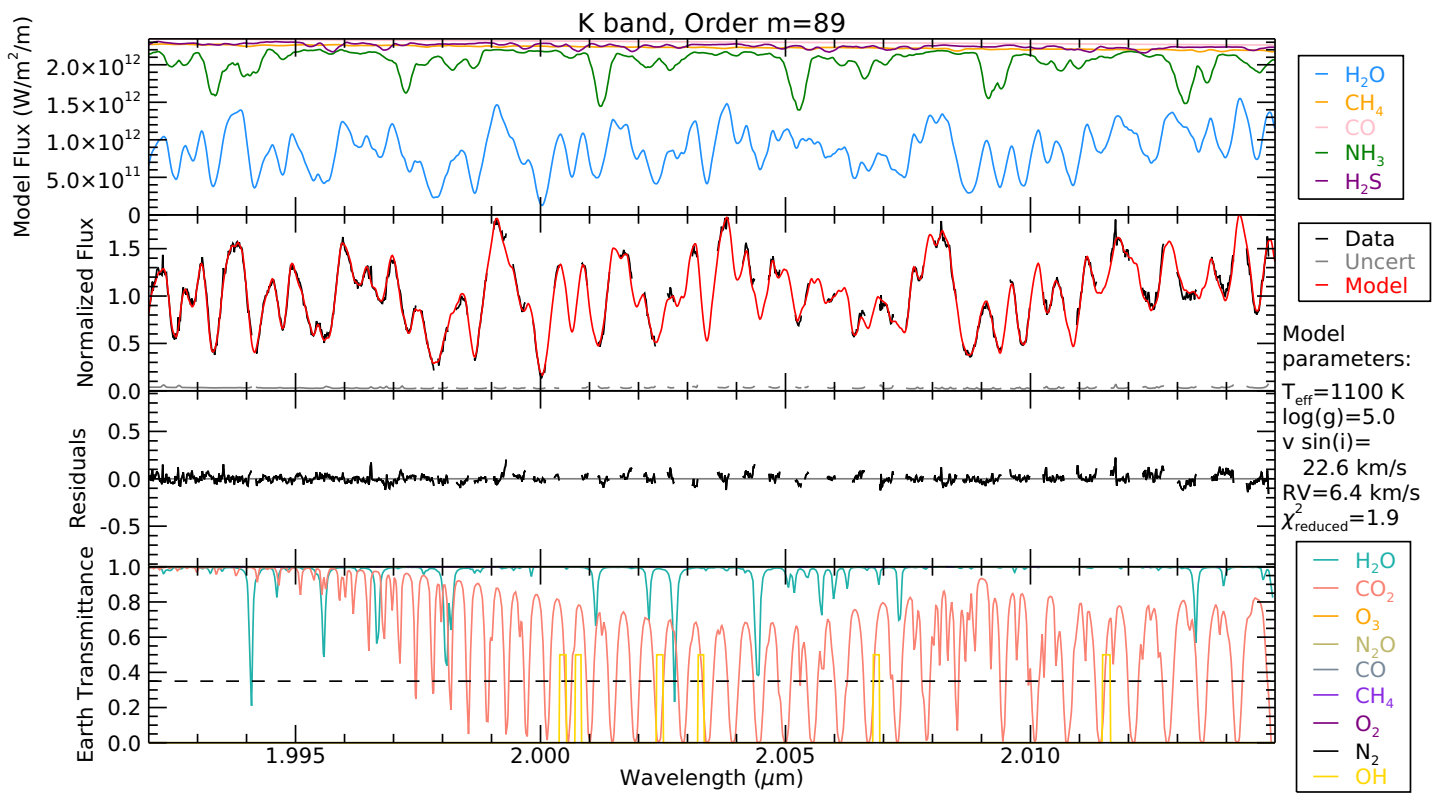
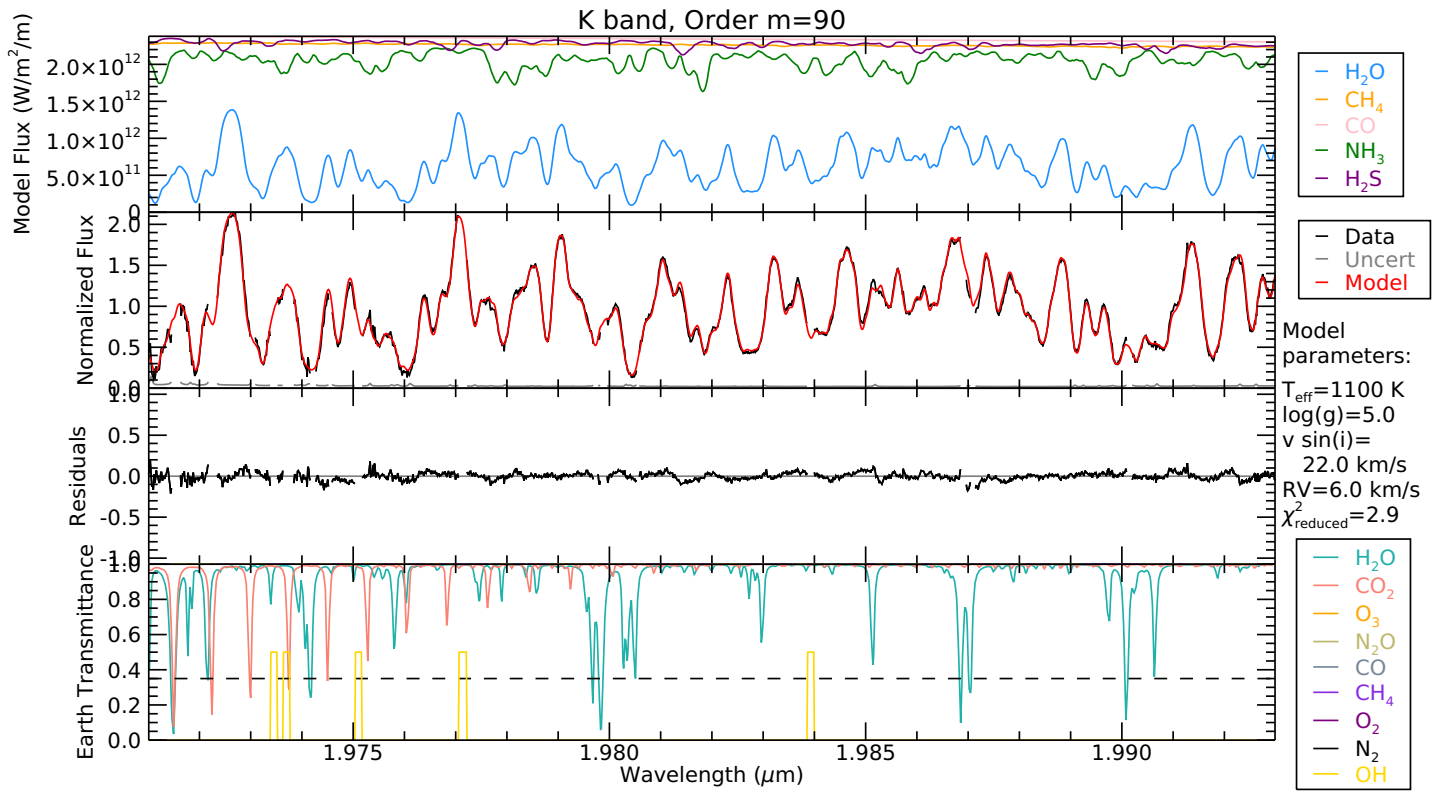


Figure 3.14: Continued.

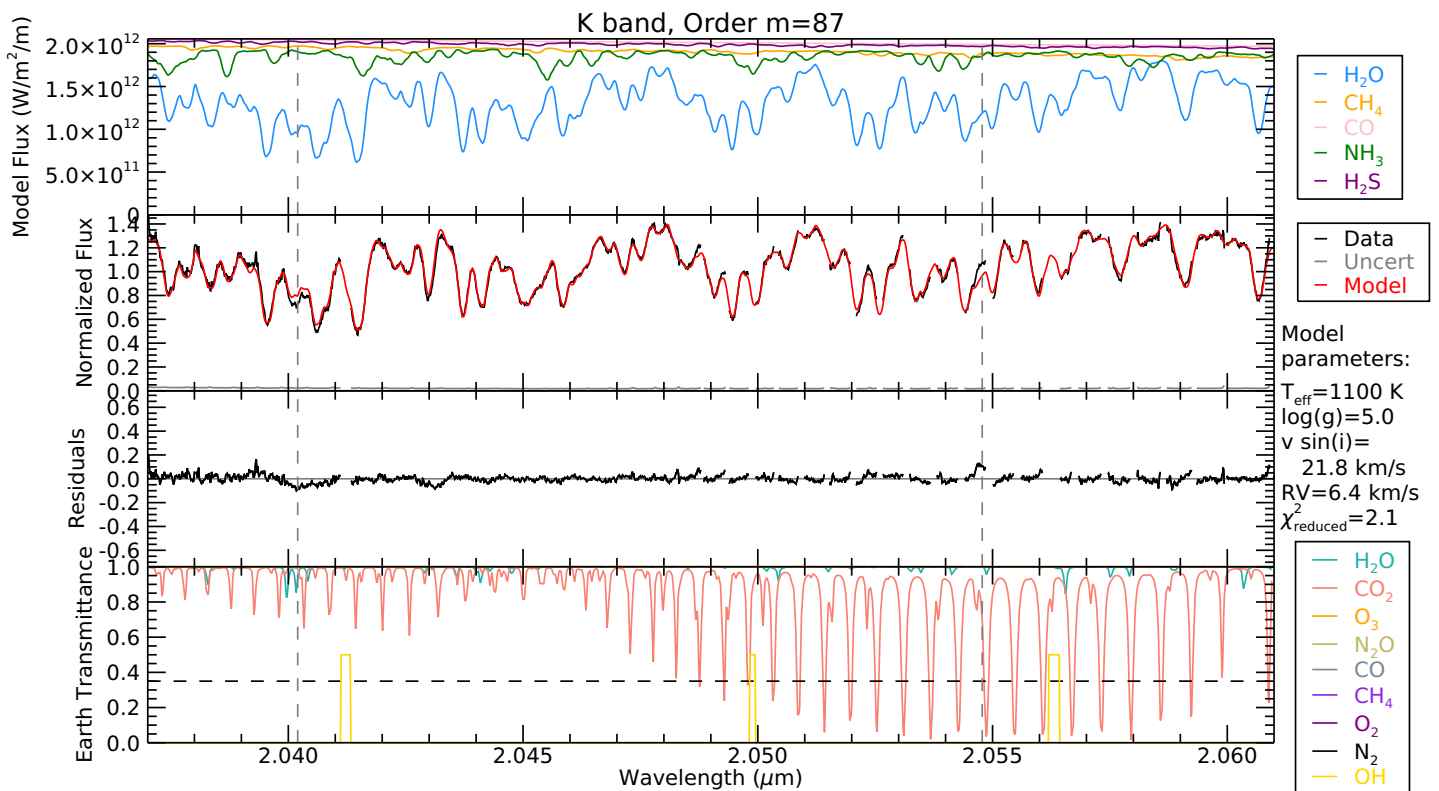
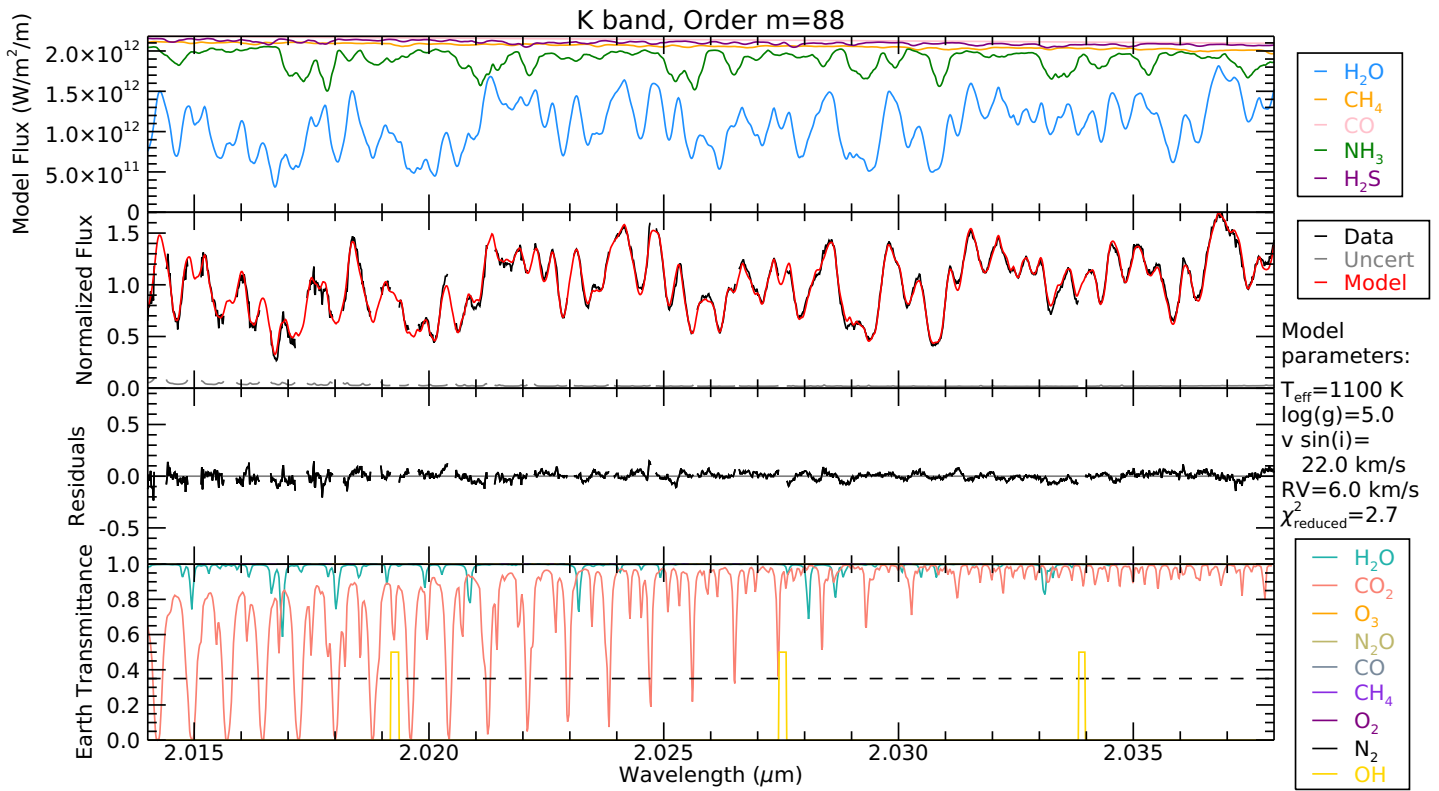


Figure 3.14: Continued.

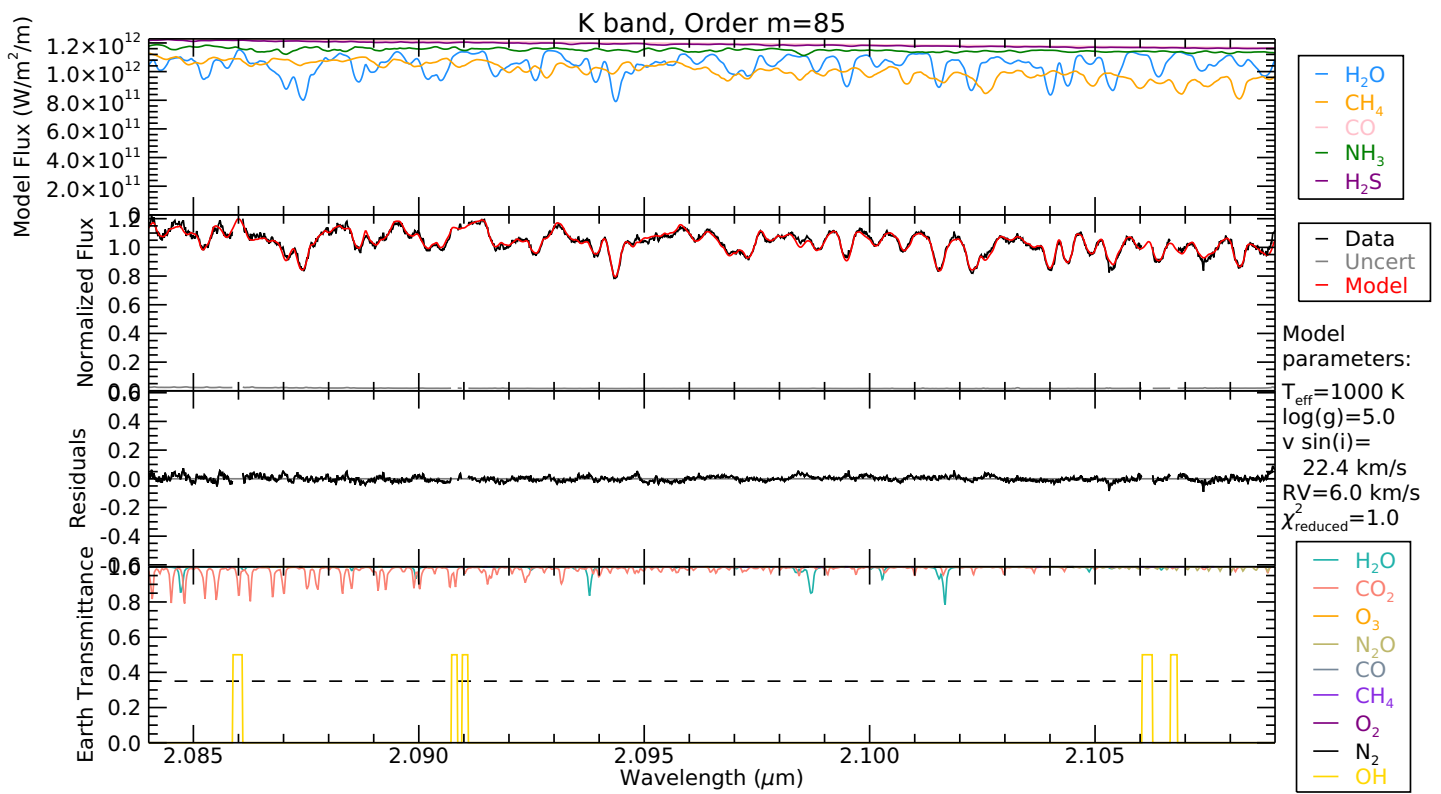
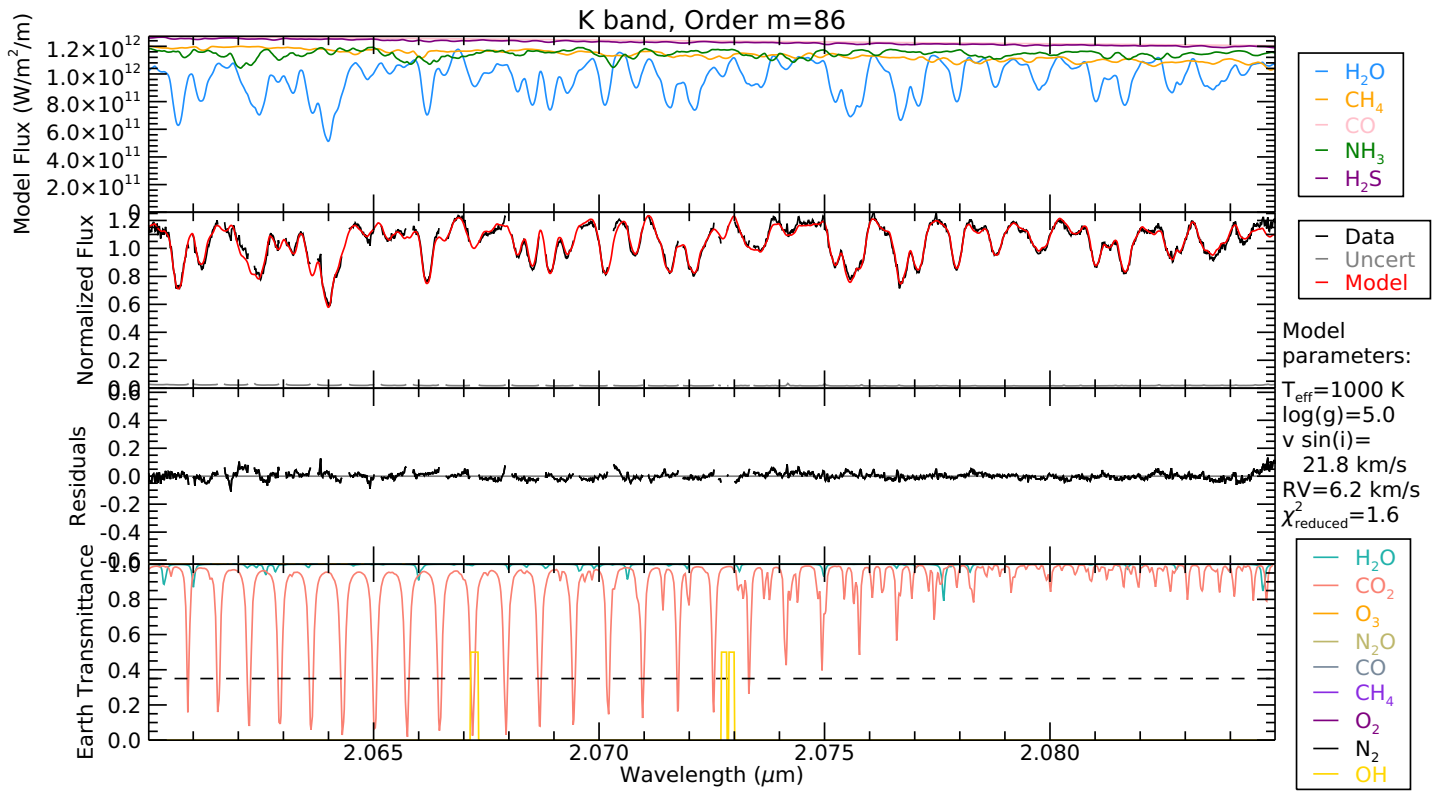


Figure 3.14: Continued.

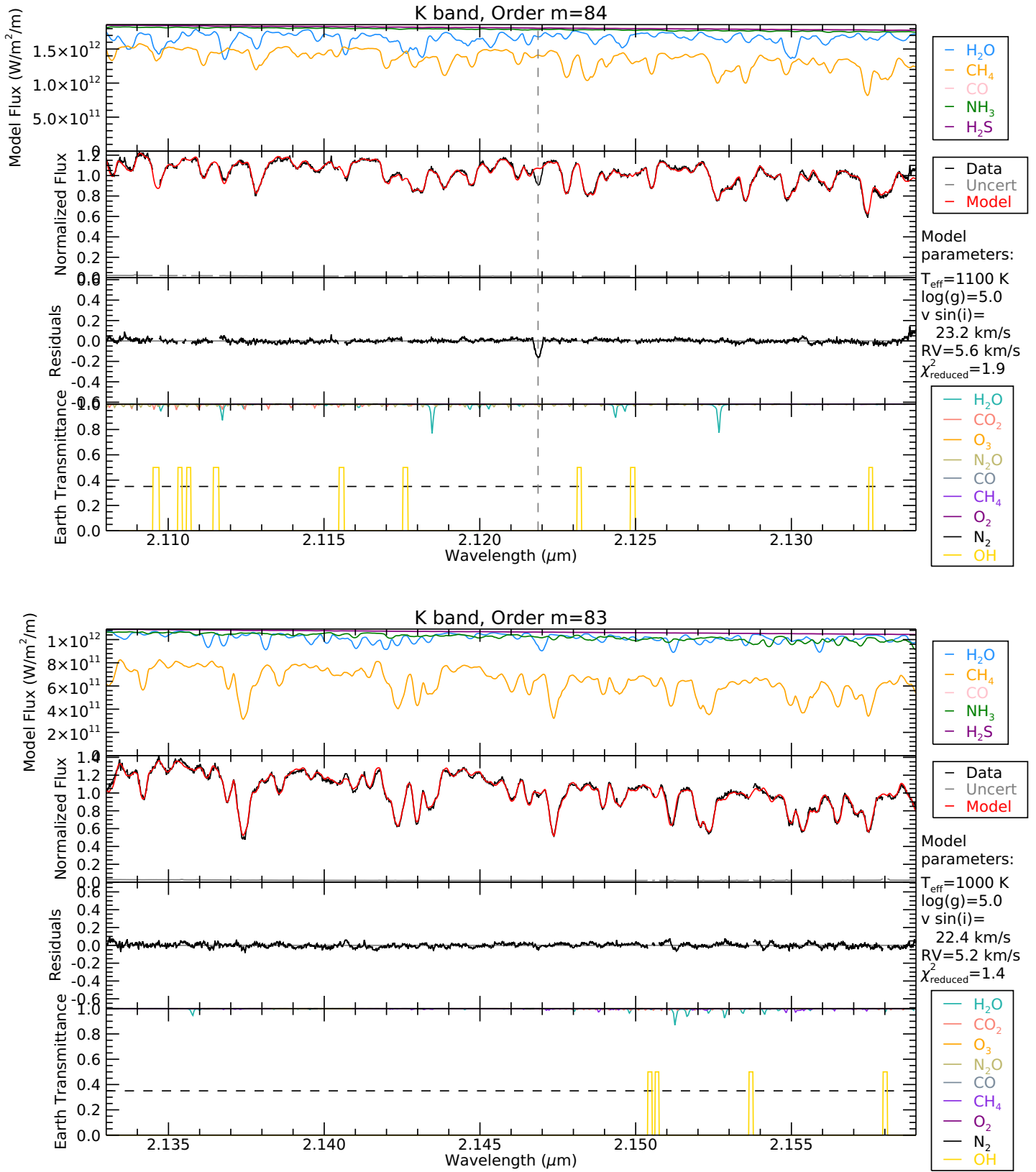


Figure 3.14: Continued.

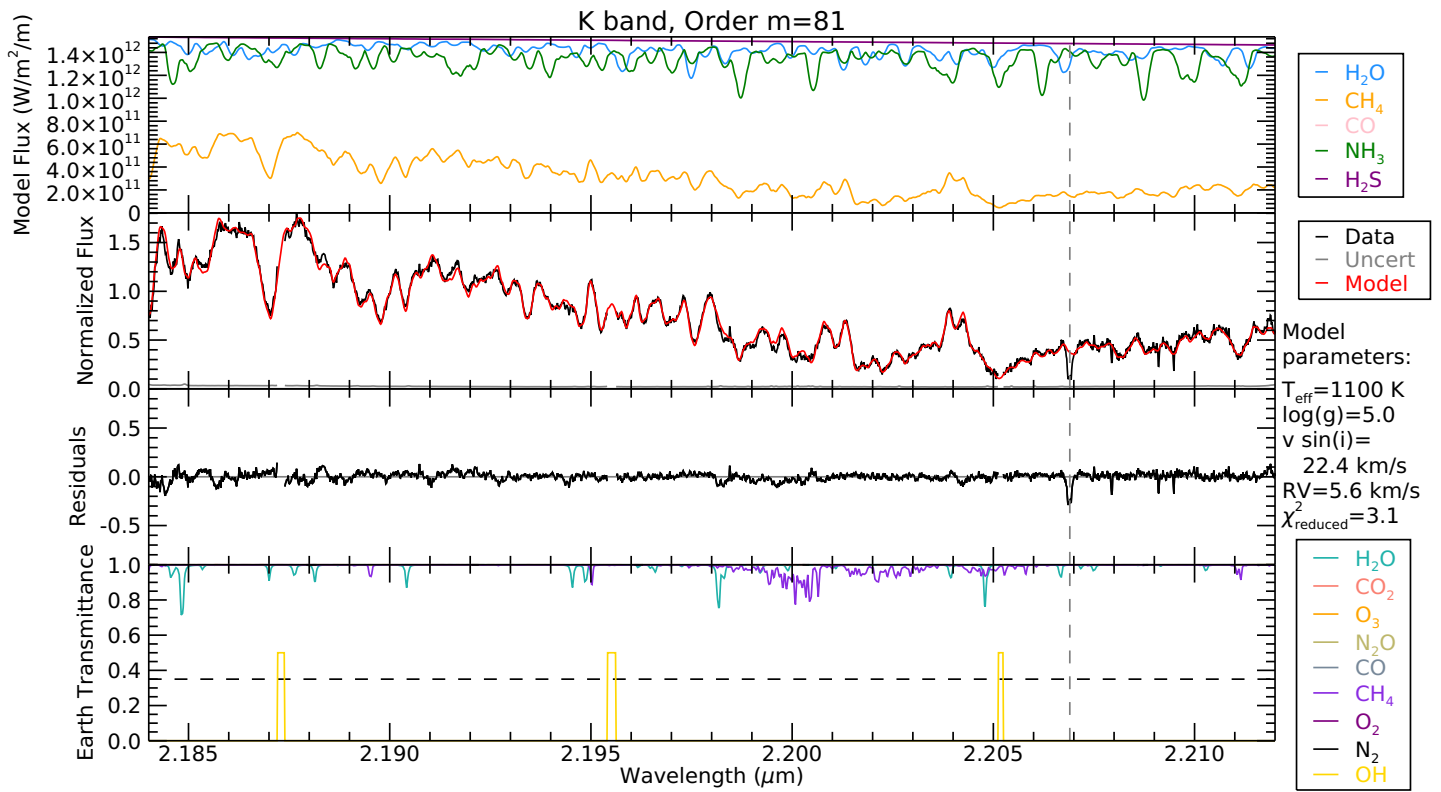
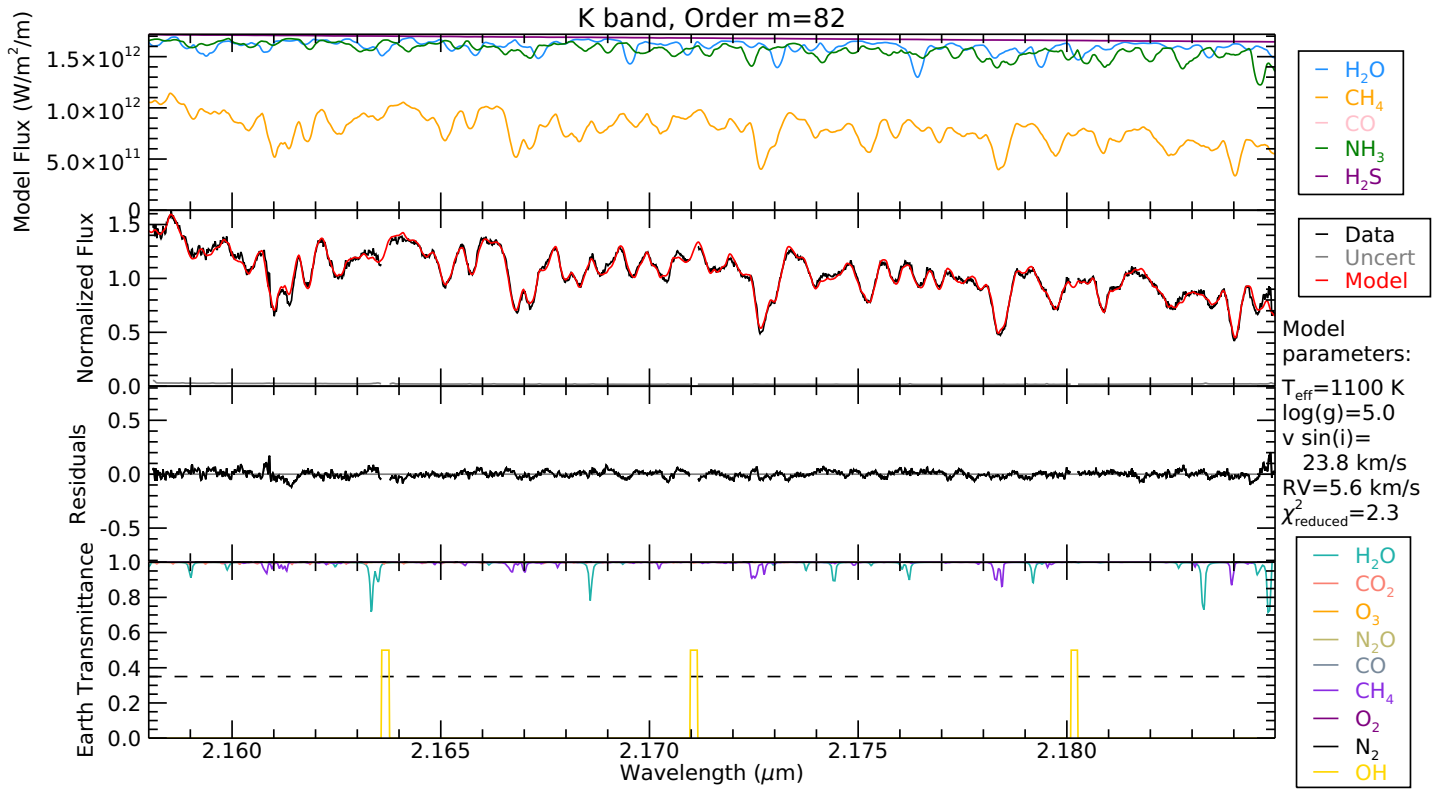


Figure 3.14: Continued.

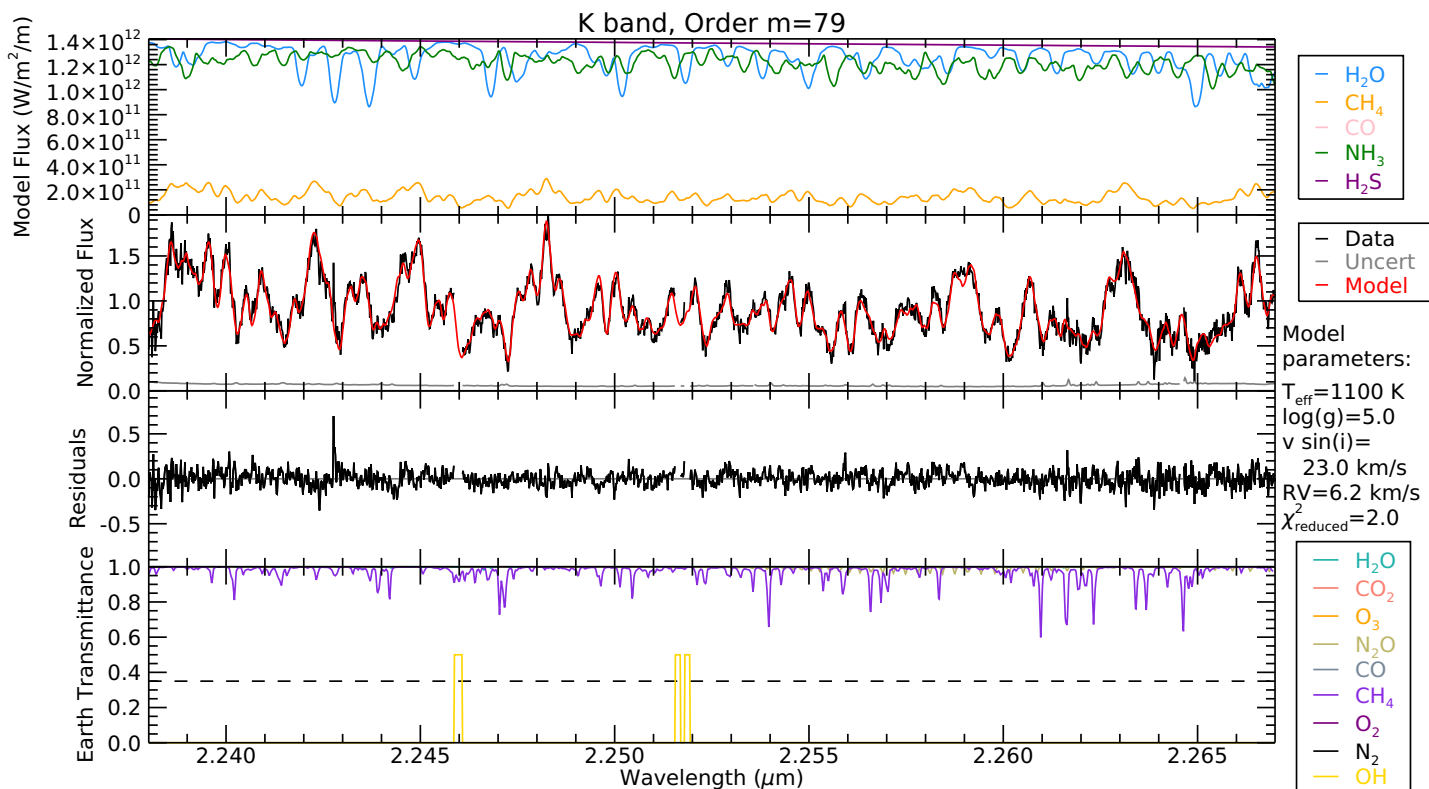
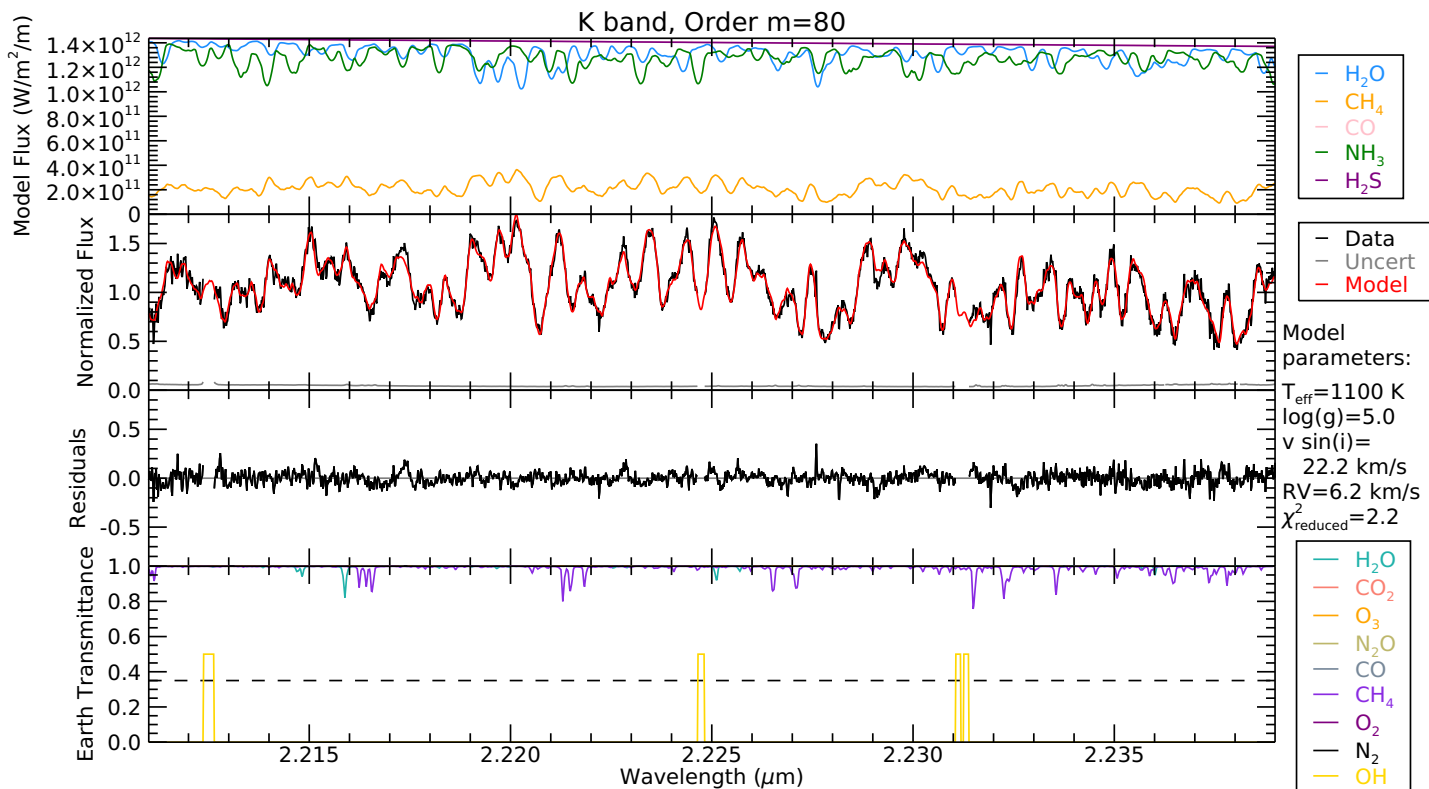


Figure 3.14: Continued.

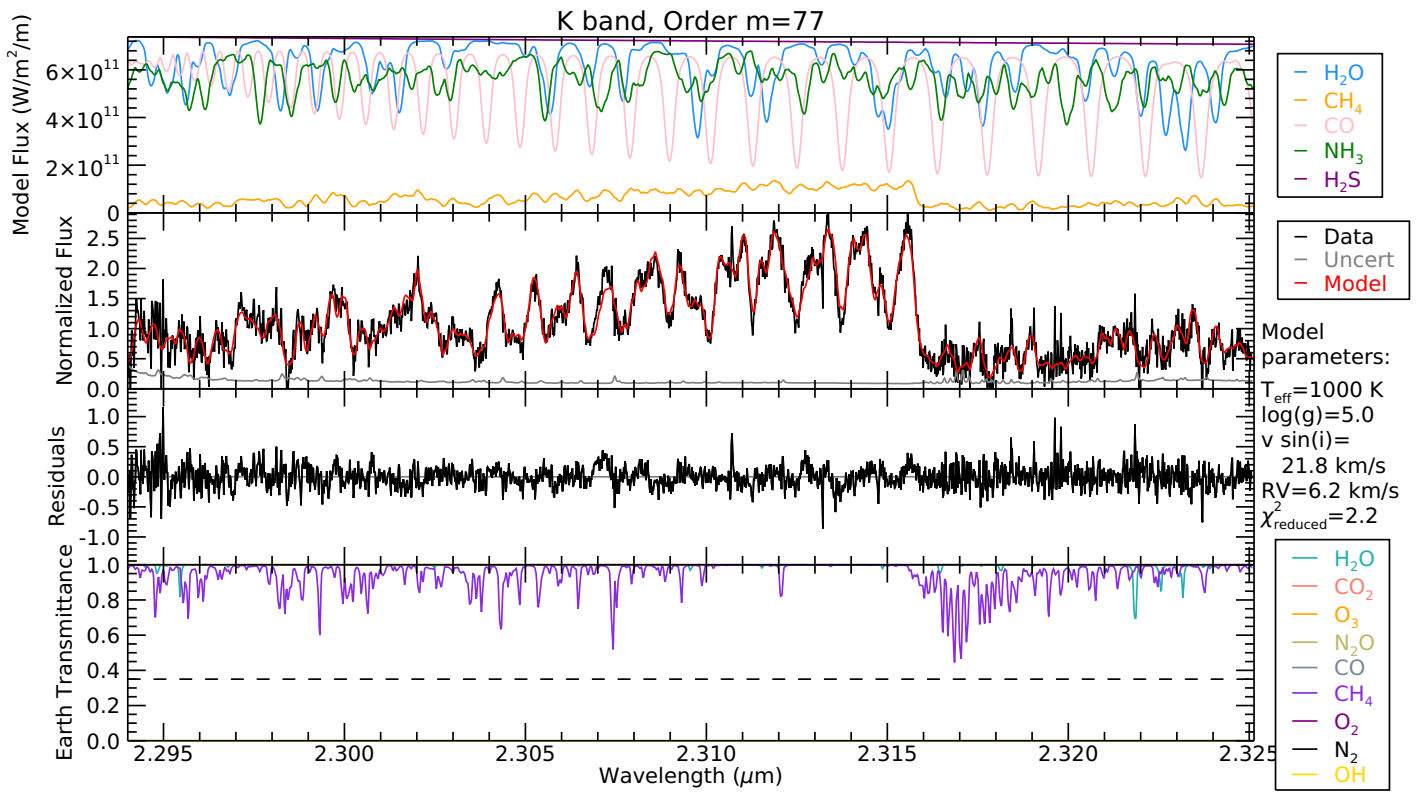
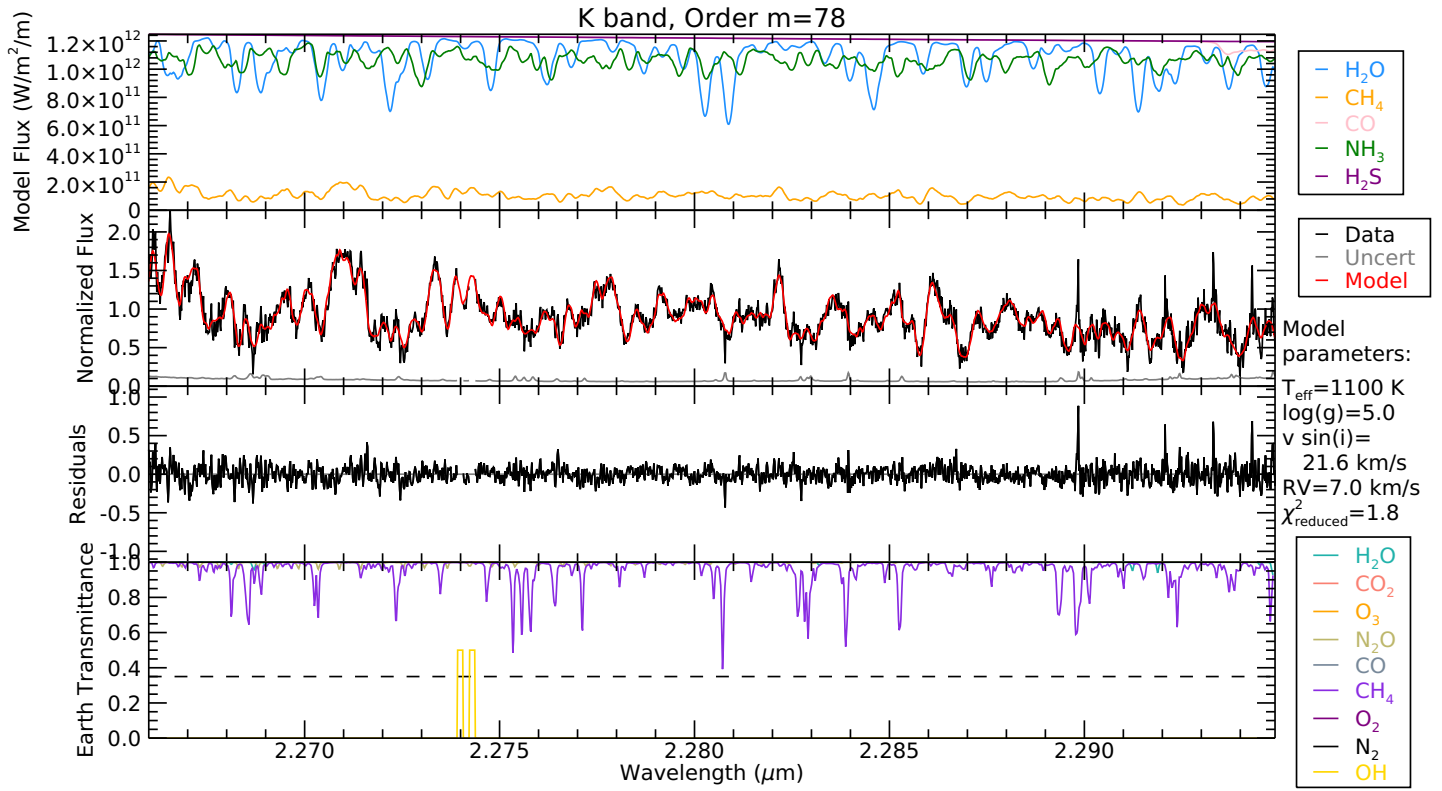


Figure 3.14: Continued.

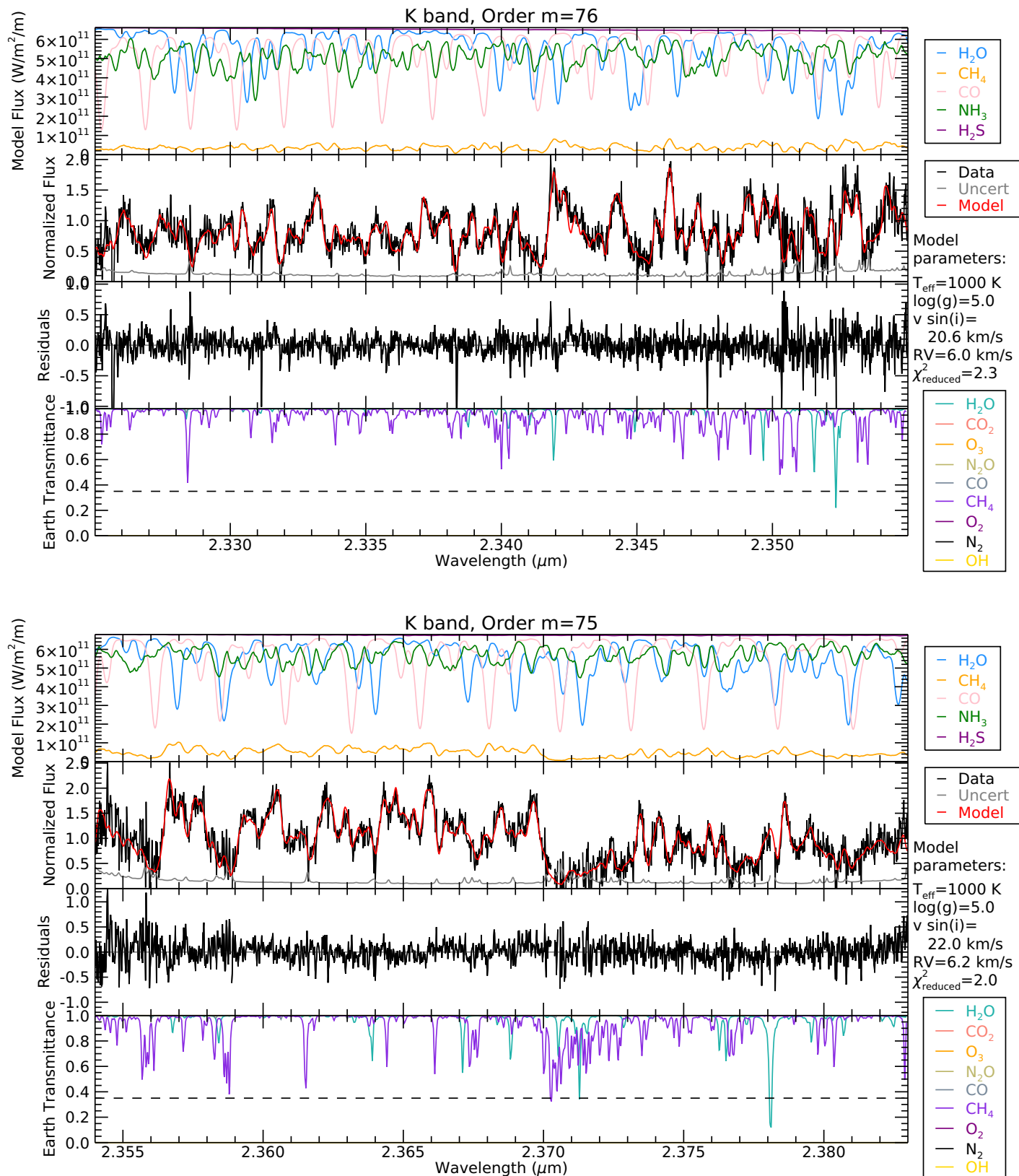


Figure 3.14: Continued.

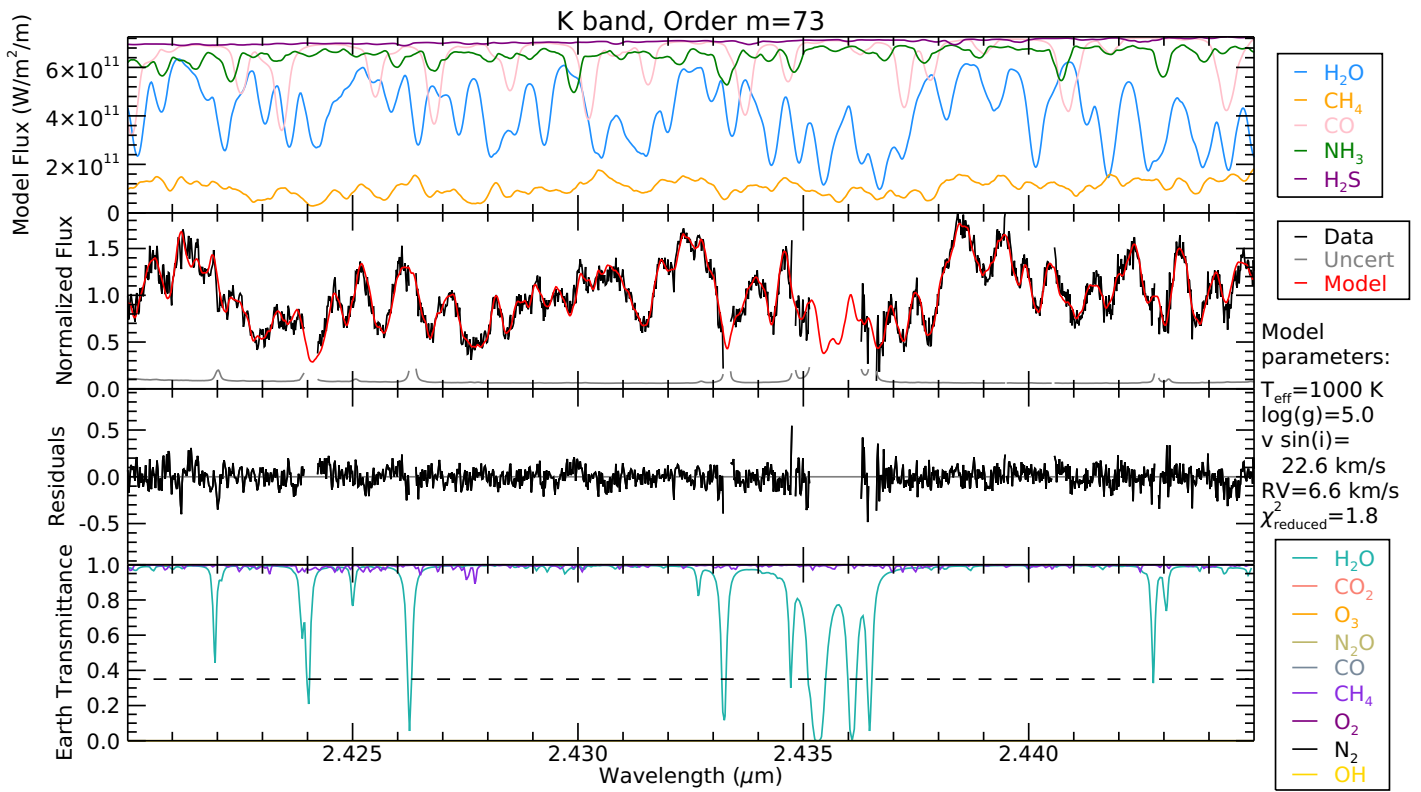
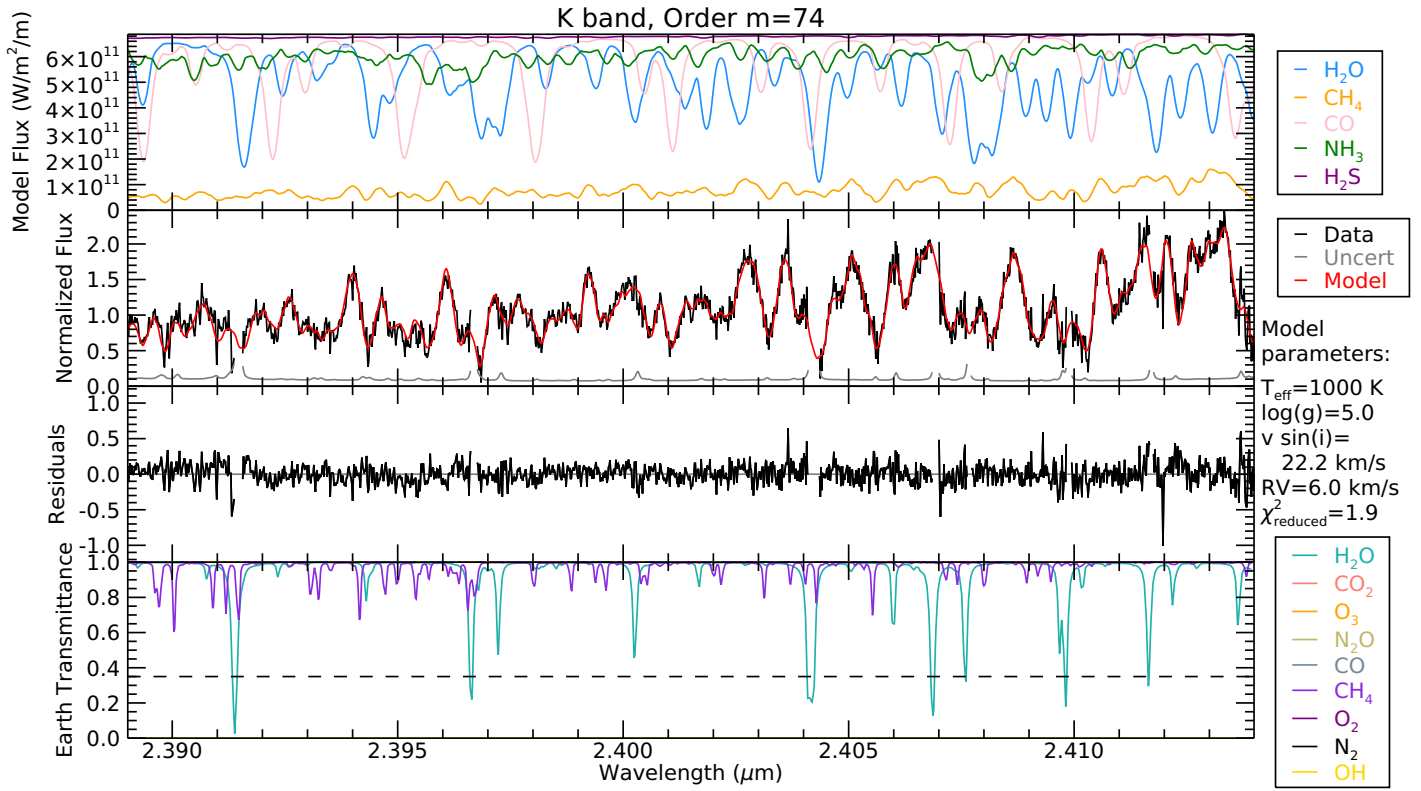


Figure 3.14: Continued.

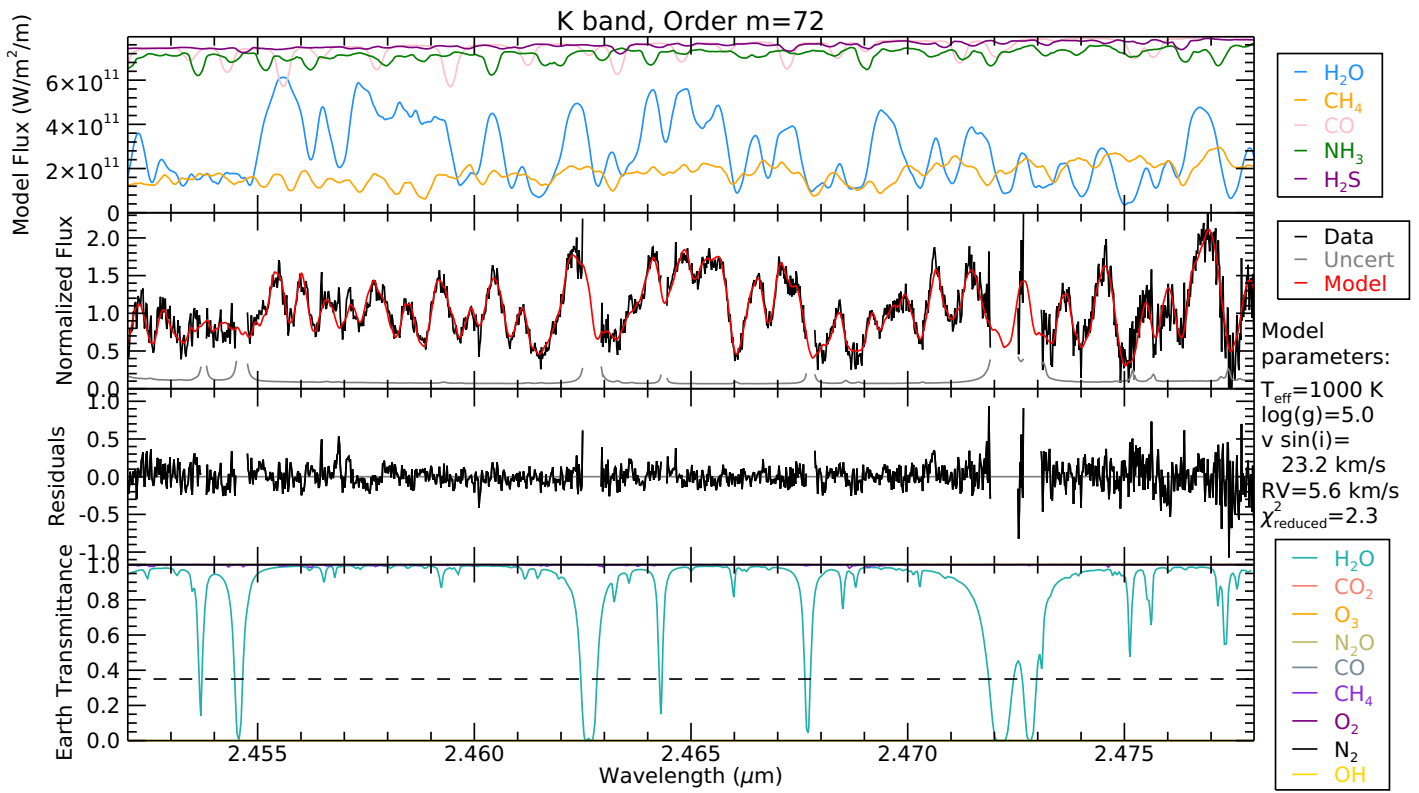


Figure 3.14: Continued.

Bibliography

- Ackerman, A. S., & Marley, M. S. 2001, *ApJ*, 556, 872, doi: [10.1086/321540](https://doi.org/10.1086/321540)
- Allard, F., & Hauschildt, P. H. 1995, *ApJ*, 445, 433, doi: [10.1086/175708](https://doi.org/10.1086/175708)
- Allard, F., Homeier, D., & Freytag, B. 2012, *Philosophical Transactions of the Royal Society of London Series A*, 370, 2765, doi: [10.1098/rsta.2011.0269](https://doi.org/10.1098/rsta.2011.0269)
- Allard, F., Homeier, D., & Freytag, B. 2014, in *Astronomical Society of India Conference Series*, Vol. 11, *Astronomical Society of India Conference Series*, 33–45
- Artigau, É., Radigan, J., Folkes, S., et al. 2010, *ApJ Letters*, 718, L38, doi: [10.1088/2041-8205/718/1/L38](https://doi.org/10.1088/2041-8205/718/1/L38)
- Azzam, A. A. A., Lodi, L., Yurchenko, S. N., & Tennyson, J. 2015, *J. Quant. Spectrosc. Radiative Transfer*, 161, 41, doi: [10.1016/j.jqsrt.2015.03.029](https://doi.org/10.1016/j.jqsrt.2015.03.029)
- Barber, R. J., Tennyson, J., Harris, G. J., & Tolchenov, R. N. 2006, *MNRAS*, 368, 1087, doi: [10.1111/j.1365-2966.2006.10184.x](https://doi.org/10.1111/j.1365-2966.2006.10184.x)
- Beichman, C., Gelino, C. R., Kirkpatrick, J. D., et al. 2014, *ApJ*, 783, 68, doi: [10.1088/0004-637X/783/2/68](https://doi.org/10.1088/0004-637X/783/2/68)
- Bochanski, J. J., Burgasser, A. J., Simcoe, R. A., & West, A. A. 2011, *AJ*, 142, 169, doi: [10.1088/0004-6256/142/5/169](https://doi.org/10.1088/0004-6256/142/5/169)
- Burgasser, A. J., Geballe, T. R., Leggett, S. K., Kirkpatrick, J. D., & Golimowski, D. A. 2006, *ApJ*, 637, 1067, doi: [10.1086/498563](https://doi.org/10.1086/498563)
- Burrows, A., Marley, M., Hubbard, W. B., et al. 1997, *ApJ*, 491, 856, doi: [10.1086/305002](https://doi.org/10.1086/305002)
- Canty, J. I., Lucas, P. W., Yurchenko, S. N., et al. 2015, *MNRAS*, 450, 454, doi: [10.1093/mnras/stv586](https://doi.org/10.1093/mnras/stv586)

- Coles, P. A., Yurchenko, S. N., & Tennyson, J. 2019, MNRAS, 490, 4638, doi: [10.1093/mnras/stz2778](https://doi.org/10.1093/mnras/stz2778)
- Cushing, M. C., Roellig, T. L., Marley, M. S., et al. 2006, ApJ, 648, 614, doi: [10.1086/505637](https://doi.org/10.1086/505637)
- Cushing, M. C., Kirkpatrick, J. D., Gelino, C. R., et al. 2011, ApJ, 743, 50, doi: [10.1088/0004-637X/743/1/50](https://doi.org/10.1088/0004-637X/743/1/50)
- Cushing, M. C., Schneider, A. C., Kirkpatrick, J. D., et al. 2021, ApJ, 920, 20, doi: [10.3847/1538-4357/ac12cb](https://doi.org/10.3847/1538-4357/ac12cb)
- Cutri, R. M., Skrutskie, M. F., van Dyk, S., et al. 2003, VizieR Online Data Catalog, II/246
- Fegley, Bruce, J., & Lodders, K. 1996, ApJ Letters, 472, L37, doi: [10.1086/310356](https://doi.org/10.1086/310356)
- Filippazzo, J. C., Rice, E. L., Faherty, J., et al. 2015, ApJ, 810, 158, doi: [10.1088/0004-637X/810/2/158](https://doi.org/10.1088/0004-637X/810/2/158)
- Fortney, J. J., Marley, M. S., Saumon, D., & Lodders, K. 2008, ApJ, 683, 1104, doi: [10.1086/589942](https://doi.org/10.1086/589942)
- Freedman, R. S., Lustig-Yaeger, J., Fortney, J. J., et al. 2014, ApJS, 214, 25, doi: [10.1088/0067-0049/214/2/25](https://doi.org/10.1088/0067-0049/214/2/25)
- Gaia Collaboration. 2018, VizieR Online Data Catalog, I/345
- Geballe, T. R., Kulkarni, S. R., Woodward, C. E., & Sloan, G. C. 1996, ApJ Letters, 467, L101, doi: [10.1086/310203](https://doi.org/10.1086/310203)
- Geballe, T. R., Saumon, D., Golimowski, D. A., et al. 2009, ApJ, 695, 844, doi: [10.1088/0004-637X/695/2/844](https://doi.org/10.1088/0004-637X/695/2/844)
- Giacobbe, P., Brogi, M., Gandhi, S., et al. 2021, Nature, 592, 205, doi: [10.1038/s41586-021-03381-x](https://doi.org/10.1038/s41586-021-03381-x)
- Golimowski, D. A., Leggett, S. K., Marley, M. S., et al. 2004, AJ, 127, 3516, doi: [10.1086/420709](https://doi.org/10.1086/420709)
- Goorvitch, D. 1994, ApJS, 95, 535, doi: [10.1086/192110](https://doi.org/10.1086/192110)
- Gray, D. F. 1992, The observation and analysis of stellar photospheres. (Cambridge University Press). <http://adsabs.harvard.edu/abs/1992oasp.book.....G>

- Guilluy, G., Sozzetti, A., Brogi, M., et al. 2019, *A&A*, 625, A107, doi: [10.1051/0004-6361/201834615](https://doi.org/10.1051/0004-6361/201834615)
- Hargreaves, R. J., Gordon, I. E., Rey, M., et al. 2020, *ApJS*, 247, 55, doi: [10.3847/1538-4365/ab7a1a](https://doi.org/10.3847/1538-4365/ab7a1a)
- Hauschildt, P. H., Allard, F., & Baron, E. 1999, *ApJ*, 512, 377, doi: [10.1086/306745](https://doi.org/10.1086/306745)
- Hood, C. E., et al. in prep.
- Irwin, P. G. J., Toledo, D., Garland, R., et al. 2018, *Nature Astronomy*, 2, 420, doi: [10.1038/s41550-018-0432-1](https://doi.org/10.1038/s41550-018-0432-1)
- . 2019, *Icarus*, 321, 550, doi: [10.1016/j.icarus.2018.12.014](https://doi.org/10.1016/j.icarus.2018.12.014)
- Lee, J.-J., & Gullikson, K. 2016, plp: v2.1 alpha 3, v2.1-alpha.3, Zenodo, doi: [10.5281/zenodo.56067](https://doi.org/10.5281/zenodo.56067)
- Léger, A., Mariotti, J. M., Mennesson, B., et al. 1996, *Icarus*, 123, 249, doi: [10.1006/icar.1996.0155](https://doi.org/10.1006/icar.1996.0155)
- Leggett, S. K., Saumon, D., Marley, M. S., et al. 2012, *ApJ*, 748, 74, doi: [10.1088/0004-637X/748/2/74](https://doi.org/10.1088/0004-637X/748/2/74)
- Leggett, S. K., Dupuy, T. J., Morley, C. V., et al. 2019, *ApJ*, 882, 117, doi: [10.3847/1538-4357/ab3393](https://doi.org/10.3847/1538-4357/ab3393)
- Li, G., Gordon, I. E., Rothman, L. S., et al. 2015, *ApJS*, 216, 15, doi: [10.1088/0067-0049/216/1/15](https://doi.org/10.1088/0067-0049/216/1/15)
- Line, M. R., Teske, J., Burningham, B., Fortney, J. J., & Marley, M. S. 2015, *ApJ*, 807, 183, doi: [10.1088/0004-637X/807/2/183](https://doi.org/10.1088/0004-637X/807/2/183)
- Line, M. R., Marley, M. S., Liu, M. C., et al. 2017, *ApJ*, 848, 83, doi: [10.3847/1538-4357/aa7ff0](https://doi.org/10.3847/1538-4357/aa7ff0)
- Line, M. R., Brogi, M., Bean, J. L., et al. 2021, *Nature*, 598, 580, doi: [10.1038/s41586-021-03912-6](https://doi.org/10.1038/s41586-021-03912-6)
- Lodders, K., & Fegley, B. 2002, *Icarus*, 155, 393, doi: [10.1006/icar.2001.6740](https://doi.org/10.1006/icar.2001.6740)
- Luhman, K. L., & Esplin, T. L. 2016, *AJ*, 152, 78, doi: [10.3847/0004-6256/152/3/78](https://doi.org/10.3847/0004-6256/152/3/78)

- Lupu, R. E., Zahnle, K., Marley, M. S., et al. 2014, *ApJ*, 784, 27, doi: [10.1088/0004-637X/784/1/27](https://doi.org/10.1088/0004-637X/784/1/27)
- Mace, G., Kim, H., Jaffe, D. T., et al. 2016, in *Society of Photo-Optical Instrumentation Engineers (SPIE) Conference Series*, Vol. 9908, *Ground-based and Airborne Instrumentation for Astronomy VI*, ed. C. J. Evans, L. Simard, & H. Takami, 99080C, doi: [10.1117/12.2232780](https://doi.org/10.1117/12.2232780)
- Mace, G., Sokal, K., Lee, J.-J., et al. 2018, in *Society of Photo-Optical Instrumentation Engineers (SPIE) Conference Series*, Vol. 10702, *Ground-based and Airborne Instrumentation for Astronomy VII*, ed. C. J. Evans, L. Simard, & H. Takami, 107020Q, doi: [10.1117/12.2312345](https://doi.org/10.1117/12.2312345)
- Marley, M. S., & Robinson, T. D. 2015, *Annu. Rev. Astron. Astrophys.*, 53, 279, doi: [10.1146/annurev-astro-082214-122522](https://doi.org/10.1146/annurev-astro-082214-122522)
- Marley, M. S., Saumon, D., Guillot, T., et al. 1996, *Science*, 272, 1919, doi: [10.1126/science.272.5270.1919](https://doi.org/10.1126/science.272.5270.1919)
- Marley, M. S., Saumon, D., Visscher, C., et al. 2021, arXiv e-prints, arXiv:2107.07434. <https://arxiv.org/abs/2107.07434>
- Miles, B. E., Skemer, A. J. I., Morley, C. V., et al. 2020, *AJ*, 160, 63, doi: [10.3847/1538-3881/ab9114](https://doi.org/10.3847/1538-3881/ab9114)
- Morley, C. V., Fortney, J. J., Marley, M. S., et al. 2012, *ApJ*, 756, 172, doi: [10.1088/0004-637X/756/2/172](https://doi.org/10.1088/0004-637X/756/2/172)
- . 2015, *ApJ*, 815, 110, doi: [10.1088/0004-637X/815/2/110](https://doi.org/10.1088/0004-637X/815/2/110)
- Niemann, H. B., Atreya, S. K., Carignan, G. R., et al. 1998, *J. Geophys. Res.*, 103, 22831, doi: [10.1029/98JE01050](https://doi.org/10.1029/98JE01050)
- Noll, K. S., Geballe, T. R., Leggett, S. K., & Marley, M. S. 2000, *ApJ Letters*, 541, L75, doi: [10.1086/312906](https://doi.org/10.1086/312906)
- Noll, K. S., Geballe, T. R., & Marley, M. S. 1997, *ApJ Letters*, 489, L87, doi: [10.1086/310954](https://doi.org/10.1086/310954)
- Noll, K. S., Knacke, R. F., Geballe, T. R., & Tokunaga, A. T. 1988, *ApJ*, 324, 1210, doi: [10.1086/165975](https://doi.org/10.1086/165975)
- Noll, K. S., McGrath, M. A., Trafton, L. M., et al. 1995, *Science*, 267, 1307, doi: [10.1126/science.7871428](https://doi.org/10.1126/science.7871428)

- Oppenheimer, B. R., Kulkarni, S. R., Matthews, K., & Nakajima, T. 1995, *Science*, 270, 1478, doi: [10.1126/science.270.5241.1478](https://doi.org/10.1126/science.270.5241.1478)
- Oppenheimer, B. R., Kulkarni, S. R., Matthews, K., & van Kerkwijk, M. H. 1998, *ApJ*, 502, 932, doi: [10.1086/305928](https://doi.org/10.1086/305928)
- Park, C., Jaffe, D. T., Yuk, I.-S., et al. 2014, in *Society of Photo-Optical Instrumentation Engineers (SPIE) Conference Series*, Vol. 9147, *Ground-based and Airborne Instrumentation for Astronomy V*, ed. S. K. Ramsay, I. S. McLean, & H. Takami, 91471D, doi: [10.1117/12.2056431](https://doi.org/10.1117/12.2056431)
- Partridge, H., & Schwenke, D. W. 1997, *J. Chem. Phys.*, 106, 4618, doi: [10.1063/1.473987](https://doi.org/10.1063/1.473987)
- Polyansky, O. L., Kyuberis, A. A., Zobov, N. F., et al. 2018, *MNRAS*, 480, 2597, doi: [10.1093/mnras/sty1877](https://doi.org/10.1093/mnras/sty1877)
- Prinn, R. G., & Barshay, S. S. 1977, *Science*, 198, 1031, doi: [10.1126/science.198.4321.1031](https://doi.org/10.1126/science.198.4321.1031)
- Radigan, J., Lafrenière, D., Jayawardhana, R., & Artigau, E. 2014, *ApJ*, 793, 75, doi: [10.1088/0004-637X/793/2/75](https://doi.org/10.1088/0004-637X/793/2/75)
- Roellig, T. L., Van Cleve, J. E., Sloan, G. C., et al. 2004, *ApJS*, 154, 418, doi: [10.1086/421978](https://doi.org/10.1086/421978)
- Rothman, L. S., Jacquemart, D., Barbe, A., et al. 2005, *J. Quant. Spectrosc. Radiative Transfer*, 96, 139, doi: [10.1016/j.jqsrt.2004.10.008](https://doi.org/10.1016/j.jqsrt.2004.10.008)
- Rothman, L. S., Gordon, I. E., Barbe, A., et al. 2009, *J. Quant. Spectrosc. Radiative Transfer*, 110, 533, doi: [10.1016/j.jqsrt.2009.02.013](https://doi.org/10.1016/j.jqsrt.2009.02.013)
- Rothman, L. S., Gordon, I. E., Barber, R. J., et al. 2010, *J. Quant. Spectrosc. Radiative Transfer*, 111, 2139, doi: [10.1016/j.jqsrt.2010.05.001](https://doi.org/10.1016/j.jqsrt.2010.05.001)
- Rothman, L. S., Gordon, I. E., Babikov, Y., et al. 2013, *J. Quant. Spectrosc. Radiative Transfer*, 130, 4, doi: [10.1016/j.jqsrt.2013.07.002](https://doi.org/10.1016/j.jqsrt.2013.07.002)
- Saumon, D., Geballe, T. R., Leggett, S. K., et al. 2000, *ApJ*, 541, 374, doi: [10.1086/309410](https://doi.org/10.1086/309410)
- Saumon, D., Marley, M. S., Abel, M., Frommhold, L., & Freedman, R. S. 2012, *ApJ*, 750, 74, doi: [10.1088/0004-637X/750/1/74](https://doi.org/10.1088/0004-637X/750/1/74)
- Schneider, A. C., Cushing, M. C., Kirkpatrick, J. D., et al. 2015, *ApJ*, 804, 92, doi: [10.1088/0004-637X/804/2/92](https://doi.org/10.1088/0004-637X/804/2/92)

- Seager, S., Bains, W., & Hu, R. 2013, *ApJ*, 775, 104, doi: [10.1088/0004-637X/775/2/104](https://doi.org/10.1088/0004-637X/775/2/104)
- Sharp, C. M., & Burrows, A. 2007, *ApJS*, 168, 140, doi: [10.1086/508708](https://doi.org/10.1086/508708)
- Snellen, I. A. G., Brandl, B. R., de Kok, R. J., et al. 2014, *Nature*, 509, 63, doi: [10.1038/nature13253](https://doi.org/10.1038/nature13253)
- Snellen, I. A. G., de Kok, R. J., de Mooij, E. J. W., & Albrecht, S. 2010, *Nature*, 465, 1049, doi: [10.1038/nature09111](https://doi.org/10.1038/nature09111)
- Sorahana, S., & Yamamura, I. 2012, *ApJ*, 760, 151, doi: [10.1088/0004-637X/760/2/151](https://doi.org/10.1088/0004-637X/760/2/151)
- Stahl, A. G., Tang, S.-Y., Johns-Krull, C. M., et al. 2021, *AJ*, 161, 283, doi: [10.3847/1538-3881/abf5e7](https://doi.org/10.3847/1538-3881/abf5e7)
- Strong, K., Taylor, F. W., Calcutt, S. B., Remedios, J. J., & Ballard, J. 1993, *J. Quant. Spectrosc. Radiative Transfer*, 50, 363, doi: [10.1016/0022-4073\(93\)90072-P](https://doi.org/10.1016/0022-4073(93)90072-P)
- Suárez, G., Metchev, S., Leggett, S. K., Saumon, D., & Marley, M. S. 2021, arXiv e-prints, arXiv:2107.14282. <https://arxiv.org/abs/2107.14282>
- Tannock, M. E., Metchev, S., Heinze, A., et al. 2021, *AJ*, 161, 224, doi: [10.3847/1538-3881/abeb67](https://doi.org/10.3847/1538-3881/abeb67)
- Tennyson, J., & Yurchenko, S. 2018, *Atoms*, 6, 26, doi: [10.3390/atoms6020026](https://doi.org/10.3390/atoms6020026)
- Tennyson, J., & Yurchenko, S. N. 2012, *MNRAS*, 425, 21, doi: [10.1111/j.1365-2966.2012.21440.x](https://doi.org/10.1111/j.1365-2966.2012.21440.x)
- Villanueva, G. L., Smith, M. D., Protopapa, S., Faggi, S., & Mandell, A. M. 2018, *J. Quant. Spectrosc. Radiative Transfer*, 217, 86, doi: [10.1016/j.jqsrt.2018.05.023](https://doi.org/10.1016/j.jqsrt.2018.05.023)
- Wenger, C., & Champion, J. P. 1998, *J. Quant. Spectrosc. Radiative Transfer*, 59, 471, doi: [10.1016/S0022-4073\(97\)00106-4](https://doi.org/10.1016/S0022-4073(97)00106-4)
- Yuk, I.-S., Jaffe, D. T., Barnes, S., et al. 2010, in *Society of Photo-Optical Instrumentation Engineers (SPIE) Conference Series*, Vol. 7735, *Ground-based and Airborne Instrumentation for Astronomy III*, ed. I. S. McLean, S. K. Ramsay, & H. Takami, 77351M, doi: [10.1117/12.856864](https://doi.org/10.1117/12.856864)
- Yurchenko, S. N., Barber, R. J., & Tennyson, J. 2011, *MNRAS*, 413, 1828, doi: [10.1111/j.1365-2966.2011.18261.x](https://doi.org/10.1111/j.1365-2966.2011.18261.x)

Yurchenko, S. N., & Tennyson, J. 2014, MNRAS, 440, 1649, doi: [10.1093/mnras/stu326](https://doi.org/10.1093/mnras/stu326)

Yurchenko, S. N., Tennyson, J., Barber, R. J., & Thiel, W. 2013, Journal of Molecular Spectroscopy, 291, 69, doi: [10.1016/j.jms.2013.05.014](https://doi.org/10.1016/j.jms.2013.05.014)

Zalesky, J. A., Line, M. R., Schneider, A. C., & Patience, J. 2019, ApJ, 877, 24, doi: [10.3847/1538-4357/ab16db](https://doi.org/10.3847/1538-4357/ab16db)

Chapter 4

Summary and Conclusions

In Chapter 1 of this thesis I have provided an overview of the basic properties of brown dwarfs, described their atmospheric structures, variability and rotation, atmospheric chemistry, and detailed the suite of atmospheric models currently available. Here I reiterate some of the main points of Chapter 1, followed by a summary of each of my projects (Chapters 2 and 3). Some ideas for future projects that build on the work done in this thesis are outlined in Section 4.1.

Brown dwarfs form through the same mechanism as stars (through the collapse of a giant molecular cloud), but are distinct from stars as they have masses below the mass required to ignite and sustain hydrogen fusion ($M \lesssim 0.070 M_{\odot}$ or $73 M_{\text{Jup}}$). The more massive brown dwarfs ($M \gtrsim 0.012 M_{\odot}$ or $13 M_{\text{Jup}}$) are able to sustain deuterium burning in their early lives. Since they lack an internal energy source, brown dwarfs tend to be low luminosity and have low effective temperatures ($T_{\text{eff}} \lesssim 2600$ K), although their interior temperatures remain hot enough to ionize hydrogen.

Brown dwarfs are classified into three spectral types: L, T, and Y. The L dwarfs are the hottest ($T_{\text{eff}} \gtrsim 1400$ K) and have atmospheres comprised of carbon monoxide and water gases, along with hydrides and alkali elements. In T dwarfs ($1400 \text{ K} \gtrsim T_{\text{eff}} \gtrsim 500$ K), water opacities strengthen, the main carbon-bearing molecule switches from carbon monoxide to methane, and sulfides and salts are present in their atmospheres. In the coolest brown dwarfs, Y dwarfs ($T_{\text{eff}} \lesssim 500$ K), ammonia joins water and methane as one of the three dominant atmospheric constituents.

These molecules settle at various altitudes in the outer regions of brown dwarfs, resulting in layered, cloudy atmospheres. Clouds are one of the most important characteristics of brown dwarfs, as they influence the spectral energy distributions and give rise to variability in the observed brightness of brown dwarfs. As surface inhomogeneities like patchy clouds and bands rotate in and out of view, the amount of flux reaching Earth varies. It is now known through extensive photometric monitoring surveys that variability in brown dwarfs is common, and

most brown dwarfs are fast rotators with rotation periods on the order of hours to tens of hours.

The fascinating properties of brown dwarfs are encapsulated in modern atmospheric and evolutionary models, which incorporate updated equations of state, opacities for exotic molecules, disequilibrium effects, and sophisticated cloud models. The atmospheric models have significantly improved our understanding of brown dwarf atmospheric physics, and models including clouds have helped to explain perplexing properties in brown dwarf observations; e.g., the colour-reversal at the L/T transition. Atmospheric models are an important tool for determining the physical parameters of brown dwarfs and for planning future observations.

In Chapter 2 of this thesis, I have presented observations and analysis that give insights to the maximum rotation rates of brown dwarfs. Using Spitzer Space Telescope mid-infrared data I determined the rotation periods of three very rapidly rotating brown dwarfs. Based on their 3.6 μm and 4.5 μm light curves, the T7, L8, and L3.5 dwarfs have the shortest periodicities measured to date: 1.08, 1.14, and 1.23 hours, respectively. Using a periodogram analysis I found significant periodogram peaks when compared to over 450 field stars, and I found no correlation between the flux and position on the detector, indicating that the observed periodicities are real. I found a wavelength-dependent amplitude difference between the three spectral types that can be explained by the dominant gas absorption species in the atmosphere.

To confirm that the brown dwarfs were truly rapidly rotating and we were not observing a repeated spot pattern on a more slowly rotating object, I investigated the degree of Doppler broadening in the near-infrared spectra of the three brown dwarfs. I compared the spectra to the most up-to-date atmospheric models and found rotation rates consistent with the short periodicities in the Spitzer data ($v \sin i$ values of 103.5, 79.0, and 82.6 km s^{-1} for the T7, L8, and L3.5, respectively).

All three L and T dwarfs spin at $\gtrsim 100 \text{ km s}^{-1}$ at their equators and are the most rapidly spinning field brown dwarfs known to date. As such, they are excellent candidates for seeking auroral radio emission, which has been linked to rapid rotation in ultra-cool dwarfs. We found that the objects have oblateness factors of between 5% and 8%, which makes them excellent targets for seeking net optical or infrared polarization. When put in to context with the full sample of measured rotation periods for L, T, and Y dwarfs, the three rapid rotators appear to lie near a short-period limit of approximately 1 hour across all brown dwarf spectral types. We therefore consider it unlikely that rotation periods much shorter than 1 hour exist for brown dwarfs.

The most up-to-date model atmospheres of brown dwarfs recreate most observations with excellent accuracy, but there are still some outstanding problems, particularly for matching

the observed spectra of cold ($T_{\text{eff}} < 1400$ K) brown dwarfs. Benchmark observations like the Gemini/IGRINS spectrum of the T6 dwarf presented in Chapter 3 are essential for confirming the completeness of model atmospheres and the accuracy of experimental and theoretical line lists used in model spectra. I studied Gemini South/IGRINS observations of the T6 dwarf 2MASS J08173001–6155158 with unprecedented resolution ($R=45,000$) and signal to noise ratio ($\text{SNR}>200$) for a late-T dwarf. After a careful confirmation of the wavelength solution, I compared the observed spectra to the most up-to-date model spectra and investigated the accuracy of the models and molecular line lists. I identified the most reliable and consistent near-infrared wavelength regions of the model spectra when compared to observations, and I found that only the most recent methane line list (Hargreaves et al., 2020) matched the observed absorption features. Additionally, I report the first unambiguous detection of hydrogen sulfide in an extra-solar atmosphere, and I identify several absorption features in the observed spectrum that do not appear in any of the models. Finally, I present a detailed near-infrared spectroscopic atlas with identified absorption features across the H and K bands. This study shows that updated line lists for water, methane, and ammonia allow for very precise empirical determinations of physical parameters, and are highly promising for the detection and characterization of exoplanets with high-dispersion spectroscopy.

4.1 Future Work

The three ultra-fast rotators presented in Chapter 2 present a unique opportunity for follow-up studies because their short rotation periods mean little time is required to observe multiple rotations. The T7 dwarf 2MASS J03480772–602227 has already been selected as a commissioning target for the James Webb Space Telescope (launch December 2021) under a Guaranteed Time Observations program (PI: T. Roellig).¹ This T7 dwarf will be investigated spectroscopically in the near-infrared and mid-infrared, and also as a near-infrared spectroscopic time series under this program.

The apparent speed limit on brown dwarf rotation rates found in Chapter 2 may help us understand brown dwarf interiors; rapid rotation may affect how the mass inside an astronomical object is distributed, and how heat is conducted through the interior. Rotation rates may also affect the hydrogen burning limit (Chowdhury et al., 2021). Additionally, fast rotation ($v \sin i \geq 60 \text{ km s}^{-1}$) has also been linked to linear polarization (e.g., Miles-Pérez et al. 2013), and to powering auroral emissions (e.g., Kao et al. 2018), making these three brown dwarfs excellent candidates for the detection of polarization and aurorae.

The large collections of measured brown dwarf rotational periods, combined with the fact

¹ <https://www.stsci.edu/jwst/phase2-public/1189.pdf>

that brown dwarfs contract to nearly constant radii ($0.8\text{--}1.0 R_{\text{Jup}}$ by ages of ≥ 500 Myr) allow for a precise determination of inclination when combined with spectroscopic $v \sin i$ measurements. Over the course of my PhD I have collected moderate- to high-dispersion near-infrared spectra of periodically variable L and T dwarfs from the Weather on Other Worlds sample (Heinze et al., 2013; Metchev et al., 2015) to investigate viewing geometry by measuring $v \sin i$. Improved $v \sin i$ measurements may be made for brown dwarfs following the guidance I provide in Chapter 3 for utilizing brown dwarf atmospheric models.

Viewing geometries may be used to investigate the promising relation between the spin axis inclination and the colours of brown dwarfs. Metchev et al. (2015) have found that variable brown dwarfs tend to be redder in colour, and Vos et al. (2017) investigated the relationship between colour and inclination, finding that redder colours correlate with high-inclinations (equator-on viewing angles) and bluer in colours correlate with low-inclinations (pole-on viewing angles). The colour-trends of the L/T transition cannot be completely explained or precisely reproduced even with the most sophisticated cloud models, but this geometric dependence may offer an explanation for these discrepancies if proven.

Any targets found to have an edge-on spin-axis inclinations will make excellent candidates for planetary transit searches, as spin-orbit alignment is expected between the host object and any surrounding planetary system. The upcoming Photometric Observations of Extrasolar Transits mission (POET; PI: J. Rowe)² aims to detect Earth-like planets around nearby cool stars, including brown dwarfs. The most efficient way to perform such a transit survey would be to target brown dwarfs which are known to be viewed close to equator-on, to increase the probability of witnessing a transit. Planets orbiting ultra-cool dwarfs also offer excellent prospects for atmospheric characterization with the James Webb Space Telescope because of the larger feature contrast during transit and eclipse spectroscopy (due to the comparable sizes of brown dwarfs and any planets they may host).

In addition to planetary searches, any further understanding of brown dwarf physics may also be extended to gas giant planets around other stars, allowing us to study atmospheric weather patterns on extra solar planets and to understand their driving mechanisms. Brown dwarfs make excellent planet analogues: they make for an easily-observed substitute because of their similar effective temperatures, radii, and atmospheric content. Many of the planets which have been directly imaged to date share observational properties with brown dwarfs. From brown dwarf atmospheric studies, we have learned that condensate cloud formation is particularly important in low-temperature atmospheres, and comparisons of the HR 8799 planets (Marois et al., 2008, 2010) to models of L dwarf atmospheres have shown that iron and silicate clouds play an important role in giant planet atmospheres (e.g., Marois et al. 2008;

² <https://kona.ubishops.ca/microsat/our-mission.html>

[Barman et al. 2011](#)). New telescopes and instruments such as the James Webb Space Telescope and the coming upgrades to the Gemini Planet Imager (GPI 2.0; coming to Gemini North in 2022) will expand our sample of directly imaged exoplanets and help us to better understand their complicated atmospheres and their shared properties with brown dwarfs. Based on my analysis in Chapter 3, the most up-to-date water and methane line lists are highly promising for the detection and characterization of exoplanets with high-dispersion spectroscopy.

Bibliography

- Barman, T. S., Macintosh, B., Konopacky, Q. M., & Marois, C. 2011, *ApJ*, 733, 65, doi: [10.1088/0004-637X/733/1/65](https://doi.org/10.1088/0004-637X/733/1/65)
- Chowdhury, S., Banerjee, P., Garain, D., & Sarkar, T. 2021, arXiv e-prints, arXiv:2107.02691. <https://arxiv.org/abs/2107.02691>
- Hargreaves, R. J., Gordon, I. E., Rey, M., et al. 2020, *ApJS*, 247, 55, doi: [10.3847/1538-4365/ab7a1a](https://doi.org/10.3847/1538-4365/ab7a1a)
- Heinze, A. N., Metchev, S., Apai, D., et al. 2013, *ApJ*, 767, 173, doi: [10.1088/0004-637X/767/2/173](https://doi.org/10.1088/0004-637X/767/2/173)
- Kao, M. M., Hallinan, G., Pineda, J. S., Stevenson, D., & Burgasser, A. 2018, *ApJS*, 237, 25, doi: [10.3847/1538-4365/aac2d5](https://doi.org/10.3847/1538-4365/aac2d5)
- Marois, C., Macintosh, B., Barman, T., et al. 2008, *Science*, 322, 1348, doi: [10.1126/science.1166585](https://doi.org/10.1126/science.1166585)
- Marois, C., Zuckerman, B., Konopacky, Q. M., Macintosh, B., & Barman, T. 2010, *Nature*, 468, 1080, doi: [10.1038/nature09684](https://doi.org/10.1038/nature09684)
- Metchev, S. A., Heinze, A., Apai, D., et al. 2015, *ApJ*, 799, 154, doi: [10.1088/0004-637X/799/2/154](https://doi.org/10.1088/0004-637X/799/2/154)
- Miles-Pérez, P. A., Zapatero Osorio, M. R., Pallé, E., & Peña Ramírez, K. 2013, *A&A*, 556, A125, doi: [10.1051/0004-6361/201321851](https://doi.org/10.1051/0004-6361/201321851)
- Vos, J. M., Allers, K. N., & Biller, B. A. 2017, *ApJ*, 842, 78, doi: [10.3847/1538-4357/aa73cf](https://doi.org/10.3847/1538-4357/aa73cf)

Curriculum Vitae

MEGAN E. TANNOCK

ORCID ID: 0000-0002-9445-2870

EDUCATION

PhD Astronomy, University of Western Ontario, London, ON, December 2021. Thesis: *Brown Dwarf Atmospheres at High Cadence and Spectral Resolution: A Speed Limit on Brown Dwarf Rotation and a Spectroscopic Atlas of a 1050 K Atmosphere*, Supervisor: Dr. S. Metchev

MSc Astronomy, University of Western Ontario, London, ON, August 2017. Thesis: *Weather on Other Worlds: the Three Fastest Rotating Ultra-Cool Dwarfs*, Supervisor: Dr. S. Metchev

BSc Honours Physics and Astronomy with Co-op Distinction, University of Victoria, Victoria, BC, April 2015. Thesis: *Testing models of high mass star formation with CFHT/WIRCam imaging of IRAS 20126+4104*, Supervisors: Dr. K. Thanjavur & Dr. K. Venn

PUBLICATIONS

Tannock, M. E.; Metchev, S. A.; Heinze, A.; Miles-Páez, P. A.; Gagné, J.; Burgasser, A.; Apai, D.; Suarez, G.; Marley, M.; Plavchan, P.; Radigan, J. *Weather on Other Worlds: the Three Fastest Rotating Ultra-Cool Dwarfs*. Accepted for publication in the *Astronomical Journal*.

Kellogg, K.; Metchev, S.; Miles-Páez, P. A.; **Tannock, M. E.** *A Statistical Survey of Peculiar L and T Dwarfs in SDSS, 2MASS, and WISE*, 2017, *The Astronomical Journal*, 154, 112.

Burningham, B.; Hardcastle, M.; Nichols, J. D.; Casewell, S. L.; Littlefair, S. P.; Stark, C.; Burleigh, M. R.; Metchev, S.; **Tannock, M. E.**; and others, *A LOFAR mini-survey for low-frequency radio emission from the nearest brown dwarfs*, 2016, *Monthly Notices of the Royal Astronomical Society*, 463, 2202.

Gerard, B.; Lawler, S.; Marois, C.; **Tannock, M.**; Matthews, B.; Venn, K., *Searching for the HR 8799 Debris Disk with HST/STIS*, 2016, *The Astrophysical Journal*, 823, 149.

Martoli, E.; Teeple, D.; Manset, N.; Devost, D.; Withington, K.; Venne, A.; **Tannock, M.**, *Open Source Pipeline for ESPaDOnS Reduction and Analysis*, 2012, *Proceedings of SPIE*, Vol. 8451, 2.

AWARDS

- 2020 Ontario Graduate Scholarship – \$15,000
- 2019 University of California Santa Cruz Other Worlds Laboratory Mini Grant – \$3,000
- 2019 William H. Wehlau Award in Astronomy – \$2,300
- 2019 Ontario Graduate Scholarship – \$15,000
- 2019 Gillis and Jenny Driesman Graduate Scholarship – \$5,000
- 2018 Ontario Graduate Scholarship – \$15,000
- 2018 Faculty of Science Graduate Student Teaching Award
- 2017 Canadian Astronomical Society Student Presentation Award, Best Poster
- 2015 University of Western Ontario Graduate Entrance Award – \$2,500
- 2014 NSERC Undergraduate Student Research Award – \$4,500
- 2014 UVic Physics and Astronomy Co-op Report Award, Honourable Mention
- 2013 UVic Physics and Astronomy Co-op Report Award, Best Report

OTHER RESEARCH EXPERIENCE

- ATLAS Electronics Upgrades Student (NSERC USRA)* May 2014 - Sept. 2014
University of Victoria, Victoria, BC
- Designed, built, and tested high-precision, low-noise, voltage controlled current sources for testing of the new ATLAS liquid-argon calorimeter electronics
- Data Analyst and Software Development Intern* May 2013 - Sept. 2013
Canada France Hawaii Telescope, Kamuela, HI
- Performed a statistical analysis of WIRCam data to upgrade the I'iwi Pipeline, assisted with determining the source of structure in dark images
- Exoplanet Research Intern* Jan. 2013 - April 2013
NRC Herzberg Institute of Astrophysics, Victoria, BC
- Investigated bound and background objects and the existence of a debris disk around HR 8799 by designing an optimized PSF subtraction
 - Reduced and analyzed high-contrast images from Keck, Spitzer, and HST
- Software Development Intern* May 2012 - Sept. 2012
Canada France Hawaii Telescope, Kamuela, HI
- Wrote and tested extensive image classes and data processing modules for the OPERA Pipeline, assisted with debugging and optimizing the code
- Instrument Monitoring and Support Intern* Sept. 2011 - Jan. 2012
Gemini North Observatory, Hilo, HI
- Debugged and completed a fully automatic Python script for monitoring the performance of the Gemini Near-Infrared Spectrograph

TEACHING EXPERIENCE

Teaching Assistant, Department of Physics and Astronomy, University of Western Ontario

- 2020 Marker, course: Astronomy 2201B, Planetary Systems
- 2019 First year physics tutorial instructor, course: Physics 1501A, 1502B
- 2019 Second year physics laboratory instructor, course: Physics 2910
- 2018 First year physics help centre instructor, course: Physics 1028A
- 2018 Second year physics laboratory instructor, course: Physics 2910
- 2018 First year physics help centre instructor, course: Physics 1029B
- 2017 First year physics help centre instructor, course: Physics 1028A
- 2017 Marker, course: Astronomy 2022B, The Origins of the Universe
- 2017 First year physics help centre instructor, course: Physics 1029B
- 2016 First year physics help centre instructor, course: Physics 1028A
- 2016 First year physics laboratory instructor, courses: Physics 1302B, 1402B, 1029B
- 2015 First year physics laboratory instructor, courses: Physics 1301A, 1401A, 1028A

OBSERVING PROPOSALS

- 2020B *Completing a High-dispersion Spectroscopic Survey for Accurate Velocimetry of Brown Dwarfs*, Gemini North/GNIRS, 23.3 hours (PI)
- 2020B *Completing a High-dispersion Spectroscopic Survey for Accurate Velocimetry of Brown Dwarfs*, Gemini South/IGRINS, 0.5 hours (PI)
- 2020A *Brown Dwarfs Viewed Equator-on: Seeking the Best Hosts for Biosignature Detection in Transiting Exoplanets*, Gemini North/GNIRS, 5.00 hours (PI)
- 2019 *Investigating the Rotation-Activity Relation in Ultracool Dwarfs*, VLA, 5.80 hours (Co-I)

- 2019 *Confirming the First Exoplanet around an L Dwarf*, Spitzer/IRAC, 316.8 hours, Director's Discretionary Time (Co-I)
- 2019A *Brown Dwarfs Viewed Equator-on: Seeking the Best Hosts for Biosignature Detection in Transiting Exoplanets*, Gemini North/GNIRS, 11.7 hours (PI)
- 2018 *Ultra-cool dwarfs viewed equator-on: surveying the best host stars for biosignature detection in transiting exoplanets*, Spitzer/IRAC, 1074.7 hours (Co-I)
- 2018B *Brown Dwarfs Viewed Equator-on: Seeking the Best Hosts for Biosignature Detection in Transiting Exoplanets*, Gemini North/GNIRS, 26.7 hours (PI)
- 2018A *Brown Dwarfs Viewed Equator-on: Seeking the Best Hosts for Biosignature Detection in Transiting Exoplanets*, Gemini South/IGRINS, 15.5 hours (PI)
- 2018A *Brown Dwarfs Viewed Equator-on: Seeking the Best Hosts for Biosignature Detection in Transiting Exoplanets*, Gemini North/GNIRS, 22.0 hours (PI)
- 2017B *Brown Dwarfs Viewed Equator-on: Seeking the Best Hosts for Biosignature Detection in Transiting Exoplanets*, IRTF/iSHELL, 1 night (PI)
- 2017B *Brown Dwarfs Viewed Equator-on: Seeking the Best Hosts for Biosignature Detection in Transiting Exoplanets*, Gemini North/GNIRS, 25.4 hours (PI)
- 2013 *Testing the core accretion model of high mass star formation with WIRCam JHKs imaging of IRAS 20126+4104*, CFHT/WIRCam, 1 hour (PI)
- 2012 *Testing the core accretion model of high mass star formation with WIRCam JHKs imaging of IRAS 20126+4104*, CFHT/WIRCam, 1 hour (PI)

CONFERENCES, PRESENTATIONS & SUMMER SCHOOLS

- 2021 Gemini Science Meeting, Online
- 2021 Canadian Astronomical Society Annual Meetings, Online
- 2021 The Cambridge Workshop on Cool Stars, Stellar Systems, and the Sun, digital poster: *Weather on Other Worlds V: the Three Fastest Rotating Ultra-Cool Dwarfs*, Online
- 2020 Other Worlds Laboratory Exoplanet Summer Program, presentation: *Spectroscopy of brown dwarfs*, University of California Santa Cruz, Santa Cruz, CA. Accepted with full funding, workshop cancelled due to pandemic
- 2020 Canadian Astronomical Society Annual Meetings, York, ON (conference moved online)
- 2020 Celebrating the Legacy of the Spitzer Space Telescope, presentation: *Weather on Other Worlds: Investigating Brown Dwarf Variability with the Spitzer Space Telescope*, Caltech, Pasadena, CA
- 2019 Other Worlds Laboratory Exoplanet Summer Program, presentation: *Spectroscopy of brown dwarfs and the implications of fast rotation*, University of California Santa Cruz, Santa Cruz, CA
- 2019 Canadian Astronomical Society Annual Meetings, poster: *A Spitzer search for rocky planets around equator-on ultra-cool dwarfs*, Montréal, QC
- 2019 Summer Schools in Statistics for Astronomers, Center for Astrostatistics, Pennsylvania State University, State College, PA
- 2019 University of Waterloo, invited talk: *Women in Physics & Astronomy: A Quick Look at Gender and Equity*, Waterloo, ON
- 2019 UWO Undergraduate Seminar, guest speaker: *Women in Physics & Astronomy: A Quick Look at Gender and Equity*, London, ON
- 2018 UWO Graduate Seminar, guest speaker, presentation: *Women in Physics & Astronomy: A Quick Look at Gender and Equity*, London, Canada

- 2018 The Cambridge Workshop on Cool Stars, Stellar Systems, and the Sun, poster: *Weather on Other Worlds: Discovery of Three Extremely Fast Rotating Brown Dwarfs*, Boston, USA
- 2018 Canadian Astronomical Society Annual Meetings, presentation: *Weather on Other Worlds: Discovery of Three Extremely Fast Rotating Brown Dwarfs*, Victoria, BC
- 2017 Introduction to Astronomical Instrumentation Summer School, Dunlap Institute, University of Toronto, Toronto, ON
- 2017 Women in Astronomy IV, poster: *Weather on Other Worlds: Discovery of Three Extremely Fast Rotating Brown Dwarfs*, Austin, TX
- 2017 Canadian Astronomical Society Annual Meetings, poster: *Weather on Other Worlds: Discovery of Three Extremely Fast Rotating Brown Dwarfs*, Edmonton, AB
- 2017 Fallona Family Interdisciplinary Research Showcase, poster: *Weather on Other Worlds: Discovery of Three Extremely Fast Rotating Brown Dwarfs*, London, ON
- 2016 The Cambridge Workshop on Cool Stars, Stellar Systems, and the Sun, poster: *Weather on Other Worlds: Discovery of Three Extremely Fast Rotating Brown Dwarfs*, Uppsala, Sweden
- 2015 Fallona Family Interdisciplinary Research Showcase, poster: *Weather on Other Worlds: Implications for JWST Spectroscopy of Variable Brown Dwarfs*, London, ON
- 2015 Enabling Transiting Exoplanet Science with JWST Workshop, poster: *Weather on Other Worlds: Implications for JWST Spectroscopy of Variable Brown Dwarfs*, Baltimore, MD
- 2014 ATLAS Canada National Student Research Presentations, presentation: *Developing Pulse forming Electronics to test the Baseplane Hadronic Endcap Calorimeterer*, Victoria, BC
- 2014 Royal Astronomical Society of Canada General Assembly, poster: *Testing models of high mass star formation with CFHT/WIRCam JHKs imaging*, Victoria, BC
- 2013 CFHT 10th Users' Meeting, poster: *Testing models of high mass star formation with CFHT/WIRCam JHKs imaging*, Campbell River, BC

TECHNICAL SKILLS

Programming Languages: IDL, Python, R, C++, Java

Astronomy Software: IRAF, PyRAF, Source Extractor, TOPCAT, APT

Other Software: LaTeX, Mathematica, GIMP, COMSOL Multiphysics Modelling, SuperMongo

Laboratory Skills: Competent with analog electronics, prototyping, soldering

OUTREACH & COMMUNITY INVOLVEMENT

- 2021 Physics World Weekly Podcast, interview
- 2021 AM980 CFPL Morning Show, interview
- 2017-2020 CASCA Graduate Student Council, representative for the University of Western Ontario
- 2017-2018 University of Western Ontario Fall Preview Day for prospective students, laboratory tour guide
- 2016-2017 University of Western Ontario Graduate Student Council member
- 2013-2014 Involved in the effort to re-open the *Centre of the Universe* astronomy outreach facility, attended shareholders' meetings, contacted media (radio interview on CFX 1070AM, article published in the Times Colonist Newspaper)
- 2012-2013 Kohala Elementary Astronomy Education Nights, volunteer
- 2011-2013 Office of Mauna Kea Management Environmental Program: mountain preservation and invasive species removal, volunteer
- 2010-2015 UVic Physics and Astronomy Student Society, vice president
- 2009-2015 Don Wright Symphonic Winds Community Ensemble, lead trumpet